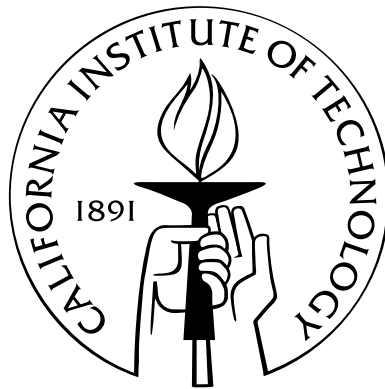


Modeling and Detecting Gravitational Waves from Compact Stellar Objects

Thesis by
Michele Vallisneri

In Partial Fulfillment of the Requirements
for the Degree of
Doctor of Philosophy



California Institute of Technology
Pasadena, California

2002
(Defended May 7, 2002)

Acknowledgements

As I sit down to write these acknowledgments, I realize what a happy journey the last four years have been, how many special and talented people I have met here at Caltech, and how many equally special people have supported me from afar. I am so lucky!

So, first of all, I wish to thank Kip Thorne, who has been everything that an advisor can be, and more. I hope I can live up to his enthusiastic and painstaking efforts to teach me, mostly by example, how to be a good scientist, how to do sound, thorough and timely research, how to live in the scientific community, and how to write clear English prose.

Kip is first, but during these years I have had other wonderful teachers. I thank Lee Lindblom for our daily chats: I never came away from them without learning something new. I thank Joel Tohline for introducing me to the wonderful world of numerical simulations, and for being a perfect host on my visit to Baton Rouge. I thank Massimo Pauri for his unfailing support of my American adventure, and for revealing to me the charm and surprise of spacetime physics. Of the other Caltech faculty that I had the good luck of interacting with, I wish to thank in particular Tom Prince, Ken Libbrecht, Marc Kamionkowski, Roger Blandford, and Sterl Phinney.

Alessandra Buonanno was a precious collaborator and a valued friend. I am thankful to her, and to Yanbei Chen, for the tremendous nonstop effort they put into the final rush to finish Chap. 4 of this thesis. As one point, I would work in the morning, Alessandra would elaborate on my output during the afternoon, and make lists of things for Yanbei to do at night. At Caltech research can truly be a 24/7 endeavor!

For support, inspiration, friendship and useful discussions (in any combination), I thank also C. Alabiso, B. Allen, L. Bildsten, L. Blanchet, L. Burko, M. Casartelli, D. Chernoff, G. M. Cicuta, R. Coisson, J. Creighton, C. Cutler, E. D'Ambrosio, T. Damour, R. De Pietri, J. Frank, J. Friedman, S. Gonçalves, G. Gonzalez, V. Kalogera, D. Kennefick, A. Lazzarini, L. Lehner, Yu. Levin, G. Mambriani, J. Mason, D. Meier, E. Onofri, M. Ortaggio, B. Owen, F. Piazza, R. Price, J. Pullin, C. Rovelli, B. Sathyaprakash, M. Scheel, A. Scotti, N. Stergioulas, K. Strain, L. Superchi, M. Tinto, G. Ushomirsky, A. Vicerè, and everybody else that I forget about now.

For kindling my love of the English language, and for helping me conceive and realize the dream of studying in the States, I thank Valeria Monguidi, Wallis Wilde-Menzozi, and Margosha Krauze.

I wish to thank also all the fellow Tapirs of the last four years, and in particular the other Kiplings, Kashif Alvi (a true friend if there is one), Mihai Bondarescu, Teviet Creighton, Scott Hughes, Patricia Purdue, Yuk Tung Liu, and Richard O’Shaughnessy. We have shared many scientific discussions and many nonscientific ones. I loved both kinds.

For making my life in California much happier and fuller than it could have been otherwise, I thank all the wonderful friends I met here, and in particular my trio of pals, Alexei, Ed and Jason; and then Tina, Andrew, Rob, Bill (especially Bill!), and all the Phys. Rev. Netters. My roommate Mika was a lot of fun to live with, and an inexhaustible resource on literally any computing machine ever made or conceived.

Chris Mach was a friend and a teacher; he taught me system administration and he fed me garlic breadsticks with Alfredo sauce. What more can you ask? Shirley Hampton, Donna Driscoll and Jo-Ann Hasbach always joined their utmost professionalism with the warmest welcoming smile. Jo-Ann Ruffolo’s advice was perhaps the strongest element in my favor during my job search; and her kindness and *joie de vivre* were always refreshing in the middle of that otherwise anxiety-ridden process.

My thanks and my love go to my family, back in Italy (Dad, Mom, Cecilia, my aunts Alberta and Maria, my mother-in-law Vittoria and brother-in-law Francesco) and here in the States (Ted and Mada). Finally, thanks to my best men, faithful friends, and fellow travelers through life, Kola and Filippo. *All that is gold does not glitter, not all those who wander are lost.*

Last but not most important of all, I thank my love, Elisa, for being always on my side, for marrying me, and for making my life happier every day. It is possible that this thesis might have been completed even without her—but it would have been a joyless and somber exercise.

Now for the institutional acknowledgments: I thank CACR for access to the HP V2500 computers at Caltech, where the primary simulations featured in Chap. 3 were performed; Mark Bartelt in particular was always very helpful. Through the years, this research was supported by NSF grants AST-9731698, AST-9987344, PHY-9796079, PHY-9900776, PHY-9907949, and PHY-0099568, and by NASA grants NAG5-4093 and NAG5-8497, and NAG5-10707. I thank also Caltech for awarding me a Special Institute Fellowship during my first year of graduate school, and the PMA Division for giving me Teaching Assistantships during my third and fourth years.

Abstract

In the next few years, the first detections of gravity-wave signals using Earth-based interferometric detectors will begin to provide precious new information about the structure, dynamics, and evolution of compact bodies, such as neutron stars and black holes, both isolated and in binary systems. The intrinsic weakness of gravity-wave signals requires a proactive approach to modeling the prospective sources and anticipating the shape of the signals that we seek to detect. Full-blown 3-D numerical simulations of the sources are playing and will play an important role in planning the gravity-wave data-analysis effort. This thesis explores the interplay between numerical source modeling and data analysis, looking closely at three case studies.

1. I evaluate the prospects for extracting equation-of-state information from neutron-star tidal disruption in neutron-star–black-hole binaries with LIGO-II, and I estimate that the observation of disrupting systems at distances that yield about one event per year should allow the determination of the neutron-star radius to about 15%, which compares favorably to the currently available electromagnetic determinations.
2. In collaboration with Lee Lindblom and Joel Tohline, I perform numerical simulations of the nonlinear dynamics of the r -mode instability in young, rapidly spinning neutron stars, and I find evidence that nonlinear couplings to other modes will not pose a significant limitation to the growth of the r -mode amplitude.
3. In collaboration with Alessandra Buonanno and Yanbei Chen, I study the problem of detecting gravity waves from solar-mass black-hole–black-hole binaries with LIGO-I, and I construct two families of *detection* templates that address the inadequacy of standard post-Newtonian theory to predict reliable waveforms for these systems.

Contents

Acknowledgements	iii
Abstract	v
1 Introduction	1
1.1 Gravitational waves as a probe into the structure and dynamics of neutron stars . . .	2
1.1.1 Neutron stars as GW sources	2
1.1.2 Neutron-star tidal disruption as a probe into the equation of state of dense nuclear matter	3
1.1.3 Gravity waves from the r -mode instability of nascent neutron stars	10
1.2 Gravitational waves from coalescing binaries of compact stellar objects	14
1.2.1 The statistics of coalescing binaries	15
1.2.2 Detecting BH–BH binaries with LIGO-I	16
1.2.3 Detection templates for BH–BH binaries	18
1.3 Bibliography	19
2 Prospects for gravitational-wave observations of neutron-star tidal disruption in neutron-star–black-hole binaries	23
2.1 Introduction	23
2.2 Neutron-star model	24
2.3 Parameter estimation	26
2.4 Conclusion	28
2.5 Bibliography	29
3 Numerical evolutions of nonlinear r-modes in neutron stars	32
3.1 Introduction	32
3.2 Basic hydrodynamics	34
3.3 Radiation-reaction force	36
3.4 Calibration runs	38

3.5	Evaluating the saturation amplitude	41
3.5.1	Evolution of the r -mode amplitude	43
3.5.2	A mechanism for r -mode saturation	43
3.5.3	Radial structure of the r -mode amplitude	45
3.5.4	Evolution of the r -mode frequency	46
3.5.5	Growth of differential rotation	48
3.5.6	Consistency of the radiation-reaction force	50
3.5.7	Density oscillations and mode saturation	51
3.5.8	Limits on mode–mode coupling	52
3.5.9	Dependence on the grid spacing	55
3.6	Testing the saturation amplitude	56
3.7	Free evolution	58
3.8	Repeated spindown episodes?	61
3.9	Conclusions	65
3.10	Appendix. Useful expressions in cylindrical coordinates	66
3.11	Bibliography	67
4	Detection template families for gravitational waves from the final stages of binary– black-hole inspirals	69
4.1	Introduction	69
4.2	The theory of matched-filtering signal detection	73
4.2.1	The statistical theory of signal detection	73
4.2.2	Template families and extrinsic parameters	76
4.2.3	Imperfect detection and discrete families of templates	80
4.2.4	Approximations for detector noise spectrum and gravitational-wave signal	83
4.3	Adiabatic models	84
4.3.1	Adiabatic PN expanded models	84
4.3.2	Adiabatic PN resummed methods: Padé approximants	89
4.4	Nonadiabatic models	95
4.4.1	Nonadiabatic PN expanded methods: Hamiltonian formalism	95
4.4.2	Nonadiabatic PN expanded methods: Lagrangian formalism	98
4.4.3	Nonadiabatic PN resummed methods: the effective-one-body approach	99
4.5	Comparison between the two-body models	104
4.6	Performance of the Fourier-domain detection templates	104
4.6.1	Internal match and metric	108
4.6.2	Construction of the detection template bank: parameter range	110

4.6.3	Construction of the detection templates bank: parameter density	114
4.6.4	Parameter estimation with the detection templates	116
4.7	Performance of the time-domain detection templates	117
4.8	Summary	121
4.9	Bibliography	130

List of Figures

2.1	Plot of noise spectral density for different LIGO configurations	24
2.2	NS radius R vs. disruption-onset frequency f_{td} , for $m = 1.4 M_{\odot}$ and $M = 2.5\text{--}80 M_{\odot}$.	26
3.1	Evolution of the r -mode amplitude in a slowly rotating star	39
3.2	Real and imaginary parts of the current multipole moment J_{22} for run C1	40
3.3	Frequency of the $m = 2$ r -mode for run C1	41
3.4	Numerical evolution of $\text{Re } J_{22}$ in production run C3	42
3.5	Numerical evolution of the r -mode amplitude α in production run C3	42
3.6	Evolution of total mass, total angular momentum, and total kinetic energy in production run C3	43
3.7	Theoretical and numerical evolution of the total energy in production run C3	44
3.8	Isodensity surfaces showing breaking waves near the end of production run C3	45
3.9	Radial amplitude density $\alpha(r)$ of the $m = 2$ r -mode in production run C3 at $t = 22.5P_0$	46
3.10	Evolution of the phase-coherence function $\Delta\phi$ in production run C3	47
3.11	Numerical evolution of the r -mode frequency ω in production run C3	47
3.12	Numerical evolution of the average stellar angular velocity $\bar{\Omega}$ in production run C3 . .	48
3.13	Numerical evolution of the differential rotation $\Delta\Omega$ in production run C3	49
3.14	Meridional structure of the differential rotation in production run C3	49
3.15	Numerical evolution of the mass moment Q_{32} and of the r -mode amplitude α in production run C3	52
3.16	Numerical evolution of the r -mode amplitude α in low-resolution run C3* and in run C3	55
3.17	Numerical evolution of the r -mode amplitude α in production runs C3–C5	57
3.18	Numerical evolution of the r -mode frequency ω in production runs C3–C5	57
3.19	Numerical evolution of the differential rotation $\Delta\Omega$ in production runs C3–C5	58
3.20	Numerical evolution of the r -mode amplitude α in production runs C6–C8	59
3.21	Numerical evolution of the r -mode frequency ω in production runs C6 and C7	60
3.22	Numerical evolution of the differential rotation $\Delta\Omega$ in production runs C6–C8	60
3.23	Numerical evolution of the r -mode amplitude α in the extended run C4	62
3.24	Numerical evolution of the r -mode frequency ω in the extended run C4	63

3.25	Differential rotation $\Delta\Omega$ through the extended run C4	63
3.26	Meridional structure of differential rotation at the end of production run C4	64
4.1	Square root of the noise spectral density $\sqrt{S_n(f)}$ for LIGO-I and VIRGO	83
4.2	(i) Normalized flux function $\mathcal{F}_{T_N}/\mathcal{F}_{\text{Newt}}$ at various PN orders for $\eta = 0.25$. (ii) Effect of the parameter $\hat{\theta}$ on the normalized flux function at 3PN and 3.5PN orders	85
4.3	(i) Energy function \mathcal{E}_{T_N} at different PN orders for $\eta = 0.25$. (ii) Percentage difference in the energy function at the LIGO-I peak-sensitivity GW frequency	86
4.4	Frequency-domain amplitude for T models at different PN orders	89
4.5	(i) Normalized flux function $\mathcal{F}_{P_N}/\mathcal{F}_{\text{Newt}}$ at different PN orders. (ii) Percentage difference in the flux function between the T- and P-approximants	90
4.6	(i) Energy function \mathcal{E}_{P_N} at different PN orders. (ii) Percentage difference in the energy function between 2PN and 3PN P-approximants	91
4.7	Percentage difference between T- and P-approximants to the energy function, at the LIGO-I peak-sensitivity GW frequency	93
4.8	Frequency-domain amplitude for the P models	94
4.9	Frequency-domain amplitude of the HT and HP models	97
4.10	Frequency-domain amplitude of the EP models	104
4.11	Binding energy $\mathcal{E}(v)$ for equal-mass BBHs	105
4.12	Signal-to-noise ratio at 100 Mpc versus total mass M for selected PN models	106
4.13	Iso-match contours for the function $\langle h(\psi_0, \psi_{3/2}), h(\psi_0 + \Delta\psi_0, \psi_{3/2} + \Delta\psi_{3/2}) \rangle$; values of Δf_{cut} (versus f_{cut}) required to obtain matches $\langle h(f_{\text{cut}}), h(f_{\text{cut}} + \Delta f_{\text{cut}}) \rangle$ of 0.95, 0.975 and 0.99.	110
4.14	Projection of the ET(2, 5/2) waveforms onto the frequency-domain detection template space	111
4.15	Projection of the PN waveforms onto the Fourier-domain detection templates	113
4.16	Projection of PN waveforms onto the P(2, 5/2) detection template space	119
4.17	Projection of PN waveforms onto the EP(3, 7/2) detection template space	120
4.18	Determinant of the Owen metric for the P(2, 5/2) and EP(3, 7/2, 0) models	121

List of Tables

1.1	Qualitative summary of the Newtonian simulations of NS tidal disruption in NS–BH binaries	9
1.2	Estimated coalescence and detection rates for compact binaries	15
2.1	Fractional uncertainty $\Delta R/R$, averaged over the range $10 \text{ km} < R < 15 \text{ km}$	28
3.1	Physical parameters for the equilibrium models	38
4.1	Location of the MECO for T-approximants	87
4.2	Cauchy convergence of the T-approximants	87
4.3	Location of the MECO for P-approximants	91
4.4	Cauchy convergence of the P-approximants	92
4.5	Cauchy convergence of the HP-approximants	96
4.6	Fitting factors for the projection of the L model onto several PN models	99
4.7	Location of the ISCO for the EOB-improved Hamiltonian	101
4.8	Cauchy convergence of the EP-approximants	102
4.9	End-to-end matches and number of templates (for $MM \simeq 0.98$) along the mass lines of Fig. 4.15	112
4.10	Ranges for the ending frequencies of PN waveforms along the mass lines of Fig. 4.15	114
4.11	Estimation of the chirp masses \mathcal{M} from the projections of the PN target models onto the Fourier-domain detection template space	117
4.12	Fitting factors between T and ET models, at 2PN and 3PN orders	124
4.13	Fitting factors for the projection of EP(3, 7/2, 0) templates onto themselves, for various choices of the parameters z_1 and z_2	125
4.14	Fitting factors between several PN models, at 2PN and 3PN orders	126
4.15	Fitting factors for the projection of the target models onto the Fourier-domain detection template family	127
4.16	Fitting factors for the projection of the target models (in the rows) onto the P(2, 5/2) detection template family	128

4.17	Fitting factors for the projection of the target models (in the rows) onto the $EP(3, 7/2, 0)$	
	detection template family	129

Chapter 1

Introduction

In the course of the next decade, the inception of gravity-wave (GW) astronomy will open an exciting new window on the physics of compact, strongly gravitating bodies, such as neutron stars (NSs) and black holes (BHs), both as isolated objects and in binaries; it will provide information complementary to that available from electromagnetic and neutrino observations; and it will produce important insights into unsolved questions such as the equation of state (EOS) of matter at nuclear densities, the evolutionary channels that create NSs and BHs, and the mechanisms behind gamma-ray bursts.

Meanwhile, sophisticated three-dimensional numerical simulations of GW sources are coming of age, allowing unprecedented investigations into the effect of the internal dynamics of compact objects on their GW emission, and slowly but surely moving toward the goals of modeling the fully relativistic dynamics of close and merging NS and BH binaries. Learning to interface numerical simulations with other general-relativistic approximation techniques and with the GW data-analysis algorithms will be of paramount importance as detector data become available. At the same time, the theory of GW detection and data analysis has become firmly established as a mature subfield of GW science. Yet the very sources that arguably give us our best chance of detecting GWs in the first ground-based searches (binary BHs with total mass $\sim 10\text{--}40M_{\odot}$) lie at the very boundary of the current data-analysis capabilities.

The interplay between analytical and numerical source modeling and data analysis is the underlying theme of this thesis. Chapter 2 and (briefly) Sec. 1.1.2 below deal with the prospects for extracting EOS information from NS tidal-disruption waves. Chapter 3 and Sec. 1.1.3 below discuss the numerical simulations of the NS r -mode instability that I have completed in collaboration with Lee Lindblom and Joel Tohline. Finally, Chapter 4 and Sec. 1.2.2 below report my work (in progress, and in collaboration with Alessandra Buonanno and Yanbei Chen) on providing detection waveforms for the detection of stellar-mass binary BHs with first-generation interferometers.

1.1 Gravitational waves as a probe into the structure and dynamics of neutron stars

Neutron stars are truly wondrous objects. They pack the mass of our Sun within diameters of 20–30 km; and they manage to be both a *bona fide* test case for the theory of general relativity, and a laboratory for the physics of matter at extreme density and temperature. Although more than a thousand NSs are known today from electromagnetic observations (most of them detected as radio pulsars), the first GW detections of these objects are eagerly awaited.

1.1.1 Neutron stars as GW sources

Detailed reviews of GW sources, of the expected event rates, and of the physics that these sources could teach us are available elsewhere [1, 2, 3]. Here I shall list briefly the most promising types of astrophysical systems from which we could learn about NSs using ground-based GW interferometers, such as LIGO and VIRGO.

1. *NS–NS and NS–BH binaries in the last few minutes of their inspirals.* For a long time, these inspiraling systems have been the prototype for the category of short-lived *chirp* signals detectable using ground-based interferometers. The reason, of course, is that NS–NS binaries have actually been observed in our galaxy [4], but also that the part of the inspiral accessible to the interferometers (with GW frequencies between 40 and 1000 Hz) sits well before the final merger of the binary, so it is described very accurately by the well-developed post-Newtonian equations for point masses (see Chap. 4). The successful observation of GWs from these inspirals will teach us about the masses, spins and locations of NSs, but not about their internal structure.

By contrast, the detection of GWs from the endpoint of NS–BH inspirals should produce detailed information about NS structure and EOS. For a wide range of binary parameters, the NS will be torn apart by the tidal field of the BH well before the final plunge into the hole, and the tidal-disruption waves will be well inside the frequency range of good interferometer sensitivity. NS–BH binaries have also been proposed as engines for gamma-ray bursts [5] and as suitable environments for the production of heavy nuclei in *r*-processes [6]. These systems are the subject of Sec. 1.1.2 and Chap. 2. The expected measured-event rates are shown in Table 1.2 and discussed briefly in Sec. 1.2.1.

2. *Rapidly spinning, deformed NSs.* This class includes the known and unknown pulsars (when their gravitational ellipticity is high enough to provide strong GWs), and the systems known as low-mass X-ray binaries (LMXB), where the NS is accreting matter and angular momentum from a companion, but instead of increasing its rotation, it is locked into spin periods of about

3 ms; it is conjectured that the angular momentum being accreted is lost to the emission of GWs [7].

To detect rapidly spinning NSs, it will be necessary to integrate the GW signal for times up to several months, so the Doppler frequency modulations caused by the earth’s spin and motion (both around the Moon and the Sun) will make it much harder to detect previously unknown sources [8]. At the same time, the shapes of these modulations will make it possible to obtain the position of the source in the sky [9], and in some cases to match the GW source with one of the objects known from electromagnetic observations.

If any GWs are detected from spinning NSs, their features will be very informative, in particular when examined in correlation with electromagnetic signals from the same source. For instance, the ratio of the GW frequency to the NS angular frequency could give information about the nature of the inhomogeneities that give rise to the GW emission, and the evolution of the GW amplitude and frequency could provide interesting data about NS physics such as crust structure and dynamics, crust–core interactions, magnetic fields, viscosity, superfluidity, and more [3].

3. *Proto-neutron stars.* Finally, NSs could be observed as the rapidly spinning, strongly asymmetric remnants of stellar-core collapse, or as the proto-NSs produced by the accretion-induced collapse of white dwarfs. Proto-NSs that spin very fast can hang up centrifugally at a stage where their radius is still large compared to that of the final NS. Such a configuration might be unstable to a bar mode, giving rise to an elongated object that would emit very strong GWs [10]. The newborn NSs might also develop a GW-induced instability in their r -modes [11]. I will discuss this possibility more extensively in Sec. 1.1.3 and Chap. 3.

For the NS in all these systems, GWs would provide information complementary to that made available by neutrino observations, focusing on the density structure and asymmetry of the collapsed stellar core rather than on its thermal structure.

1.1.2 Neutron-star tidal disruption as a probe into the equation of state of dense nuclear matter

Although modern equations of state for dense nuclear matter have benefited greatly from sophisticated theoretical computations and experimental measurements of nucleon–nucleon interactions [13, 14], our knowledge of the internal structure of NSs is still plagued by a considerable uncertainty that will be resolved only by setting stringent observational constraints.

All measurable NS parameters are relevant to this task, but it is especially promising to exploit the correspondence between the EOS and the NS mass-radius curve. Let us see briefly how this

is possible. The relativistic model of nonrotating NSs may be considered as a mapping from the (barotropic) NS EOS, $p(\rho)$, through the Oppenheimer–Volkoff (OV) equations,

$$\frac{dm(r)}{dr} = 4\pi r^2 \rho(r), \quad \frac{d\rho(r)}{dr} = -[\rho(r) + p(r)] \frac{m(r) + 4\pi r^3 p(r)}{r(r - 2m(r))}, \quad (1.1)$$

to equations that involve macroscopic NS quantities, such as a mass-radius curve $M(R)$. [In Eq. (1.1) $\rho(r)$ and $p(r)$ are the density and pressure of the spherically symmetric NS at the radius r , and $m(r)$ is the mass inside the radius r .] Let us work through the details of this mapping. First, we set the central density ρ_c ; then, we solve the OV equations and compute the NS radius $R = R(\rho_c)$ and total mass $M = M(\rho_c)$; finally, we eliminate ρ_c from these two equations, completing our mapping of the EOS $p(\rho)$ into the mass-radius relation $M(R)$.

Lindblom [15] has shown how to invert the OV mapping using even a few $M(R)$ data points (see also [14]). If $p(\rho)$ is known up to a certain density ρ_{max} from other observations and experiments, we can start with the least dense observed NS, and integrate the OV equations backward, from the surface of the star [where we know R and $M(R)$] down to the radius where $\rho = \rho_{max}$. We are left with a stellar core of known mass and radius, and we can use an analytic approximation for the solution of the OV equations (or a numerical shooting technique) to get p_c and ρ_c ; we then add the point $p_c(\rho_c)$ to the EOS, and repeat for the next NS. The result is a sequence of points along the curve $p(\rho)$. This analysis can be generalized to include rotationally deformed models, and to account for the statistical uncertainty in the $M(R)$ data¹.

Unfortunately, although many parameters, including mass and radius, have been measured for most of the ~ 1200 known NSs [13, 14, 17], to date there are no joint determinations of M and R , and the few values available for the radius are woefully imprecise, as we discuss in the next subsection.

The electromagnetic determination of NS masses

The masses of more than twenty NSs in binary pulsars have been measured by studying the modulations in the pulsar signal induced by the orbital dynamics [4]. The best measurements come from the six known NS–NS binary pulsars, but less accurate determinations are still possible for binaries where the companion is a white dwarf or a main-sequence star. This is because the measurement of both masses from orbital effects alone (except for eclipsing binaries) requires the detection of at least two of the post-Keplerian parameters that characterize relativistic effects such as periastron advance, second-order Doppler effect and gravitational redshift, Shapiro time delay, and orbital decay due to GW emission. Relativistic effects are easier to measure in short-period, eccentric NS–NS

¹Recently, Harada [16] has shown how other macroscopic parameters of NSs (such as moments of inertia, baryonic masses, binding energies, gravitational redshifts) can be used in this same framework to recover information about the EOS.

binaries, while binaries with white dwarfs or main-sequence stars tend to have larger periods and smaller eccentricities. In this case, the NS mass can be recovered if the companion mass is determined reliably from its electromagnetic spectrum. In any case, all results are compatible with a very narrow underlying Gaussian distribution, $M = 1.36 \pm 0.04 M_{\odot}$ [4].

The measurement of NS masses is also possible in X-ray pulsars and bursters. The former are believed to be NSs accreting matter from a high-mass companion ($M_c \gtrsim 10 M_{\odot}$); the pulses are emitted from the matter accreting on the magnetic poles, modulated with the period of the accreting star. Masses are measured from X-ray pulse delays, optical radial velocities and X-ray eclipses. X-ray bursters, by contrast, are believed to originate from the thermonuclear explosion of matter accreted onto the surface of an NS from a low-mass companion ($M \lesssim 1.2 M_{\odot}$). The determination of masses is obtained from a combination of time-delay effects, optical radial-velocity curves, and constraints on the inclination from X-ray eclipses. According to recent determinations, the X-ray pulsar Vela X-1 has $M = 1.87^{+0.23}_{-0.17} M_{\odot}$ [18], while the X-ray burster Cygnus X-2 has $M = 1.8 \pm 0.4 M_{\odot}$ [19]. These masses are higher than the values determined in radio pulsars, and they probably reflect the presence of the matter accreted from the companion. Last, NS masses can be constrained from the quasi-periodic oscillations (QPOs) of X-rays emitted from the gas accreting onto NSs from nearly circular orbits in binaries with low-mass companions. There is evidence that the oscillations mirror the orbital frequency of the accreting matter, which sets a tentative constraint on the NS mass [20].

The electromagnetic determination of NS radii

The determination of NS radii is much harder. The best prospects come perhaps from the direct measurement of the so-called *thermal radius* for objects like Geminga (RX J1856.5-3754). This is the nearest known NS candidate (estimated at 120 pc from parallax and circumstantial evidence), and it is not a pulsar, which should prevent contamination of the thermal emission by magnetic effects². The surface temperature is $\simeq 6 \cdot 10^5$ K, and the application of the Stefan–Boltzmann law yields a red-shifted radius $R_{\infty} = R/\sqrt{1 - 2GM/R} = 15$ km, which implies $R \simeq 12$ km [21] (but the 1σ error for R is 7 km!). Quite interestingly, a recent reinterpretation [24] of the Chandra data for Geminga using a nonmetallic atmospheric model (as seems appropriate given that no distinct lines were found in the spectrum) suggests that $R_{\infty} \simeq 3.8$ – 8.2 km, too small for most current NS models, but not for an even denser object such as a *strange star*.

In June 2003, Geminga will pass within 0.3 sec of a background star of magnitude 26.5, displacing the apparent position of this star by about $\delta\varphi = 0.6$ mas. This displacement is proportional to the NS mass; so if $\delta\varphi$ can be measured to a precision ~ 0.1 mas (as might be feasible with the Hubble Space Telescope enhanced by the Advanced Camera for Surveys), the NS mass will be determined with an error $\sim 15\%$ ([22]; see however [21]).

²However, the failure to observe this object as a pulsar might be simply due to an unfortunate beam alignment.

The thermal radius can also be derived from the measured flux of X-ray bursts, if the distance to the star is known and if the spectrum can be considered approximately thermal; however, the bursts are likely to come from restricted hot spots on the NS surface, which will result in the underestimation of the *physical* radius. Perhaps more promising is the extraction of M/R from X-ray–burst oscillations. The burst amplitude is always strongly modulated by the rotational period of the NS; however, even when the hot spot is on the far side of the star, the signal received on Earth does not vanish completely, because of the strong light bending in the gravitational field on the NS. The strength of this effect constrains the value of M/R , and therefore the value of R if M is already known; for the binaries 4U 1636-53 and 4U 1728-34, $M/R \lesssim 0.16$ with a 90% confidence [23].

Finally, it was hoped that absorption lines in the photosphere of NSs would provide M/R and M/R^2 through, respectively, gravitational redshift and pressure broadening (a simple hydrostatic argument shows that in stellar atmospheres pressure is approximately proportional to gravity). However, in practice it has been very hard to detect any usable absorption lines [17]. The bottom line is that, to date, NS radii have not been determined by electromagnetic observations with errors better than a factor of two.

The gravity-wave determination of NS masses and radii

In 1987, Thorne suggested that the GWs from the NS–BH inspirals that end in the tidal disruption of the NS can be used to determine the NS radius [25]. NS–BH mergers are one of the standard GW sources for second-generation interferometers (see Table 1.2). The waveforms generated by these events will contain two kinds of information. The early part of the inspiral (during which the NS and BH are still relatively distant, and the dynamics can be described accurately by post-Newtonian equations of motion in the point-mass approximation) will tell us about the masses and the spins of the NS and BH. The late part of the inspiral, depending on the binary parameters, can see the BH tidal field become so strong that it disrupts the NS on a dynamical timescale. Physical intuition then suggests that the details of the disruption process, as encoded in GWs, should carry useful information about the internal structure of the NS, and in particular about its EOS. In Chap. 2 (and, briefly, in the next subsection) I present my estimation of the prospects for extracting this information from the GWs that could be measured from a realistic event.

Saijo and Nakamura [26] have suggested that it might be possible to measure the NS radius directly from the spectrum of the GWs emitted in NS–BH coalescences. These authors have used BH perturbation theory to compute the spectrum of GWs emitted by a disk of dust inspiraling into a rotating BH. When the radius R_{disk} is larger than the wavelength of the quasi-normal modes of the BH, the spectrum acquires several peaks with separation $\propto R_{\text{disk}}^{-1}$, irrespective of M and a . Saijo and Nakamura conjecture that the same structure would be visible in the spectrum of GW signals from

NS–BH binaries, providing direct information about the radius. However, two key issues are left unaddressed. First, the particles of the disk move along geodesics, and the large relative deviation of the geodesics in the vicinity of the BH seems to be a necessary condition for the appearance of the spectral features; but in reality, NS matter is strongly constrained by the gravitation and pressure of the star (except, perhaps, in the regime of severe tidal disruption). Second, for coalescence events that happen at realistic distances the signal strength might be too low to let us resolve the form-factor structure in the spectrum.

A simple analytical model for NS tidal disruption

In the next few paragraphs I present a short synopsis of my analysis of the prospects for the GW measurement of NS radii, which I carry out in Chap. 2.

The simplest possible representation of an NS inspiraling into a BH is a quasi-equilibrium sequence of *relativistic Roche-Riemann ellipsoids*. These ellipsoids are equilibrium configurations of a self-gravitating, polytropic, Newtonian fluid, moving on circular, equatorial geodesics in the Kerr spacetime, and subject to the BH relativistic tidal field [27]. For these configurations, once the orbital separation r and the BH mass M and spin a are set, we can still choose the NS mass m and radius R .

As it inspirals toward the BH, an NS with parameters m and R would be represented by the appropriate Roche-Riemann ellipsoid at each separation r , until we reach a *critical* r_{cr} , beyond which no more equilibrium configurations exist. I identify this end of the equilibrium sequence with the onset of dynamical tidal disruption, and from r_{cr} I obtain the GW frequency at tidal disruption, $f_{\text{td}} = f_{\text{td}}(m, R, M, a)$. I find that f_{td} depends strongly on the NS radius, and that, for the standard NS mass $1.4M_{\odot}$ and for a variety of likely BH masses, the disruption waveforms lie in the band of good interferometer sensitivity for the advanced interferometers such as LIGO-II. It follows that, in principle, we could use the waveforms from an NS tidal-disruption event to measure both the NS mass and the NS radius.

To see how *well* we could measure them, I call on the theory of *matched-filtering parameter estimation* ([28]; see also Chap. 4). The general idea is that GWs will be detected by correlating the measured signal s to a bank of theoretical *templates* $\{u_i\}$, which represent our best approximation of the realistic GW signal as a function of the binary parameters (labeled by i). If the *match* $\langle s, u_i \rangle$ (the correlation between u_i and s) is much higher than the match $\langle u_i, n \rangle$ that the template would give, on the average, with noise alone, then we claim that we have a detection. To know how well we can estimate R , we ask how probable it is that a particular realization of detector noise would lead us to mistake the template u_R (appropriate for the NS radius R) with the nearby template $u_{R+\Delta R}$: the answer is given in terms of the match $\langle u_R, u_{R+\Delta R} \rangle$.

In the realistic case, the templates depend on *all* the parameters of the binary, and there can

be correlations in the ways that different parameters modify the templates. In my simple model, I assume that all parameters except f_{td} (and consequently, R) are already known well from of the early part of the inspiral signal, so all that is left to do is to find R . Thus, to compute the match $\langle u_R, u_{R+\Delta R} \rangle$ I construct a bank of signal templates that differ only in the GW frequency at the onset of tidal disruption. Because I am not interested in modeling accurately the relativistic dynamics of the binary, but only the effects of tidal disruption, I choose to generate my waveform templates from simple quadrupole-governed Newtonian inspirals [29], cutting off the signal more or less abruptly³ when the instantaneous GW frequency reaches f_{td} . Computing the match between nearby templates, I estimate the granularity to which f_{td} can be measured for a given signal strength (inversely proportional to distance), and propagate this error to the NS radius. The final result of this exercise is that, employing advanced ground-based interferometers, such as LIGO-II [3], we should be able to measure the NS radius to 15%, for tidal-disruption events at distances that may yield from $\sim 10^{-2}$ to 20 events per year (see Table 1.2 below). This estimated 15% error seems very competitive with respect to the electromagnetic determinations of R surveyed above. Lattimer and Prakash [14] argue that a single determination of an NS radius with error $\sim 10\%$ might be enough to constrain the NS EOS significantly.

Numerical simulations of neutron-star tidal disruption

Detailed relativistic numerical simulations are still needed to confirm these prospects, and will be essential as a foundation to interpret any tidal-disruption waveforms that might be measured in reality. The first Newtonian simulations [31] of NS–BH systems, carried out using both smooth particle hydrodynamics [6, 32] and Eulerian techniques [5, 33], show that the ultimate fate of the system depends strongly on the stiffness of the EOS, and confirm that disruption events have much to teach us about the NS EOS.

Specifically, Lee and Kluzniak [6, 32] have performed smooth-particle-hydrodynamics (SPH) simulations, where the NS is modeled as a self-gravitating Newtonian polytrope, and the BH is represented by an M/r potential with an absorbing membrane at the event horizon; the NS is subject to an effective radiation-reaction force computed from the motion of its center of mass. These authors have considered both irrotational and tidally locked initial configurations (where, respectively, the NS has no spin, or is rotating with the orbital angular velocity), with mass ratios of a few.

Janka and colleagues [5, 33] have performed Eulerian simulations where the NS is modeled as a self-gravitating Newtonian fluid with a physical equation of state, and the BH is again an M/r potential with absorbing membrane; a radiation-reaction force is introduced in the approximation

³Bildsten and Cutler [30] estimate that complete disruption would take place in ~ 1 –3 orbital periods, while the disrupted NS would spread into a ring in ~ 1 –2 periods, significantly reducing the GW amplitude.

NS EOS	tidal disruption	accretion disk	tidal tails	GW after disruption
very stiff	incomplete; light remnant on elliptical orbit	for higher mass ratios	never	lower-amplitude inspiral signal from remnant
stiff	almost complete	always	in irrotational binaries	sudden shutoff
soft	complete	always	always	sudden shutoff

Table 1.1: Qualitative summary of the Newtonian simulations [6, 32, 5, 33] of NS tidal disruption in NS–BH binaries.

we just mentioned. These authors considered irrotational, tidally locked and counterrotating initial configurations, with mass ratios of a few.

The behavior observed in these simulations is summarized in Table 1.1. Simply put, the loss of angular momentum to GWs decreases the orbital separation until Roche overflow occurs; then a mass-transfer stream appears and there is a rapid, violent accretion episode onto the BH. What follows depends on the stiffness of the NS EOS:

1. For very stiff EOSs (with polytropic index $n = 0.5$), the NS is not completely accreted and survives as a remnant (probably unstable) in an eccentric orbit; secondary accretion episodes are possible; and an accretion disk is formed, but only if $M_{\text{NS}}/M_{\text{BH}} > 0.5$.
2. For stiff EOSs ($n = 0.66$), the NS is almost completely disrupted, and there is always a thick accretion disk of $0.2\text{--}0.3M_{\odot}$; irrotational initial configurations lead to more violent encounters where larger tidal bulges deform the NS, and eventually long tidal tails are formed with enough energy to escape the binary.
3. For soft EOSs ($n > 0.66$), tidal disruption is always complete regardless of the initial mass ratio; both a massive accretion disk and a large one-armed spiral are formed.

Altogether, these simulations show that hydrodynamical effects play an important role in the global behavior of the system at small separations; the mass-transfer process is always unstable, and it can by itself destabilize the orbit. The outcome of the coalescence process is very sensitive to the assumed stiffness of the EOS, which bodes well for the extraction of EOS parameters from tidal-disruption waveforms; and except for the stiffest EOS, the gravity-wave shutoff at tidal disruption is sudden and complete, which shows that the sudden-shutoff approximation, used in my simple models (see Sec. 2 above and Chap. 2), might not be too far off the truth.

It is possible to improve on these simulations; indeed, in collaboration with Lee Lindblom and Joel Tohline, I have begun to work toward this goal. We are setting up a framework for Eulerian numerical simulations that will follow the evolution of the NS in its freely falling reference frame, as it inspirals toward the BH. The advantage of this approach is that it enables us to devote all

of our computational power (and memory) to modeling the hydrodynamics of the NS, which is the most important and interesting aspect of the tidal-disruption process. We plan to obtain the orbital evolution of the binary by solving post-Newtonian expanded equations for the general-relativistic two-body problem; and we plan to model the star as a Newtonian, polytropic fluid that is evolving in the inertial reference frame centered on the NS center of mass, and that is subject to the relativistic tidal field of the BH. We should improve on the Lee et al. [6, 32] simulations because Eulerian hydrodynamics is inherently more accurate than SPH in modeling violent processes involving fluid interfaces, such as the surface of the NS; and we should improve on the Janka et al. [5, 33] simulations because we will be able to resolve the NS more finely; finally, we should improve on both sets of simulations by including relativistic corrections to the orbital evolution and to the BH potential that acts on the NS.

1.1.3 Gravity waves from the r -mode instability of nascent neutron stars

All rotating stars possess a class of circulation modes (r -modes) that are driven toward instability by gravitational radiation reaction; in hot, rapidly rotating young NSs, this destabilizing effect might be so strong that it dominates viscous dissipation. Once an r -mode achieves sufficient amplitude, the star is quickly spun down as angular momentum is lost to gravitational radiation [11, 12]. For stars with initial angular velocity $\Omega \sim 1000$ Hz, the timescale for the growth of the most unstable r -mode is ~ 40 s. In recent years, r -modes have attracted considerable interest as a promising GW source for ground-based detectors, and as a possible explanation for the failure to observe any young pulsars that are rotating at angular velocities close to their theoretical spin limit (such rapidly rotating NSs were expected, but not by everybody, in supernova remnants).

However, the astrophysical relevance of r -modes is still in doubt, pending judgment on two separate issues. First, this instability (discovered by analyzing the linearized Euler equations for perfect fluids) might not be confirmed after all the complicated physics that occurs in NSs is taken into account, including relativistic effects, physical-EOS effects, solid crust effects, magnetic fields, rotation laws, exotic sources of viscosity, and so on [11, 12]. Second, the amount of angular momentum removed from the star and the strength of the GW radiation emitted depend critically on the maximum mode amplitude that can be reached; but the growth of the mode might be limited to a very small *saturation amplitude* by magnetic-field effects [34], by turbulent boundary-layer effects at the crust-core interface [35], or by leakage of energy to other (damped) modes through nonlinear hydrodynamical couplings.

There have been several attempts to investigate the nonlinear dynamics of the r -modes, including leakage of energy to other modes, by means of second-order Lagrangian perturbation theory ([36], see also Sec. 4 below), and of relativistic numerical simulations in the Cowling approximation [37].

In addition, in collaboration⁴ with Lee Lindblom and Joel Tohline, I have carried out Newtonian numerical simulations that include radiation reaction as an effective force. Much in the spirit of this thesis, this work is a good illustration of how numerical techniques can be employed to supplement analytical work in the modeling of GW sources, and to guide data-analysis strategies. It is the subject of the next section and, more in detail, of Chap. 3.

Numerical evolutions of nonlinear r -modes in neutron stars

The simulation of NS instabilities is a difficult task. First, the hydrodynamical timescale (which, through the Courant condition, determines the lengths of time that can be explored within a given allotment of CPU time) is much shorter than the timescales for the growth of instabilities (in the case of r -modes, this is the GW radiation-reaction timescale). Second, the microscopic and macroscopic physics of NSs can be very complex, with important effects arising from such different physical ingredients as the proton/neutron fractional composition of the nucleon gas, the possibility of superfluid phases, the presence of strong magnetic fields, and so on. Third, relativistic corrections can be important, but fully relativistic hydrodynamics (with the Einstein metric being evolved *on a par* with the fluid variables) is still somewhat beyond the capabilities of current codes and machines [43]. Even the less ambitious codes that implement the Cowling approximation [43] (where the dynamics of the fluid are played out in a fixed background metric) are still rather unwieldy, and saddled by very large numerical viscosities with respect to their Newtonian counterparts.

Lindblom, Tohline, and I address the second and third concerns by choosing to work with a simple Newtonian polytropic fluid. Our rationale is that the structure of r -modes is not very sensitive to the underlying EOS, and we expect that the qualitative features of the nonlinear hydrodynamics should also be essentially correct in our simplified model. Other physical processes (magnetic fields, superfluidity) can be very important for the overall picture of the instability, but they probably have little bearing on the issue of nonlinear couplings. We do need to include at least one relativistic effect: radiation reaction, which drives the mode unstable, is added as an effective force [44] proportional to the derivatives of the current multipole moments.

We address the first concern (the long instability timescale) by increasing the strength of the effective radiation-reaction force by a factor of about 4500, to bring down the r -mode growth timescale to values comparable to the rotation period. Even with this kludge, the physical behavior that we observe should still be realistic, *if* the nonlinear dynamics of the mode (including its couplings to other modes) happens at the hydrodynamical timescale, which is modeled correctly in our simulations. (However, see Sec. 4 below.)

⁴The respective contributions to this project can be characterized as follows. Joel Tohline provided his proven numerical code, which I ported to the CACR HP supercomputers; he also contributed his considerable expertise on numerical hydrodynamics. Lee Lindblom set up the basic framework for the simulations and completed the initial analytical work. Under his supervision, I ran the code on a daily basis, designed and performed several runs, tests, and analyses, and wrote most of the paper that appears in this thesis as Chap. 3.

Our simulations were based on a second-order-accurate finite-difference code developed at LSU by Tohline and his students [38] to tackle a variety of astrophysical problems. The LSU code was parallelized [39] in the domain-decomposition paradigm using the well-known MPI [40] library. We ran it for a $128 \times 64 \times 128$ cylindrical grid on 16 nodes of the HP V-2500 supercomputers at Caltech’s Center for Advanced Computing Research [41].

We solved the Newtonian Euler and Poisson equations, after setting up the initial equilibrium configuration as a simple, rigidly rotating polytrope (with $n = 1$, $M = 1.4 M_{\odot}$, $R = 12.5$ km, and rotation period $P_0 = 1.21$ ms), obtained by solving self-consistently the Bernoulli and Poisson equations [42]. We then added a seed mode (a small-amplitude, slow-rotation approximation to the most unstable r -mode, the one with $l = m = 2$) to the initial velocity distribution of the NS. The seed mode was set to the dimensionless amplitude $\alpha = 0.1$ (equivalent to mode velocities $\sim 10\%$ of the rigid-rotation velocity).

We then let the star evolve, and we monitored the r -mode amplitude by extracting the ($l = 2, m = 2$) current multipole from the NS velocity field. The r -mode frequency was determined from the quasi-periodic oscillations of this multipole. The behavior that we observed was very surprising. The mode grew exponentially (in good accord with theory) until $\alpha \sim 2$; then the growth began to be limited by some unidentified nonlinear process; eventually, the amplitude peaked at $\alpha = 3.35$, and then fell down to very low values within few rotation periods. Our movie of the growing, then crashing r -mode can be found on the Web [46].

What nonlinear process was responsible for limiting the growth of the r -mode, and for causing its rapid demise? We discovered a clue when we examined the evolution of the energy and angular momentum in the course of the simulation. Even after the emission of angular momentum into GWs fell to zero, the star continued to lose energy; surely, something other than GWs must be responsible for this loss. Our explanation was the following. To first order in its characteristic amplitude, the r -mode is only a *velocity* mode; to second order, however, there is an associated density perturbation that appears as a traveling wave with four crests (two in each hemisphere) on the surface of the star; see our movie [46]. As the amplitude reached its maximum, these propagating crests turned into large, breaking waves, and the edges of the waves developed strong shocks that began to dump kinetic energy into thermal energy, eventually killing the r -mode.

In the traditional scenario for GW emission from r -modes [47], the unstable r -mode would grow until it reached a dimensionless amplitude of about one, and then it would saturate and persist at that amplitude (for several months) until it would have lost most of its angular momentum; during that time, the frequency of the r -mode would decrease in proportion to the NS spin. The prospective picture of r -mode GW signals that emerges from our evolutions is quite different. Most interestingly, the r -mode spindown episodes are faster (only a few minutes), and the GW frequency remains remarkably constant as the angular velocity of the star decreases. As a result, the search for

r -mode signals changes from a month-long, pulsar-like search (which must account for the Doppler shifts generated by Earth’s movement in the solar system) to an easier, shorter chirp-like search, with encouraging prospects for detection [48].

Our code provided a nice laboratory to perform several more evolutions and tests.

1. We performed basic tests of the robustness of the code and of our diagnostics, evolving stars with different angular velocities, with or without r -mode perturbations, and at different grid resolutions.
2. We investigated the dependence of the saturation amplitude on the artificial amplification of radiation reaction. Our computing budget made it impossible to increase the radiation-reaction timescale; instead, we reduced it even more, finding that the r -mode saturated faster, but at essentially the same amplitude.
3. We studied the *unforced* evolutions of unit-amplitude r -modes, finding that they were essentially stable for as long as we could evolve them. These results are compatible with the relativistic evolutions (also unforced) performed by Stergioulas and Font [37].

Recent developments

In two recent papers, Arras and colleagues [36] study the saturation of r -modes by three-mode nonlinear coupling to other *inertial* (Coriolis-restored) modes in neutron stars. They identify two relevant saturation mechanisms: in the *weak driving* limit, the unstable *parent* r -mode transfers energy by way of *parametric resonance* [49] to a pair of quasi-resonant, overdamped *daughter* modes. When the parent mode becomes large enough, it starts to excite these daughter modes. Eventually, they get to amplitudes such that essentially all the energy that the radiation reaction imparts to the parent mode is immediately transferred to them and dissipated. The saturation amplitude of the parent mode depends on the strength of the parent-mode driving, and on the daughter-mode damping coefficients and quality factors.

In the *strong driving* limit, the nonlinear energy transfer is faster than the damping of the daughter modes; eventually a large family of daughter modes (spread over an *inertial range*) becomes excited, and the parent mode is saturated by leakage of energy out of the inertial⁵ range to other damped modes; in this case, the saturation amplitude of the parent mode depends only on the efficiency of nonlinear energy transfer to the daughter modes. After evaluating the nonlinear coupling coefficients and the damping rates for inertial modes, Arras and colleagues conclude that this *strong driving* scenario is relevant to the case of r -modes, both for rapidly spinning nascent stars and for recycled stars in low mass X-ray binaries; they obtain a saturation amplitude of

⁵The noun *inertial* has quite different meanings when it is used in the phrases *inertial range* and *inertial mode*.

$\sim 0.7 \cdot 10^{-2} (\nu_{\text{star}}/1\text{kHz})^{5/2}$, or $\sim 0.4 \cdot 10^{-2}$ for the star in our simulation [64]. They also argue that the results discussed in the previous section are artifacts of our unphysically large driving force.

Also recently, Jones suggested [51] and Owen and Lindblom verified [50] that, if the NS core contains hyperons in addition to neutrons and protons, then bulk viscosity due to the nonleptonic weak interactions

$$n + n \Leftrightarrow p + \Sigma^-, \quad n + p \Leftrightarrow p + \Lambda \quad (1.2)$$

will suppress the r -mode instability after the core temperature drops below $3 \cdot 10^9$ K. Now, the standard modified URCA process⁶ will cool the NS to $3 \cdot 10^9$ K in one day; however, for modern, proton-rich EOSs, direct URCA will cool the NS to $3 \cdot 10^9$ K within a few s. It seems that the window of opportunity for the r -mode instability is shrinking more and more.

Still, in the end, I believe it is fair to argue that there is such uncertainty about the structure and dynamics of NSs that the final verdict on the r -mode instability will come only from their detection with GW interferometers, or from the failure to detect them; so it is reasonable to devote some resources to GW searches for r -mode signals (perhaps with shapes similar to those predicted by our simulations).

1.2 Gravitational waves from coalescing binaries of compact stellar objects

Binaries of compact stellar object are the standard source for the class of *chirp* signals that will be sought by ground-based GW interferometers. There are many reasons for this, not least the fact that the effects of GWs have been first observed (albeit indirectly) in such a binary, the Hulse–Taylor pulsar. But there is more to it: because they are the incarnation of the (unsolved) general-relativistic two-body problem, binaries have come to represent the very essence of Einstein’s theory of gravitation. This is especially true for binaries consisting of two BHs, objects made of *pure spacetime curvature*.

⁶Direct URCA processes are simply β -decay and its inverse,

$$n \Leftrightarrow p + e^- + \bar{\nu}_e, \quad p \Leftrightarrow p + e^+ + \nu_e, \quad (1.3)$$

or the similar processes involving a hyperon. On the other hand, modified URCA sees the participation of a spectator nucleon,

$$n + (n, p) \Leftrightarrow p + (n, p) + e^- + \bar{\nu}_e, \quad p + (n, p) \Leftrightarrow n + (n, p) + e^+ + \nu_e, \quad (1.4)$$

so it is suppressed with respect to direct URCA; however, it might be the only available cooling mechanism if the conservation of momentum in Eq. (1.3) cannot be satisfied because the accessible phase-space is saturated with fermions.

system	event rate	LIGO-I		LIGO-II	
		visible to	det./yr	visible to	det./yr
NS–NS	1 to 500 GEM	20 Mpc	3×10^{-4} to 0.3	300 Mpc	1–800
NS–BH	0.1 to 100 GEM	43 Mpc	4×10^{-4} to 0.6	650 Mpc	1–1500
BH–BH (field)	0.1 to 10 GEM	100 Mpc	4×10^{-3} to 0.6	$z = 0.4$	30–4000
BH–BH (clusters)	1 to 10 GEM	100 Mpc	0.04–0.6	$z = 0.4$	300–4000

Table 1.2: Estimated coalescence and detection rates for compact binaries [GEM \equiv (events in our galaxy)/Myr]. From [52, 3]. LIGO-II numbers are for a wideband optical configuration and sapphire test masses. The rates for BH–BH binaries distinguish between sources in standard galaxies and in globular and other star clusters, which can act as incubators for binaries (single BHs, heavier than most stars in the cluster, sink to the center via tidal friction, where they find and capture other BHs; three-body interactions then *harden* the resulting binaries, and often eject them from the cluster [53]; recent investigations [54] suggest that four-body interactions might actually cause the binaries to coalesce within the clusters, creating a hierarchy of BHs with masses ~ 100 – $1000M_{\odot}$).

1.2.1 The statistics of coalescing binaries

The estimated galactic coalescence rates for binaries of compact objects are shown in Table 1.2, together with their expected detection rates, computed for first- and second-generation LIGO interferometers by extrapolating out through the universe [52, 3]. The rates for NS–NS binaries, which have actually been observed as radio pulsars in our galaxy [4], are best estimated by modeling the selection effects intrinsic to pulsar surveys. For each observed binary i , Phinney ([55]; see also Kalogera et al. [52]) computes the scale factor

$$S_i = \frac{\text{Volume(galaxy)}}{\text{Volume(searched)}}, \quad (1.5)$$

which gives (roughly) the number of systems similar to i that are present in the galaxy. The galactic coalescence rate is then approximated as $\sum_i S_i/\tau_i$, where τ_i is the lifetime of the binary i . The determination of the S_i is very delicate, because it must account for all the selection effects that limit the observability of pulsars from Earth surveys (such as beaming, faintness, spatial distribution, and so on). This procedure is fragile also because of the very limited sample of observed objects. It gives the galactic event rate, 1 to 500 GEM, shown in Table 1.2.

Because no BH–NS or BH–BH binaries have yet been identified reliably, predictions on their coalescence rates can be obtained only from theoretical *population-synthesis* models [52]. These involve complex Monte Carlo computations that must include reasonable representations of poorly understood processes, such as the formation of stars and binaries, and their evolution (including single-star evolution, orbital evolution and decay, mass transfer episodes, core collapse and supernova explosions, and so on). As a consequence, the resulting event rates are very uncertain. For NS–NS binaries the theoretical predictions are in good agreement with the extrapolations from pulsar surveys [52], but this could be just a coincidence.

To extrapolate the galactic event rate to the volume of universe accessible to GW interferometers, we assume that the coalescence rate is proportional to the rate of formation of stellar progenitors, and that the properties of primordial binaries in other galaxies are similar to those in ours. Then we can use scaling arguments based on B-band luminosity density, galaxy number density, or cluster number density. Kalogera and colleagues [52] obtain a scaling factor $\sim 10^{-2}$ Mpc for $h = 0.65$.

The last step toward detection rates is the determination of the volume of universe where GW detectors can actually observe a given source. The distance from Earth that can be probed by a given detector is inversely proportional to the strength of the signal, which scales as $\mathcal{M}^{5/6}$ [for a binary with masses m_1 and m_2 , the *chirp mass* \mathcal{M} is given by $\mathcal{M} = (m_1 m_2)^{3/5} / (m_1 + m_2)^{1/5}$]. This scaling gives an intrinsic advantage, detection-wise, to the heavier NS–BH and especially BH–BH binaries over NS–NS binaries. Barring surprises, if LIGO-I detects a coalescing binary, it will probably be made of two BHs.

1.2.2 Detecting BH–BH binaries with LIGO-I

The final chapter of this thesis reports my work (in collaboration⁷ with Alessandra Buonanno and Yanbei Chen) on templates for the detection of GW signals from the coalescence of *nonspinning* BH–BH binaries with total masses between 10 and $40M_\odot$. These are among the most promising sources for first-generation ground-based interferometers, but the possibility of detecting them with standard matched-filtering techniques is seriously imperiled by our ignorance about the gravitational waveforms that they generate. The spins of the two BHs *are* expected to play a very significant role in the late stages of the inspiral [57], so the analysis of nonspinning binaries reported in Chap. 4 is preliminary to considering the effects of spin, which is currently work in progress.

Most GW signals sought by ground-based GW interferometers are so weak that they can be detected only⁸ if we have a previous knowledge of their shape, by *correlating* the interferometer output with a theoretically determined *signal template* ([28]; see also Sec. 4.2). The higher the correlation, the more confidence we have that a signal closely resembling the template is actually present in the experimental data. This detection scheme (and the estimation of upper limits if no detection is made) depends on the assumption that the equations used to compute the theoretical templates represent faithfully the evolution of the actual physical system.

The present knowledge of the weak-gravity regime of GR justifies the assumption that the post-Newtonian (PN) approximation [59] can model accurately the inspiral stage of NS–NS coalescences, at least for GW frequencies within the range of good interferometer sensitivity. [The PN approxima-

⁷All three authors have contributed to all the different analytical and numerical tasks inherent in this project, but I have been responsible most especially for assembling a *Mathematica* package capable of synthesizing waveform templates from several phasing and orbital equations and of evaluating the *overlaps* between template families, while Alessandra Buonanno has paid attention especially to the analytical framework.

⁸The principal exception is merger waves for BH–BH binaries, if they last for very few cycles. In this case, filtering the signal with templates is not much more efficient than looking for excess power in the detector output [56].

tion is essentially a perturbative expansion of the Einstein equations in the characteristic Keplerian velocity $v = (\pi M f_{\text{GW}})^{1/3}$, where M is the total mass of the binary, and f_{GW} is the instantaneous GW frequency.] Since NS–NS binaries have been for a long time the standard chirp source, this assumption has in fact guided the development of the theory of GW data analysis.

Unfortunately, the same does not hold true for BH–BH binaries with total masses between 10 and $40M_{\odot}$. These enter the LIGO frequency range at a very late stage in their inspiral, when only 50–800 orbits are left before the merger, and when the post-Newtonian expansions used to compute waveform templates fail to converge properly. Several techniques have been suggested to accelerate the convergence of the PN series, but they have been shown to lead to very different waveforms, so no particular template family based on any such technique can be trusted to represent adequately the physical signals.

To address this concern, we considered all the PN approximation schemes (for *nonspinning* BHs) that have appeared in the literature, including:

1. *Adiabatic models*, where we apply the energy balance equation $d(\text{PN energy})/dt = -(\text{GW flux})$ to evolve the binary through a sequence of quasi-stationary circular orbits; different ways to resum the PN energy and flux functions generate distinct models [60].
2. *Hamiltonian schemes*, where we solve the Hamilton equations obtained from the PN Hamiltonian (possibly resummed) [60].
3. *Direct schemes*, where we use the PN analog of the Newtonian equations of motion, including radiation-reaction terms [61].

Under the hypothesis (admittedly, a strong one) that the variety of signals thus obtained spans enough volume in signal space to encompass the actual physical signals, we then looked for an *effective* family of templates that can approximate all of these *target* models equally well, and interpolate between them. With luck (if, as it were, the various PN models are not all wrong in the same direction) the effective family will also be a reasonable approximation to the true physical signals.

The effective family need not be one of the PN models, and in general it will not be indexed by the same physical parameters [such as total mass M and mass ratio $\nu = m_1 m_2 / (m_1 + m_2)^2$] as the PN models are. Instead, we should see the effective family as a collection of signal shapes selected phenomenologically to approximate the physical waveforms (at least in our wishful thinking). Such a family will be useful mainly for the purpose of signal detection, rather than for parameter estimation.

Under the same hypothesis, we can use the *distance* (in signal space) that separates the effective template family from the target models to estimate the distance between the effective family and the real physical signals. As we shall see in Chap. 4, in the theory of matched-filtering detection we can give a quantitative formulation to the notion of distance *between* and *within* signal families.

The distance between the effective family and the real signals (or equivalently a quantity called the *fitting factor* [62]) sets an upper limit on the efficiency of the former to detect the latter (given as probabilities for false alarms and false dismissals). The distance between templates within the effective family can be used to determine how widely spaced⁹ the templates can be placed (and therefore how many we need) to achieve a certain detection efficiency (the required spacing is equivalent to a quantity called the *minimum match* [63]).

1.2.3 Detection templates for BH–BH binaries

We have identified two effective template families that can match all the credible target models with fitting factors of 0.95 or better (corresponding to a loss in event rate $\lesssim 15\%$, for most physical parameters). These are:

1. *Adiabatic or Hamiltonian models* with resummed PN energy/Hamiltonian and flux, with mass ratio parameter ν *pushed to nonphysical values*. It seems that the mere formal extension of the models along the ν axis is able to recapture much of the effect of solving different equations with differently resummed PN functions.
2. *Frequency-domain models* that represent the amplitude and phasing of the waveform’s Fourier transform as polynomials in the frequency f_{GW} . We select the specific powers that appear in these polynomials by inspecting the power-series expansion (in f_{GW}) found for the amplitude and phasing of PN adiabatic models under the stationary-phase approximation. However, we do not constrain the coefficients to their PN functional dependence on the physical binary parameters. This is somewhat in the spirit of the Fast Chirp Transform techniques introduced by Prince and colleagues [58].

The expected performance of both families improves if we employ several copies of the same template, *cut off* at different final frequencies. The manner in which the true waveform behaves at the end is very uncertain, and the cut incorporates this uncertainty.

For both classes of effective template families, we estimate that the number of templates required to achieve a total match $\gtrsim 0.92$ (including the effects of both fitting factor and minimum match, and corresponding to a loss in event rate $\lesssim 20\%$) is manageable ($\sim 10^4$). This number includes the replication of templates with different frequency cuts, and the extension of the effective template bank *between* and *beyond* the parameter ranges that are needed to approximate the target models well. Such an extension is desirable because we take the target models as a loose guide, but not a strict prescription, of how the true signal might look like.

Summarizing, we claim that first-generation ground-based interferometers have a fighting chance to detect GW signals from BH–BH binaries with more than 80% of the detection rate that would

⁹Any detection algorithm used in practice can make use only of *discrete* families of templates!

result from using the unknown true signals as templates. This goal can be achieved by adopting an approach that emphasizes detection over parameter estimation, and that makes use of effective template banks that extend beyond the range of parameters that would normally correspond to physical values.

1.3 Bibliography

- [1] V. Ferrari, proceedings of the 25th J. Hopkins Workshop on Current Problems in Particle Theory, 2001: A Relativistic Spacetime Odyssey, Florence, Sep. 3–5, 2001, [astro-ph/0201265](#).
- [2] S. A. Hughes, S. Márka, P. L. Bender, and C. J. Hogan, proceedings of the 2001 Snowmass Meeting, Snowmass Village, Colorado, June 30–July 21, 2001, [astro-ph/0110349](#).
- [3] K. S. Thorne, “The Scientific Case for Advanced LIGO Interferometers,” LIGO Doc. P-000024-00-D (2001).
- [4] See, for instance, S. E. Thorsett, and D. Chakrabarty, *Astrophys. J.* **512**, 288 (1999).
- [5] H.–T. Janka, T. Eberl, M. Ruffert, and C. Fryer, *Astrophys. J.* **527**, L39 (1999).
- [6] W. Lee, *MNRAS* **318**, 606 (2000).
- [7] L. Bildsten, *Astrophys. J. Lett.* **501**, L89 (1998); G. Ushomirsky, C. Cutler, and L. Bildsten, *MNRAS* **319**, 902 (2000), and references therein.
- [8] P. R. Brady, T. Creighton, C. Cutler, and B. F. Schutz, *Phys. Rev. D* **57**, 2101 (1998).
- [9] P. Jaranowski and A. Krolak, *Phys. Rev. D* **59**, 063003 (1999).
- [10] See, for instance, M. Shibata, T. W. Baumgarte, and S. L. Shapiro, *Astrophys. J.* **542**, 453 (2000).
- [11] For a recent review, see L. Lindblom, in *Gravitational Waves: A Challenge to Theoretical Astrophysics*, V. Ferrari, J. C. Miller, and L. Rezzolla, eds. (ICTP, Trieste, 2001), [astro-ph/0101136](#).
- [12] K. D. Kokkotas, proceedings of the 25th J. Hopkins Workshop on Current Problems in Particle Theory, 2001: A Relativistic Spacetime Odyssey, Florence, Sep. 3–5, 2001.
- [13] See, for instance, H. Heiselberg and V. Pandharipande, *Ann. Rev. Nucl. Part. Sci.* **50**, 481–524 (2000); S. Balberg and S. L. Shapiro, in *Handbook of Elastic Properties*, M. Levy, H. Bass, R. Stern, eds. (San Diego, Academic Press, 2001).
- [14] J. M. Lattimer and M. Prakash, *Astrophys. J.* **550**, 426 (2001).

- [15] L. Lindblom, *Astrophys. J.* **398**, 569 (1992).
- [16] T. Harada, *Phys. Rev. C* **64**, 048801 (2001).
- [17] See, for instance, M. H. Van Kerkwijk, proceedings of the Jan van Paradijs Memorial Symposium, Amsterdam, June 6–8, 2001. [astro-ph/0110336](#).
- [18] O. Barziv, L. Kaper, M. H. Van Kerkwijk, J. H. Telting, J. Van Paradijs, *Astro. & Astrophys.* **377**, 925 (2001).
- [19] J. A. Orosz and E. Kuulkers, *MNRAS* **305**, 132 (1999).
- [20] M. C. Miller, F. K. Lamb, G. B. Cook, *Astrophys. J.* **509**, 793 (1998).
- [21] D. L. Kaplan, M. H. van Kerkwijk, and J. Anderson, [astro-ph/0111174](#).
- [22] B. Paczynski, [astro-ph/0107443](#).
- [23] N. R. Nath, T. E. Strohmayer, and J. H. Swank, *Astrophys. J.* **564**, 353 (2002).
- [24] J. J. Drake et al., *Astrophys. J.*, in print, [astro-ph/0204159](#).
- [25] K. S. Thorne, in *Three hundred years of gravitation*, S. Hawking and W. Israel, eds. (Cambridge, Cambridge University Press, 1987), p. 330; A. Abramovici et al., *Science* **256**, 325 (1992).
- [26] M. Saijo and T. Nakamura, *Phys. Rev. D* **63**, 064004 (2001); *Phys. Rev. Lett.* **85**, 2665 (2001).
- [27] S. Chandrasekhar, *Ellipsoidal figures of equilibrium* (Yale University Press, New Haven, 1969); M. Shibata, *Prog. Theor. Phys.* **96**, 917 (1996); P. Wiggins and D. Lai, *Astrophys. J.* **532**, 530 (2000).
- [28] See, for instance, L. S. Finn, *Phys. Rev. D* **46**, 5236 (1992); L. S. Finn and D. F. Chernoff, *Phys. Rev. D* **47**, 2198–2219 (1993).
- [29] See, for instance, C. W. Misner, K. S. Thorne, and J. A. Wheeler, *Gravitation* (W. H. Freeman and Co., San Francisco, 1973).
- [30] L. Bildsten and C. Cutler, *Astrophys. J.* **400**, 175 (1992).
- [31] For a review of numerical simulations of GW sources, including references to NS–NS and NS–BH simulations, see J. M. Centrella, proceedings of the Conference on Stellar Collisions, American Museum of Natural History, June 2000, [gr-qc/0011109](#)
- [32] W. Lee and W. Kluźniak, *Acta Astron.* **45**, 705 (1995); *Astrophys. J. Lett.* **494**, L53 (1998); *Astrophys. J.* **526**, 178 (1999); *MNRAS* **308**, 780 (1999); *MNRAS* **328**, 583 (2001).

- [33] H.–T. Janka and M. Ruffert, in *Proceedings of the 10th workshop on “Nuclear Astrophysics”*, W. Hillebrandt and E. Müller, eds. (Garching, Germany, Max-Planck-Institut für Astrophysik, 2000), p. 136.
- [34] L. Rezzolla, F. L. Lamb, D. Markovic, and S. L. Shapiro, *Phys. Rev. D* **64**, 104013 (2001); *Phys. Rev. D* **64**, 104014 (2001).
- [35] Y. Wu, C. D. Matzner, and P. Arras, *Astrophys. J.* **549**, 1011–1020 (2001).
- [36] P. Arras et al., [astro-ph/0202345](#); A. K. Schenk et al., *Phys. Rev. D* **65**, 024001 (2002).
- [37] N. Stergioulas and J. A. Font, *Phys. Rev. Lett.* **86**, 1148 (2001).
- [38] K. C. B. New and J. E. Tohline, *Astrophys. J.* **490**, 311 (1997); H. S. Cohl and J. E. Tohline, *Astrophys. J.* **527**, 527 (1999); J. E. Cazes and J. E. Tohline, *Astrophys. J.* **532**, 1051 (2000).
- [39] P. M. Motl, J. Tohline, and J. Frank, *Astrophys. J. Suppl. Ser.* **138**, 121 (2002).
- [40] MPI forum Web site, www.mpi-forum.org.
- [41] CACR Web site, www.cacr.caltech.edu.
- [42] I. Hachisu, *Astrophys. J. Suppl. Ser.* **61**, 479 (1986); *Astrophys. J. Suppl. Ser.* **62**, 461 (1986).
- [43] J. A. Font, *Living Reviews in Relativity*, www.livingreviews.org (2000).
- [44] L. Rezzolla, M. Shibata, H. Asada, T. W. Baumgarte, and S. L. Shapiro, *Astrophys. J.* **525**, 935 (1999).
- [45] L. Lindblom, B. J. Owen, and S. M. Morsink, *Phys. Rev. Lett.* **80**, 4843 (1998).
- [46] Michele Vallisneri’s *r*-mode Web page, including movies of the instability, www.vallis.org/rmode.
- [47] B. J. Owen, L. Lindblom, C. Cutler, B. F. Schutz, A. Vecchio, and N. Andersson, *Phys. Rev. D* **58**, 084020 (1998).
- [48] B. J. Owen and L. Lindblom, *Class. Quant. Grav.* **19**, 1247–1254 (2002).
- [49] Y. Wu and P. Goldreich, *Astrophys. J.* **546**, 469 (2001).
- [50] B. J. Owen and L. Lindblom, *Phys. Rev. D* **65**, 063006 (2002).
- [51] P. B. Jones, *Phys. Rev. Lett.* **86**, 1384 (2001); *Phys. Rev. D* **64**, 1384 (2001).
- [52] K. Belczynski, V. Kalogera, T. Bulik, *Astrophys. J.*, in print (2002), [astro-ph/0111452](#); V. Kalogera, R. Narayan, D. N. Spergel, J. H. Taylor, *Astrophys. J.* **556**, 340–356 (2001).

- [53] S. F. Portegies Zwart and S. L. W. McMillan, *Astrophys. J.* **528**, L17–L20 (2000).
- [54] M. C. Miller and D. P. Hamilton, [astro-ph/0202298](#).
- [55] E. S. Phinney, *Astrophys. J.* **380**, L17 (1991).
- [56] W. G. Anderson et al., *Phys. Rev. D* **63**, 042003 (2001).
- [57] T. A. Apostolatos et al., *Phys. Rev. D* **49**, 6274 (1994); T. A. Apostolatos, *ibid.* **52**, 605 (1995); **54**, 2438 (1996).
- [58] F. A. Jenet and T. A. Prince, *Phys. Rev. D* **62**, 122001 (2000).
- [59] See, for instance, L. Blanchet, proceedings of the 16th International Conference on General Relativity and Gravitation, Durban, South Africa, July 15–21, 2001, [gr-qc/0201050](#).
- [60] See, for instance, T. Damour, B. R. Iyer, and B. S. Sathyaprakash, *Phys. Rev. D* **63**, 044023 (2001); see also Secs. 4.3, 4.4 of this thesis.
- [61] L. E. Kidder, C. M. Will, and A. G. Wiseman, *Phys. Rev. D* **47**, 4183(R) (1993); L. E. Kidder, *Phys. Rev. D* **52**, 821 (1995).
- [62] T. A. Apostolatos, *Phys. Rev. D* **52**, 605 (1995).
- [63] B. J. Owen, *Phys. Rev. D* **53**, 6749–6761 (1996).
- [64] L. Lindblom, proceedings of the 11th Japanese Workshop on General Relativity and Gravitation, Tokyo, Jan 9–12, 2002.

Chapter 2

Prospects for gravitational-wave observations of neutron-star tidal disruption in neutron-star–black-hole binaries

For an inspiraling neutron-star–black-hole binary (NS–BH), we estimate the gravity-wave frequency f_{td} at the onset of NS tidal disruption. We model the NS as a tidally distorted, homogeneous, Newtonian ellipsoid on a circular, equatorial geodesic around a Kerr BH. We find that f_{td} depends strongly on the NS radius R , and estimate that LIGO-II (ca. 2006–2008) might measure R to 15% precision at 140 Mpc (this distance yields about one event per year under current estimates). This suggests that LIGO-II might extract valuable information about the NS equation of state from tidal-disruption waves.

Originally published as M. Vallisneri, *Phys. Rev. Lett.* **84**, 3519–3522 (2000).

2.1 Introduction

The equation of state of the bulk nuclear matter inside a neutron star (NS) is poorly understood [1]. For example, candidate equations of state that are compatible with nuclear physics experiments and theory predict, for a $1.4 M_{\odot}$ NS, a radius anywhere from about 8 km to 16 km [2]. Thorne has conjectured that insights into the equation of state might come from measurements of the gravitational waveforms emitted by merging NS–NS binaries or tidally disrupting NS’s in neutron-star–black-hole (NS–BH) binaries [3, 4]. More recently, Newtonian models of NS–NS mergers have given strong evidence that the merger waves *do* carry equation-of-state information, but for NS–NS are emitted at frequencies (~ 1400 – 2800 Hz) too high for measurement by LIGO-type gravity-wave interferometers [5, 6]. In this chapter, we show that the prospects for NS–BH measurements are much brighter.

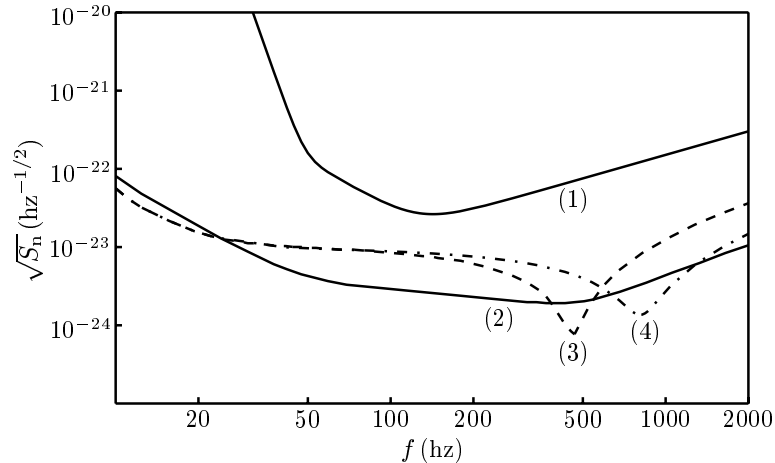


Figure 2.1: Plot of (square root of) noise spectral density for different LIGO configurations: (1) LIGO-I; (2) LIGO-II wideband; (3), (4) LIGO-II narrowband centered on 500 and 850 Hz. Curves (1)-(3) are from [7]; curve (4) was produced by K. A. Strain using the same detector specifications as in [7].

Central to these prospects is the question of whether NS tidal-disruption waves lie in the band of good interferometer sensitivity (for LIGO-II, $\sim 30\text{--}1000$ Hz [7]; see Fig. 2.1). Numerical modeling of NS tidal disruption in NS–BH binaries is only now getting underway [8] and has not yet included computations of the emitted gravity waves or even their frequency bands. As a result, the best frameworks now available for estimating the tidal-disruption gravity-wave band are highly simplified, quasi-analytic models by Shibata [9] and by Wiggins and Lai [10], which represent the inspiraling NS as an irrotational [11], incompressible or polytropic Newtonian ellipsoid, moving on a circular, equatorial geodesic orbit around a Kerr BH, and being tidally distorted by the Kerr Riemann tensor. For simplicity we focus on Shibata’s homogeneous models, and then appeal to the polytropic models for evidence that compressibility has only small effects.

2.2 Neutron-star model

In Shibata’s analysis, the NS gravitational field, its centrifugal potential, and the Newtonian tidal potential constructed from the Kerr Riemann tensor are all quadratic functions of position. As a result, a class of equilibrium solutions are the classic irrotational, homogeneous *Roche-Riemann ellipsoids* [12]. Given a choice of the binary parameters M , a and r (the BH mass and angular momentum per unit mass, and the orbital separation, i. e., the Boyer-Lindquist radius of the geodesic), there is a one-parameter family of such NS models with density ρ ranging downward through the family to a minimum $\rho_{\text{cr}}(M, a, r)$.

We model the inspiraling NS as one of Shibata’s irrotational ellipsoids, identified by its mass

m , and its density ρ or mean radius $R = (3m/4\pi\rho)^{1/3}$. In our simple framework, the uncertainty in $m(R)$ embodies the uncertainty about the NS equation of state. We describe the inspiral as a sequence of circular, equatorial Kerr geodesics that shrink inward until the NS reaches the innermost stable circular orbit, $r = r_{\text{isco}}$, or begins to tidally disrupt [which happens at the radius r_{td} where the star's density ρ matches the critical density $\rho_{\text{cr}}(M, a, r_{\text{td}})$].

The Kerr geometry provides a one-to-one correspondence between the orbital radius r_{td} and the gravity-wave frequency f_{td} at which tidal disruption begins:

$$f_{\text{td}}(M, a, r_{\text{td}}) = \frac{1}{\pi(a + \sqrt{r_{\text{td}}^3/M})} \quad (2.1)$$

(here and below we set $G = c = 1$). It is this f_{td} that LIGO-II can measure. Having measured f_{td} and determined the masses M and m from the observed inspiral waveforms [13], one can compute r_{td} and then the NS density $\rho = \rho_{\text{cr}}(M, a, r_{\text{td}})$ and the mean NS radius R . Thereby, the LIGO-II observations can determine a point on the NS mass-radius curve $m(R)$, which represents the NS equation of state in our simplified analysis. Even one such point could give valuable information about the *real* NS equation of state, and several such points could determine it remarkably well [14].

To estimate the accuracy with which LIGO-II might determine the NS radius R , we need the explicit relationship between R and the disruption-onset frequency f_{td} . More precisely, we need $R(m, M, a, f_{\text{td}})$, which can be derived as follows: (i) $r_{\text{td}}(M, a, f_{\text{td}})$ is obtained by inverting Eq. (2.1); (ii) $\rho_{\text{cr}}(M, a, r_{\text{td}})$ is obtained by solving Eq. (3.9) of [9] for the ratios of semiaxes of the equilibrium configurations, and then extremizing Eq. (3.10) of [9], in which $\tilde{\Omega}^2 = M/(\pi\rho r^3)$; (iii) then R is obtained as $R = [3m/4\pi\rho_{\text{cr}}(M, a, r_{\text{td}})]^{1/3}$. The result has the form

$$R(m, M, a, f_{\text{td}}) = m^{1/3}M^{2/3} \hat{D}\left[\frac{a}{M}, f_{\text{td}}M\right], \quad (2.2)$$

where \hat{D} is a dimensionless function with remarkably weak¹ dependence on a/M . This $R(f_{\text{td}})$ is shown in Fig. 2.2 for various M , for $a/M = 0.998$ (the curves for other a/M are almost identical to these), and for $m = 1.4 M_{\odot}$ [15]. The radii shown, $R = 8\text{--}16$ km for $m = 1.4 M_{\odot}$, correspond to the range of predictions by plausible NS equations of state [2]. The curves in Fig. 2.2 are well approximated by the formula (with $G = c = 1$)

$$\frac{R}{m^{1/3}M^{2/3}} \approx \begin{cases} 0.145 (f_{\text{td}}M)^{-0.71} & \text{for } f_{\text{td}}M \lesssim 0.045, \\ 0.069 (f_{\text{td}}M)^{-0.95} & \text{for } f_{\text{td}}M \gtrsim 0.045. \end{cases} \quad (2.3)$$

Although the BH spin parameter a has negligible influence on the function $R(f_{\text{td}})$, it strongly

¹This is because apart from a weak dependence on a/M , the orbital frequency of Kerr geodesics scales with orbital separation in the same way as the tidal strength, $\sim M/r^3$.

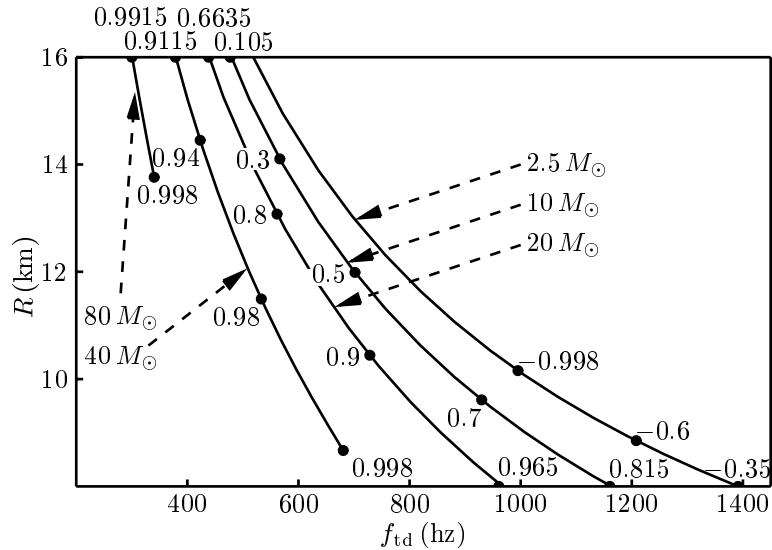


Figure 2.2: NS radius R vs. disruption-onset frequency f_{td} , for $m = 1.4 M_{\odot}$ and $M = 2.5\text{--}80 M_{\odot}$. The black dots, parametrized by a/M , specify the onset of plunge into the BH; tidal disruption is measurable only for f_{td} left of the plunge point, i. e., for R above it. Negative a/M indicates retrograde NS orbits.

influences the radius r_{isco} of the innermost stable circular orbit [16]. If the NS is still intact when it reaches r_{isco} , it then will plunge rapidly into the BH and the tidal-disruption waves, if any, are likely to be so weak and short-lived as to be useless for measuring NS properties. Thus, there is not much hope of measuring tidal disruption unless $f_{\text{td}} < f_{\text{plunge}} = [\text{Eq. (2.1)} \text{ with } r_{\text{td}} \text{ replaced by } r_{\text{isco}}(M, a)]$; i. e., unless f_{td} is left of the relevant big dot in Fig. 2.2.

Figure 2.2 and the above discussion show that (i) for a wide range of realistic parameters, tidal disruption occurs before the plunge begins, and (ii) for all realistic parameters except a very narrow range ($M \lesssim 10 M_{\odot}$ and $R \lesssim 10 \text{ km}$), the tidal-disruption waves fall in the range of good LIGO sensitivity, $f \lesssim 1000 \text{ Hz}$. The Lai-Wiggins polytropic NS models [10] give similar curves and conclusions: for polytropic indices $n = 0.5$ and 1.0 , which approximate NS equations of state, the $R(f_{\text{td}})$ curves are displaced upward in frequency from those of Fig. 2.2 by a mere ~ 50 and $\sim 100 \text{ Hz}$.

2.3 Parameter estimation

Turn now to an estimate of the accuracy to which LIGO-II could measure f_{td} (and then R) using *Wiener optimal filtering* [17, 18]. The measured gravity-wave data stream $g(t)$ is compared to a set of theoretical inspiral *templates* $h(\theta^i; t)$, indexed by the parameters θ^i of the binary; a “best fit” $\hat{\theta}^i$ is found which maximizes the likelihood of observing $g(t)$ given a “true” signal $h(\hat{\theta}^i; t)$, and given a statistical model of the detector noise [a Gaussian² random process with zero mean and spectral

²It is expected that non-Gaussian noise will be removed by coincidence between several detectors.

density $S_n(f)$]. For strong enough signals, $\hat{\theta}^i$ will have a gaussian distribution centered around its “true value” $\tilde{\theta}^i$, with covariance matrix [18]

$$C_{ij} = (\Gamma^{-1})_{ij}, \quad \Gamma_{ij} \approx 2 \left\langle \frac{\partial h}{\partial \theta^i}(\hat{\theta}^k) \left| \frac{\partial h}{\partial \theta^j}(\hat{\theta}^k) \right. \right\rangle, \quad (2.4)$$

where the “inner product” $\langle \dots \rangle$ is defined for any two real data streams $g(t)$, $h(t)$ in terms of their Fourier transforms $\tilde{g}(f)$, $\tilde{h}(f)$ by

$$\langle g, h \rangle = \int_{-\infty}^{\infty} df \frac{\tilde{g}(f)\tilde{h}^*(f)}{S_n(|f|)}. \quad (2.5)$$

Because so little is known about the tidal disruption and our NS models are so crude, we use the simplest of templates in our analysis: slow-motion, quadrupolar waveforms for point particles in circular, Keplerian orbits with quadrupole-governed inspiral. The Fourier-transformed waveform, squared and averaged over binary directions and orientations, is given by³

$$\langle |\tilde{h}_b|^2 \rangle = \frac{\pi}{30} \frac{\mu M_T^3}{d^2} \frac{1}{(\pi M_T f)^{7/3}} \theta(f_{\text{plunge}} - f), \quad (2.6)$$

where μ and M_T are the reduced and total masses, d is the distance to the binary, and the step function shuts off the signal at the onset of plunge.

For typical observations, optimal filtering of the inspiral signal should give good estimates of M and m [13]. We therefore assume that the accuracy in measuring R is limited only by the uncertainty⁴ of f_{td} . The estimation of f_{td} depends heavily on the details of the tidal-disruption waveforms, which are largely unknown. However, it is reasonable to expect tidal disruption to be a sudden event that significantly weakens gravity-wave emission within a few dynamical time-scales after f_{td} has been reached⁵. Correspondingly, we employ a toy model where the inspiral waveform of Eq. (2.6) dies out over a frequency band $(f_{\text{td}}, f_{\text{td}} + \delta f)$:

$$\tilde{h}_{\text{td}}(f) = \begin{cases} \tilde{h}_b(f) & \text{if } f < f_{\text{td}}, \\ \tilde{h}_b(f)\Theta\left(\frac{f-f_{\text{td}}}{\delta f}\right) & \text{if } f_{\text{td}} < f < f_{\text{td}} + \delta f, \\ 0 & \text{if } f > f_{\text{td}} + \delta f, \end{cases} \quad (2.7)$$

where $\Theta(x) = 1 - x$ (linear decay), or $\Theta(x) = 10^{-x}$ (exponential decay). The standard deviation of the “best fit” \hat{f}_{td} is given by Eq. (2.4) as $\Delta \hat{f}_{\text{td}} = [\Gamma_{f_{\text{td}} f_{\text{td}}}(\tilde{h}_{\text{td}})]^{-1/2}$.

³See Eq. (44) of [3], but change $\pi/12$ to $\pi/6$ (typo). A further factor of $1/5$ accounts for detector orientations.

⁴For a signal-to-noise ratio $\gtrsim 10$ (fairly typical of the observations examined in this chapter), and if spins can be treated as negligible, $\Delta m/m$, $\Delta M/M \lesssim 0.02$ [13], and from Eq. (2.3) the influence of Δm and ΔM on ΔR gives $\Delta R/R \sim 0.005$. If spins are important these errors increase tenfold, but might be considerably reduced if the *a priori* knowledge of m from known NS–NS binaries [15] can be applied to NS–BH systems.

⁵Bildsten and Cutler [11] estimate that complete disruption would take place in ~ 1 – 3 orbital periods, while the disrupted NS would spread into a ring in ~ 1 – 2 periods, significantly reducing the gravity-wave amplitude. These rough estimates are confirmed qualitatively by numerical simulations of NS–NS binaries (see [11] for references).

$\Delta R/R$ (%) for $10 \text{ km} < R < 15 \text{ km}$												
$M \setminus S_n$	lin. decay			exp. decay			e. d., $n = 1$			lin. decay		
	$\delta f = f_{\text{td}}/6$			$\delta f = f_{\text{td}}/2$			$\delta f = f_{\text{td}}/2$			$\delta f = f_{\text{td}}/2$		
	(2)	(3)	(4)	(2)	(3)	(4)	(2)	(3)	(4)	(2)	(3)	(4)
$2.5 M_\odot^1$	12	18 ³	8	20	–	13	24 ³	–	25	21 ³	–	17
$10 M_\odot^2$	14	17 ³	10	23	–	17	25 ³	–	21	25 ³	–	19
$20 M_\odot^2$	10	16	10	16	14 ³	16	23	–	14	22	25 ³	16
$40 M_\odot^2$	7	6	11	11	10	19	20	10 ³	20	17	19	23

¹At 65 Mpc. ²At 140 Mpc. ³For $12 \text{ km} < R < 15 \text{ km}$.

Table 2.1: Fractional uncertainty $\Delta R/R$, averaged over the range $10 \text{ km} < R < 15 \text{ km}$. Rows: BH masses; columns: gravity-wave decay models and detector noise curves [labeled by (2)–(4) as in Fig. 2.1]. No quote is given if $\Delta R/R > 25\%$.

We have evaluated $\Delta \hat{f}_{\text{td}}$ numerically, using the signal model from Eqs. (2.6), (2.7) and the inner product (2.5) with the LIGO-II noise curves $S_n(f)$ of Fig. 2.1. We have then computed the 2σ range of the NS radii R from the relation $R_\pm = R(m, M, a, \hat{f}_{\text{td}} \mp 2\Delta \hat{f}_{\text{td}})$ [Eq. (2.2)]. The uncertainty in R , defined as $\Delta R = (R_+ - R_-)/2$, scales roughly linearly with d [because $\Delta \hat{f}_{\text{td}}$ is proportional to d through Eqs. (2.4), (2.6)], and is quite sensitive to the choice of the shutoff model [it scales roughly as $(\delta f)^{1/2}$ and is lower for the exponential decay than for the linear one]. In Table 2.1 we report the fractional uncertainty $\Delta R/R$, averaged over the range $10 \text{ km} < R < 15 \text{ km}$, for choices of parameters motivated by the following.

The NS mass m was set to be $1.4 M_\odot$ [15]. The distance d and the BH masses M were chosen to represent two different scenarios: (i) low-mass BH’s, with $M = 2.5 M_\odot$ at 65 Mpc (about one merger/yr according to Bethe and Brown [19]); (ii) higher mass BH’s, with $M = 10, 20$, and $40 M_\odot$, at 140 Mpc (massive main-sequence binaries are thought to produce NS–BH binaries with $M \sim 10 M_\odot$ and coalescence rates up to about one event/yr out to 140 Mpc, but possibly much less [20]; capture NS–BH binaries formed in globular clusters might have M as large as hundreds of M_\odot [21], but with exceedingly uncertain rates). Finally, we considered three different gravity-wave shutoff models: (i) an optimal-precision model with linear decay and $\delta f = f_{\text{td}}/6$ (the lower limit set by the uncertainty principle on the frequency spread of waves emitted during 3 orbital periods, supposedly a typical time-scale for complete disruption, cfr. note 5); (ii) a fiducial model with exponential decay and $\delta f = f_{\text{td}}/2$ (a scaling supported by numerical calculations of tidal-disruption waveforms in NS–NS binaries [5]); this model was also used to evaluate errors for $n = 1$ polytropes; (iii) a conservative model with linear decay and $\delta f = f_{\text{td}}/2$.

2.4 Conclusion

The estimates for our fiducial decay model suggest that R may be determined with a precision of $\sim 15\%$ using the 850 Hz-narrowband LIGO-II configuration [curve (4) of Fig. 2.1], and with a somewhat

worse precision for wideband LIGO-II [curve (2)]. If the optimal-precision decay model is correct, the error might be as low as $\sim 6\text{--}10\%$. The usefulness of the 500 Hz-narrowband interferometer [curve (3) of Fig. 2.1] is limited to the heavier BH's or to the larger NS's, which have lower f_{td} . Our estimates are inferior for the Lai-Wiggins compressible polytropes [10] examined in the least favorable case ($n = 1$), and for the most conservative decay model; even then, an 850 Hz-narrowband LIGO-II might be able to provide significant information about R .

The accuracy of our analysis is limited by several factors. Sources of error in the frequency $f_{\text{td}}(m, M, a, R)$ at which tidal disruption begins to significantly change the inspiral waveforms include (i) the use of the test-mass approximation for the NS orbit, when actually $m \ll M$, especially for the low-mass Bethe-Brown case; (ii) the use of the Riemann tensor to compute tidal forces when the NS diameter is not, typically, small compared to the distance from the NS center to the horizon⁶; (iii) the idealization of the NS as a homogeneous or polytropic ellipsoid; (iv) the fact that the point at which the observed waveforms show a clear deviation from a standard inspiral may actually come a few orbits earlier (due to tidal coupling) or later than f_{td} .

Our method presupposes a reliable technique to distinguish a plunge shutoff of the inspiral waves from a tidal-disruption shutoff. In fact, it seems likely that the tidal-disruption waveform will actually contain features that not only distinguish it from a plunge shutoff, but that also carry equation-of-state information which is richer than in our crude model. For example, simulations [5] of tidal disruption in NS–NS binaries show a spectrum with an inspiral cutoff followed by a valley, a moderately sharp peak, and a cliff; however, the NS–BH case is likely to be different, and the issue will ultimately be settled only by detailed numerical simulations.

Given these large uncertainties, our results can only be rough indications of the prospects for learning about NS's from tidal-disruption waveforms. They do, however, suggest that observations of tidal disruption in NS–BH binaries might be possible in 2006–2008 with LIGO-II, and might yield useful insights into the NS equation of state. The success of this endeavor will require the development of better theoretical and numerical techniques for modeling NS tidal disruption and computing the dependence of the disruption waveforms on the NS equation of state; we strongly advocate such an effort.

2.5 Bibliography

- [1] G. Baym, in *Isolated Pulsars*, proceedings of the Los Alamos Workshop, Taos, New Mexico, 1992, K. A. Van Riper, R. Epstein, and C. Ho, eds. (Cambridge University Press, 1993), p. 1.
- [2] C. Cutler, L. Lindblom, and R. J. Splinter, *Astrophys. J.* **363**, 603 (1990).

⁶The ratio $r_{\text{td}}/2R$ is $\sim 3\text{--}5$ for $m = 1.4 M_{\odot}$ and $M = 2.5 M_{\odot}$; ~ 5 for $M = 10 M_{\odot}$; $\sim 6\text{--}8$ for $M = 20 M_{\odot}$. The ratios are slightly higher if we use the proper distance to the BH horizon instead of r_{td} .

- [3] K. S. Thorne, in *Three hundred years of gravitation*, S. Hawking and W. Israel, eds. (Cambridge University Press, 1987), p. 330.
- [4] A. Abramovici et al., *Science* **256**, 325 (1992).
- [5] X. Zhuge, J. M. Centrella, and S. L. W. McMillan, *Phys. Rev. D* **50**, 6247 (1994); **54**, 7261 (1996).
- [6] S. Hughes, Ph.D. thesis, Caltech, 1998; F. A. Rasio and S. L. Shapiro, *Class. Quantum Grav.* **16**, R1 (1999).
- [7] E. Gustafson, D. Shoemaker, K. Strain, and R. Weiss, *LSC White Paper on Detector Research and Development* (LIGO-Project document, September 11, 1999).
- [8] See Wiggins and Lai [10] for references.
- [9] M. Shibata, *Prog. Theor. Phys.* **96**, 917 (1996); for earlier tidally locked models see L. G. Fishbone, *Astrophys. J.* **175**, L155 (1972); **185**, 43 (1973); **195**, 499 (1975).
- [10] P. Wiggins and D. Lai, *Astrophys. J.* **532**, 530 (2000); see also D. Lai, F. Rasio and S. L. Shapiro, *ibid.* **423**, 344 (1994).
- [11] L. Bildsten and C. Cutler, *Astrophys. J.* **400**, 175 (1992) have shown that the NS cannot be tidally locked to the BH, so Shibata's irrotational models are more realistic than Fishbone's tidally locked ones [9].
- [12] S. Chandrasekhar, *Ellipsoidal figures of equilibrium* (Yale University Press, New Haven, 1969).
- [13] C. Cutler and É. É. Flanagan, *Phys. Rev. D* **49**, 2658 (1994).
- [14] L. Lindblom, *Astrophys. J.* **398**, 569 (1992).
- [15] $1.4 M_{\odot}$ is the value, to within $\sim \pm 0.1 M_{\odot}$, of all well-measured NS masses in NS–NS binaries. See, for instance, S. E. Thorsett and D. Chakrabarty, *Astrophys. J.* **512**, 288 (1999).
- [16] J. M. Bardeen, W. H. Press, and S. A. Teukolsky, *Astrophys. J.* **178**, 347 (1972).
- [17] L. A. Wainstein and L. D. Zubakov, *Extraction of signals from noise* (Prentice-Hall, Englewood Cliffs, 1962).
- [18] L. S. Finn, *Phys. Rev. D* **46**, 5236 (1992).
- [19] H. A. Bethe and G. E. Brown, *Astrophys. J.* **506**, 780 (1998).
- [20] V. Kalogera, proceedings of the 3rd Amaldi Conference on Gravitational Waves, Caltech, 1999, and references therein. Extrapolation of event rates from the galaxy to the universe follows S. E. Phinney, *Astrophys. J.* **380**, L17 (1991).

- [21] S. R. Kulkarni, P. Hut and S. McMillan, *Nature* **364**, 421 (1993); S. Sigurdsson and L. Hernquist, *ibid.* **364**, 423.

Chapter 3

Numerical evolutions of nonlinear r -modes in neutron stars

Nonlinear evolution of the gravitational radiation (GR) driven instability in the r -modes of neutron stars is studied by full numerical 3-D hydrodynamical simulations. The growth of the r -mode instability is found to be limited by the formation of shocks and breaking waves when the dimensionless amplitude of the mode grows to about three in value. This maximum mode amplitude is shown by numerical tests to be rather insensitive to the strength of the GR driving force. Upper limits on the strengths of possible nonlinear mode-mode coupling are inferred. Previously unpublished details of the numerical techniques used are presented, and the results of numerous calibration runs are discussed.

Originally published as L. Lindblom, J. E. Tohline, and M. Vallisneri, *Phys. Rev. D* **65**, 084039 (2002).

3.1 Introduction

In recent years, the gravitational radiation (GR) driven instability in the r -modes of rotating neutron stars has received considerable interest, both as a source of gravitational waves for detectors such as the Laser Interferometer Gravitational-Wave Observatory (LIGO), and as an astrophysical process capable of limiting the rotation rates of neutron stars. In any rotating star, the r -modes are driven towards instability by GR [1, 2]: as the star emits gravity waves (primarily through a gravitomagnetic effect), the GR reaction acts back on the fluid by lowering the (already negative) angular momentum of the mode. This in turn causes the amplitude of the mode to grow. In most stars internal dissipation suppresses the r -mode instability, but this may not be the case for hot, rapidly rotating neutron stars [3, 4]. For neutron stars with millisecond rotation periods, the timescale for the growth of the instability is about 40 s. In the absence of any limiting process, GR would force the dimensionless amplitude of the most unstable ($m = 2$) r -mode to grow to a value of order unity within about

ten minutes of the birth of such a star. (At unit amplitude, the characteristic r -mode velocities are comparable to the rotational velocity of the star.)

The strength of the GR emitted and the timescale on which the neutron star loses angular momentum and spins down depend critically on the maximum amplitude to which the r -mode grows. Initial estimates assumed that the amplitude would grow to a value of order unity before an undescribed nonlinear process saturated the mode. After saturation, it was assumed that the spindown would proceed as a quasi-stationary process, reducing the angular velocity to one tenth of its initial value within about one year. In this scenario, gravitational waves from spindown events might be detectable with LIGO II [5].

However, at present no one knows with certainty how large the amplitude of the r -modes will grow. It may well be that the nonlinear hydrodynamics of the star might limit the growth of r -modes to very small values. This could happen, for instance, if the r -modes were to leak energy by nonlinear coupling into other modes faster than GR reaction could restore it. In this case the r -mode instability would not play any interesting role in real astrophysical systems.

In a short paper [6], we presented the preliminary results of fully nonlinear, three-dimensional numerical simulations aimed at investigating the growth of r -modes. In our simulations, we modeled a young neutron star as a rapidly rotating, isentropic, Newtonian polytrope; we added a small-amplitude seed r -mode and we solved the hydrodynamic equations driven by an effective GR reaction force. We found that r -mode saturation intervenes at amplitudes far larger than expected (~ 3), supporting the astrophysical relevance of r -modes and the possibility of detecting r -mode gravity waves. The details of the GR signature emitted by the r -mode instability that we observe in our simulations are rather different than previously envisioned, and these details suggest that this radiation may be more easily detected than previously thought: the radiation is more monochromatic and is emitted in a shorter, more powerful burst (see Ref. [6] and the final section of this chapter).

Our results are compatible with the conclusions of Stergioulas and Font [7], who performed relativistic simulations of r -modes on a fixed neutron-star geometry, and found no saturation even at large amplitudes. A second point of comparison can be made with the work of Schenk and colleagues [8]. They have attacked the problem analytically, developing a perturbative formalism to study the nonlinear interactions of the modes of rotating stars, and proving that the couplings of r -modes to many other rotational modes are small (they are forbidden by selection rules, or they vanish to zeroth order in the angular velocity of the star).

This chapter is an expanded account of the results first presented in Ref. [6]: throughout these pages, we describe our simulations in greater detail; we discuss their relevance and their limitations in the light of Refs. [7, 8]; and we present the results of several additional simulations aimed at enlightening particular aspects of the problem. In Sec. 3.2 we write down the basic hydrodynamic equations, and we define a number of mathematical quantities that will be used to monitor the

nonlinear evolution of the r -modes. In Sec. 3.3 we implement the effective current-quadrupole gravitational radiation-reaction force. In Sec. 3.4 we integrate the fluid equations with r -mode initial data in slowly rotating stars, and we compare the results with the small-amplitude, slow-rotation analytical expressions: we demonstrate that the integration reproduces faithfully the analytical predictions to the expected degree of accuracy. In Secs. 3.5–3.8 we study the nonlinear evolution of r -mode initial data in rapidly rotating stars, concentrating on the nonlinear saturation of the r -modes, and analyzing in detail the evolution of several hydrodynamical quantities. Finally, we summarize our conclusions in Sec. 3.9.

3.2 Basic hydrodynamics

We study the solutions to the Newtonian fluid equations,

$$\partial_t \rho + \vec{\nabla} \cdot (\rho \vec{v}) = 0, \quad (3.1)$$

$$\rho(\partial_t \vec{v} + \vec{v} \cdot \vec{\nabla} \vec{v}) = -\vec{\nabla} p - \rho \vec{\nabla} \Phi + \rho \vec{F}^{\text{GR}}, \quad (3.2)$$

$$\partial_t \tau + \vec{\nabla} \cdot (\tau \vec{v}) = 0, \quad (3.3)$$

where \vec{v} is the fluid velocity, ρ and p are the density and pressure, Φ is the Newtonian gravitational potential, and \vec{F}^{GR} is the gravitational radiation reaction force. Equation (3.3) is a recasting of the energy equation for adiabatic flows, where τ is the *entropy tracer* [9]; for polytropic equations of state, τ is related to the internal energy (per unit mass) ϵ by the relation $\tau = (\epsilon \rho)^{1/\gamma}$, where γ is the adiabatic exponent. The Newtonian gravitational potential is determined by Poisson's equation,

$$\nabla^2 \Phi = 4\pi G \rho, \quad (3.4)$$

while the gravitational radiation reaction force will be discussed in Sec. 3.3.

We solve Eqs. (3.1)–(3.4) numerically in a rotating reference frame, using the computational algorithm developed at LSU to study a variety of astrophysical hydrodynamic problems [10]. The code performs an explicit time integration of the equations using a finite-difference technique that is accurate to second order both in space and time, and uses techniques very similar to those of the familiar ZEUS code [11]. For most of our simulations, we adopt a cylindrical grid with 64 cells in the radial direction, and 128 cells in the axial and azimuthal directions.

In the limit of slow rotation, we define the r -modes of rotating Newtonian stars (using the normalization of Lindblom, Owen and Morsink [3]) as the solutions of the perturbed fluid equations

having the Eulerian velocity perturbation

$$\delta\vec{v} = \alpha_0 R \Omega_0 \left(\frac{r}{R}\right)^l \vec{Y}_{ll}^B e^{i\omega_0 t}, \quad (3.5)$$

where R and Ω_0 are the radius and angular velocity of the unperturbed star, α_0 is the dimensionless r -mode amplitude, and \vec{Y}_{ll}^B is a vector spherical harmonic of the magnetic type, defined by

$$\vec{Y}_{lm}^B = [l(l+1)]^{-1/2} r \vec{\nabla} \times (r \vec{\nabla} Y_{lm}). \quad (3.6)$$

The r -mode frequency is given by [12]

$$\omega_0 = -\frac{(l-1)(l+2)}{l+1} \Omega_0. \quad (3.7)$$

To monitor the nonlinear evolution of the r -modes, it is helpful to introduce nonlinear generalizations of the amplitude and frequency of the mode. These quantities are defined most conveniently in terms of the current multipole moments of the fluid,

$$J_{lm} = \int \rho r^l \vec{v} \cdot \vec{Y}_{lm}^{B*} d^3x. \quad (3.8)$$

In slowly rotating stars, the J_{22} moment is proportional to the amplitude of the $m = 2$ r -mode, the most unstable mode, and the one that we will study. To track the evolution of this mode even in the nonlinear regime, we define the normalized, dimensionless amplitude

$$\alpha = \frac{2|J_{22}|}{\tilde{J} M R^3 \Omega_0}, \quad (3.9)$$

where M is the total mass of the star and \tilde{J} is defined by

$$\tilde{J} M R^4 = \frac{1}{4\pi} \int \rho r^4 d^3x \simeq \int \rho r^6 dr. \quad (3.10)$$

The quantity \tilde{J} is evaluated once and for all at the beginning of each of our evolutions. For slowly rotating stars, the definition (3.9) of the mode amplitude reduces to the one given by Eq. (3.5).

In slowly rotating stars, and in all situations where the leading contribution to J_{22} comes from the $m = 2$ r -mode, the time derivative dJ_{22}/dt is proportional to the frequency of the mode: $dJ_{22}/dt = i\omega J_{22}$. Thus we are led to define the nonlinear generalization of the r -mode frequency as

$$\omega = -\frac{1}{|J_{22}|} \left| \frac{dJ_{22}}{dt} \right|. \quad (3.11)$$

As shown by Rezzolla et al. [14], we can re-express dJ_{22}/dt as an integral over the standard fluid

variables,

$$J_{22}^{(1)} \equiv \frac{dJ_{22}}{dt} = \int \rho \left[\vec{v} \cdot (\vec{\nabla} \vec{Y}_{22}^{B*}) \cdot \vec{v} - \vec{\nabla} \Phi \cdot \vec{Y}_{22}^{B*} \right] d^3x. \quad (3.12)$$

The definitions, Eqs. (3.9) and (3.11), of mode amplitude and mode frequency are very stable numerically, because they are expressed in terms of integrals over the fluid variables. In the Appendix, we give explicit expressions for J_{22} and $J_{22}^{(1)}$ in the cylindrical coordinate system used in our numerical analysis.

While we monitor the nonlinear evolution of the r -mode, we are also interested in tracking the star's average angular velocity as well as its degree of differential rotation. With this in mind, we define the average angular velocity

$$\bar{\Omega} \equiv J/I, \quad (3.13)$$

where the angular momentum and the moment of inertia are given respectively by

$$J = \int \rho \varpi^2 \Omega(\varpi, z, \varphi) d^3x, \quad (3.14)$$

$$I = \int \rho \varpi^2 d^3x. \quad (3.15)$$

Here ϖ is the cylindrical radial coordinate, and the local angular velocity $\Omega(\varpi, z, \varphi) \equiv v_{\hat{\varphi}}/\varpi$, where $v_{\hat{\varphi}}$ is the proper azimuthal component of the fluid velocity. We also define the average differential rotation $\Delta\Omega$ as the weighted variance of Ω ,

$$\begin{aligned} (\Delta\Omega)^2 &= I^{-1} \int \rho \varpi^2 (\Omega - \bar{\Omega})^2 d^3x \\ &= I^{-1} \int \rho \varpi^2 \Omega^2 d^3x - \bar{\Omega}^2. \end{aligned} \quad (3.16)$$

3.3 Radiation-reaction force

The gravitational radiation-reaction force due to a time-varying current quadrupole is given by the expression

$$\begin{aligned} F_a^{\text{GR}} &= \kappa \frac{16 G}{45 c^7} \left(2v_j \epsilon_{jal} x_m S_{lm}^{(5)} + v_j \epsilon_{jkl} x_k S_{la}^{(5)} \right. \\ &\quad \left. - v_j \epsilon_{akl} x_k S_{lj}^{(5)} - \epsilon_{akl} x_k x_m S_{lm}^{(6)} \right), \end{aligned} \quad (3.17)$$

see Blanchet [13], and Eq. (20) of Rezzolla et al. [14]. Here $S_{jk}^{(n)}$ represents the n 'th time derivative of the current quadrupole tensor,

$$S_{jk} = \int \rho(\vec{x} \times \vec{v})_{(j}x_k) d^3x; \quad (3.18)$$

ϵ_{jkl} is the totally antisymmetric tensor, and the vector x_k represents the Cartesian coordinates of the point at which the force is evaluated. The parameter κ that appears in Eq. (3.17) has the value $\kappa = 1$ in general relativity. For reasons discussed below, we find it useful to consider other values of κ in our numerical simulations.

We find that a straightforward application of Eq. (3.17) in numerical evolutions is nearly impossible. There are two problems: first, it is very hard to evaluate reliably time derivatives of such a high order; second, various sources of numerical noise (even small errors in the initial equilibrium configuration of the fluid, and the numerical drift of the center of mass) can generate contributions to the current quadrupole tensor that overwhelm those of the pure r -mode motion. So we need to introduce special numerical techniques and simplifications to overcome these problems.

In order to reduce the influence of extraneous noise sources on the evolution, it is helpful to re-express the current quadrupole tensor in terms of the current multipole moments defined in Eq. (3.8). There is a one-to-one correspondence between the J_{2m} current multipoles and S_{ij} :

$$S_{yy} - S_{xx} + 2iS_{xy} = \sqrt{\frac{16\pi}{5}} J_{22}, \quad (3.19)$$

$$S_{xz} - iS_{yz} = \sqrt{\frac{4\pi}{5}} J_{21}, \quad (3.20)$$

$$S_{xx} + S_{yy} = -S_{zz} = \sqrt{\frac{8\pi}{15}} J_{20}. \quad (3.21)$$

In a slowly rotating star, the $m = 2$ r -mode excites J_{22} , but not J_{21} and J_{20} . In contrast, the principal sources of numerical noise contribute primarily to J_{20} . Thus, we evaluate only the J_{22} contribution to \vec{F}^{GR} : we use Eq. (3.17) to evaluate \vec{F}^{GR} , taking the S_{ij} determined from Eqs. (3.19)–(3.21), but setting $J_{21} = J_{20} = 0$. We find that this scheme reduces considerably the numerical noise in the radiation reaction force, and reproduces faithfully the analytical description of r -modes in slowly rotating stars (see Sec. 3.4).

The second major problem is evaluating the numerical time derivatives of S_{jk} , or equivalently the time derivatives of J_{22} . Whenever the radiation-reaction timescale is much longer than the r -mode period $2\pi/\omega$, the dominant contribution to the derivatives $S_{jk}^{(n)}$ comes from terms proportional to powers of the r -mode frequency:

$$S_{jk}^{(n)} \approx (i\omega)^n S_{jk}, \quad J_{22}^{(n)} \approx (i\omega)^n J_{22}. \quad (3.22)$$

Parameter	Symbol	<i>Slow</i>	<i>Fast</i>
		C1, C2	C3–C8
polytropic index	n	1	1
total mass	M	$1.4 M_{\odot}$	$1.4 M_{\odot}$
equatorial radius	R_{eq}	12.7 km	18.4 km
polar R/equatorial R	$R_{\text{pol}}/R_{\text{eq}}$	0.98	0.59
nonrotating ¹ R	R_0	12.5 km	12.5 km
angular velocity	Ω_0	1.45 krad/s	5.34 krad/s
rotation period	P_0	4.32 ms	1.18 ms
energy ratio	$T_{\text{rot}}/ W $	3.98×10^{-3}	0.10072
simulation RR timescale	$\tau_{\text{RR}}^{(s)}$	$0.459 P_0$	$9.4374 P_0$
physical RR timescale	$\tau_{\text{RR}}^{(p)}$	$2.8 \times 10^7 P_0$	$4.2 \times 10^4 P_0$

Table 3.1: Physical parameters for the equilibrium models.

Even when the r -mode amplitude becomes large, the expression (3.22) will be accurate as long as the timescale for the evolution of α and ω is longer than $2\pi/\omega$. Now, J_{22} and $J_{22}^{(1)}$ are easily evaluated using the integral expressions in Eqs. (3.8) and (3.12); thus, the time derivatives needed in Eq. (3.17) are given simply by $J_{22}^{(5)} = \omega^4 J_{22}^{(1)}$ and $J_{22}^{(6)} = -\omega^6 J_{22}$, where we determine ω numerically using Eq. (3.11). In the Appendix, we present explicit expressions for the components of the effective radiation-reaction force in cylindrical coordinates.

3.4 Calibration runs

In order to test the accuracy of our hydrodynamic evolution code and of our approximations for the gravitational radiation-reaction force, we investigate the evolution of a small-amplitude r -mode in a slowly rotating star.

We provide initial data for this study by solving the time-independent fluid equations for a slowly, rigidly rotating stellar model. We model the neutron star as an $n = 1$ polytrope, generated by the self consistent field technique developed by Hachisu [15]. Table 3.1 shows the physical parameters for this model, labeled *Slow*; in particular, the ratio of rotational kinetic energy to gravitational binding energy is $T_{\text{rot}}/|W| = 0.00398$, and the angular velocity is 26% of the maximum possible value (estimated as $\Omega_{\text{max}} = \frac{2}{3}\sqrt{\pi G \bar{\rho}}$).

We then adjust the velocity field of this equilibrium model by adding the velocity perturbation of an $m = 2$ r -mode of amplitude α_0 :

$$\vec{v} = \varpi \Omega_0 \vec{e}_{\hat{\varphi}} + \alpha_0 R \Omega_0 \left(\frac{r}{R}\right)^2 \text{Re}(\vec{Y}_{22}^B). \quad (3.23)$$

In the Appendix, we write out explicitly the components of this initial velocity field in our cylindrical coordinate system. Because Eq. (3.23) is the exact representation of a pure $m = 2$ r -mode only in

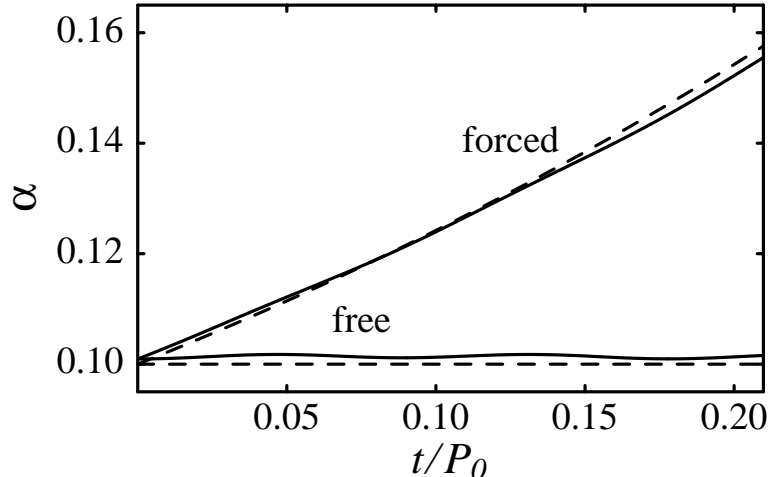


Figure 3.1: Evolution of the r -mode amplitude in a slowly rotating star. The solid curves plot the results of numerical evolutions (with and without gravitational radiation reaction) while the dashed curves plot the analytical predictions. For the curves marked “free,” $\kappa = 0$; for the curves marked “forced,” $\kappa \simeq 6 \times 10^7$.

the small-amplitude, small-rotation limit, we expect that the frequency and the amplitude measured in our numerical experiment using Eqs. (3.9)–(3.11) will be different from their theoretical values α_0 and $-\frac{4}{3}\Omega_0$ by terms of order $O(\alpha^2)$, and $O(\Omega^2/\Omega_{\text{max}}^2)$.

We perform two numerical integrations of the equations of motion, for this slowly rotating initial configuration. In the first run (C1), we let the star evolve under purely Newtonian hydrodynamics, setting the strength κ of the radiation reaction (3.17) to zero. In the second run (C2), we force the mode by setting $\kappa \simeq 6 \times 10^7$. With this unphysically large value the amplitude of the r -mode grows appreciably within a time that we can conveniently follow numerically. (The Courant limit for the evolution timestep is set by the speed of sound in the fluid, and by the size of the grid cells; for $\Omega_0 = 0.26\Omega_{\text{max}}$, one complete rotation of the star takes about 70000 timesteps).

Figure 3.1 illustrates the evolution of the mode amplitude α in runs C1 and C2, as a function of t/P_0 , where $P_0 = 2\pi/\Omega_0$ is the initial rotation period of the star. The solid curves trace the numerical evolution of α [as defined in Eq. (3.9)], whereas the dashed curves trace the theoretical predictions for this evolution, obtained in the small-amplitude, slow-rotation limit [3].

When $\kappa = 0$, the theoretical prediction for the evolution of the amplitude is just $\alpha = \alpha_0$, and we can verify that the numerical evolution tracks the analytical curve within the expected deviations of order α^2 . When $\kappa \neq 0$, the analytical prediction for the evolution of the amplitude is

$$\alpha = \alpha_0 e^{t/\tau_{GR}}, \quad (3.24)$$

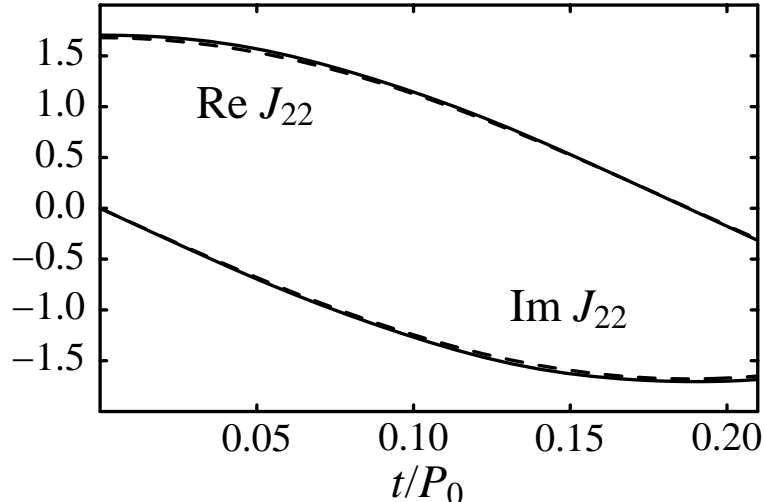


Figure 3.2: Real and imaginary parts of the current multipole moment J_{22} (in arbitrary units), for a slowly rotating star evolved without gravitational radiation reaction (run C1). The solid curves trace the numerical evolutions, the dashed curves trace the analytical predictions.

where the radiation-reaction timescale is given by [3]

$$\frac{1}{\tau_{\text{GR}}} = 2\pi \left(\frac{256}{405} \right)^2 \kappa \frac{G}{c^7} \tilde{J} M R^4 \Omega_0^6. \quad (3.25)$$

For this model, $\tau_{\text{GR}} = 0.46P_0$. As we can see in Fig. 3.1, the numerical evolution tracks the small-amplitude, slow-rotation analytical result within the expected accuracy, even if the radiation-reaction force is so unphysically strong.

Although this slow rotation numerical evolution was only carried out over a small fraction (0.2) of a rotation period (and therefore over a small fraction of the r -mode oscillation period), the evolution extended for about 7.3 dynamical times and 4.6 sound-crossing times.

In Figs. 3.2 and 3.3, we display two additional diagnostics for the undriven ($\kappa = 0$) slow-rotation evolution (C1). In Fig. 3.2 we plot the real and imaginary parts of the current multipole moment J_{22} : the solid curves trace the numerical evolution, whereas the dashed curves trace the analytical expression

$$J_{22} = \frac{1}{2} \alpha M R^3 \tilde{J} \Omega_0 e^{i\omega t}. \quad (3.26)$$

Again the deviations are within the expected accuracy of the analytical results. The deviations appear to be caused by the excitation of modes other than the pure $m = 2$ r -mode; the spurious excitations appear because the initial data [Eq. (3.23)] are only accurate to first order in α . Figure 3.3 depicts the evolution of the frequency ω [as defined in Eq. (3.11)]. The deviations from the analytical result, $\omega_0 = -\frac{4}{3}\Omega_0$, are within the expected accuracy. The magnified scale used to display ω in Fig. 3.3 makes the presence of the small-amplitude, short-period extraneous modes quite apparent.

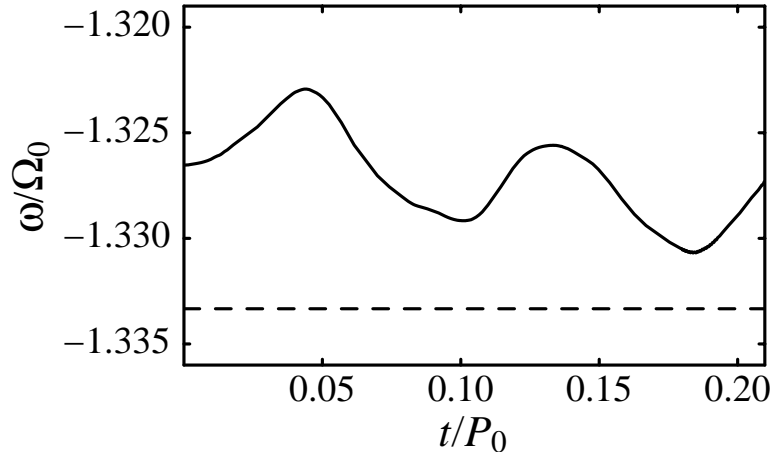


Figure 3.3: Frequency of the $m = 2$ r -mode, for a slowly rotating star evolved without gravitational radiation reaction (run C1). The solid curve is determined numerically from Eq. (3.11). For comparison, the dashed line shows the analytical value $\omega_0 = -\frac{4}{3}\Omega_0$.

3.5 Evaluating the saturation amplitude

In our production runs, we investigate the nonlinear behavior of the r -mode in a rapidly rotating stellar model, under a variety of physical conditions (different initial amplitudes and different values for the radiation-reaction coefficient κ).

Again, we provide initial data by solving the time-independent fluid equations for an $n = 1$ polytrope. The physical parameters for this model, labeled *Fast*, are reported in Table 3.1; in particular, the ratio of rotational kinetic energy to gravitational binding energy is $T_{\text{rot}}/|W| = 0.10072$, and the angular velocity is 95% of its maximum value.

We perform a numerical integration of the equations of motion starting from the rapidly rotating initial configuration, *Fast*, using Eq. (3.23) to add a slow-rotation, small-amplitude r -mode field, with $\alpha_0 = 0.1$. Because the radiation-reaction force is so much stronger for this model (it is proportional to $\omega^6 \propto \Omega^6$), we find that we can set $\kappa = 4487$, which yields an r -mode growth time $\tau_{\text{RR}}^{(s)} = 9.43P_0$. This choice of κ is still much larger than its physical value (unity), but it should yield a reasonable picture of the nonlinear evolution of the r -mode, if the timescales for all the relevant hydrodynamical processes (including nonlinear couplings to other modes) are comparable to P_0 , or shorter. Indeed, if the average sound-crossing time τ_S is representative of the relevant hydrodynamical timescales, then our condition is satisfied: a rough estimate gives $\tau_S = R_0/\bar{c}_S \simeq 0.16P_0 \simeq \tau_{\text{RR}}^{(s)}/60$, where we have approximated \bar{c}_S as the average speed of sound in the equivalent spherical polytrope.

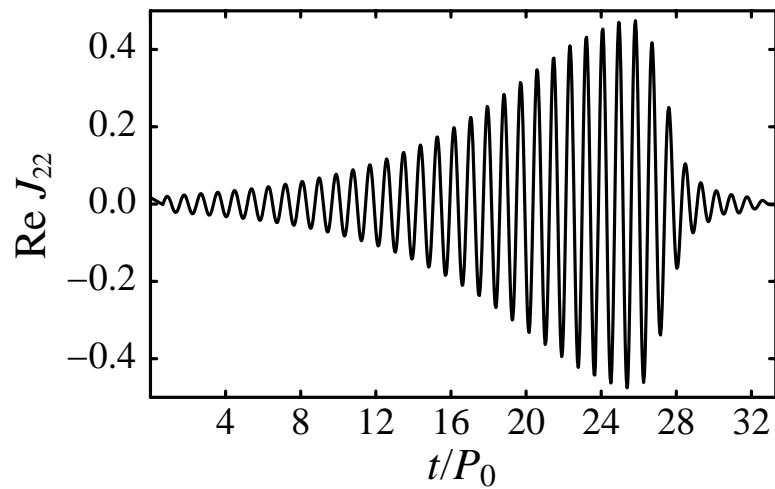


Figure 3.4: Numerical evolution of $\text{Re } J_{22}$ (arbitrary units) for a rapidly rotating star driven by gravitational radiation reaction (production run C3). The sinusoidal approximation, used to compute ω and $J_{22}^{(n)}$, is evidently appropriate for this run.

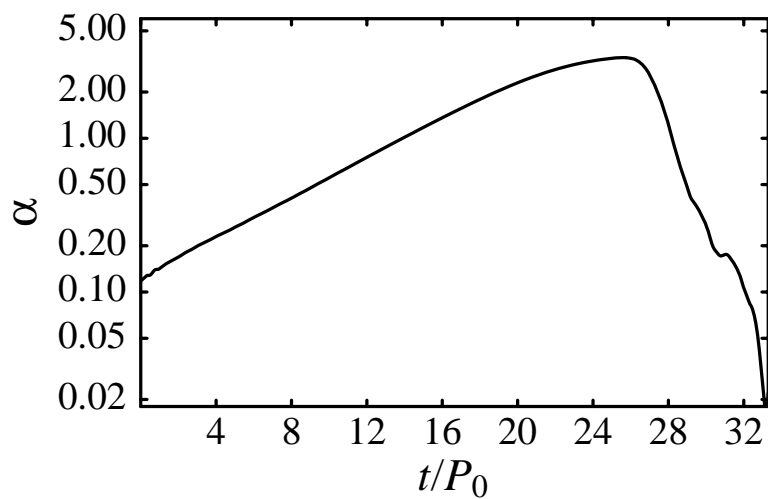


Figure 3.5: Numerical evolution of the r -mode amplitude α in production run C3.

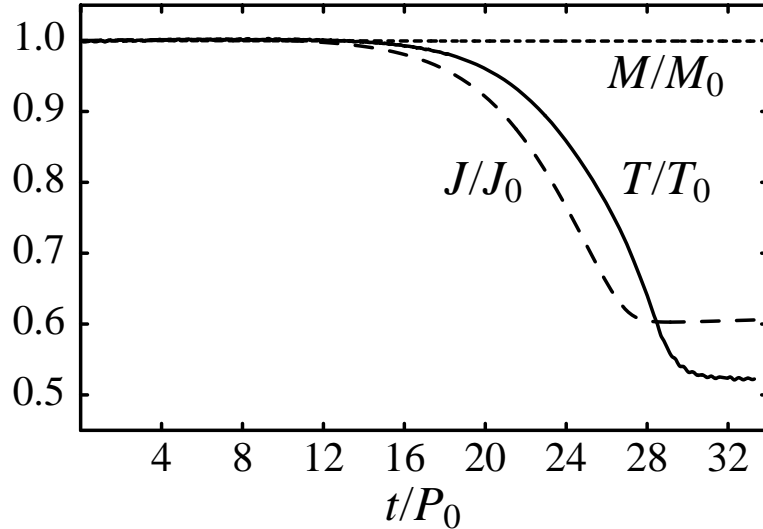


Figure 3.6: Evolution of total mass, total angular momentum, and total kinetic energy in production run C3. The quantities are plotted as fractions of their initial value.

3.5.1 Evolution of the r -mode amplitude

We follow the evolution through $t = 33P_0$. Because the rotation of the star is progressively reduced by radiation reaction, and because the star develops differential rotation, at the end of the evolution the star has performed, *on the average*, only about 31 rotations [we obtain this number from $\int \bar{\Omega} dt / (2\pi)$]. In Fig. 3.4 we plot the numerically determined evolution of $\text{Re} J_{22}$: the curve is a very smooth sinusoid, whose frequency is essentially constant, and whose envelope is determined by the (relatively slow) evolution of the r -mode amplitude. So the approximations used to compute ω and $J_{22}^{(n)}$ (discussed in Sec. 3.3) are in fact quite good in this situation.

In Fig. 3.5 we plot the numerical evolution of the r -mode amplitude α . At the beginning of the evolution, the computed diagnostic α agrees with the theoretical value α_0 to $\sim 10\%$, within the expected accuracy. The growth is exponential (as predicted by perturbation theory) until $\alpha \approx 1.8$. Then some nonlinear process begins to limit the growth, until the amplitude peaks at $\alpha = 3.35$ and then falls rapidly within a few rotation periods. After this the r -mode is effectively not excited.

3.5.2 A mechanism for r -mode saturation

What nonlinear process is responsible for the behavior of the r -mode amplitude? What causes the mode to saturate and disappear from the star? To answer these questions, we study the evolution of the total mass, total angular momentum, and total kinetic energy of the star, which are plotted in Fig. 3.6.

Because the mass is constant, the damping of the r -mode cannot be caused by ejection of matter from the simulation grid. On the other hand, we expect that the star should lose energy and angular

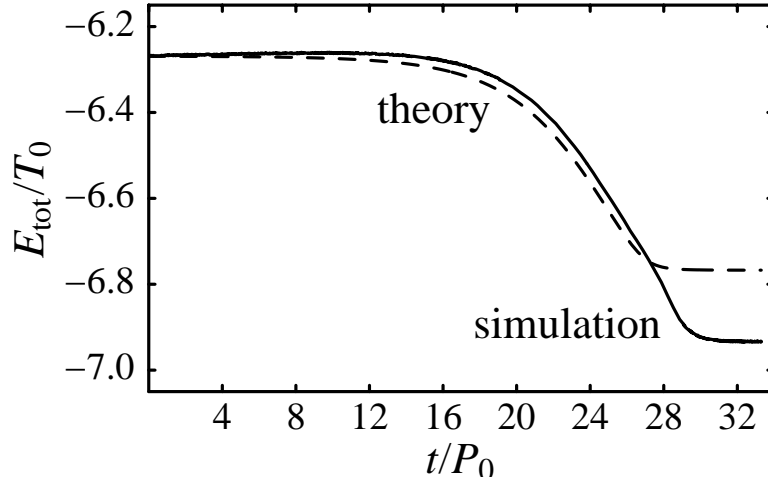


Figure 3.7: Theoretical and numerical evolution of the total energy for production run C3. The total energy is plotted in units of the initial rotational energy (because the system is bound, E_{tot} must be negative).

momentum as it radiates gravitational radiation in accord with the prediction of general relativity [14, 17]:

$$\left(\frac{dE}{dt}\right)_{J_{22}} = \frac{|\omega|}{2} \left(\frac{dJ}{dt}\right)_{J_{22}} = -\frac{128\pi G}{225 c^7} \kappa \omega^6 |J_{22}|^2. \quad (3.27)$$

The evolution of the angular momentum mirrors this equation quite closely (within a few percent); for energy, however, Eq. (3.27) is only accurate until shortly after the catastrophic fall of the r -mode amplitude (at $t \simeq 28P_0$; see Fig. 3.7). Before that time, the star loses about 40% of its initial angular momentum and 36% of its initial kinetic energy. After that time, the amplitude and (therefore) the radiation-reaction force are much reduced, so J becomes essentially constant; however, the kinetic energy continues to decrease, losing an additional 12% of its initial value during the next three rotation periods.

If the r -mode were damped by a hydrodynamical process that conserved energy, such as the transfer of energy to other modes, then Eq. (3.27) should portray accurately the evolution of the kinetic energy. But this is not what we see: instead, some *purely hydrodynamic* process continues to decrease the energy (by a sizable amount!) after the gravitational-radiation losses become negligible.

We believe that we have identified this process. To first order in the amplitude, the r -mode is only a *velocity* mode; to second order, however, there is also an associated density perturbation, proportional to Y_{32} , which appears as a wave with four crests (two in each hemisphere) on the surface of the star. (We will present a quantitative analysis later in this section.) As the amplitude reaches its maximum, these crests become large, breaking waves: the edges of the waves develop strong shocks that dump kinetic energy into thermal energy. In doing so they damp the r -mode. Figure 3.8 illustrates the surface waves at $t = 28P_0$ and $t = 29P_0$ along selected meridional slices.

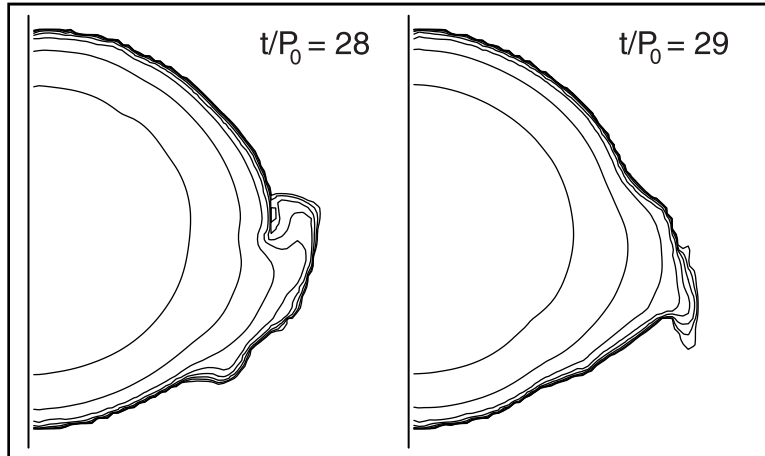


Figure 3.8: Isodensity surfaces showing breaking waves near the end of production run C3.

Our code is written in such a way that the evolution of the shocks is always *kinematically* correct. In particular, the continuity equation ensures that mass is properly conserved, and that the proper density jump occurs across the shocks; and the Euler equation ensures that momentum is properly conserved, and that the proper pre- and post-shock velocities arise. However, our code does not allow the energy dissipated in the shock to increase the entropy of the fluid, which remains always barotropic and isentropic. Consequently, the presence of shocks shows up as a decrease in the total energy of the star. Indeed, in this production run (C3) gravitational radiation reduces the *total* energy by 9% of its initial magnitude through $t = 28P_0$, and dissipation in shocks subtracts a further 3% in the last three rotations. (For comparison, 12% of the initial kinetic energy is lost in the last three rotations compared to 36% before that time.)

Ignoring the thermal effects of shocks is useful to reduce the computational burden and the complexity of the hydrodynamic code, and it is in fact a fairly reasonable approximation for neutron star matter, where the pressure comes mostly from the Fermi pressure of the degenerate neutrons, so the equation of state can be effectively modeled as temperature independent.

3.5.3 Radial structure of the r -mode amplitude

We define the radial amplitude density $\alpha(r)$ (where r is the *spherical* radius) by expressing the integral Eq. (3.8) for J_{22} in spherical coordinates, and omitting the radial integration:

$$\alpha(r)e^{i\phi(r)} = \frac{2}{\tilde{J}MR^2\Omega_0} \int \rho r^2 \vec{v} \cdot \vec{Y}_{22}^{B*} r^2 \sin\theta d\theta d\varphi. \quad (3.28)$$

We removed the absolute value around the integral for J_{22} so that we can keep track of the local mode phase $\phi(r)$. With this definition, $\alpha \exp[i\phi] = \int \alpha(r) \exp[i\phi(r)] dr/R$, where ϕ is the global

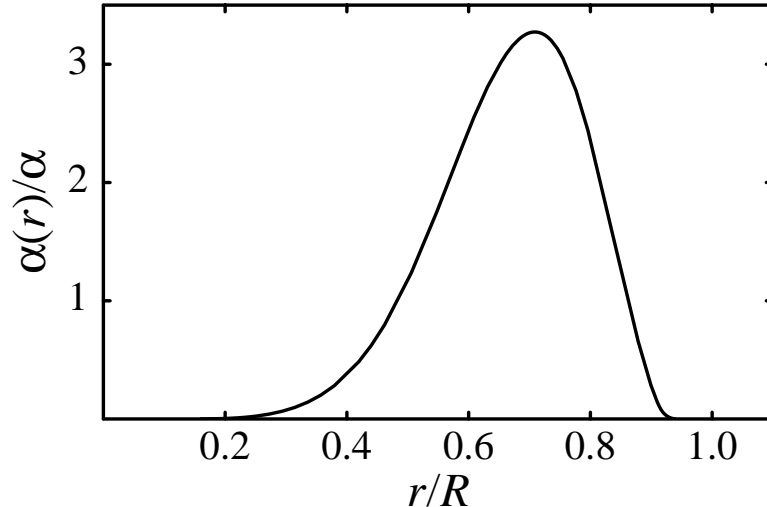


Figure 3.9: Radial amplitude density $\alpha(r)$ of the $m = 2$ r -mode for production run C3 at $t = 22.5P_0$.

phase of the r -mode.

The amplitude $\alpha(r)$ is plotted in Fig. 3.9 for the production run C3 at the time $t = 22.5P_0$. Throughout the entire evolution, the mode is concentrated mostly between the spherical radii $r = 0.5R$ and $0.9R$, and the shape of $\alpha(r)$ is fitted reasonably well by taking $\delta v \propto (r/R)^2$ [see Eq. (3.5)] and $\rho \propto (\sin \pi r/R)/(\pi r/R)$ as appropriate for a spherical, $n = 1$ polytrope.

It is also interesting to study the phase coherence of the r -mode, which we define as

$$(\Delta\phi)^2 = \frac{\int \alpha(r) |e^{i\phi(r)} - e^{i\phi}|^2 dr}{\int \alpha(r) dr}. \quad (3.29)$$

Figure 3.10 plots the evolution of $\Delta\phi$, which is small until the r -mode saturates at $t \approx 26P_0$. For $\Delta\phi \approx 1$, the local phase $\phi(r)$ spans approximately 2π : the mode has lost coherence completely. In this situation, there are large regions in the star where the radiation-reaction force pushes out of phase with the local mode oscillations; this mismatch accelerates the damping of the mode.

3.5.4 Evolution of the r -mode frequency

Figure 3.11 shows the numerical evolution of the r -mode frequency ω . The evolution of ω is quite smooth when the amplitude of the r -mode is large; when the amplitude is small (for $t \lesssim 10P_0$ and for $t \gtrsim 28P_0$), we see that other modes make noticeable contributions to J_{22} , and therefore to ω . At the beginning of the run, the numerical ω matches the theoretical prediction to within the expected accuracy of about 10%. These values for the frequency are also consistent with those obtained via a Fourier transform of J_{22} [18].

Surprisingly, the r -mode frequency remains approximately constant throughout the evolution,

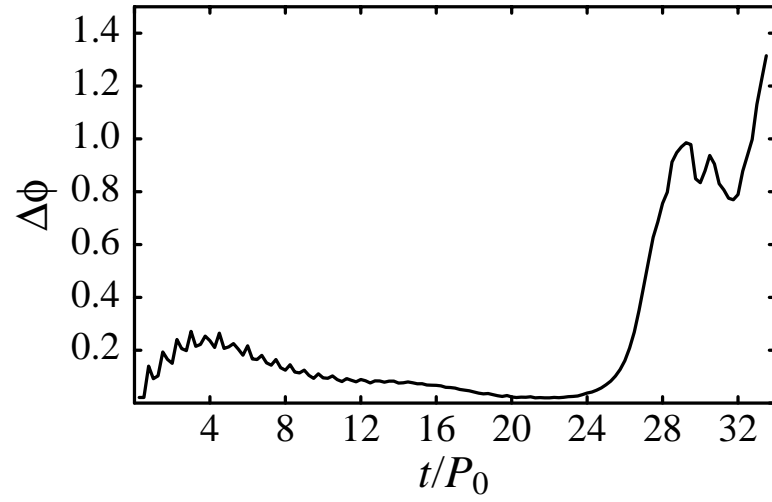


Figure 3.10: Evolution of the phase-coherence function $\Delta\phi$ in production run C3.

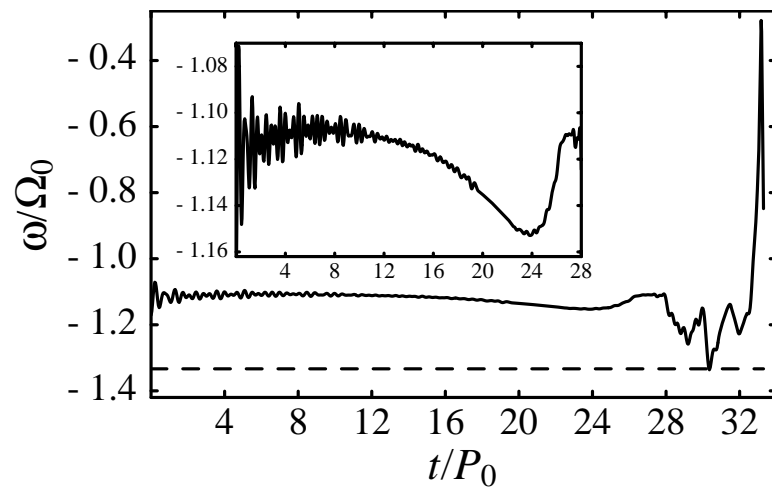


Figure 3.11: Numerical evolution of the r -mode frequency ω in production run C3.

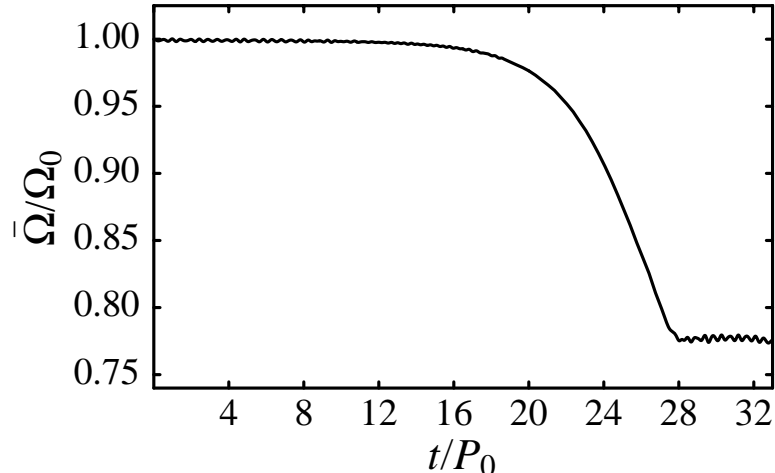


Figure 3.12: Numerical evolution of the average stellar angular velocity $\bar{\Omega}$ in production run C3.

and it does not follow the decline of the average angular velocity $\bar{\Omega}$ (plotted in Fig. 3.12). Altogether, the angular velocity decreases by about 22.5% while the total angular momentum decreases by 40%. (As the star spins down, it becomes less flattened, and the change in the moment of inertia accounts for the difference between the decrease of J and that of $\bar{\Omega}$.) The stability of the r -mode frequency has important implications for the possible detection of r -mode gravity waves (see Sec. 3.9).

We also point out that the approximate expressions for the GR reaction force, Eqs. (3.17)–(3.22), that we use here are accurate only when the motion of the fluid has nearly sinusoidal time dependence. Figure 3.11 illustrates that the evolution in our simulation remains quite sinusoidal until about $t = 28P_0$. After this point our expression for the GR reaction force is not reliable. After this point in our simulation, however, the fluid evolution is dominated by nonlinear hydrodynamic forces including shocks, and the GR reaction force is negligible. Thus our inability to model accurately the GR force during the late stages of the evolution does not effect our results.

3.5.5 Growth of differential rotation

During this simulation (run C3), the average differential rotation $\Delta\Omega$ [defined in Eq. (3.16)] grows to a maximum of approximately $0.41\bar{\Omega}$ (see Fig. 3.13). After a rapid increase in the first three rotation periods, when the linear r -mode eigenfunction of Eq. (3.23) evolves into its proper nonlinear, rapid-rotation form, $\Delta\Omega/\bar{\Omega}$ increases approximately as $\alpha^{0.75}$ until $\alpha \simeq 1$, and then approximately as α until α begins to saturate. When α is maximum, $\Delta\Omega = 0.25\bar{\Omega}$. As the amplitude falls, $\Delta\Omega$ continues to grow (even more steeply), as long as there is significant gravitational radiation. After $t = 28P_0$, $\Delta\Omega$ decreases to about 80% of its peak value. So the final configuration of the star (where the presence of the r -mode is essentially negligible) still has a very large differential rotation.

But we should not concentrate exclusively on the averaged quantity $\Delta\Omega/\bar{\Omega}$, which does not cap-

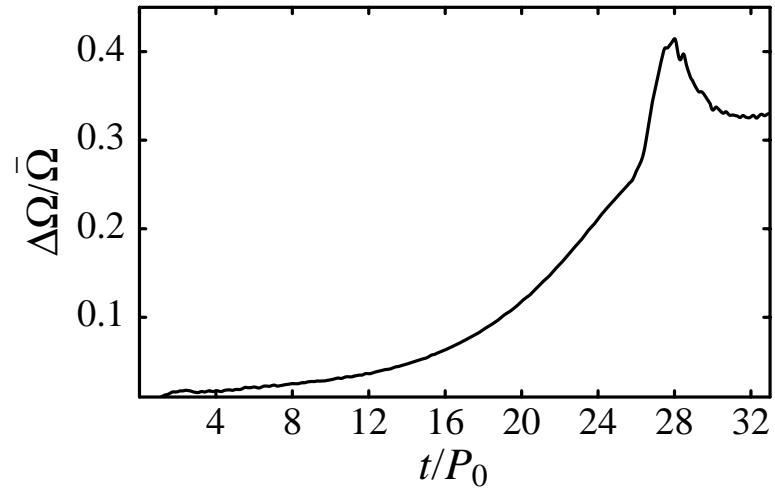


Figure 3.13: Numerical evolution of the differential rotation $\Delta\Omega$ in production run C3.

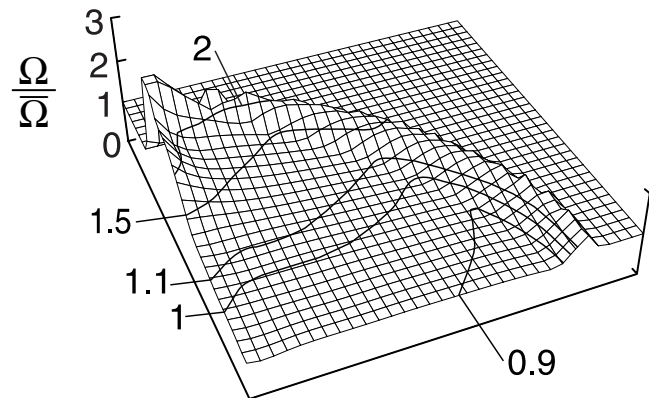


Figure 3.14: Meridional structure of the differential rotation in production run C3. The plot shows the value of the azimuthally averaged angular velocity $\Omega(\varpi, z)/\bar{\Omega}$, at time $t = 25.6P_0$.

ture fully the spatial structure of differential rotation. Figure 3.14 illustrates the spatial dependence of the azimuthally averaged angular velocity,

$$\Omega(\varpi, z) = \frac{1}{2\pi} \int \Omega(\varpi, z, \varphi) d\varphi, \quad (3.30)$$

at the time when the amplitude is maximum, $t = 25.6P_0$. The differential rotation is confined mostly to a thin shell of material near the surface of the star, and is particularly concentrated near each polar cap. The bulk of the material in the star remains fairly rigidly rotating.

3.5.6 Consistency of the radiation-reaction force

In these simulations we have assumed that the only relevant contribution to the radiation reaction force comes from the current quadrupole moment, and in particular from J_{22} . However, in the post-Newtonian approximation to general relativity, the lowest-order contribution to radiation reaction comes from the mass quadrupole term, followed by mass octupole and current quadrupole. To verify that our approximation is justified for the physical states considered here, we evaluate the additional energy that would have been lost to gravitational waves throughout our simulation if we had included the lowest-order mass multipole terms.

The mass multipole moments Q_{lm} are defined by

$$Q_{lm} = \int \rho r^l Y_{lm}^* d^3x. \quad (3.31)$$

In the presence of density oscillations with sinusoidal dependences in the coordinates t and φ (*i.e.*, $\delta\rho_{lm} \propto e^{i\omega_{lm}t + im\varphi}$) the flux of energy into gravitational waves is given by [19, 20]

$$\left(\frac{dE}{dt}\right)_{Q_{2m}} = -\frac{8\pi G}{75 c^5} \omega_{2m}^6 |Q_{2m}|^2; \quad (3.32)$$

$$\left(\frac{dE}{dt}\right)_{Q_{3m}} = -\frac{8\pi G}{6615 c^7} \omega_{3m}^8 |Q_{3m}|^2. \quad (3.33)$$

where Q_{2m} and Q_{3m} are, respectively, the mass quadrupole and mass octupole moments induced by these density fluctuations. Contributions of higher order are suppressed by very small fractional coefficients.

Comparing Eqs. (3.32) and (3.33) with Eq. (3.27) we find that the contribution of the density oscillations associated with the r -mode at frequency ω to the energy flux is negligible whenever

$$\frac{3c^2}{16} \frac{|Q_{2m}|^2}{|J_{2m}|^2} \ll 1, \quad \frac{5\omega^2}{2352} \frac{|Q_{3m}|^2}{|J_{2m}|^2} \ll 1. \quad (3.34)$$

We find that in our simulation both ratios are of order 10^{-3} before the r -mode saturates (at

$t \simeq 25P_0$). The strongest contribution to the quadrupole term comes from Q_{22} , although the Fourier transform of this moment does not show any definite frequency of oscillation. The strongest contribution to the octupole term comes from the Y_{32} dependence of the density in the $m = 2$ r -mode (see the next subsection).

Between $t \simeq 25P_0$ and $t \simeq 32P_0$ (when α is back to its initial value ≈ 0.1) the mass quadrupole term would have provided a correction of order 10% to the current quadrupole; although even then we see no evidence of a definite oscillation frequency correlated to the r -mode. Only after $t \simeq 32P_0$, when the fluid motion in the star becomes quite turbulent and the r -mode is very weak, is the gravitational radiation generated by the mass multipoles comparable to the radiation from J_{22} .

On the whole, we find that our approximation, which ignores the contributions from the mass multipoles, is well justified throughout the more interesting part of the evolution.

3.5.7 Density oscillations and mode saturation

The evolution of the isodensity surfaces in our neutron star shows very clearly the presence of the lowest-order Eulerian density perturbation $\delta\rho$ associated with the $m = 2$ r -mode. The lowest order expression for $\delta\rho$ was derived by Lindblom, Owen and Morsink [3] in the small-amplitude, slow-rotation approximation. Solving Eq. (5) of Ref. [3] with $m = 2$ and with polytropic index $n = 1$, and then substituting $\delta\Psi$ back into Eq. (4) of Ref. [3], we get

$$\delta\rho = \alpha_0 \frac{7\pi^2}{15} \sqrt{\frac{2}{3}} \frac{\Omega_0^2}{G} j_3\left(\frac{\pi r}{R_0}\right) Y_{32}(\theta, \varphi) e^{i\omega t}, \quad (3.35)$$

where j_3 is the spherical Bessel function. The mass multipole associated with this $\delta\rho$ is

$$\delta Q_{32} = \alpha_0 \frac{7\pi}{15} \sqrt{\frac{2}{3}} \frac{\Omega_0^2 R_0^5}{G} j_4(\pi) Y_{32}(\theta, \varphi) e^{i\omega t}, \quad (3.36)$$

where $j_4(\pi) = 0.151425$.

We study the evolution of Q_{32} throughout run C3. We find that Q_{32} (and therefore the density perturbation with angular dependence given by Y_{32}) is indeed proportional to α , at least as long as the growth of α remains exponential; after that, Q_{32} grows more slowly than α , and it reaches a maximum a few rotation periods before α (see Fig. 3.15). The phase evolution of the density perturbation is also consistent with expectations: the Fourier transform of $Q_{32}(t)$ shows a very definite peak at the r -mode (numerical) frequency ω .

A quantitative check shows that Eq. (3.36) predicts the observed magnitude of Q_{32} with an accuracy of about 50%; this error is consistent with the next-order terms ($\sim \Omega^4$ and α^2) not included in this expression. In the slowly rotating calibration model C1, we find that Q_{32} is given by Eq. (3.36) to within about 1%.

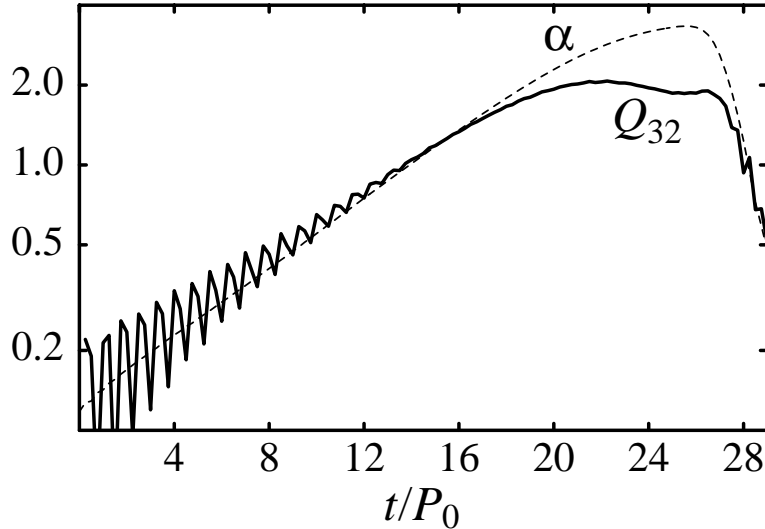


Figure 3.15: Numerical evolution of the mass moment Q_{32} (solid line) and of the r -mode amplitude α , in production run C3. The curve for Q_{32} was renormalized to emphasize the linear relation between α and Q_{32} during the growth of the r -mode.

We point out that we do not explicitly include any density perturbation in the initial configuration of the star; rather, the density perturbation is immediately generated by the hydrodynamic evolution of the fluid as a consequence of the initial velocity perturbation. The evolution of the amplitude of the density perturbation provides more insight into the mechanism that causes the r -mode to saturate: on the surface of the star, $\delta\rho$ appears as four large wave crests; at a critical amplitude these crests stop growing, and within a few rotation periods they turn into breaking waves that damp the r -mode.

3.5.8 Limits on mode–mode coupling

In the numerical evolution C3, nonlinear hydrodynamic processes do not prevent the gravitational radiation instability from driving the dimensionless amplitude of the r -mode to values of order unity. In particular, the energy of the r -mode is not channeled into other modes by nonlinear hydrodynamic coupling until the amplitude of the mode becomes quite large. It is possible however that the nonlinear processes that would limit the growth of the r -mode act only on timescales that are longer than our artificially brief simulation growth time $\tau_{\text{RR}}^{(s)}$, but still shorter than the physical $\tau_{\text{RR}}^{(p)}$.

Can our numerical simulation place any limits at all on the possibility of nonlinear coupling? We know that in our simulation the amplitude of the r -mode grows exponentially until $\alpha \approx 2$, so the nonlinear interaction with other modes must be negligible at least until that time. This observation allows us to set a limit on the strength of the nonlinear couplings between the modes; and from

this limit we can infer a *lower limit* on the saturation amplitude that may be achieved when the radiation-reaction coupling is adjusted to its physical value. Of course, the inference is only justified for the nonlinear interaction of the r -mode with other modes that are correctly modeled in our simulation (for instance, the finite azimuthal resolution of the grid sets an upper limit on the m of the modes that can be resolved), and with our physical assumptions (for instance, the buoyant g -modes of realistic neutron stars will not be present with our choice of the equation of state).

Our argument is based on the Lagrangian description of the nonlinear evolution of the mode amplitude developed by Schenk et al. [8]. In this formalism, the modes interact at the lowest order by way of *three-mode couplings*: roughly speaking, quadratic interactions between pairs of modes drive the evolution of the amplitude of a third mode. Because at the beginning of our simulation all modes except the r -mode have negligible amplitude, we expect that the most important three-mode nonlinear term might be one that couples two r -modes to a third mode [8]. Following Ref. [8] we consider the coupled equations for the r -mode and a generic mode X obtained in second-order Lagrangian perturbation theory:

$$\frac{dc_R}{dt} + i\omega_R c_R = \frac{c_R}{\tau_{RR}} + \frac{i\omega_R}{2} \frac{\kappa_{XRR}^*}{\epsilon_R} c_R^* c_X^*, \quad (3.37)$$

$$\frac{dc_X}{dt} + i\omega_X c_X = \frac{i\omega_X}{2} \frac{\kappa_{XRR}^*}{\epsilon_X} c_R^* c_R^*, \quad (3.38)$$

where c_R and c_X are the complex amplitudes (including phases) of the modes; ω_R and ω_X are their frequencies; ϵ_R and ϵ_X are the nonlinear mode energies at unit amplitude; and τ_{RR} is the radiation-reaction e-folding time of the r -mode. Finally, κ_{XRR}^* is the nonlinear interaction energy for unit amplitude modes. Schenk, *et al.* [8] give expressions for the κ_{XRR} of coupled generic Newtonian modes in rotating stars. In writing Eqs. (3.37) and (3.38) we have omitted the coupling terms proportional to κ_{XXR}^* , which are forbidden by a z -parity selection rule [8]: the r -mode has odd z parity, so it cannot couple quadratically to the mode X .

From our numerical evolution C3, we know that the amplitude of the r -mode grows very nearly exponentially until $\alpha \simeq 2$:

$$c_R(t) \simeq c_R(0) e^{-i\omega_R t + t/\tau_{RR}^{(s)}}, \quad (3.39)$$

where $\tau_{RR}^{(s)}$ is the artificially short radiation-reaction timescale used in our simulation. (Although it is convenient to take $|c_R| \simeq \alpha$, our argument still applies as long as $|c_R|$ is merely proportional to α .) Therefore, we also know that until $|c_R| \simeq 2$, the second term on the right side of Eq. (3.37) is negligible compared to the first. In this case,

$$\frac{1}{\tau_{RR}^{(s)}} \gg \left| \frac{i\omega_R}{2} \frac{\kappa_{XRR}^*}{\epsilon_R} c_X^* \right|. \quad (3.40)$$

We now use Eq. (3.39) to integrate Eq. (3.38) and compute c_X :

$$c_X(t) = c_X(0)e^{-i\omega_X t} + \frac{i\omega_X \kappa_{XRR}^*}{2 \epsilon_X} \frac{[c_R^*(t)]^2 - [c_R^*(0)]^2 e^{-i\omega_X t}}{2i\omega_R + i\omega_X + 2/\tau_{RR}^{(s)}}. \quad (3.41)$$

Now we set $c_X(0) \simeq 0$ and $|c_R(t)| \gg |c_R(0)|$ for the time late in the simulation when $c_R \simeq 2$, and find

$$|c_X(t)| \simeq \left| \frac{\kappa_{XRR}^*}{\epsilon_X} \right| \frac{|\omega_X \tau_{RR}^{(s)}| |c_R^*(t)|^2}{2\sqrt{(\tau_{RR}^{(s)} \delta\omega)^2 + 4}}, \quad (3.42)$$

where $\delta\omega \equiv 2\omega_R + \omega_X$. We define the *resonance index* $\gamma^{(s)} = |\omega_R/\omega_X| [(\tau_{RR}^{(s)} \delta\omega)^2 + 4]^{1/2}$, whose value is close to unity, $\gamma^{(s)} \simeq 1$, when the system is near resonance, $\delta\omega \simeq 0$. We use this bound on $|c_X(t)|$ in Eq. (3.40) to obtain

$$\frac{1}{\tau_{RR}^{(s)}} \gg \frac{|\kappa_{XRR}^*|^2}{4\epsilon_X \epsilon_R} \omega_R^2 \tau_{RR}^{(s)} \frac{|c_R^*(t)|^2}{\gamma^{(s)}}. \quad (3.43)$$

We can rewrite this inequality in terms of the r -mode period $P_R = 2\pi/\omega_R$:

$$\left[\frac{P_R}{\tau_{RR}^{(s)}} \right]^2 \gg \pi^2 \frac{|c_R(t)|^2}{\gamma^{(s)}} \left| \frac{\kappa_{XRR}^*}{\epsilon_X} \right|^2 \frac{\epsilon_X}{\epsilon_R}. \quad (3.44)$$

We now set $|c_R(t)| = 2$ (the value at which the evolution of the amplitude begins to show deviation from exponential) and $P_R/\tau_{RR}^{(s)} = 1/10$ (the value for our simulation), and obtain

$$\left| \frac{\kappa_{XRR}^*}{\epsilon_X} \right|^2 \frac{\epsilon_X}{\epsilon_R} \ll \frac{\gamma^{(s)}}{400\pi^2}. \quad (3.45)$$

Thus, our numerical evolution puts a limit on the strength of the coupling between the r -mode and other modes in the star.

We now ask how the saturation amplitude would change if the radiation-reaction timescale assumed its physical value $\tau_{RR}^{(p)}$ instead of the value $\tau_{RR}^{(s)}$ used in our simulation C3. The key to doing this is to realize that Eqs. (3.37) and (3.38) describe the coupled mode evolution in the physical case if we just substitute $\tau_{RR}^{(p)}$ for $\tau_{RR}^{(s)}$. The mode X is capable of stopping the unstable growth of the r -mode only when the magnitude of the second term on the right side of Eq. (3.37) becomes comparable to the first. Through an analysis similar to the one that led to Eq. (3.44), it is straightforward to find the following condition on the saturation amplitude of the r -mode,

$$\left[\frac{P_R}{\tau_{RR}^{(p)}} \right]^2 \simeq \pi^2 \frac{|c_R^{\text{sat}}|^2}{\gamma^{(p)}} \left| \frac{\kappa_{XRR}^*}{\epsilon_X} \right|^2 \frac{\epsilon_X}{\epsilon_R}. \quad (3.46)$$

We now use the upper limit for $|\kappa_{XRR}^*|$ from Eq. (3.45) from our numerical evolution, to obtain a

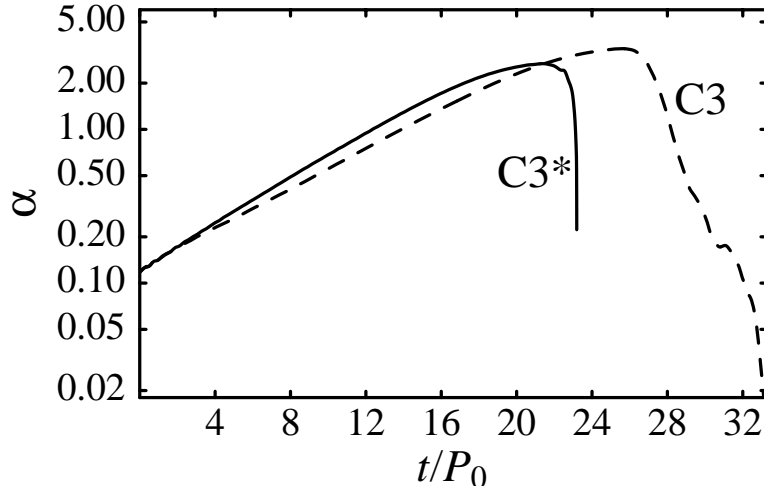


Figure 3.16: Numerical evolution of the r -mode amplitude α in low-resolution run C3* (solid curve) and in run C3 (dashed curve).

lower limit for the amplitude c_R^{sat} , at which the r -mode would be saturated in the physical case:

$$|c_R^{\text{sat}}| \gg 20 \frac{P_R}{\tau_{\text{RR}}^{(p)}} \sqrt{\frac{\gamma^{(p)}}{\gamma^{(s)}}}. \quad (3.47)$$

Since $\gamma^{(p)} > \gamma^{(s)}$, this equation yields $|c_R^{\text{sat}}| \gg 4 \times 10^{-4}$ for run C3. So if the dominant mode–mode coupling is of the form given in Eqs. (3.37) and (3.38), our simulation places a relatively large lower limit on the r -mode saturation amplitude. However, the r -mode could instead be limited by *parametric resonance* [21] with a suitable pair of modes (satisfying the resonance condition $\omega_R + \omega_Y + \omega_Z \simeq 0$). It appears that our simulation does not provide a very strong lower limit on the saturation amplitude that could be imposed by this kind of process.

3.5.9 Dependence on the grid spacing

We wish to confirm that our standard computational grid can resolve the spatial structure of the r -mode well enough to give reliable predictions about the saturation amplitude of the mode. For this purpose, we have performed a simulation (run C3*) with the same parameters of run C3, but on a grid with only half the spatial resolution (i. e., 32 cells in the radial direction, and 64 cells in the axial and azimuthal directions). Figure 3.16 compares the evolution of α in runs C3 and C3*. The two curves are very similar, but in run C3* saturation is reached a bit earlier, at $t/P_0 = 21.4$, and at a somewhat lower amplitude $\alpha = 2.68$. This may be caused by the larger numerical viscosity that must be present in the coarser grid. The evolution of the other diagnostics is also very similar in the two runs.

Thus, the simulation run C3* suggests that the qualitative results of our simulations are independent of the resolution adopted. The r -mode saturation amplitudes on the two grids agree to within about 20%. Interestingly, the extrapolation to the infinite resolution case suggests that the physical saturation amplitude might be even larger than 3.3.

3.6 Testing the saturation amplitude

Even in the absence of a saturation mechanism due to mode–mode coupling as described above, it is possible that the saturation amplitude in our simulation might still depend on the strength of the radiation-reaction force. In our simulation we see that the r -mode grows until density waves on the surface of the star break and form shocks. It is possible that this occurs just because in our simulation we are pushing the fluid too hard with the radiation-reaction force, much harder than it would be appropriate in the physical case. To explore how the evolution depends on the strength of this driving force, we go back to the time in run C3 before any signs of nonlinear saturation are seen, when $\alpha = 1.8$. We start a new run (C4) there, increasing the value of κ (which determines the strength of the radiation-reaction force) to 5967 (1.33 times its value in run C3). The new growth timescale is about $7.5P_0$. (Undoubtedly, a test with $\kappa \ll 4487$ would have been more compelling; but our evolutions are so computationally expensive that we were forced to increase rather than decrease the strength of the driving force.)

In a separate run (C5), we test the influence of the *history* of the evolution of the r -mode on its saturation amplitude. Namely, we ask if an r -mode that started out as the *linear* initial data of Eq. (3.23), with a very large amplitude, would evolve much differently from an r -mode that started out small and was built up gradually to large amplitude by the radiation reaction force. To answer this question, we start with the *Fast* equilibrium model, and we add a linear r -mode velocity field with $\alpha_0 = 1.8$. For this run we keep $\kappa = 4497$.

Figures 3.17, 3.18, and 3.19 show the evolution of the diagnostic parameters α , ω and $\Delta\Omega$ for runs C3–C5. As expected, the r -mode does grow faster in run C4, but its maximum value is essentially the same (the maximum $\alpha = 3.338$ at $t = 24.12P_0$) as in run C3. In this run, the r -mode amplitude increases from $\alpha = 1.8$ to $\alpha = 3.338$ within a time $\Delta t \simeq 6P_0$ (compared to $\Delta t \simeq 8P_0$ in run C3) as would be expected given that the driving force is $\frac{4}{3}$ times that of run C3.

In run C5, the growth of the r -mode is initially slower than in run C3, as the linear r -mode velocity field evolves toward its correct nonlinear form. Eventually its maximum occurs at essentially the same amplitude as before ($\alpha = 3.337$). Figures 3.17 and 3.18 show that during run C5 α and ω undergo short-period oscillations; this happens because the initial velocity field is only a small-amplitude approximation to the *real* $m = 2$ r -mode eigenfunction. So other spurious modes with fairly large amplitude are excited initially in run C5. Note that these extraneous modes must make

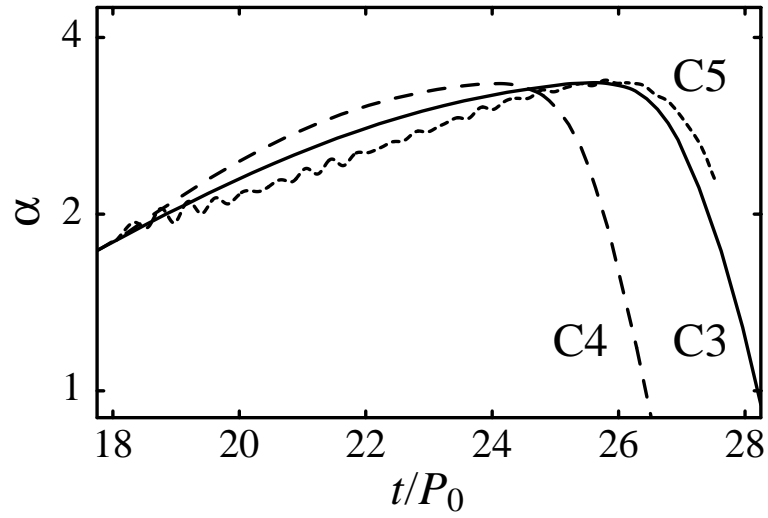


Figure 3.17: Numerical evolution of the r -mode amplitude α in production runs C3–C5.

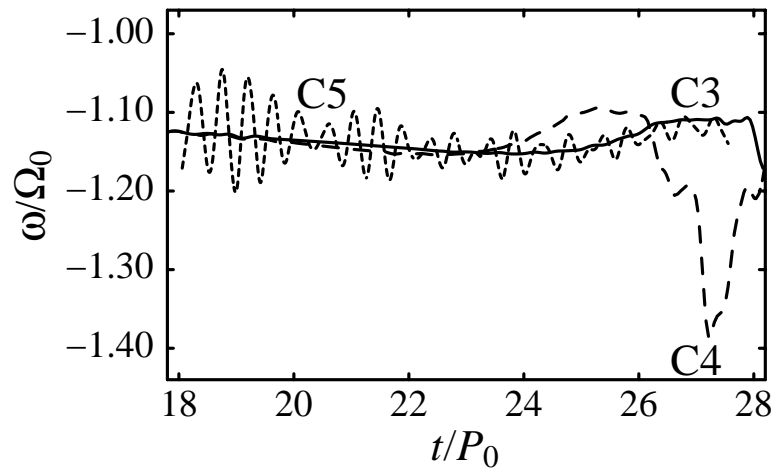


Figure 3.18: Numerical evolution of the r -mode frequency ω in production runs C3–C5.

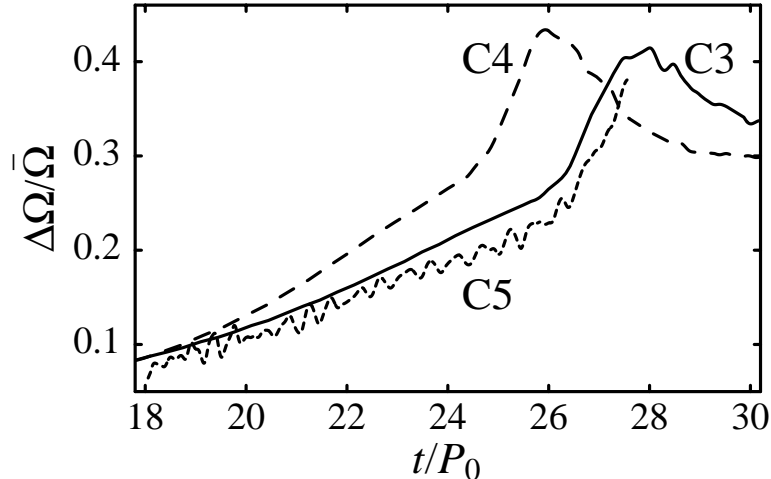


Figure 3.19: Numerical evolution of the differential rotation $\Delta\Omega$ in production runs C3–C5.

nonzero contributions to J_{22} if they are to show up in our diagnostics. Here the extraneous modes cause a rapid modulation of α and ω with a dominant period of about $0.5P_0$. Finally, it is interesting to consider the evolution of $\Delta\Omega$ (Fig. 3.19), which is very similar in the three runs.

These runs provide limited evidence that the saturation amplitude of the r -mode does not depend (strongly) on our artificially large radiation reaction force. The nonlinear hydrodynamical process that leads to shock formation appears to be triggered by attaining a certain critical amplitude of the r -mode, with little dependence on the strength of the radiation-reaction force. Thus if no mode–mode coupling occurs on timescales longer than our unphysically short $\tau_{RR}^{(s)}$, then our results suggest that the maximum amplitude $\alpha \approx 3$ is a reasonable guess for the physical case ($\kappa = 1$) as well.

3.7 Free evolution

Stergioulas and Font [7] have also studied the nonlinear evolution of r -mode initial data, but using relativistic hydrodynamics in a fixed background geometry. In their evolution using this *relativistic Cowling approximation*, the gravitational interactions of the mode with itself and with the rest of the star are neglected. The principal difference between their model and ours therefore is that theirs has no radiation reaction and no r -mode growth.

Stergioulas and Font find that, for an initial r -mode amplitude $\alpha_0 = 1.0$, no *significant* suppression of the mode is observed during 13 rotation periods. They define their mode amplitude using a post-Newtonian expression for the eigenfunction that differs from our Eq. (3.23) except in the Newtonian limit. And their method of evaluating the mode amplitude numerically also differs from ours. They read the mode amplitude from the value of the fluid’s velocity at a single point within the star, while we define α in terms of integrals over the entire star. In the slow-rotation

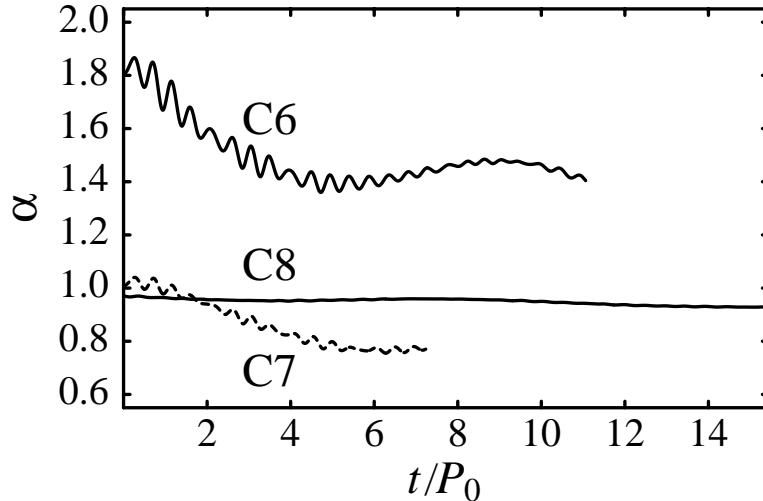


Figure 3.20: Numerical evolution of the r -mode amplitude α in production runs C6–C8.

Newtonian limit our two definitions agree. Stergioulas and Font observe that the amplitude of the velocity oscillations (shown in Fig. 2 of Ref. [7]) decrease by about 50% during the course of their simulation, an effect that they attribute to numerical viscosity [7]. In order to compare our own simulations more directly with theirs, we performed a series of evolutions in which we turned off the radiation-reaction force by setting $\kappa = 0$.

In production runs C6 and C7, we augment our rapidly rotating equilibrium configuration with the approximate r -mode velocity field of Eq. (3.23). For run C6, we choose the initial α_0 so that α [as measured by our numerical diagnostic, Eq. (3.9)] is initially 1.8: the value at which we start to observe deviations from exponential growth in run C3. For run C7, we choose α_0 so that the initial α is 1.0, in order to make a direct comparison with Stergioulas' and Font's published results. We have evolved these systems through respectively 11 and 7 initial rotation periods (several hydrodynamical timescales, according to our rough estimate of the speed of sound for the rapidly rotating model).

We plot the evolution of α and ω for these simulations in Figs. 3.20 and 3.21. The wavy appearance of the curves suggests that, by using the linear eigenfunction, Eq. (3.23), for amplitudes of order unity, we have excited spurious modes in addition to the basic $m = 2$ r -mode. We have already observed this behavior in run C5. The rapid modulation of α and ω has a period of about $0.5P_0$, and the amplitude of the modulation is smaller for run C7. (This is reasonable: for lower α we expect the approximate expression, Eq. (3.23), to be more accurate and so to excite smaller amplitude spurious modes.)

In both runs, α loses about 20% of its initial value during the first four rotation periods. In the next few rotation periods, however, the average value of α remains unchanged (although in run C6 we can see a further modulation of the amplitude with a period of about $8P_0$). Throughout the

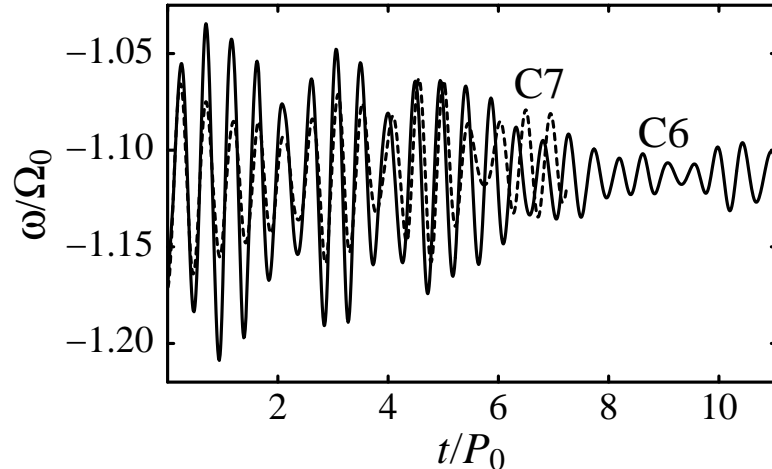


Figure 3.21: Numerical evolution of the r -mode frequency ω in production runs C6 and C7.

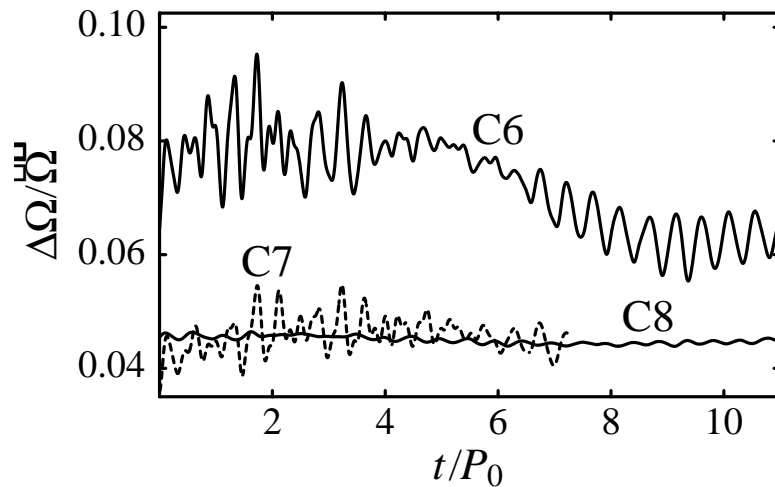


Figure 3.22: Numerical evolution of the differential rotation $\Delta\Omega$ in production runs C6–C8.

runs, the r -mode frequency ω oscillates around $\omega = -1.12\Omega_0$, consistent with its value in run C3 for the same value of α (i. e., 1.44). As the run is started, the differential rotation $\Delta\Omega$ (which is zero in the initial, rigidly rotating star) increases almost immediately to values that are consistent with those observed in run C3 for the same amplitude; compare Figs. 3.22 and 3.13. As α decreases, $\Delta\Omega$ decreases consistently. (In run C7, $\Delta\Omega$ settles to a value slightly higher than what we expected from its value in run C3 when $\alpha = 0.82$; but we did not run this evolution as far as run C6, so at the end of our simulation the value of $\Delta\Omega$ might still be evolving.)

Finally, we study the free nonlinear evolution of an r -mode that was *grown* to the amplitude $\alpha = 1$. To do so, we go back to the time in run C3 when $\alpha = 1$, and start a new run (C8) using the C3 data at this time. We evolve these data setting κ to zero in the subsequent evolution. We

follow this evolution through an additional 15.4 initial rotation periods. During this time the mode amplitude α is essentially constant, see Fig. 3.20, except for a slow secular decline due to numerical viscosity at 0.23% per revolution, and a few very small amplitude oscillations. The r -mode frequency is quite constant, and the phase coherence function, and the differential rotation $\Delta\Omega$ also remain quite small in this case (see Fig. 3.22). The r -mode amplitude in run C3 remains above unity for 14.3 rotation periods, so run C8 demonstrates that the LSU hydrodynamic code [10, 9] used here reliably and stably evolves large amplitude r -modes in rapidly rotating stars for the duration of our simulations.

Comparing runs C6, C7, and C8, we infer that the strong decrease in the amplitude observed in runs C6 and C7 occurs as nonlinear hydrodynamics reorganizes the initial linear r -mode velocity field to the correct nonlinear form for amplitudes of order unity. After the reorganization is complete (within a few rotation periods), α decreases only because of numerical viscosity. (In run C5, this same phenomenon caused the slower growth of the amplitude compared to run C3.) By contrast, the small decrease in run C8 appears to be caused entirely by numerical viscosity.

Altogether, we find that our results are compatible with those of Stergioulas and Font [7]: no nonlinear saturation effect is evident in the free nonlinear evolution of r -modes, at least for amplitudes of order unity.

3.8 Repeated spindown episodes?

The first attempt to analyze the nonlinear evolution of r -modes by Owen et al. [5] was based on a simple two-parameter model consisting of a rotating star with angular velocity Ω and its r -mode with amplitude α . Using this model the mode was found to grow exponentially until it reached some maximum level α_{\max} , where it was assumed to remain saturated. Energy and angular momentum were expected to be removed from the star by gravitational radiation during this saturation phase until the r -mode regained stability (because of increased internal dissipation brought about by cooling or because the angular momentum of the star was reduced to a very low level). In this initial picture gravitational radiation was expected to spin down the star on a timescale of about one year. The radiation emitted was expected to sweep down in frequency from $\frac{4}{3}$ times the initial angular velocity of the star to $\frac{4}{3}$ times its final value: ranging from perhaps 1 kHz initially to perhaps 100 Hz.

Our simulations suggest a very different picture. We find that, once the amplitude of the r -mode reaches α_{\max} , it is quickly reduced by the action of the breaking waves and shocks, instead of remaining saturated at this value for a very long time. At the end of our simulation the star still has 60% of its initial angular momentum, and its average angular velocity is 77.5% of Ω_0 . Thus the star is left rotating relatively rapidly, leaving open the possibility of subsequent episodes of r -mode

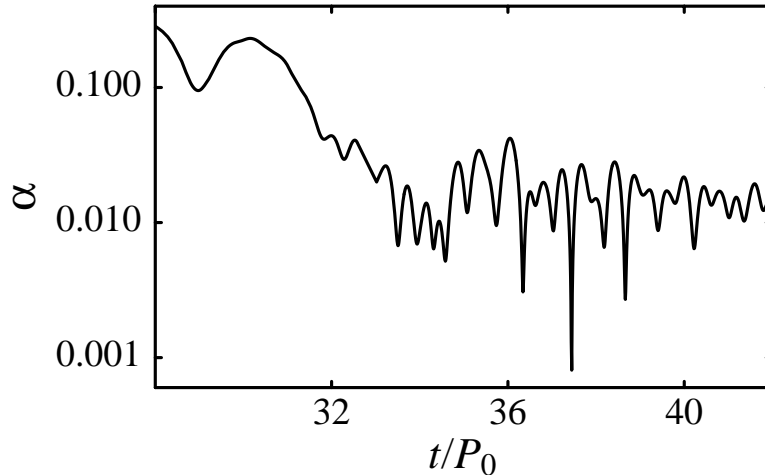


Figure 3.23: Numerical evolution of the r -mode amplitude α in the extended run C4.

instability and spindown.

To investigate this possibility, we extend run C4, evolving our star for 13 more initial rotation periods after α has gone back to its initial value (0.1), or (equivalently) for nine periods after α reaches its minimum (~ 0.01). The evolution of the amplitude for this case is plotted in Fig. 3.23. After $t = 33P_0$, the fluid motion is quite turbulent, but we see no sign that α is starting to grow again. The evolution of the r -mode frequency (Fig. 3.24) is also erratic, probably because here the sinusoidal approximation begins to fail (remember that ω is approximated as $-(1/J_{22})d|J_{22}|/dt$). In fact, after $t = 33P_0$ we have found it necessary to impose an *ad hoc* limit on the value of ω ; otherwise, ω grows to about $-17\Omega_0$, and the radiation-reaction force (proportional to ω^6) becomes huge, pushing the fluid to superluminal velocities.

Nine periods should be more than enough to see a second r -mode growth episode, if it occurs at all. Although at the end of the simulation the average angular velocity of the star is lower than Ω_0 , the growth timescale is determined by the r -mode frequency, which is even higher than at the beginning of the run. What keeps the r -mode then from resuming its growth?

One hypothesis is that because of its strong differential rotation the post-spindown configuration of the star is one which stabilizes the r -mode. The value of $\Delta\Omega$ for the last few periods is plotted in Fig. 3.25. The increase of $\Delta\Omega$ observed between $t = 32P_0$ and $t = 36P_0$ is not caused by radiation reaction, but by a global, energy-conservative reorganization of the fluid. At the end of this process, the spatial structure of differential rotation is very different from what it was at α_{\max} : compare Fig. 3.14 ($t = 25.6P_0$ in run C3) with Fig. 3.26 ($t = 42P_0$ in run C4). The latter plot shows a star that is rotating on cylinders (except for the outer layer), with $\Omega(\varpi, z)$ almost proportional to ϖ .

Karino et al. [22] derived linearized structure equations for the r -modes of differentially rotating Newtonian stars. When differential rotation is so strong that *corotation points* appear (that is, when

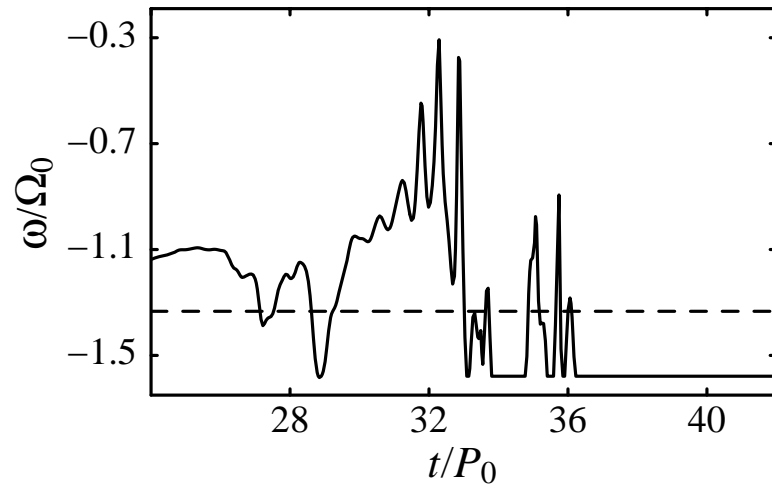


Figure 3.24: Numerical evolution of the r -mode frequency ω in the extended run C4.

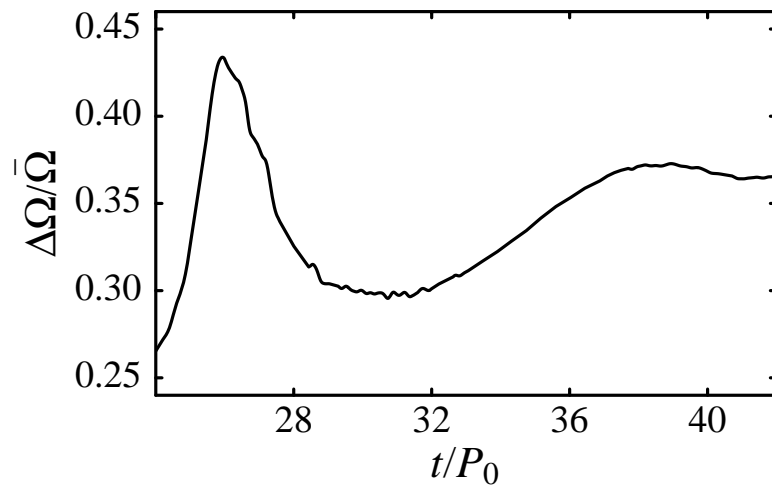


Figure 3.25: Differential rotation $\Delta\Omega$ through the extended run C4.

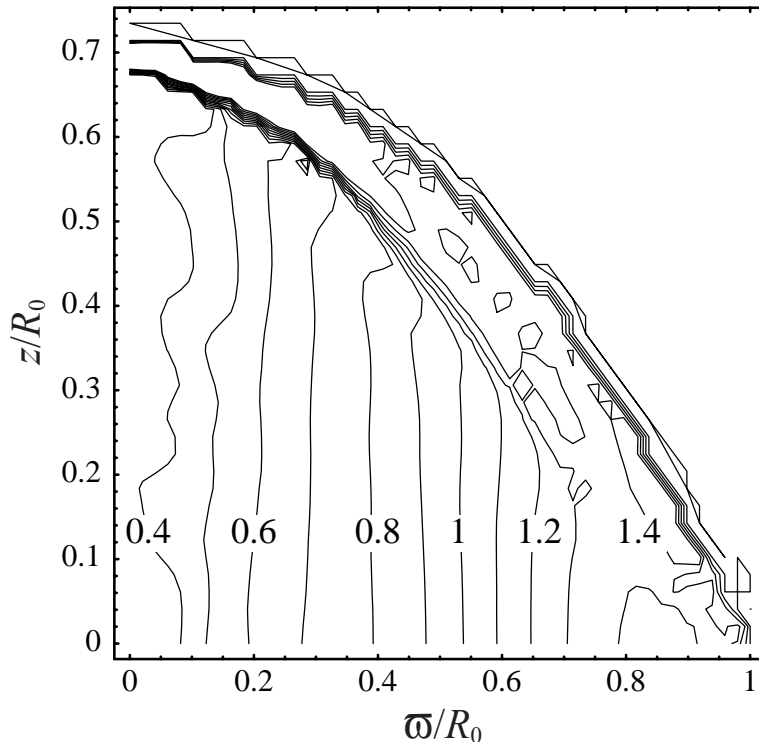


Figure 3.26: Meridional structure of differential rotation at the end of production run C4. This contour plot shows level contours for the value of the azimuthally averaged angular velocity $\Omega(\varpi, z)/\Omega$, at time $t = 42P_0$.

there exists a ϖ such that $\omega + m\Omega(\varpi) = 0$), the mode equations go singular. (The presence of a corotation point at the cylindrical radius ϖ means that the velocity pattern of the mode appears to stand still in the frame rotating with angular velocity $\Omega(\varpi)$.) A comparison of the differential rotation of Fig. 3.26 with the value of ω suggests the presence of corotation points in the final configuration of our star. By itself, however, the singularity of the linearized mode equations does not necessarily mean that r -modes are impossible.

A second, probably more likely possibility is that, in the very noisy environment manifest in Figs. 3.23 and Figs. 3.24, the growing r -mode is unable to get locked in phase with the approximate expression for the driving force that we use here. The actual radiation reaction force [Eq. (3.17)] is a function of the frequency of the r -mode. Since we do not know exactly what this frequency is, we use the expression (3.11) to approximate it. This approximation works extremely well as long as the r -mode makes the dominant contribution to $J_{22}^{(1)}$; yet, in the turbulent post-spindown environment, the r -mode no longer dominates the evolution of J_{22} . Hence, our expression for the gravitational radiation reaction force is no longer correct: it fails to maintain phase coherence with the r -mode and so prevents the growth of the mode.

If the r -mode really does not exist in the chaotic post-spindown environment, then it will be

necessary to wait for viscosity to damp differential rotation before the r -mode can grow again. However, viscosity might be unable to do this before the star cools so much that the r -mode is stabilized (either because the star forms a crust or because viscosity itself has grown too strong). This possibility is worrisome, because the same environmental conditions (strong differential rotation and generalized noise) that characterize the end of run C4 are likely to occur in the young supernova remnants where r -modes are expected to arise in nature. Still, we think it more likely that the absence of a second growth episode in our simulation is the result of our expression for the radiation reaction force, which is too simple for this chaotic situation.

3.9 Conclusions

We have completed a series of numerical 3-D hydrodynamical simulations of the nonlinear evolution of the GR driven instability in the r -modes of rotating neutron stars. We have verified that the current-quadrupole GR reaction force implemented in our code is accurate by reproducing the analytical predictions (for slowly rotating stars) with our full 3-D numerical integration code. In our simulations, the amplitude of the ($m = 2$) r -mode is driven to a value of about three before nonlinear hydrodynamic forces stop its growth by the formation of shocks and breaking surface waves. We showed that the value of this maximum amplitude is insensitive to the strength of the GR driving force by repeating the simulation for different strengths and different initial fluid configurations. We also repeated our simulation using a coarser numerical grid to verify the robustness of our results (the maximum mode amplitude changes only by about 20% when the number of grid points is reduced by a factor of 8), and to show in particular that numerical viscosity is not playing a critical role in our simulations.

In our simulation we have artificially increased the strength of the GR reaction force in order to reduce the problem to one that can be studied with the available computer resources. We have shown, however, that the results of our simulation can be used to infer limits on the real physical problem as well. We used the results of our simulations to derive a lower limit of a few times 10^{-4} on the saturation amplitude of the r -mode in a real neutron star due to possible (but unseen) nonlinear mode-mode couplings. This lower limit applies to couplings with modes that are well described by our simulation: that is, the modes of a barotropic fluid with spatial structures larger than about 2% of the radius of the star.

Recent analysis of the effects of magnetic fields [23], and exotic forms of bulk viscosity [4] suggest that the r -mode instability may not play as important a role in astrophysical situations as was once thought. However, the considerable uncertainty that exists about both the macroscopic and microscopic states of a neutron star makes it impossible at the present time to conclude that the r -mode instability plays no astrophysical role. Thus it seems reasonable to us that some effort be

put into gravitational wave searches for r -mode signals having forms qualitatively similar to those predicted by simulations such as this.

3.10 Appendix. Useful expressions in cylindrical coordinates

In this Appendix, we give explicit expressions in cylindrical coordinates (ϖ, z, φ) for a number of useful quantities used in our simulations. The components of the the initial r -mode velocity field used in our numerical evolutions are

$$v^\varpi = \alpha_0 \sqrt{\frac{5}{16\pi}} \frac{\Omega_0}{R} z \varpi \sin 2\varphi, \quad (3.48)$$

$$v^z = -\alpha_0 \sqrt{\frac{5}{16\pi}} \frac{\Omega_0}{R} \varpi^2 \sin 2\varphi, \quad (3.49)$$

and

$$v^{\hat{\varphi}} = \Omega_0 \varpi + \alpha_0 \sqrt{\frac{5}{16\pi}} \frac{\Omega_0}{R} z \varpi \cos 2\varphi. \quad (3.50)$$

We refer the azimuthal component of the velocity to the orthonormal coordinate $\hat{\varphi}$, so that $v^{\hat{\varphi}}$ and $v_{\hat{\varphi}}$ have the same numerical value and we can use them interchangeably.

The integrals that determine J_{22} and its first time-derivative $J_{22}^{(1)}$ are,

$$J_{22} = \sqrt{\frac{5}{16\pi}} \int \rho e^{-2i\varphi} [z v_{\hat{\varphi}} + i(z v_\varpi - \varpi v_z)] \varpi^2 d\varpi dz d\varphi, \quad (3.51)$$

and

$$J_{22}^{(1)} = \sqrt{\frac{5}{16\pi}} \int \rho e^{-2i\varphi} [T_1 + iT_2] \varpi d\varpi dz d\varphi, \quad (3.52)$$

where

$$T_1 \equiv 2z v_\varpi v_{\hat{\varphi}} - \varpi v_z v_{\hat{\varphi}} - z \frac{\partial \Phi}{\partial \varphi}, \quad (3.53)$$

$$T_2 \equiv z(v_\varpi^2 - v_{\hat{\varphi}}^2) - \varpi v_\varpi v_z + \varpi^2 \frac{\partial \Phi}{\partial z} - z \varpi \frac{\partial \Phi}{\partial \varpi}. \quad (3.54)$$

The components of the radiation-reaction force in cylindrical coordinates are obtained from Eq. (3.17) by expressing the current multipole tensor S_{jk} in terms of the current multipole moments J_{2m} via Eqs. (3.19)–(3.21):

$$F_z^{\text{GR}} = -\kappa \frac{16}{45} \sqrt{\frac{4\pi}{5}} \frac{G}{c^7} \rho \varpi \times \text{Im} \left\{ e^{2i\varphi} \left[3(v_\varpi + i v_{\hat{\varphi}}) J_{22}^{(5)} + \varpi J_{22}^{(6)} \right] \right\}, \quad (3.55)$$

and

$$F_{\hat{\phi}}^{\text{GR}} - iF_{\varpi}^{\text{GR}} = \kappa \frac{16}{45} \sqrt{\frac{4\pi}{5}} \frac{G}{c^7} \rho \varpi e^{2i\varphi} \left[3v_z J_{22}^{(5)} + z J_{22}^{(6)} \right], \quad (3.56)$$

where $\kappa = 1$ in general relativity theory. The fifth and sixth time derivatives of J_{22} are obtained as $J_{22}^{(5)} = \omega^4 J_{22}^{(1)}$, and $J_{22}^{(6)} = -\omega^6 J_{22}$.

3.11 Bibliography

- [1] N. Andersson, *Astrophys. J.* **502**, 708 (1998).
- [2] J. L. Friedman and S. M. Morsink, *Astrophys. J.* **502**, 714 (1998).
- [3] L. Lindblom, B. J. Owen, and S. M. Morsink, *Phys. Rev. Letters* **80**, 4843 (1998).
- [4] L. Lindblom and B. J. Owen, *Phys. Rev. D*, in print.
- [5] B. J. Owen, L. Lindblom, C. Cutler, B. F. Schutz, A. Vecchio, and N. Andersson, *Phys. Rev. D* **58**, 084020 (1998).
- [6] L. Lindblom, J. Tohline, and M. Vallisneri, *Phys. Rev. Lett.* **86**, 1152 (2001).
- [7] N. Stergioulas and J. A. Font, *Phys. Rev. Lett.* **86**, 1148 (2001).
- [8] A. K. Schenk, P. Arras, É. É. Flanagan, S. A. Teukolsky, and I. Wasserman, *Phys. Rev. D* **65**, 024001 (2002).
- [9] J. E. Tohline, “The Structure, Stability, and Dynamics of Self-Gravitating Systems” (work in progress), http://www.phys.lsu.edu/astro/H_Book.current/H_Book.shtml
- [10] K. C. B. New and J. E. Tohline, *Astrophys. J.* **490**, 311 (1997); H. S. Cohl and J. E. Tohline, *ibid.* **527**, 527 (1999); J. E. Cazes and J. E. Tohline, *ibid.* **532**, 1051 (2000); P. Motl, J. E. Tohline, and J. Frank, *Astrophys. J., Suppl. Ser.* **138**, 121 (2002).
- [11] J. M. Stone and M. L. Norman, *Astrophys. J., Suppl. Ser.* **80**, 753 (1992).
- [12] J. Papaloizou and J. E. Pringle, *Mon. Not. Roy. Astro. Soc.* **182**, 423 (1978).
- [13] L. Blanchet, *Phys. Rev. D* **55**, 714 (1997).
- [14] L. Rezzolla, M. Shibata, H. Asada, T. W. Baumgarte, and S. L. Shapiro, *Astrophys. J.* **525**, 935 (1999).
- [15] I. Hachisu, *Astrophys. J., Suppl. Ser.* **61**, 479 (1986); **62**, 461 (1986).
- [16] S. Chandrasekhar, *An Introduction to the Study of Stellar Structure* (Dover, New York, 1967).

- [17] K. S. Thorne, *Rev. Mod. Phys.* **52**, 299 (1980).
- [18] B. J. Owen and L. Lindblom, *Class. Quant. Grav.*, in print, [gr-qc/0111024](#)
- [19] K. S. Thorne, *Astrophys. J.* **158**, 997 (1969).
- [20] J. R. Ipser and L. Lindblom, *Astrophys. J.* **373**, 213 (1991).
- [21] W. Dziembowski and M. Krolikowska, *Acta Astron.* **35**, 5 (1985).
- [22] S. Karino, S. Yoshida, and Y. Eriguchi, *Phys. Rev. D* **64**, 024003 (2001).
- [23] L. Rezzolla, F. L. Lamb, D. Markovic, and S. L. Shapiro, *Phys. Rev. D* **64**, 104013 (2001); *ibid.* **64**, 104014 (2001).

Chapter 4

Detection template families for gravitational waves from the final stages of binary–black-hole inspirals

We investigate the problem of detecting gravitational waves from binaries of non-spinning black holes with masses $m = 5\text{--}20M_{\odot}$, moving on quasi-circular orbits, which are arguably the most promising sources for first-generation ground-based detectors. We analyze and compare all the currently available post-Newtonian approximations for the relativistic two-body dynamics; for these binaries, different approximations predict different waveforms. We then construct examples of detection template families that embed all the approximate models, and that could be used to detect the true gravitational-wave signal (but not to characterize accurately its physical parameters). We estimate that the fitting factor for our detection families is $\gtrsim 0.95$ (corresponding to a loss in event rate $\lesssim 15\%$) and we estimate that the discretization of the template family, for about 10^4 templates, increases the loss to $\lesssim 20\%$.

In collaboration with A. Buonanno and Y. Chen, to be published. Please refer to the refereed paper for an extended version of this chapter.

4.1 Introduction

A network of broadband ground-based laser interferometers, aimed at detecting gravitational waves (GWs) in the frequency band $10\text{--}10^3$ Hz, is currently beginning operation and, hopefully, will start the first science runs within this year (2002). This network consists of the British–German GEO, the American Laser Interferometer Gravitational-wave Observatory (LIGO), the Japanese TAMA and the Italian–French VIRGO (which will begin operating in 2004) [1].

The first detection of gravitational waves with LIGO and VIRGO interferometers is likely to

come from binary black-hole systems where each black hole has a mass¹ of a few M_\odot , and the total mass is roughly in the range $10\text{--}40M_\odot$ [2], and where the orbit is quasi-circular (it is generally assumed that gravitational radiation reaction will circularize the orbit by the time the binary is close to the final coalescence [3]). It is easy to see why. Assuming for simplicity that the GW signal comes from a quadrupole-governed, Newtonian inspiral that ends at a frequency outside the range of good interferometer sensitivity, the signal-to-noise ratio ρ is $\propto \mathcal{M}^{5/6}/d$ (see, e.g., Sec. XXX of Ref. [4]), where $\mathcal{M} = M\eta^{3/5}$ is the *chirp mass* (with $M = m_1 + m_2$ the total mass and $\eta = m_1m_2/M^2$), and d is the distance between the binary and the Earth. Therefore, for a given signal-to-noise detection threshold (see Sec. 4.2) and for equal-mass binaries ($\eta = 1/4$), the larger is the total mass, the larger is the distance d that we are able to probe. [In Sec. 4.5 we shall see how this result is modified when we relax the assumption that the signal ends outside the range of good interferometer sensitivity.]

For example, a black-hole–black-hole binary (BBH) of total mass $M = 20M_\odot$ at 100 Mpc gives (roughly) the same S/N as a neutron-star–neutron-star binary (BNS) of total mass $M = 2.8M_\odot$ at 20 Mpc. The expected measured-event rate scales as the third power of the probed distance, although of course it depends also on the system’s coalescence rate per unit volume in the universe. To give some figures, computed using LIGO-I’s sensitivity specifications, if we assume that BBHs originate from main-sequence binaries [5], the estimated detection rate per year is $\lesssim 4 \times 10^{-3}\text{--}0.6$ at 100 Mpc [6, 7], while if globular clusters are considered as incubators of BBHs [8] the estimated detection rate per year is $\sim 0.04\text{--}0.6$ at 100 Mpc [6, 7]; by contrast, the BNS detection rate per year is in the range $3 \times 10^{-4}\text{--}0.3$ at 20 Mpc [6, 7]. The very large cited ranges for the measured-event rates reflect the uncertainty implicit in using population-synthesis techniques and extrapolations from the few known galactic BNSs to evaluate the coalescence rates of binary systems. [In a recent article [9], Miller and Hamilton suggest that four-body effects in globular clusters might enhance considerably the BBH coalescence rate, brightening the prospects for detection with first-generation interferometers; the BBHs involved might have relatively high BH masses ($\sim 100M_\odot$) and eccentric orbits, and they will not be considered in this chapter.]

The GW signals from standard comparable-mass BBHs with $M = 10\text{--}40M_\odot$ contain only few (50–800) cycles in the LIGO–VIRGO frequency band, so we might expect that the task of modeling the signals for the purpose of data analysis could be accomplished easily. However, the frequencies of best interferometer sensitivity correspond to GWs emitted during the final stages of the inspiral, where the post-Newtonian (PN) expansion [10], which for compact bodies is essentially an expansion in the characteristic orbital velocity v/c , begins to fail. It follows that these sources require a very careful analysis. As the two bodies draw closer, and enter the nonlinear, strong-curvature phase, the motion becomes relativistic, and it becomes harder and harder to extract reliable information

¹These are binaries formed either from massive main-sequence progenitor binary stellar systems (field binaries), or from capture processes in globular clusters or galactic centers (capture binaries).

from the PN series. For example, using the Keplerian formula $v = (\pi M f_{\text{GW}})^{1/3}$ [where f_{GW} is the GW frequency] and taking $f_{\text{GW}} = 153$ Hz [the LIGO-I peak-sensitivity frequency], we get $v(M) = 0.14(M/M_{\odot})^{1/3}$; hence, for BNSs $v(2.8M_{\odot}) = 0.2$, but for BBHs $v(20M_{\odot}) = 0.38$ and $v(40M_{\odot}) = 0.48$.

The final phase of the inspiral (at least when BH spins are negligible) includes the transition from the adiabatic inspiral to the plunge, beyond which the motion of the bodies is driven (almost) only by the conservative part of the dynamics. Beyond the plunge, the two BHs merge, forming a single rotating BH in a very excited state; this BH then eases into its final stationary Kerr state, as the oscillations of its quasi-normal modes die out. In this phase the gravitational signal will be a superposition of exponentially damped sinusoids (ringdown waveform). For nonspinning BBHs, the plunge starts roughly at the innermost stable circular orbit (ISCO) of the BBH. At the ISCO, the GW frequency [evaluated in the Schwarzschild test-mass limit as $f_{\text{GW}}^{\text{ISCO}}(M) \simeq 0.022/M$] is $f_{\text{GW}}^{\text{ISCO}}(20M_{\odot}) \simeq 220$ Hz and $f_{\text{GW}}^{\text{ISCO}}(30M_{\odot}) \simeq 167$ Hz. These frequencies are well inside the LIGO and VIRGO bands.

The data analysis of inspiral, merger (or plunge), and ringdown of compact binaries was first investigated by Flanagan and Hughes [11], and more recently by Damour, Iyer and Sathyaprakash [12]. Flanagan and Hughes [11] model the inspiral using the standard quadrupole prediction (see, e.g., Ref. [4]), and assume an ending frequency of $0.02/M$ (the point where, they argue, PN and numerical-relativity predictions start to deviate by $\sim 5\%$ [13]). They then use a crude argument to estimate upper limits for the total energy radiated in the merger phase ($\sim 0.1M$) and in the ringdown phase ($\sim 0.03M$) of the coalescences of maximally spinning BHs. Damour, Iyer and Sathyaprakash [12] study the nonadiabatic PN-resummed model of Refs. [14, 15, 16], where the plunge can be seen as a natural continuation of the inspiral [15] rather than a separate phase; the total radiated energy is $0.07M$ in the merger and $0.07M$ in the ringdown [17]. (All these values for the energy should be also compared with the value, $0.25\text{--}0.3M$, estimated recently in Ref. [18] for the plunge and ringdown.) When we deal with nonadiabatic models, we too shall choose not to separate the various phases. Moreover, because the ringdown phase does not give a significant contribution to the signal-to-noise ratio for $M \leq 200M_{\odot}$ [11, 12], we shall not include it in our investigations.

BHs are expected to have large spins: various studies [19, 20] have shown that when this is the case, the time evolution of the GW phase and amplitude during the inspiral will be significantly affected by spin-induced modulations and irregularities. These effects can become dramatic, if the two BH spins are large and are not aligned or antialigned with the orbital angular momentum. There is a considerable chance that the analysis of interferometer data, carried out without taking into account spin effects, could miss the signals from spinning BBHs altogether. We shall tackle the crucial issue of spin in a separate paper [21].

The purpose of the present chapter is to discuss the problem of the failure of the PN expansion

during the last stages of inspiral for nonspinning BHs, and the possible ways to deal with this failure. This problem is known in the literature as the intermediate binary black hole (IBBH) problem [22]. Of course, the best way to solve this problem would be to solve the Einstein equations numerically. Unfortunately, despite the considerable progress made by the numerical-relativity community in recent years [13, 23, 24, 25], a reliable estimate of the waveforms emitted by BBHs is still some time ahead (some results for the plunge and ringdown waveforms were obtained very recently [18], but they are not very useful for our purposes, because they do not include the last stages of the inspiral before the plunge, and their initial data are endowed with large amounts of spurious GWs). To overcome this gap and tackle the delicate issue of the late orbital evolution of BBHs, various nonperturbative analytical approaches to that evolution (also known as PN resummation methods) have been proposed [26, 14, 15, 16].

The main features of PN resummation methods can be summarized as follows: (i) they provide an analytic (gauge-invariant) resummation of the orbital energy function \mathcal{E} and gravitational flux function \mathcal{F} (which, as we shall see in Sec. 4.3, are the two crucial ingredients to compute the gravitational waveforms in the adiabatic limit); (ii) they can describe the motion of the bodies (and provide the gravitational waveform) beyond the adiabatic approximation; and (iii) in principle they can be extended to higher PN orders. More importantly, they can provide initial dynamical data for the two BHs at the beginning of the plunge (such as their positions and momenta), which can be used (in principle) in numerical relativity to help build the initial gravitational data (the metric and its time derivative) and then to evolve the full Einstein equations through the merger phase. However, these resummation methods are based on some assumptions that, although plausible, have not been proved: for example, when the orbital energy and the gravitational flux functions are derived in the comparable-mass case, it is assumed that they are smooth deformations of the analogous quantities in the test-mass limit. Moreover, in the absence of both exact solutions and experimental data, we can test the robustness and reliability of the resummation methods only by internal convergence tests.

In this chapter we follow a more conservative point of view. We shall maintain skepticism about the correctness of waveforms based on resummation as well as all other waveforms ever computed for the late BBH inspiral and plunge, and we shall develop families of search templates that incorporate this skepticism. More specifically, we shall be concerned only with detecting BBH GWs, and not with extracting physical parameters, such as masses and spins, from the measured GWs. The rationale for this choice is twofold. First, detection is the more urgent problem at a time when GW interferometers are about to start their science runs; second, a viable detection strategy must be constrained by the computing power available to process a very long stream of data, while the study of detected signals to evaluate physical parameters can concentrate many resources on a small stretch of detector output.

This is the strategy that we propose: we guess (and hope) that the conjunction of the waveforms from all the post-Newtonian models computed to date spans a region in signal space that includes (or almost includes) the true signal. We then choose a *detection* template bank that approximates very well all the PN expanded and resummed models (henceforth denoted as *target models*). If our guess is correct, the *effectualness* [26] of the detection model in approximating the targets (i.e., its capability of reproducing their signal shapes) should be indicative of its effectualness in approximating the true signals. Because our goal is the *detection* of BBH GWs, we shall not require the detection template bank to be *faithful* [26] (i.e., to have a small bias in the estimation of the masses).

This chapter is organized as follows. In Sec. 4.2, we briefly review the theory of matched-filtering GW detections, which underlies the searches for GWs from inspiraling binaries. Then in Secs. 4.3, 4.4, and 4.5 we present the target models and give a detailed analysis of the differences between them, both from the point of view of the orbital dynamics and of the gravitational waveforms. More specifically, in Sec. 4.3 we introduce the two-body adiabatic models, both PN expanded and resummed; in Sec. 4.4 we introduce nonadiabatic approximations to the two-body dynamics; and in Sec. 4.5 we discuss the main differences between the various models. Our proposals for the detection template bank are discussed in Sec. 4.6, where we also build the Owen metric [27] for the template banks and use it to evaluate the number of templates needed for detection. Section 4.7 summarizes our conclusions.

Throughout this chapter we adopt the LIGO noise curve given in Fig. 4.1 and Eq. (4.44), and used also in Ref. [12]. Because the noise curve anticipated for VIRGO [see Fig. 4.1] is quite different (both at low frequencies, and in the location of its peak-sensitivity frequency) our results cannot be applied naively to VIRGO. We plan to repeat our study for VIRGO in the near future.

4.2 The theory of matched-filtering signal detection

The technique of matched-filtering detection for GW signals is based on the systematic comparison of the measured detector output s with a bank of theoretical *signal templates* $\{u_i\}$ that represent a good approximation to the class of physical signals that we seek to measure. This theory was developed by many authors over the years, who have published excellent expositions [28, 27, 11, 29, 53]. However, given that the results relevant to our purposes are somewhat scattered throughout the literature, in the following pages we give a comprehensive pedagogical introduction to the theory.

4.2.1 The statistical theory of signal detection

This section is based on Finn and Chernoff's revision [28, 30] of the classical theory of signal detection [31] (see also [29, 32, 33]). The detector output s consists of noise n and possibly of a true gravitational signal h_i (part of a family $\{h_i\}$ of signals generated by different sources for different

source parameters, detector orientations, and so on). Although we may be able to characterize the properties of the noise in several ways, each separate *realization* of the noise is unpredictable, and it might in principle fool us by hiding a physical signal (hence the risk of a *false dismissal*) or by simulating one (*false alarm*). Thus, the problem of signal detection is essentially probabilistic: we seek to evaluate the conditional probability $P(h|s)$ that s *actually contains* one of the h_i . Using Bayes' theorem, we can write

$$P(h|s) = \frac{P(s|h)P(h)}{P(s)} = \frac{P(h) \sum_i p(h_i)P(s|h_i)}{P(h) \sum_i p(h_i)P(s|h_i) + P(0)P(s|0)}, \quad (4.1)$$

where $P(h)$ and $P(0)$ are the *a priori* probabilities that a signal belonging to the family $\{h_i\}$ is present or absent; $P(s)$ is the *a priori* probability of observing the data stream s , which can be broken up into the conditional probabilities $P(s|h_i)$ and $P(s|0)$ of observing s given the presence or absence of h_i ; finally, $p(h_i)$ specifies the *a priori* probability density of the signals within the family $\{h_i\}$.

While the determination of the *a priori* probabilities $P(0)$, $P(h)$ and $p(h_i)$ can be a delicate task, a precise characterization of the noise is necessary to evaluate $P(s|h_i)/P(s|0)$, that is, the ratio of the probabilities that either one of the h_i or *noise alone* could have produced the detector output s . $P(h|s)$ can be rewritten as

$$P(h|s) = \frac{\Lambda}{\Lambda + P(0)/P(h)}, \quad (4.2)$$

where

$$\Lambda = \sum_i p(h_i)\Lambda(h_i) = \sum_i p(h_i) \frac{P(s|h_i)}{P(s|0)}. \quad (4.3)$$

The mathematical steps involved in the computation of Λ are easily laid down for a generic model of noise, but it is only in the much simplified case of *normal noise* that it is possible to obtain manageable formulas; and while noise will definitely *not* be normal in a real detector, the Gaussian formulas can still provide useful guidelines for the detection problems. Eventually, the statistical analysis of detector search runs will be carried out with numerical Montecarlo techniques that make use of the measured characteristics of the noise.

We shall then compute $P(s|0)$ in the case of normal noise, and then proceed to obtain $P(s|h_i)$ as $P(s - h_i|0)$. The probability of obtaining s as a realization of a random process with correlation function $C_n(\tau) = \overline{n(0)n(\tau)}$ is given by

$$P(s|0) = \frac{1}{\mathcal{P}} \exp \left[-\frac{1}{2} \iint C_n^{-1}(t_1, t_2) s(t_1) s(t_2) dt_1 dt_2 \right], \quad (4.4)$$

where \mathcal{P} is a function of the noise parameters, but not of s , and where C_n^{-1} is defined by

$$\int C_n(t_1, \tau) C_n^{-1}(\tau, t_2) d\tau = \delta(t_1 - t_2). \quad (4.5)$$

The Fourier transform² of $C_n^{-1}(t_1, t_2)$ with respect to t_1 is just

$$\widetilde{C_n^{-1}}(f, t_2) = \frac{2e^{2\pi i f t_2}}{S_n(f)}, \quad (4.6)$$

where $S_n(f)$, the one-sided *spectral power density*, is defined by

$$\overline{\tilde{n}^*(f_1) \tilde{n}(f_2)} = \frac{1}{2} \delta(f_1 - f_2) S_n(f_1) \quad \text{for } f_1 > 0, \quad (4.7)$$

and $S_n(f_1) = 0$ for $f_1 < 0$. The spectral power density is related to C_n by the Wiener–Khinchine theorem (see, e.g., [57]),

$$S_n(f) = 2 \int_{-\infty}^{+\infty} C_n(\tau) e^{2\pi i f \tau} d\tau. \quad (4.8)$$

Using Parseval's theorem we get

$$P(s|0) = \frac{1}{\mathcal{P}} \exp \left[- \iint \frac{\tilde{s}^*(f) s(t_2)}{S_n(|f|)} e^{2\pi i f t_2} df dt_2 \right] = \frac{1}{\mathcal{P}} \exp \left[- \int \frac{\tilde{s}^*(f) \tilde{s}(f)}{S_n(|f|)} df \right]. \quad (4.9)$$

For real signals g, h , we follow Cutler and Flanagan [34] in defining the symmetric inner product

$$\langle g, h \rangle = 2 \int_{-\infty}^{+\infty} \frac{\tilde{g}^*(f) \tilde{h}(f)}{S_n(|f|)} df = 4 \operatorname{Re} \int_0^{+\infty} \frac{\tilde{g}^*(f) \tilde{h}(f)}{S_n(f)} df, \quad (4.10)$$

so finally

$$\frac{P(s|h_i)}{P(s|0)} = \frac{P(s - h_i|0)}{P(s|0)} = \frac{\exp \left[-\frac{1}{2} \langle s - h_i, s - h_i \rangle \right]}{\exp \left[-\frac{1}{2} \langle s, s \rangle \right]} = \exp \left[\langle s, h_i \rangle - \frac{1}{2} \langle h_i, h_i \rangle \right]. \quad (4.11)$$

It turns out that it is inconvenient, in practice, to evaluate the probability $P(h|s)$ directly, because the *a priori* probabilities $P(h)$ and $P(0)$ are in general poorly known. What we can do, instead, is to recognize that the ratio $\Lambda(h_i)$ and any other monotonic function of the inner product $\langle s, h_i \rangle$ are *statistics* that (for different realizations of the noise) will be distributed around low values if the physical signal h_i is absent, and around high value if the signal is present. Thus, we shall establish a *decision rule* as follows [31]: we will claim a detection if the value of a statistic (for a given instance of s and for a specific h_i) is higher than a predefined threshold. We can then study the probability distribution of the statistic to estimate the probability of false alarm (the probability that the statistic is higher than the threshold even if the physical signal is absent) and of false

²In our convention, we define the Fourier transform of a signal $h(t)$ as $F[h(t)] = \tilde{h}(f) = \int h(t) e^{-i2\pi f t} dt$; the inverse transform is then given by $F^{-1}[\tilde{h}(f)] = h(f) = \int h(f) e^{i2\pi f t} df$.

dismissal (the probability that the statistic is lower than the threshold even if the physical signal is present).

The statistic that is generally used is the *signal-to-noise ratio* ρ (for the measured signal s after filtering by h_i), defined as

$$\rho(h_i) = \frac{\langle s, h_i \rangle}{\text{rms} \langle n, h_i \rangle} = \frac{\langle s, h_i \rangle}{\sqrt{\langle h_i, h_i \rangle}}, \quad (4.12)$$

where the equality follows because

$$\text{rms} \langle n, h_i \rangle = \left[\overline{\langle h_i, n \rangle \langle n, h_i \rangle} \right]^{1/2} = \left[\int_{-\infty}^{+\infty} \int_{-\infty}^{+\infty} \frac{\tilde{h}(f_1) \tilde{h}^*(f_2) \overline{\tilde{n}^*(f_1) \tilde{n}(f_2)}}{S_n(f_1) S_n(f_2)} df_1 df_2 \right]^{1/2} = \sqrt{\langle h_i, h_i \rangle}, \quad (4.13)$$

where we have used the definition of $S_n(f)$, Eq. (4.7). In the case when $s = n$, it is easy to prove that ρ is a normal variable with a mean of zero and a variance of one (because $\text{rms} \langle s, h_i \rangle = \text{rms} \langle n, h_i \rangle = \sqrt{\langle h_i, h_i \rangle}$). If instead $s = h_i + n$, then ρ is a normal variable with mean $\sqrt{\langle h_i, h_i \rangle}$ (because $\overline{\langle s, h_i \rangle} = \overline{\langle h_i + n, h_i \rangle} = \langle h_i, h_i \rangle$) and unit variance (because $\overline{(\langle s, h_i \rangle - \langle h_i, h_i \rangle)^2} = \overline{\langle n, h_i \rangle^2} = \langle h_i, h_i \rangle$). The *threshold* ρ_* for detection is set as a tradeoff between the resulting false-alarm probability,

$$\mathcal{F} = \sqrt{\frac{1}{2\pi}} \int_{\rho_*}^{+\infty} e^{-\rho^2/2} d\rho = \frac{1}{2} \text{erfc}(\rho_*/\sqrt{2}) \quad (4.14)$$

(where erfc is the *complementary error function* [35]), and the probability of correct detection

$$\mathcal{D} = \frac{1}{2} \text{erfc}[(\rho_* - \sqrt{\langle h_i, h_i \rangle})/\sqrt{2}] \quad (4.15)$$

(the probability of false dismissal is just $1 - \mathcal{D}$).

4.2.2 Template families and extrinsic parameters

We can now go back to the initial strategy of comparing the measured signal against a bank of \mathcal{N}_i templates $\{u_i\}$ that represent a plurality of sources of different types and physical parameters. For each stretch s of detector output, we shall compute the signal-to-noise ratio $\langle s, u_i \rangle / \sqrt{\langle u_i, u_i \rangle}$ for all the u_i , and then apply our rule to decide whether the physical signal corresponding to any one of the u_i is actually present within s [4]. Of course, the threshold ρ_* needs to be adjusted so that the probability \mathcal{F}_{tot} of false alarm *over all the templates* is still acceptable. Under the assumption that all the inner products $\langle n, u_i \rangle$ of the templates with noise alone are statistically independent variables [given Eq. (4.13), this hypothesis entails $\langle u_i, u_j \rangle \simeq 0$], \mathcal{F}_{tot} is just $1 - (1 - \mathcal{F})^{\mathcal{N}_i} \sim \mathcal{N}_i \mathcal{F}$. If the templates are not statistically independent, this number is an upper limit on the false alarm rate. Before evaluating the dependence of ρ_* on \mathcal{F}_{tot} , we first want to note that, for any template u_i , there are a few obvious ways (parametrized by the so-called *extrinsic parameters*) of changing

the signal shape that do not warrant the inclusion of the modified signals as separate templates³.

The simplest such parameter is just the signal *amplitude*. It is expedient to *normalize* the templates u_i so that $\langle u_i, u_i \rangle = 1$, and $\rho(u_i) = \langle s, u_i \rangle$. Indeed, throughout the rest of this chapter we shall always assume normalized templates. If s contains a scaled version $h_i = \mathcal{A}u_i$ of a template u_i (here \mathcal{A} is known as the signal *strength*), then $\overline{\rho(u_i)} = \mathcal{A}$. However, the statistical distribution of ρ is the same *in the absence of the signal*. Then the problem of detection signals of known shape and unknown amplitude is easily solved by using a single normalized template and the same threshold ρ_* as used for the detection of completely known signals [31]. Quite simply, the stronger an actual signal, the easier it will be to reach the threshold⁴.

The other extrinsic parameters are the signal *phase* and *time of arrival*. Any true signal h can be written in all generality as

$$h(t) = \mathcal{A}_h a_h[t - t_h] \cos[\Phi_h(t - t_h) + \phi_h], \quad (4.16)$$

where $a_h(t) = 0$ for $t < 0$, where $\Phi_h(0) = 0$, and where $a_h(t)$ is normalized so that $\langle h, h \rangle = \mathcal{A}_h^2$. While the template bank $\{u_i\}$ must contain signal shapes that represent all the physically possible functional forms $a(t)$ and $\Phi(t)$, it is possible to modify our search strategy so that the variability in ϕ_h and t_h is automatically taken into account without creating additional templates.

Let us look at phase first, and try to match h with a continuous one-parameter subfamily of templates $u(\phi_t; t) = a_h(t) \cos[\Phi_h(t) + \phi_t]$. The correct phase $\phi_t = \phi_h$ can be obtained by maximizing $\langle h, u(\phi_t) \rangle$ over all the ϕ_t . For any ϕ_t , the template $u(\phi_t)$ can also be written

$$u(\phi_h; t) = \cos(\phi_t)u(0; t) + \sin(\phi_t)u(\pi/2; t); \quad (4.17)$$

then the maximum

$$\max_{\phi_t} \langle h, u(\phi_t) \rangle = \sqrt{|\langle h, u(0) \rangle|^2 + |\langle h, u(\pi/2) \rangle|^2} = \langle h, u(\phi_h) \rangle \quad (4.18)$$

is found for $\phi_t = \arctan \langle h, u(\pi/2) \rangle / \langle h, u(0) \rangle = \phi_h$. It follows that for each time signal shape $\{a(t), \Phi(t)\}$, we need to keep in our template bank only two copies of the corresponding u_i , for $\phi_t = 0$ and $\phi_t = \pi/2$. The signal-to-noise ratio of the detector output s against u_i , for the best possible value of ϕ_t , is automatically found as [31]

$$\rho_\phi = \max_{\phi_t} \langle s, u_i(\phi_t) \rangle = \sqrt{|\langle s, u_i(0) \rangle|^2 + |\langle s, u_i(\pi/2) \rangle|^2}, \quad (4.19)$$

³Owen [27] was the first to speak about *intrinsic* and *extrinsic* parameters, although the distinction had been present implicitly in the theory of signal detection for a long time.

⁴Notice however that the probability of false dismissal $1 - \mathcal{D}$ does depend on the statistical distribution of \mathcal{A} . In the case of normal distribution ($\overline{\mathcal{A}} = 0$, $\overline{\mathcal{A}^2} = \mathcal{A}_{\text{rms}}^2$), then $\mathcal{D} = \text{erfc}[\rho_*/\sqrt{2(1 + \mathcal{A}_{\text{rms}}^2)}]$ [31].

where we orthonormalized the two bases (so that $\langle u_i(0), u_i(\pi/2) \rangle = 0$ and $\langle u_i(0), u_i(0) \rangle = 1$, $\langle u_i(\pi/2), u_i(\pi/2) \rangle = 1$); then the statistical distribution of this phase-maximized statistic (always under the assumption of normal noise) is a slight modification from the simpler case of completely known signal shape: for the case of noise alone⁵, ρ_ϕ follows the *Raleigh distribution* [31]

$$p_0(\rho_\phi) = \rho_\phi e^{-\rho_\phi^2/2}, \quad (4.20)$$

and the false-alarm probability for a threshold ρ_{ϕ^*} is just

$$\mathcal{F} = e^{-\rho_{\phi^*}^2/2}. \quad (4.21)$$

Throughout this chapter, we will find it useful to consider inner products that are maximized (or minimized) with respect to the phases of *both* templates and reference signals. In particular, we shall follow Damour, Iyer and Sathyaprakash in making a distinction between the *best match* or *maxmax match*

$$\max\max\langle h, u_i \rangle = \max_{\phi_h} \max_{\phi_t} \langle h(\phi_h), u_i(\phi_t) \rangle, \quad (4.22)$$

which represents the most favorable combination of phases between the signals h and u_i , and the *minmax match*

$$\min\max\langle h, u_i \rangle = \min_{\phi_h} \max_{\phi_t} \langle h(\phi_h), u_i(\phi_t) \rangle, \quad (4.23)$$

which represents the safest estimate in the realistic situation, where we cannot choose the phase of the physical measured signal, but only of the template used to match the signal. Damour, Iyer and Sathyaprakash [see Appendix B of Ref. [26]] show that both quantities are easily computed as

$$\left(\begin{array}{c} \max\max \\ \min\max \end{array} \right) = \left\{ \frac{A+B}{2} \pm \left[\left(\frac{A+B}{2} \right)^2 + C^2 \right]^{1/2} \right\}^{1/2}, \quad (4.24)$$

where

$$A = \langle h(0), u_i(0) \rangle^2 + \langle h(0), u_i(\pi/2) \rangle^2, \quad B = \langle h(\pi/2), u_i(0) \rangle^2 + \langle h(\pi/2), u_i(\pi/2) \rangle^2, \quad (4.25)$$

$$C = \langle h(0), u_i(0) \rangle \langle h(\pi/2), u_i(0) \rangle + \langle h(0), u_i(\pi/2) \rangle \langle h(\pi/2), u_i(\pi/2) \rangle. \quad (4.26)$$

Notice that in these formulas we have assumed that the two bases $\{h(0), h(\pi/2)\}$ and $\{u_i(0), u_i(\pi/2)\}$ have been orthonormalized.

We now move on to the *time of arrival*. To see why t_h is an extrinsic parameter, we point out

⁵In presence of the signal, ρ_ϕ is distributed according to the more complicated *Rice distribution* [31].

that in the time domain the inner product $\langle h, u \rangle$ expresses a cross-correlation product between the two signals and a noise kernel: in the simplified case of white noise (where $S_n(f) = S_w$ and the kernel is also constant), we have

$$\langle h, u \rangle = \frac{2}{S_w} \int_{-\infty}^{+\infty} \tilde{h}^*(f) \tilde{u}(f) df = \frac{2}{S_w} \int_{-\infty}^{+\infty} h(t) u(t) dt. \quad (4.27)$$

The correlation between $h(t)$ and a time-shifted version $u(t - t_0)$ of $u(t)$ is just

$$\mathcal{C}[h(t), u(t - t_0)] = \int_{-\infty}^{+\infty} h(t) u(t - t_0) dt = \int_{-\infty}^{+\infty} \tilde{h}^*(f) \tilde{u}(f) e^{i2\pi f t_0} df, \quad (4.28)$$

where we used a well-known property of the Fourier transform of time-shifted signals. The cross-correlation will be maximum when t_0 is such that the two signals are synchronized as best as possible. In particular, for the $h(t)$ given by Eq. (4.16), if $u(t) = a_h(t) \cos[\Phi_h(t) + \phi_h]$, then \mathcal{C} will be maximum for $t_0 = t_h$.

Going back to the general case, the correct signal to noise for the normalized, time-shifted template $u(t - t_0)$ against the signal s is just

$$\langle s, u(t_0) \rangle = 4 \operatorname{Re} \int_0^{+\infty} \frac{\tilde{s}^*(f) \tilde{u}(f)}{S_n(f)} e^{i2\pi f t_0} df. \quad (4.29)$$

These integrals can be computed at the same time for all the time of arrivals $\{t_0\}$, using a *fast Fourier transform* technique that requires $\sim N_s \log N_s$ operations (where N_s is the number of the samples that describe the signals) as opposed to $\sim N_s^2$ required to compute all the integrals separately [36].

We now go back to adjusting the threshold ρ_* for a search over a vast template bank, using the estimate (4.21) for the false-alarm probability. Assuming that the statistics ρ_ϕ for each signal shape *and* starting time are independent, we require that

$$e^{-\rho_{\phi_*}^2/2} \simeq \frac{\mathcal{F}_{\text{tot}}}{N_{\text{times}} N_{\text{shapes}}}, \quad (4.30)$$

or

$$\rho_* \simeq \sqrt{2(\log N_{\text{times}} + \log N_{\text{shapes}} - \log \mathcal{F}_{\text{tot}})}. \quad (4.31)$$

It turns out that for 10^{15} starting times (equivalent to templates displaced by 3 ms, over one year [37]), and for a number of shapes up to a few billions, a threshold of order ten will yield false-alarm probabilities $\lesssim 10^{-9}$. If two detectors are used in coincidence, ρ_* is reduced to ~ 6 [37].

4.2.3 Imperfect detection and discrete families of templates

There are two distinct reasons why the detection of a physical signal h by matched filtering with a template bank $\{u_i\}$ might result in signal-to-noise ratios lower than the optimal signal-to-noise ratio,

$$\rho_{\text{opt}} = \sqrt{\langle h, h \rangle}. \quad (4.32)$$

First, the templates, understood as a *continuous* family of functional shapes indexed by one or more *intrinsic parameters* λ^A (such as the masses, spins, etc.), might give an unfaithful representation of h , introducing errors in the representation of the phasing or the amplitude. The loss of signal-to-noise ratio due to unfaithful templates is quantified by the *fitting factor* FF (defined below, and introduced by Apostolatos [38]). The second reason why the signal-to-noise ratio will be degraded with respect to its optimal value is that, even if our templates are perfect representations of the physical signals, in practice we will not adopt a continuous family of templates, but we will be limited to using a discrete bank $\{u_i \equiv u(\lambda_i^A)\}$. This loss of signal-to-noise ratio depends on how finely templates are laid down over parameter space [39]; a notion of metric in template space (the *Owen metric* [27, 40]) can be used to guide the disposition of templates so that the loss (in the perfect-template abstraction) is limited to a fixed, predetermined value (the *minimum match* MM, defined below and introduced by Owen[27]).

The fitting factor FF [38] characterizes the loss in signal-to-noise ratio due to the projection of the signal h onto the continuous template family $\{u(\lambda^A)\}$:

$$\text{FF}(h, u(\lambda^A)) = \frac{\max_{\lambda^A} \langle h, u(\lambda^A) \rangle}{\sqrt{\langle h, h \rangle}}. \quad (4.33)$$

In general, we will be interested in the FF of the continuous template bank in representing a *family* of physical signals $\{h(\theta^A)\}$, dependent upon one or more physical parameters θ^A : so we shall write $\text{FF}(\theta^A) = \text{FF}(h(\theta^A), u(\lambda^A))$. Notice, first, that although it is convenient to index the template family by the same physical parameters θ^A that characterize $h(\theta^A)$, this is by no means necessary. The template parameters λ^A might be a different number than the physical parameters (indeed, this is desirable when the θ^A get to be very many), and they might not carry any direct physical meaning. Second, notice that the value of the FF will depend on the parameter range chosen to maximize the λ^A .

The minimum match MM [27] characterizes the loss of signal-to-noise ratio due to the projection of a continuous family of templates $\{u(\lambda^A)\}$ onto a discretized version $\{u(\lambda_i^A)\}$ of itself:

$$\text{MM} = \min_{\hat{\lambda}^A} \max_{\lambda_i^A} \langle u(\hat{\lambda}^A), u(\lambda_i^A) \rangle = \min_{\hat{\lambda}^A} \max_{\Delta \lambda_i^A} \langle u(\hat{\lambda}^A), u(\hat{\lambda}^A + \Delta \lambda_i^A) \rangle, \quad (4.34)$$

where $\Delta\lambda_i^A \equiv \lambda_i^A - \hat{\lambda}^A$. Within the continuous family, the inner product $\langle u(\hat{\lambda}^A), u(\hat{\lambda}^A + \Delta\lambda^A) \rangle$ (or *match*) can be expanded about its maximum of 1 at $\Delta\lambda^A = 0$:

$$\langle u(\hat{\lambda}^A), u(\hat{\lambda}^A + \Delta\lambda^A) \rangle = M(\hat{\lambda}^A, \hat{\lambda}^A + \Delta\lambda^A) = 1 + \frac{1}{2} \frac{\partial^2 M}{\partial \Delta\lambda^A \partial \Delta\lambda^B} \Big|_{\hat{\lambda}^C} \Delta\lambda^B \Delta\lambda^C + \dots, \quad (4.35)$$

so the *mismatch* $1 - M$ between $u(\hat{\lambda}^A)$ and the nearby template $u(\hat{\lambda}^A + \Delta\lambda^A)$ can be seen as the square of the proper distance in a differential manifold indexed by the coordinates λ^A [27],

$$1 - M(\hat{\lambda}^A, \hat{\lambda}^A + \Delta\lambda^A) = g_{BC} \Delta\lambda^B \Delta\lambda^C, \quad (4.36)$$

where

$$g_{BC} = -\frac{1}{2} \frac{\partial^2 M}{\partial \Delta\lambda^A \partial \Delta\lambda^B} \Big|_{\hat{\lambda}^C}. \quad (4.37)$$

This is the *Owen metric* for the template space $\{u(\lambda^A)\}$.

If, for simplicity, we lay down the n -dimensional discrete template bank $\{u(\lambda_i^A)\}$ along a hypercubical grid of cellsize dl in the metric g_{AB} (a grid in which all the templates on nearby corners have a mismatch of dl with each other), the minimum match occurs when $\hat{\lambda}^A$ lies exactly at the center of one of the hypercubes: then $1 - \text{MM} = n(dl/2)^2$. Conversely, given MM, the volume of the corresponding hypercubes is given by $V_{\text{MM}} = (2\sqrt{(1 - \text{MM})/n})^n$. The number of templates required to achieve a certain MM is obtained by integrating the proper volume of parameter space within the region of physical interest, and then dividing by V_{MM} :

$$\mathcal{N}[g, \text{MM}] = \frac{\int \sqrt{|g|} d\lambda^A}{\left(2\sqrt{[1 - \text{MM}]/n}\right)^n}. \quad (4.38)$$

In practice, if the metric is not constant over parameter space it will not be possible to lay down the templates on an exact hypercubical grid of cellsize dl , so \mathcal{N} will be somewhat higher than predicted by Eq. (4.38). However, we estimate that this number should be correct within a factor of two, which is adequate for our purposes.

In the worst possible case, the combined effect of unfaithful modeling ($\text{FF} < 1$) and discrete template family ($\text{MM} < 1$) will degrade the optimal signal-to-noise ratio by a factor of about $\text{FF} + \text{MM} - 1$: in other words, the two separate losses $1 - \text{FF}$ and $1 - \text{MM}$ must be summed. Notice however that while we were able to choose MM, FF is a function of the point θ^A , so if an estimate of $\text{FF}(\theta^A)$ is available it makes sense to modulate MM over parameter space to achieve a constant total loss $\text{MM}_{\text{T}} = \text{FF} + \text{MM} - 1$; then the number of templates becomes

$$\mathcal{N}_{\text{T}}[g, \text{MM}] = \int \frac{\sqrt{|g|} d\hat{\lambda}^A}{\left(2\sqrt{[\text{FF}(\hat{\lambda}^A) - \text{MM}_{\text{T}}]/n}\right)^n}; \quad (4.39)$$

here $\text{FF}(\hat{\lambda}^A)$ is understood as $\text{FF}(\hat{\theta}^A(\hat{\lambda}^A))$, where $\hat{\theta}^A(\hat{\lambda}^A)$ gives the inverse projection map from each $\hat{\lambda}^A$ to the $\hat{\theta}^A$ for which $u(\hat{\lambda}^A)$ is the best match for $h(\hat{\theta}^A)$. Clearly, $\mathcal{N}_T \rightarrow \infty$ as $\text{MM}_T \rightarrow \text{FF}$, because a continuous family of templates is needed to achieve a total loss equal to the fitting factor.

The estimate $\text{FF} + \text{MM} - 1$ for the total signal-to-noise loss is exact when, in the space of signals, the two segments that join $h(\hat{\theta}^A)$ to its projection $u(\hat{\lambda}^A)$ and $u(\hat{\lambda}^A)$ to the nearest discrete template $u(\hat{\lambda}_i^A)$ can be considered orthogonal:

$$\langle h(\hat{\theta}^A) - u(\hat{\lambda}^A), u(\hat{\lambda}^A) - u(\hat{\lambda}_i^A) \rangle \simeq 0. \quad (4.40)$$

Although this assumption is generally very accurate if FF and MM are small enough, it is possible to be more careful, and define an *external metric* g_{AB}^E [41] that characterizes the mismatch between $h(\hat{\theta}^A)$ and a template $u(\hat{\lambda}^A + \Delta\lambda^A)$ that is displaced with respect to the projection of $h(\hat{\theta}^A)$:

$$\langle h(\hat{\theta}^A), u(\hat{\lambda}^A + \Delta\lambda^A) \rangle = \text{FF}(\hat{\theta}^A) - g_{BC}^E \Delta\lambda^B \Delta\lambda^C + \dots, \quad (4.41)$$

where

$$g_{BC}^E = -\frac{1}{2} \left. \frac{\partial^2 \langle h(\hat{\theta}^A), u(\hat{\lambda}^A + \Delta\lambda^A) \rangle}{\partial \Delta\lambda^A \partial \Delta\lambda^B} \right|_{\hat{\lambda}^C=0}. \quad (4.42)$$

Then the number of templates needed to achieve a given MM_T is given by Eq. (4.39) with the metric g_{BC} replaced by g_{BC}^E .

Since the strength of gravity-wave signals scales as the inverse of the distance⁶, the matched-filtering scheme, with a chosen signal-to-noise threshold ρ_* , will allow the reliable detection of a signal h , characterized by the signal strength $\mathcal{A}_{d_0} = \sqrt{\langle h, \bar{h} \rangle}$ at the distance d_0 , out to a maximum distance

$$\frac{d_{\max}}{d_0} = \frac{\mathcal{A}_{d_0}}{\rho_*}. \quad (4.43)$$

If we assume that the measured GW events happen with a homogeneous event rate throughout the accessible portion of the universe, then the detection rate will scale as d_{\max}^3 . It follows that the use of unfaithful, discrete templates $\{u_i\}$ to detect the signal h will effectively reduce the signal strength, and therefore d_{\max} , by a factor $\text{FF} + \text{MM} - 1$. This loss in the signal-to-noise ratio can also be seen as an increase in the detection threshold ρ_* necessary to achieve the required false-alarm rate, because the imperfect templates introduce an element of uncertainty. In either case, the detection rate will be reduced by a factor $(\text{FF} + \text{MM} - 1)^3$.

⁶The amplitude of the measured gravity-wave signals depends not only on the actual distance to the source, but also on the reciprocal orientation between the detector and the direction of propagation of the waves. A combination of several detectors will be needed, in general, to evaluate the distance to a gravity-wave source starting from the signal-to-noise ratio alone.

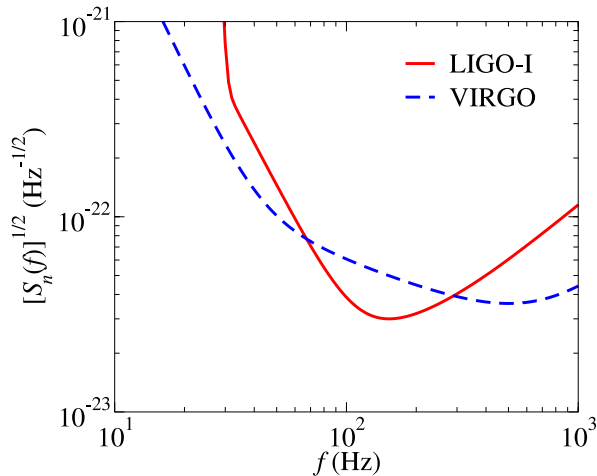


Figure 4.1: Square root of the noise spectral density $\sqrt{S_n(f)}$ versus frequency f , for LIGO-I [Eq. (4.44)], and VIRGO.

4.2.4 Approximations for detector noise spectrum and gravitational-wave signal

For LIGO-I we use the analytic fit to the noise power spectral density given in Ref. [12], and plotted in Fig. 4.44:

$$\frac{S_n(f)}{\text{Hz}^{-1}} = 9.00 \times 10^{-46} \left[\left(4.49 \frac{f}{f_0} \right)^{-56} + 0.16 \left(\frac{f}{f_0} \right)^{-4.52} + 0.52 + 0.32 \left(\frac{f}{f_0} \right)^2 \right], \quad (4.44)$$

where $f_0 = 150$ Hz. The first term in the square brackets represents seismic noise, the second and third, thermal noise, and the fourth, photon shot noise.

Throughout this chapter, we shall compute BBH waveforms in the quadrupole approximation (we shall compute the phase evolution of the GWs with the highest possible accuracy, but we shall omit all harmonics higher than the quadrupole, and we shall omit post-Newtonian corrections to the amplitude; this is a standard approach in the field, see, e.g., [10]). The signal received at the interferometer can then be written as [4, 30]

$$h(t) = \frac{\Theta}{d_L} M \eta (\pi M f_{\text{GW}})^{2/3} \cos \varphi_{\text{GW}}, \quad (4.45)$$

where f and φ_{GW} are the instantaneous GW frequency and phase at the time t , d_L is the *luminosity distance*, M and η are respectively the BBH total mass $m_1 + m_2$ and the dimensionless mass ratio $m_1 m_2 / M^2$, and where we have taken $G = c = 1$. The coefficient Θ depends on the inclination of the BBH orbit with respect to the plane of the sky, and on the polarization and direction of propagation of the GWs with respect to the orientation of the interferometer. Finn and Chernoff [30] examine

the distribution of Θ , and show that $\Theta_{\max} = 4$, while $\text{rms } \Theta = 8/5$. We shall use this last value when we compute optimal signal-to-noise ratios. The waveform given by Eq. (4.45), after dropping the factor $\Theta M \eta / d_L$, is known as *restricted waveform*.

4.3 Adiabatic models

We turn, now, to a discussion of the currently available mathematical models for the inspiral of BBHs. We begin in this section with adiabatic models. BBH adiabatic models treat the orbital inspiral as a quasi-stationary sequence of circular orbits, indexed by the invariantly defined velocity

$$v = (M\dot{\varphi})^{1/3} = (\pi M f_{\text{GW}})^{1/3}. \quad (4.46)$$

The evolution of the inspiral (and in particular of the orbital phase φ) is completely determined by the *energy-balance equation*

$$\frac{d\mathcal{E}(v)}{dt} = -\mathcal{F}(v), \quad (4.47)$$

This equation relates the time derivative of the energy function $\mathcal{E}(v)$ (which is related to the total relativistic energy E_{tot} by $E_{\text{tot}} = (m_1 + m_2)(1 + \mathcal{E})$, and which is conserved in absence of radiation reaction) to the gravitational-flux (or luminosity) function $\mathcal{F}(v)$. Both functions are known for quasi-circular orbits as a PN expansion in v . It is easily shown that Eq. (4.47) is equivalent to the system (see, e.g., Ref. [26])

$$\frac{d\varphi_{\text{GW}}}{dt} = \frac{2v^3}{M}, \quad \frac{dv}{dt} = -\frac{\mathcal{F}(v)}{M d\mathcal{E}(v)/dv}. \quad (4.48)$$

In accord with the discussion around Eq. (4.45), we shall only consider the *restricted waveform* $h(t) = v^2 \cos \varphi_{\text{GW}}(t)$, where the GW phase φ_{GW} is twice the orbital phase φ .

4.3.1 Adiabatic PN expanded models

The equations of motion for two compact bodies at 2.5PN order were first derived in Refs. [42]. The 3PN equations of motion have been obtained by two separate groups of researchers: Damour, Jaranowski and Schäfer [43] used the Arnowitt–Deser–Misner (ADM) canonical approach, while Blanchet, Faye and de Andrade [44] worked with the PN iteration of the Einstein equations in the harmonic gauge. Recently Damour and colleagues [45], working in the ADM formalism and applying dimensional regularization, determined uniquely the *static parameter* that enters the 3PN equations of motion [43, 44] and that was until then unknown. Thus at present the energy function \mathcal{E} is known up to 3PN order.

The gravitational flux emitted by compact binaries was first computed at 1PN order in Ref. [46].

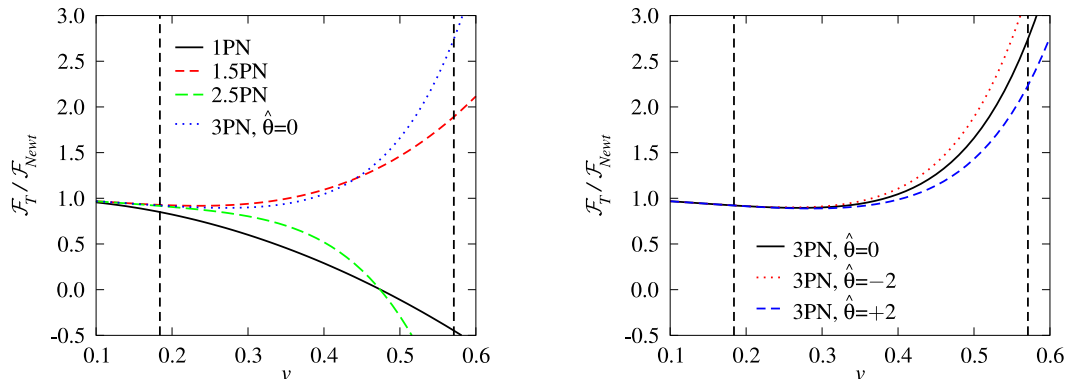


Figure 4.2: In the left panel, we plot the normalized flux function $\mathcal{F}_{T_N}/\mathcal{F}_{\text{Newt}}$ versus v , at different PN orders for equal-mass binaries, $\eta = 0.25$. In the right panel, we plot the effect of the unknown parameter $\hat{\theta}$ on the normalized flux function $\mathcal{F}_{T_N}/\mathcal{F}_{\text{Newt}}$ at 3PN and 3.5PN orders. Note that the 1.5PN and 2PN flux, and the 3PN and 3.5PN flux, are so close that they cannot be distinguished in these plots. The two long-dashed vertical lines correspond to $v \simeq 0.18$ and $v \simeq 0.53$; they show the velocity range that corresponds to the LIGO frequency band $40 \leq f_{\text{GW}} \leq 240$ Hz for BBHs with total mass in the range $10\text{--}40M_\odot$.

It was subsequently determined at 2PN order with a formalism based on multipolar and post-Minkowskian approximations, and, independently, with the direct integration of the relaxed Einstein equations [47]. Nonlinear effects of tails at 2.5PN and 3.5PN orders were computed in Refs. [48]. More recently, Blanchet and colleagues derived the gravitational-flux function for quasi-circular orbits up to 3.5PN order [49, 50]. However, at 3PN order [49, 50] the gravitational-flux function depends on an arbitrary parameter (in our notation, $\hat{\theta}$) that could not be fixed in the regularization scheme used by these authors.

PN energy and flux

Denoting by \mathcal{E}_{T_N} and \mathcal{F}_{T_N} the N^{th} -order Taylor approximant (T-approximant) to the energy and the flux functions, we have

$$\mathcal{E}_{T_{2N}}(v) \equiv \mathcal{E}_{\text{Newt}}(v) \sum_{k=0}^N \mathcal{E}_k(\eta) v^{2k}, \quad (4.49)$$

$$\mathcal{F}_{T_N}(v) \equiv \mathcal{F}_{\text{Newt}}(v) \sum_{k=0}^N \mathcal{F}_k(\eta) v^k, \quad (4.50)$$

where “Newt” stands for Newtonian order, and the subscripts $2N$ and N stand for post 2N -Newtonian and post N -Newtonian order. The quantities in these equations are

$$\mathcal{E}_{\text{Newt}}(v) = -\frac{1}{2}\eta v^2, \quad \mathcal{F}_{\text{Newt}}(v) = \frac{32}{5}\eta^2 v^{10}, \quad (4.51)$$

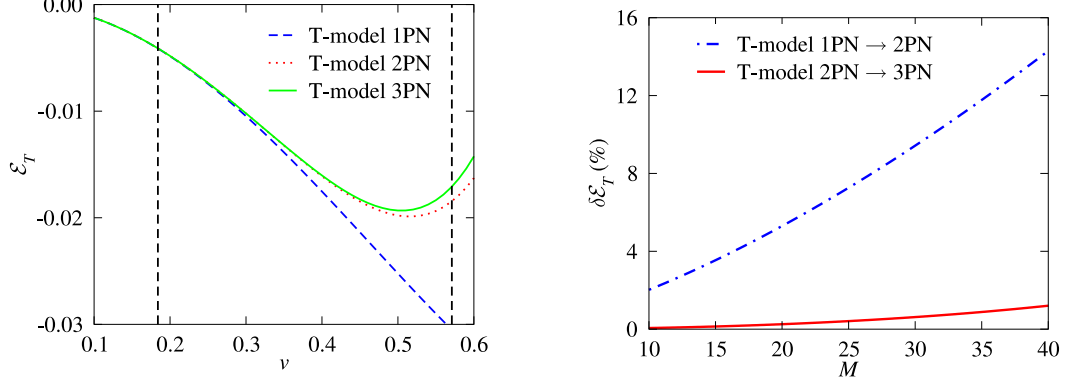


Figure 4.3: In the left panel, we plot the energy function \mathcal{E}_{T_N} versus v , at different PN orders for $\eta = 0.25$. In the right panel, we plot the percentage difference $\delta\mathcal{E}_{T_N} = 100 |(\mathcal{E}_{T_{N+1}} - \mathcal{E}_{T_N})/\mathcal{E}_{T_N}|$ versus the total mass M , for $N = 1, 2$, at the LIGO-I peak-sensitivity GW frequency. The two long-dashed vertical lines in the left figure correspond to $v \simeq 0.18$ and $v \simeq 0.53$; they show the velocity range that corresponds to the LIGO frequency band $40 \leq f_{\text{GW}} \leq 240$ Hz for BBHs with total mass in the range $10\text{--}40M_\odot$.

$$\mathcal{E}_0(\eta) = 1, \quad \mathcal{E}_1(\eta) = -\frac{3}{4} - \frac{\eta}{12}, \quad \mathcal{E}_2(\eta) = -\frac{27}{8} + \frac{19}{8}\eta - \frac{\eta^2}{24}, \quad (4.52)$$

$$\mathcal{E}_3(\eta) = -\frac{675}{64} + \left(\frac{34445}{576} - \frac{205}{96}\pi^2\right)\eta - \frac{155}{96}\eta^2 - \frac{35}{5184}\eta^3, \quad (4.53)$$

$$\mathcal{F}_0(\eta) = 1, \quad \mathcal{F}_1(\eta) = 0, \quad \mathcal{F}_2(\eta) = -\frac{1247}{336} - \frac{35}{12}\eta, \quad \mathcal{F}_3(\eta) = 4\pi, \quad (4.54)$$

$$\mathcal{F}_4(\eta) = -\frac{44711}{9072} + \frac{9271}{504}\eta + \frac{65}{18}\eta^2, \quad \mathcal{F}_5(\eta) = -\left(\frac{8191}{672} + \frac{535}{24}\eta\right)\pi, \quad (4.55)$$

$$\begin{aligned} \mathcal{F}_6(\eta) = & \frac{6643739519}{69854400} + \frac{16}{3}\pi^2 - \frac{1712}{105}\gamma_E - \frac{856}{105}\log(16v^2) + \\ & \left(-\frac{2913613}{272160} + \frac{41}{48}\pi^2 - \frac{88}{3}\hat{\theta}\right)\eta - \frac{94403}{3024}\eta^2 - \frac{775}{324}\eta^3, \end{aligned} \quad (4.56)$$

$$\mathcal{F}_7(\eta) = \left(-\frac{16285}{504} + \frac{176419}{1512}\eta + \frac{19897}{378}\eta^2\right)\pi. \quad (4.57)$$

Here $\hat{\theta}$ is the arbitrary 3PN flux parameter [49, 50]. From Table I of Ref. [50] we read that the extra number of GW cycles accumulated by the PN terms of a given order decreases (roughly) by an order of magnitude when we increase the PN order by one. Hence, we find it reasonable to expect that at 3PN order the parameter $\hat{\theta}$ should be of order unity, and we choose as typical values $\hat{\theta} = 0, \pm 2$.

M	$f_{\text{GW}}^{\text{1PN}}(\text{Hz})$	$f_{\text{GW}}^{\text{2PN}}(\text{Hz})$	$f_{\text{GW}}^{\text{3PN}}(\text{Hz})$
$(5 + 5) M_{\odot}$	3376	886	832
$(10 + 10) M_{\odot}$	1688	442	416
$(15 + 15) M_{\odot}$	1125	295	277
$(20 + 20) M_{\odot}$	844	221	208

Table 4.1: Location of the maximum binding Energy for Circular Orbits (MECO), computed using the T-approximants \mathcal{E}_{T_N} to the energy function.

N	$(5 + 20) M_{\odot}$	$(10 + 10) M_{\odot}$	$(15 + 15) M_{\odot}$
	$\langle T_N, T_{N+1} \rangle$	$\langle T_N, T_{N+1} \rangle$	$\langle T_N, T_{N+1} \rangle$
0	0.437	0.557	0.620
1	0.554	0.587	0.632
2 ($\hat{\theta} = +2$)	0.479	0.548	0.551
2 ($\hat{\theta} = -2$)	0.457	0.504	0.510

Table 4.2: Test for the Cauchy convergence of the T-approximants. The values quoted are maxmax matches obtained by maximizing with respect to the extrinsic parameters, but not to the intrinsic parameters (i.e., the matches are computed for T waveforms with the same masses, but different PN orders).

In Fig. 4.2 we plot the flux as a function of v at various PN orders for the equal mass case $\eta = 0.25$. To convert v to a GW frequency we can use

$$f_{\text{GW}} \simeq 3.2 \times 10^3 \left(\frac{20M_{\odot}}{M} \right) v^3. \quad (4.58)$$

The two long-dashed vertical lines in Fig. 4.2 correspond to $v \simeq 0.18$ and $v \simeq 0.53$; they show the velocity range that corresponds to the LIGO frequency band $40 \leq f_{\text{GW}} \leq 240$ Hz for BBHs with total mass in the range $10\text{--}40M_{\odot}$. At the LIGO-I peak-sensitivity frequency, which is 153 Hz according to our noise curve, and for a $(10+10)M_{\odot}$ BBH, we have $v \simeq 0.362$; and the percentage difference between subsequent PN orders is $1.5\text{PN} \rightarrow 2\text{PN} : -0.2\%$; $2\text{PN} \rightarrow 2.5\text{PN} : -34\%$; $2.5\text{PN} \rightarrow 3\text{PN}(\hat{\theta} = 0) : +43\%$; $3\text{PN} \rightarrow 3.5\text{PN}(\hat{\theta} = 0) : +0.04\%$. The percentage difference between the 3PN fluxes with $\hat{\theta} = \pm 2$ is $\sim 7\%$. It is interesting to notice that while there is a big difference between the 1PN and 1.5PN orders, and between the 2PN and 2.5PN orders, the 3PN and 3.5PN fluxes are rather close. Of course this observation is insufficient to conclude that the PN sequence is converging at 3.5PN order.

In the left panel of Fig. 4.3, we plot the T-approximants for the energy function versus v , at different PN orders, while in the right panel we plot the percentage difference of the energy function between successive PN orders. We note that the 1PN and 2PN energies are distant, but the 2PN and 3PN energies are quite close.

Definition of the models

The evolution equations (4.48) for the adiabatic inspiral lose validity (the inspiral ceases to be adiabatic) a little before v reaches $v_{\text{MECO}}^{T_N}$, where MECO stands for Maximum binding Energy Circular Orbit [51]. This $v_{\text{MECO}}^{T_N}$ is computed as the value of v at which $d\mathcal{E}_{T_N}(v)/dv = 0$. In building our adiabatic models we evolve Eqs. (4.48) right up to v_{MECO} and stop there. We call this the *ending frequency* for these waveforms, and in Table 4.1 we show this frequency for some BH masses. However, for certain binaries, the 1PN and 2.5PN flux functions can go to zero before $v = v_{\text{MECO}}^{T_N}$ [see the left panel of Fig. 4.2]. In those cases we choose for the ending frequency the value of $f = v^3/(\pi M)$ where $\mathcal{F}(v) = 0$.

We shall refer to the models discussed in this section as $T(n\text{PN}, m\text{PN})$, where $n\text{PN}$ ($m\text{PN}$) denotes the maximum PN order of the terms included for the energy (the flux). We shall consider $(n\text{PN}, m\text{PN}) = (1, 1.5), (2, 2.5)$ and $(3, 3.5, \hat{\theta})$ [at 3PN order we need to indicate also a choice of the arbitrary flux parameter $\hat{\theta}$].

Waveforms and matches

In Table 4.2, for three typical choices of BBH masses, we perform a convergence test using Cauchy's criterion [26], namely, the sequence T_N converges if and only if for each k , $\langle T_N, T_{N+k} \rangle \rightarrow 1$ as $N \rightarrow \infty$. One requirement of the criterion would be $\langle T_N, T_{N+1} \rangle \rightarrow 1$ as $N \rightarrow \infty$. The values quoted assume optimization on the extrinsic parameters but not on the intrinsic parameters. These results suggest that the PN expansion is far from converging.

In Fig. 4.4 we plot the frequency-domain amplitude versus frequency for the T waveforms, at different PN orders, for a $(15 + 15)M_{\odot}$ BBH. The Newtonian amplitude, $\mathcal{A}_{\text{Newt}}(f) = f^{-7/6}$, is also shown for comparison. In the 1PN and 2.5PN cases the flux function goes to zero before $v = v_{\text{MECO}}^{T_N}$. This means that the radiation-reaction effects become negligible during the last phase of evolution, so the binary is able to spend many cycles at those final frequencies, skewing the amplitude with respect to the Newtonian result. At 2PN and 3PN (or 3.5PN) orders, the evolution is stopped at $v = v_{\text{MECO}}^{T_N}$, and, although $f_{\text{MECO}}^{\text{GW}} \simeq 270 - 300$ Hz (see Table 4.1) the amplitude starts to deviate from $f^{-7/6}$ around 100 Hz. This is a consequence of the abrupt termination of the signal in the time domain.

The effect of the arbitrary parameter $\hat{\theta}$ on the T waveforms can be seen in Table 4.14 in the intersection between the rows and columns labeled $T(3, 7/2, +2)$ and $T(3, 7/2, -2)$. For three choices of BBH masses, this table shows the maxmax matches between the *search* models at the top of the columns and the *target* models at the left end of the rows, *maximized over the mass parameters of the search models in the columns*. These matches are rather high, suggesting that the effect of changing $\hat{\theta}$ is just a remapping of the BBH mass parameters. Therefore, in the following we shall

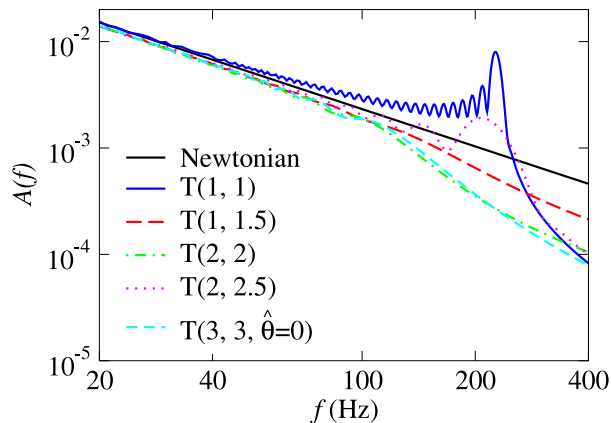


Figure 4.4: Frequency-domain amplitude versus frequency for the T-approximated (restricted) waveforms, at different PN orders, for a $(15 + 15)M_{\odot}$ BBH. The 3PN and 3.5PN curves cannot be distinguished in this graph.

consider only the case of $\hat{\theta} = 0$.

A quantitative measure of the difference between the (2PN, 2.5PN) and (3PN, 3.5PN) T waveforms can be seen in Table 4.14 in the intersection between the rows and columns labeled T(...). For three choices of BBH masses, this table shows the maxmax matches between the search models in the columns and the target models in the rows, maximized over the search-model parameters M and η ; in the search, η is restricted to its physical range $0 < \eta \leq 1/4$, where 0 corresponds to the test-mass limit, while $1/4$ is obtained in the equal-mass case. These matches can be interpreted as the fitting factors [see Eq. (4.33)] for the projection of the target models onto the search models. The values are quite low: if the (3PN, 3.5PN) T-approximants turned out to give the true physical signals and if we used the (2PN, 2.5PN) T-approximants to detect them, we would lose ~ 32 – 49% of the events.

4.3.2 Adiabatic PN resummed methods: Padé approximants

The PN approximation outlined above can be used quite generally to compute the shape of the GWs emitted by BNSs or BBHs, but it *cannot be trusted* in the case of binaries with comparable masses in the range $M \simeq 10$ – $40M_{\odot}$, because for these sources LIGO and VIRGO will detect the GWs emitted when the motion is strongly relativistic, and the convergence of the PN series is very slow. To cope with this problem, Damour, Iyer and Sathyaprakash [26] proposed a new class of models based on the systematic application of Padé resummation to the PN expansions of $\mathcal{E}(v)$ and $\mathcal{F}(v)$. This is a standard mathematical technique used to accelerate the convergence of poorly converging or even divergent power series.

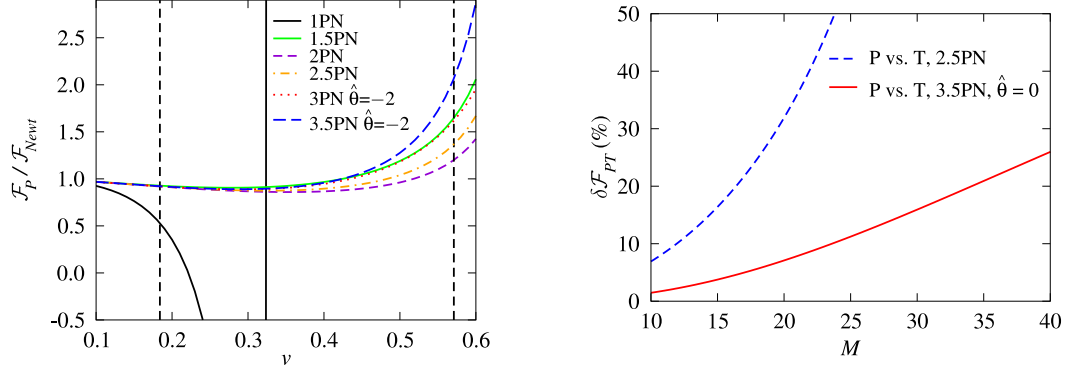


Figure 4.5: In the left panel, we plot the normalized flux function $\mathcal{F}_{P_N}/\mathcal{F}_{\text{Newt}}$ versus v , at different PN orders. The two long-dashed vertical lines give $v \simeq 0.18$ and $v \simeq 0.53$; they show the velocity range that corresponds to the LIGO frequency band $40 \leq f_{\text{GW}} \leq 240$ Hz for BBHs with total mass in the range $10\text{--}40M_\odot$. In the right panel, we plot the percentage difference between the T- and P-approximants, $\delta\mathcal{F}_{PT}(v_{\text{peak}}) = 100|\mathcal{F}_{P_N}(v_{\text{peak}}) - \mathcal{F}_{T_N}(v_{\text{peak}})|/\mathcal{F}_{T_N}(v_{\text{peak}})$, versus the total mass M , for $N = 2, 3$, at the LIGO-I peak-sensitivity GW frequency $f_{\text{peak}} = 153$ Hz [note: $v_{\text{peak}} = (\pi M f_{\text{peak}})^{1/3}$].

If we know the function $g(v)$ only through its Taylor approximant $G_N(v) = g_0 + g_1 v + \dots + g_N v^N \equiv T_N[g(v)]$, the central idea of Padé resummation [52] is the replacement of the power series $G_N(v)$ by the sequence of rational functions

$$P_K^M[g(v)] = \frac{A_M(v)}{B_K(v)} \equiv \frac{\sum_{j=0}^M a_j v^j}{\sum_{j=0}^K b_j v^j}, \quad (4.59)$$

with $M + K = N$ and $T_{M+K}[P_K^M(v)] = G_N(v)$ (without loss of generality, we can set $b_0 = 1$). We expect that for $M, K \rightarrow +\infty$, $P_K^M[g(v)]$ will converge to $g(v)$ more rapidly than $T_N[g(v)]$ converges to $g(v)$ for $N \rightarrow +\infty$.

PN energy and flux

Damour, Iyer and Sathyaprakash [26] proposed the following Padé-approximated (P-approximated) $\mathcal{E}_{P_N}(v)$ and $\mathcal{F}_{P_N}(v)$ (for $N = 2, 3$) [26, 16]:

$$\mathcal{E}_{P_N} = \sqrt{1 + 2\eta \sqrt{1 + e_{P_N}(v)} - 1} - 1, \quad (4.60)$$

$$\mathcal{F}_{P_N} = \frac{32}{5} \eta^2 v^{10} \frac{1}{1 - v/v_{\text{pole}}^{P_N}} f_{P_N}(v, \eta), \quad (4.61)$$

where

$$e_{P_2}(v) = -v^2 \frac{1 + \frac{1}{3}\eta - (4 - \frac{9}{4}\eta + \frac{1}{9}\eta^2) v^2}{1 + \frac{1}{3}\eta - (3 - \frac{35}{12}\eta) v^2}, \quad (4.62)$$

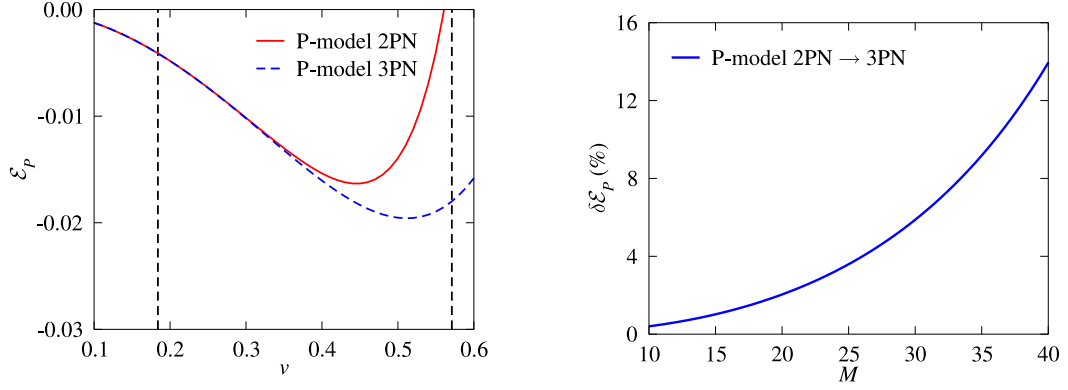


Figure 4.6: In the left panel, we plot the energy function \mathcal{E}_{P_N} versus v , at different PN orders. In the right panel, we plot the percentage difference between 2PN and 3PN P-approximants, $\delta\mathcal{E}_P(v_{\text{peak}}) = 100 |[\mathcal{E}_{P_3}(v_{\text{peak}}) - \mathcal{E}_{P_2}(v_{\text{peak}})]/\mathcal{E}_{P_2}(v_{\text{peak}})|$ versus the total mass M , evaluated at the LIGO-I peak-sensitivity GW frequency $f_{\text{peak}} = 153$ Hz [note: $v_{\text{peak}} = (\pi M f_{\text{peak}})^{1/3}$].

M	$f_{\text{GW}}^{2\text{PN}}$ (Hz)	$f_{\text{GW}}^{3\text{PN}}$ (Hz)
$(5 + 5) M_{\odot}$	572	866
$(10 + 10) M_{\odot}$	286	433
$(15 + 15) M_{\odot}$	191	289
$(20 + 20) M_{\odot}$	143	216

Table 4.3: Maximum binding energy for circular orbits (MECO) using P-approximants for the energy function \mathcal{E}_{P_N} .

$$e_{P_3}(v) = -v^2 \frac{1 - (1 + \frac{1}{3}\eta + w_3(\eta)) v^2 - (3 - \frac{35}{12}\eta - (1 + \frac{1}{3}\eta) w_3(\eta)) v^4}{1 - w_3(\eta) v^2}, \quad (4.63)$$

$$w_3 = \frac{40}{36 - 35\eta} \left[\frac{27}{10} + \frac{1}{16} \left(\frac{41}{4}\pi^2 - \frac{4309}{15} \right) \eta + \frac{103}{120}\eta^2 - \frac{1}{270}\eta^3 \right], \quad (4.64)$$

$$f_{P_2}(v) = \left(1 + \frac{c_1 v}{1 + \frac{c_2 v}{1 + \dots}} \right)^{-1} \quad (\text{up to } c_5), \quad (4.65)$$

$$f_{P_3}(v) = \left(1 - \frac{1712}{105} v^6 \log \frac{v}{v_{\text{MECO}}^{P_2}} \right) \left(1 + \frac{c_1 v}{1 + \frac{c_2 v}{1 + \dots}} \right)^{-1} \quad (\text{up to } c_7). \quad (4.66)$$

Here the dimensionless coefficients c_i depend only on η . The c_k 's are explicit functions of the coefficients f_k ($k = 1, \dots, 5$),

N	$(5 + 20) M_\odot$	$(10 + 10) M_\odot$	$(15 + 15) M_\odot$
	$\langle P_N, P_{N+1} \rangle$	$\langle P_N, P_{N+1} \rangle$	$\langle P_N, P_{N+1} \rangle$
$2 (\widehat{\theta} = +2)$	0.909	0.919	0.898
$2 (\widehat{\theta} = -2)$	0.942	0.968	0.943

Table 4.4: Test for the Cauchy convergence of the P-approximants. The values quoted are maxmax matches obtained by maximizing with respect to the extrinsic parameters, but not to the intrinsic parameters (i.e., the matches are computed for T waveforms with the same masses, but different PN orders).

$$c_1 = -f_1, \quad c_2 = f_1 - \frac{f_2}{f_1}, \quad c_3 = \frac{f_1 f_3 - f_2^2}{f_1 (f_1^2 - f_2)}, \quad (4.67)$$

$$c_4 = -\frac{f_1 (f_2^3 + f_3^2 + f_1^2 f_4 - f_2 (2 f_1 f_3 + f_4))}{(f_1^2 - f_2) (f_1 f_3 - f_2^2)}, \quad (4.68)$$

$$c_5 = -\frac{(f_1^2 - f_2) (-f_3^3 + 2 f_2 f_3 f_4 - f_1 f_4^2 - f_2^2 f_5 + f_1 f_3 f_5)}{(f_1 f_3 - f_2^2) (f_2^3 + f_3^2 + f_1^2 f_4 - f_2 (2 f_1 f_3 + f_4))}, \quad (4.69)$$

where

$$f_k = \mathcal{F}_k - \frac{\mathcal{F}_{k-1}}{v_{\text{pole}}^{P_2}}. \quad (4.70)$$

Here \mathcal{F}_k is given by Eqs. (4.54)–(4.57) [for $k = 6$ and $k = 7$, the term $-856/105 \log(16v^2)$ should be replaced by $-856/105 \log(16(v_{\text{MECO}}^{P_2})^2)$]. The coefficients c_7 and c_8 are straightforward to compute, but we do not show them because they involve rather long expressions. The quantity $v_{\text{MECO}}^{P_2}$ is the MECO of the energy function e_{P_2} (defined by $de_{P_2}(v)/dv = 0$).

The quantity $v_{\text{pole}}^{P_2}$, given by

$$v_{\text{pole}}^{P_2} = \frac{1}{\sqrt{3}} \sqrt{\frac{1 + \frac{1}{3}\eta}{1 - \frac{35}{36}\eta}}, \quad (4.71)$$

is the pole of e_{P_2} , which plays an important role in the scheme proposed by Damour, Iyer and Sathyaprakash [26]. It is used to augment the Padé resummation of the PN expanded energy and flux with information taken from the test-mass case, where the flux (known analytically up to 5.5PN order) has a pole at the light ring. Under the hypothesis of *structural stability* [26], the flux should have a pole at the light ring also in the comparable-mass case. In that case, the light ring corresponds to the pole of the energy, so the analytic structure of the flux is modified to include $v_{\text{pole}}^{P_2}(\eta)$. At 3PN order, where the energy has no pole, we choose (somewhat arbitrarily) to keep using the value $v_{\text{pole}}^{P_2}(\eta)$ (the resulting 3PN approximation to the test-mass flux is still very good).

In the left panel of Fig. 4.5, we plot the P-approximants for the flux function $\mathcal{F}_{P_N}(v)$, at different PN orders. Note that at 1PN order the P-approximant has a pole. At the LIGO-I peak-sensitivity frequency, 153 Hz, for a $(10+10)M_\odot$ BBH the value of v is $\simeq 0.362$, and the percentage difference in $\mathcal{F}_{P_N}(0.362)$, between successive PN orders is 1.5PN \rightarrow 2PN : -8% ; 2PN \rightarrow 2.5PN : $+2.2\%$;

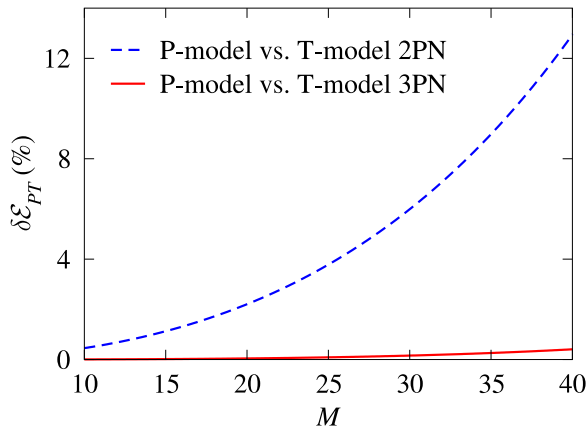


Figure 4.7: Percentage difference $\delta\mathcal{E}_{PT}(v_{\text{peak}}) = 100 |[\mathcal{E}_{P_N}(v_{\text{peak}}) - \mathcal{E}_{T_N}(v_{\text{peak}})]/\mathcal{E}_{P_N}(v_{\text{peak}})|$ versus the total mass M , for $N = 2, 3$, at the LIGO-I peak-sensitivity GW frequency $f_{\text{peak}} = 153$ Hz [note: $v_{\text{peak}} = (\pi M f_{\text{peak}})^{1/3}$].

2.5PN \rightarrow 3PN ($\hat{\theta} = -2$) : +3.6%; 3PN \rightarrow 3.5PN ($\hat{\theta} = -2$) : +0.58%. The percentage differences decrease as we increase the PN order. It is known that in the test-mass limit the P-approximants converge quite well to the known exact flux function (see Fig. 3 of Ref. [26]); however, in the equal-mass case we cannot be sure that the same is happening, because the exact flux function is unknown. (If we assume that the equal-mass flux function is a smooth deformation of the test-mass flux function, with η the deformation parameter, then we could expect that it does.)

In the right panel of Fig. 4.5, we plot the percentage differences between the T- and P-approximant flux functions at different PN orders, versus the total mass M at the LIGO-I peak-sensitivity GW frequency (153 Hz). In the left panel of Fig. 4.6, we plot the P-approximants of the energy function versus v , at 2PN and 3PN orders, while in the right panel we plot the percentage difference between the 2PN and 3PN P-approximants, versus v .

Definition of the models

When computing the waveforms for P-approximant adiabatic models, the integration of Eqs. (4.48) is stopped at $v = v_{\text{MECO}}^{P_N}$, which is the solution of the equation $d\mathcal{E}_{P_N}(v)/dv = 0$. This will be the *ending frequency* for these waveforms, and in Table 4.3 we show this frequency for typical BBH masses. Henceforth, we shall refer to the P-approximant models as P(n PN, m PN), with $(n\text{PN}, m\text{PN}) = (2, 2.5), (3, 3.5, \hat{\theta})$. [Recall that n PN and m PN are the maximum post-Newtonian order of the terms included in the energy and flux functions $\mathcal{E}(v)$ and $\mathcal{F}(v)$.]

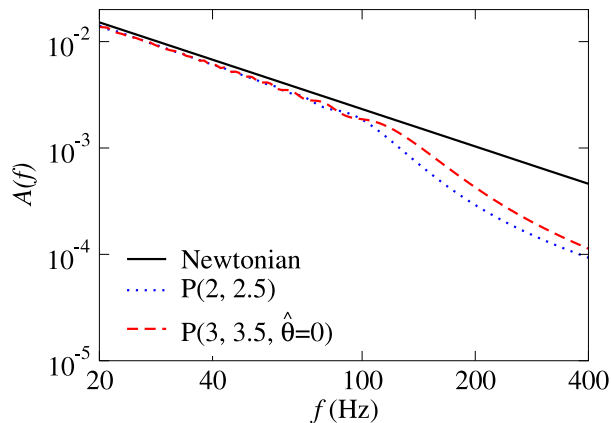


Figure 4.8: Frequency-domain amplitude versus frequency for the P-approximated (restricted) waveform, at different PN orders, for a $(15 + 15)M_{\odot}$ BBH.

Waveforms and matches

In Table 4.4, for three typical choices of BBH masses, we perform a convergence test using Cauchy’s criterion [26]. The values are quite high, especially if compared to the same test for the T-approximants, shown in Table 4.2. However, as we already remarked, we do not have a way of testing whether they are converging to the true limit.

In Fig. 4.8 we plot the frequency-domain amplitude of the P-approximated (restricted) waveform, at different PN orders, for a $(15 + 15)M_{\odot}$ BBH. The Newtonian amplitude, $\mathcal{A}_{\text{Newt}}(f) = f^{-7/6}$, is also shown for comparison. At 2.5PN and 3.5PN orders, the evolution is stopped at $v = v_{\text{MECO}}^{\text{PN}}$, and, although $f_{\text{MECO}}^{\text{GW}} \simeq 190 - 290$ Hz (see Table 4.3), the amplitude starts to deviate from $f^{-7/6}$ around 100 Hz, well inside the LIGO frequency band. Again, this is a consequence of the abrupt termination of the signal in the time domain.

A quantitative measure of the difference between the 2PN and 3PN P waveforms can be seen in Table 4.14 in the intersection between the rows and columns labeled P(...). For three choices of BBH masses, this table shows the maxmax matches between the search models in the columns and the target models in the rows, maximized over the search-model parameters M and η , with the restriction $0 < \eta \leq 1/4$. These matches are quite high. The same table shows also the maximized matches (i.e., fitting factors) *between T and P models*: matches are low between 2PN T-approximants and 2PN P-approximants (and viceversa), between 2PN T-approximants and 3PN P-approximants (and viceversa), but they are *high* between 3PN T-approximants and 3PN P-approximants.

Why this happens can be understood from Figs. 4.5, 4.7 by noticing that at 3PN order the percentage difference between the binding energies is rather small ($\leq 0.5\%$), and that the percentage difference in the flux (although still $\sim 10\%$) is much smaller than for the 2PN approximations.

4.4 Nonadiabatic models

By contrast with the models discussed in Sec. 4.3, in nonadiabatic models we solve equations of motions that involve (almost) all the degrees of freedom of the BBH systems. Once again, all waveforms are computed in the restricted approximation of Eq. (4.45), taking the GW phase φ_{GW} as twice the orbital phase φ .

4.4.1 Nonadiabatic PN expanded methods: Hamiltonian formalism

Working in the ADM gauge, Damour, Jaranowski and G. Schäfer have derived a PN expanded Hamiltonian for the general-relativistic two-body dynamics [43, 45, 16]:

$$\widehat{H}(\mathbf{q}, \mathbf{p}) = \widehat{H}_{\text{Newt}}(\mathbf{q}, \mathbf{p}) + \widehat{H}_{1\text{PN}}(\mathbf{q}, \mathbf{p}) + \widehat{H}_{2\text{PN}}(\mathbf{q}, \mathbf{p}) + \widehat{H}_{3\text{PN}}(\mathbf{q}, \mathbf{p}), \quad (4.72)$$

where

$$\widehat{H}_{\text{Newt}}(\mathbf{q}, \mathbf{p}) = \frac{\mathbf{p}^2}{2} - \frac{1}{q}, \quad \widehat{H}_{1\text{PN}}(\mathbf{q}, \mathbf{p}) = \frac{1}{8}(3\eta - 1)(\mathbf{p}^2)^2 - \frac{1}{2} \left[(3 + \eta)\mathbf{p}^2 + \eta(\mathbf{n} \cdot \mathbf{p})^2 \right] \frac{1}{q} + \frac{1}{2q^2}, \quad (4.73)$$

$$\begin{aligned} \widehat{H}_{2\text{PN}}(\mathbf{q}, \mathbf{p}) &= \frac{1}{16} (1 - 5\eta + 5\eta^2) (\mathbf{p}^2)^3 + \frac{1}{8} \left[(5 - 20\eta - 3\eta^2) (\mathbf{p}^2)^2 - 2\eta^2 (\mathbf{n} \cdot \mathbf{p})^2 \mathbf{p}^2 - 3\eta^2 (\mathbf{n} \cdot \mathbf{p})^4 \right] \frac{1}{q} \\ &\quad + \frac{1}{2} \left[(5 + 8\eta)\mathbf{p}^2 + 3\eta(\mathbf{n} \cdot \mathbf{p})^2 \right] \frac{1}{q^2} - \frac{1}{4}(1 + 3\eta) \frac{1}{q^3}, \end{aligned} \quad (4.74)$$

$$\begin{aligned} \widehat{H}_{3\text{PN}}(\mathbf{q}, \mathbf{p}) &= \frac{1}{128} (-5 + 35\eta - 70\eta^2 + 35\eta^3) (\mathbf{p}^2)^4 \\ &\quad + \frac{1}{16} \left[(-7 + 42\eta - 53\eta^2 - 5\eta^3) (\mathbf{p}^2)^3 + (2 - 3\eta)\eta^2 (\mathbf{n} \cdot \mathbf{p})^2 (\mathbf{p}^2)^2 + 3(1 - \eta)\eta^2 (\mathbf{n} \cdot \mathbf{p})^4 \mathbf{p}^2 - 5\eta^3 (\mathbf{n} \cdot \mathbf{p})^6 \right] \frac{1}{q} \\ &\quad + \left[\frac{1}{16} (-27 + 136\eta + 109\eta^2) (\mathbf{p}^2)^2 + \frac{1}{16} (17 + 30\eta)\eta (\mathbf{n} \cdot \mathbf{p})^2 \mathbf{p}^2 + \frac{1}{12} (5 + 43\eta)\eta (\mathbf{n} \cdot \mathbf{p})^4 \right] \frac{1}{q^2} \\ &\quad + \left\{ \left[-\frac{25}{8} + \left(\frac{1}{64}\pi^2 - \frac{335}{48} \right) \eta - \frac{23}{8}\eta^2 \right] \mathbf{p}^2 + \left(-\frac{85}{16} - \frac{3}{64}\pi^2 - \frac{7}{4}\eta \right) \eta (\mathbf{n} \cdot \mathbf{p})^2 \right\} \frac{1}{q^3} \\ &\quad + \left[\frac{1}{8} + \left(\frac{109}{12} - \frac{21}{32}\pi^2 \right) \eta \right] \frac{1}{q^4}. \end{aligned} \quad (4.75)$$

Here, we consider the reduced nonrelativistic Hamiltonian $\widehat{H} \equiv H^{\text{NR}}/\mu$, in the center-of-mass frame, as a function of the reduced canonical variables $\mathbf{p} \equiv \mathbf{p}_1/\mu = -\mathbf{p}_2/\mu$, and $\mathbf{q} \equiv (\mathbf{x}_1 - \mathbf{x}_2)/M$, where \mathbf{x}_1 and \mathbf{x}_2 are the positions of the BH centers of mass in quasi-Cartesian ADM coordinates (see Refs. [43, 45, 16]); the scalars q and p are the (coordinate) lengths of the two vectors; and the vector \mathbf{n} is just \mathbf{q}/q .

Equations of motion

The polar coordinates (r, φ) can be obtained from the \mathbf{q} with the usual Cartesian-to-polar transformation. We restrict the motion to a plane, and we introduce radiation-reaction (RR) effects as in

N	$(5 + 20) M_\odot$	$(10 + 10) M_\odot$	$(15 + 15) M_\odot$
	$\langle \text{HP}_N, \text{HP}_{N+1} \rangle$	$\langle \text{HP}_N, \text{HP}_{N+1} \rangle$	$\langle \text{HP}_N, \text{HP}_{N+1} \rangle$
0	0.117	0.194	0.211
1	0.094	0.162	0.155
2 ($\hat{\theta} = +2$)	0.267	0.367	0.326
2 ($\hat{\theta} = -2$)	0.265	0.355	0.315

Table 4.5: Test for the Cauchy convergence of the HP-approximants. The values quoted are maxmax matches obtained by maximizing with respect to the extrinsic parameters, but not to the intrinsic parameters (i.e., the matches are computed for T waveforms with the same masses, but different PN orders).

Ref. [15]. The equations of motion then read

$$\frac{dr}{d\hat{t}} = \frac{\partial \hat{H}}{\partial p_r}(r, p_r, p_\varphi), \quad \frac{d\varphi}{d\hat{t}} = \hat{\omega} \equiv \frac{\partial \hat{H}}{\partial p_\varphi}(r, p_r, p_\varphi), \quad (4.76)$$

$$\frac{dp_r}{d\hat{t}} + \frac{\partial \hat{H}}{\partial r}(r, p_r, p_\varphi) = \hat{F}^r(r, p_r, p_\varphi), \quad \frac{dp_\varphi}{d\hat{t}} = \hat{F}^\varphi[\hat{\omega}(r, p_r, p_\varphi)], \quad (4.77)$$

where $\hat{t} = t/M$, $\hat{\omega} = \omega M$; and where $\hat{F}^\varphi \equiv F^\varphi/\mu$ and $\hat{F}^r \equiv F^r/\mu$ are the reduced angular and radial components of the RR force. Assuming $F^r \ll F^\varphi$ [15], averaging over an orbit, and using the balance equation (4.47), we can express the angular component of the radiation-reaction force in terms of the GW flux at infinity [15]. More explicitly, if we use the P-approximated flux, we have

$$\hat{F}^\varphi \equiv F_{P_N}[v_\omega] = -\frac{1}{\eta v_\omega^3} \mathcal{F}_{P_N}[v_\omega] = -\frac{32}{5} \eta v_\omega^7 \frac{f_{P_N}(v_\omega; \eta)}{1 - v_\omega/v_{\text{pole}}(\eta)}. \quad (4.78)$$

while if we use the T-approximated flux we have

$$\hat{F}^\varphi \equiv F_{T_N}[v_\omega] = -\frac{1}{\eta v_\omega^3} \mathcal{F}_{T_N}[v_\omega], \quad (4.79)$$

where $v_\omega \equiv \hat{\omega}^{1/3} \equiv (d\varphi/d\hat{t})^{1/3}$. This v_ω is used in Eq. (4.45) to compute the restricted waveform.

Definition of the models

In order to build a quasi-circular orbit with initial GW frequency f_0 , our initial conditions (r_{init} , $p_{r \text{ init}}$, $p_{\phi \text{ init}}$) are set by imposing $\dot{\varphi}_{\text{init}} = \pi f_0$, $\dot{p}_{r \text{ init}} = 0$ and $dr_{\text{init}}/d\hat{t} = -\mathcal{F}/(\eta d\hat{H}/dr)_{\text{circ}}$, as in Ref. [53]. The initial orbital phase φ_{init} remains a free parameter.

For these models, the criterion used to stop the integration of Eqs. (4.76), (4.77) is rather arbitrary. We decided to push the integration of the dynamical equations up to the time when we begin to observe unphysical effects due to the failure of the PN expansion, or when the assumptions that underlie Eqs. (4.77) [such as $\hat{F}^r \ll \hat{F}^\varphi$], cease to be valid. Therefore, we stop the integration

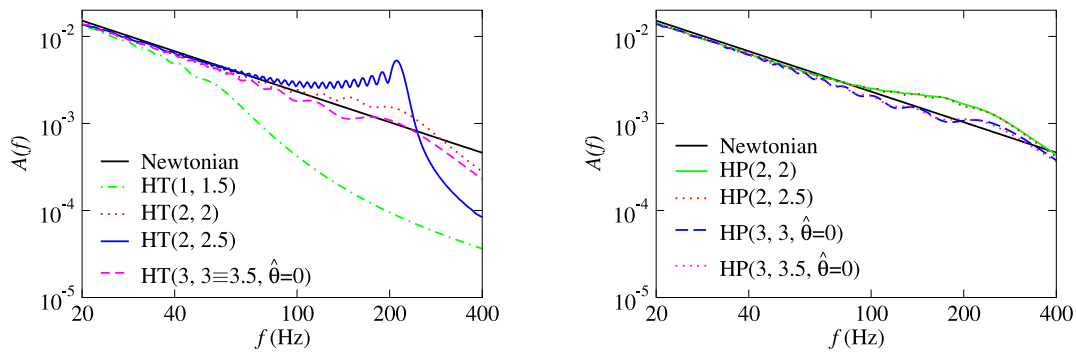


Figure 4.9: Frequency-domain amplitude versus frequency for the HT and HP (restricted) waveforms, at different PN orders, for a $(15 + 15)M_{\odot}$ BBH.

when $\mathcal{F}_{T_N} = 0$, and we define the *ending frequency* for these waveforms as the instantaneous GW frequency at that time. [To be consistent with the assumption of quasi-circular motion, we require also that the radial velocity be always much smaller than the orbital velocity, and we stop the integration when $|\dot{r}| > 0.3(r\dot{\varphi})$ if that occurs before $\mathcal{F}_{T_N} = 0$.]

We shall refer to these models as HT(n PN, m PN) (when the T-approximant is used for the flux) or HP(n PN, m PN) (when the P-approximant is used for the flux), where n PN (m PN) denotes the maximum PN order of the terms included in the Hamiltonian (the flux). We shall consider $(n$ PN, m PN) = (1,1.5), (2,2.5), (3,3.5, $\hat{\theta}$).

Waveforms and matches

In Table 4.5, for three typical choices of BBH masses, we perform a convergence test using Cauchy's criterion [26]. The values are very low. In Fig. 4.9 we plot the frequency-domain amplitude of the (restricted) waveform, at different PN orders, for a $(15 + 15)M_{\odot}$ BBH. The Newtonian amplitude, $\mathcal{A}_{\text{Newt}}(f) = f^{-7/6}$, is also shown for comparison. For HT(2,5/2), the flux function goes to zero first, so the binary is able to spend many cycles at high frequencies, skewing the amplitude with respect to the Newtonian result, and producing the oscillations seen in Fig. 4.9. For HP and for HT at all other PN orders, by contrast with the adiabatic models [see Figs. 4.4, 4.8], the dynamical evolution ends with a plunge (of sorts) where the motion is still quasi-circular. As a result, the amplitude does not plunge at high frequency, and in fact it does not deviate much (especially at 3PN order) from the Newtonian result.

Quantitative measures of the difference between HT and HP models at 3PN order, and of the difference between the Hamiltonian models and the adiabatic models, can be seen in Table 4.14. For three choices of BBH masses, this table shows the maxmax matches between the search models in the columns and the target models in the rows, maximized over the search-model parameters M

and η , with the restriction $0 < \eta \leq 1/4$. Notice that the matches with the adiabatic models are low at 2PN order, but very high at 3PN order. Once again we see that at 3PN order the various models are not very different, at least when the match is maximized over the target-model parameters (i.e., for the purpose of signal detection as opposed to parameter-estimation).

4.4.2 Nonadiabatic PN expanded methods: Lagrangian formalism

Equations of motion

Working in the harmonic gauge, Damour and Deruelle [42], and then Kidder, Will and Wiseman [54] have used a Lagrangian formalism to derive equations of motions for the general-relativistic two-body dynamics. The equations read

$$\ddot{\mathbf{x}} = \mathbf{a}_N + \mathbf{a}_{\text{PN}} + \mathbf{a}_{2\text{PN}} + \mathbf{a}_{2.5\text{RR}} + \mathbf{a}_{3.5\text{RR}}, \quad (4.80)$$

where

$$\mathbf{a}_N = -\frac{M}{r^2} \hat{\mathbf{n}}, \quad (4.81)$$

$$\mathbf{a}_{\text{PN}} = -\frac{M}{r^2} \left\{ \hat{\mathbf{n}} \left[(1 + 3\eta)v^2 - 2(2 + \eta)\frac{M}{r} - \frac{3}{2}\eta\dot{r}^2 \right] - 2(2 - \eta)\dot{r}\mathbf{v} \right\}, \quad (4.82)$$

$$\begin{aligned} \mathbf{a}_{2\text{PN}} = & -\frac{M}{r^2} \left\{ \hat{\mathbf{n}} \left[\frac{3}{4}(12 + 29\eta) \left(\frac{M}{r}\right)^2 + \eta(3 - 4\eta)v^4 + \frac{15}{8}\eta(1 - 3\eta)\dot{r}^4 \right. \right. \\ & \left. \left. - \frac{3}{2}\eta(3 - 4\eta)v^2\dot{r}^2 - \frac{1}{2}\eta(13 - 4\eta)\frac{M}{r}v^2 - (2 + 25\eta + 2\eta^2)\frac{M}{r}\dot{r}^2 \right] \right. \\ & \left. - \frac{1}{2}\dot{r}\mathbf{v} \left[\eta(15 + 4\eta)v^2 - (4 + 41\eta + 8\eta^2)\frac{M}{r} - 3\eta(3 + 2\eta)\dot{r}^2 \right] \right\}, \quad (4.83) \end{aligned}$$

$$\mathbf{a}_{2.5\text{RR}} = \frac{8}{5}\eta\frac{M^2}{r^3} \left\{ \dot{r}\hat{\mathbf{n}} \left[18v^2 + \frac{2}{3}\frac{M}{r} - 25\dot{r}^2 \right] - \mathbf{v} \left[6v^2 - 2\frac{M}{r} - 15\dot{r}^2 \right] \right\}, \quad (4.84)$$

$$\begin{aligned} \mathbf{a}_{3.5\text{RR}} = & \frac{8}{5}\eta\frac{M^2}{r^3} \left\{ \dot{r}\hat{\mathbf{n}} \left[\left(\frac{87}{14} - 48\eta\right)v^4 - \left(\frac{5379}{28} + \frac{136}{3}\eta\right)v^2\frac{M}{r} + \frac{25}{2}(1 + 5\eta)v^2\dot{r}^2 + \left(\frac{1353}{4} + 133\eta\right)\dot{r}^2\frac{M}{r} \right. \right. \\ & \left. \left. - \frac{35}{2}(1 - \eta)\dot{r}^4 + \left(\frac{160}{7} + \frac{55}{3}\eta\right)\left(\frac{M}{r}\right)^2 \right] - \mathbf{v} \left[-\frac{27}{14}v^4 - \left(\frac{4861}{84} + \frac{58}{3}\eta\right)v^2\frac{M}{r} + \frac{3}{2}(13 - 37\eta)v^2\dot{r}^2 \right. \right. \\ & \left. \left. + \left(\frac{2591}{12} + 97\eta\right)\dot{r}^2\frac{M}{r} - \frac{25}{2}(1 - 7\eta)\dot{r}^4 + \frac{1}{3}\left(\frac{776}{7} + 55\eta\right)\left(\frac{M}{r}\right)^2 \right] \right\}. \quad (4.85) \end{aligned}$$

Here the vector $\mathbf{x} \equiv \mathbf{x}_1 - \mathbf{x}_2$ is the difference, in pseudo-Cartesian harmonic coordinates [42, 54], between the positions of the BH centers of mass; the vector $\mathbf{v} = d\mathbf{x}/dt$ is the corresponding velocity; the scalar r is the (coordinate) length of \mathbf{x} ; the vector $\hat{\mathbf{n}} \equiv \mathbf{x}/r$; and, overdots denote time derivatives with respect to the post-Newtonian time.

Note that we have included neither the 3PN order corrections $a_{3\text{PN}}$ derived in Ref. [44], nor the 4.5PN order term $a_{4.5\text{PN}}$ for the radiation-reaction force computed in Ref. [55]. Unlike the Hamiltonian models, where the radiation-reaction effects were averaged over circular orbits but

L(2,1)	T(2,5/2)			P(2,5/2)			EP(2,5/2)			HT(3,7/2,0)		
	mm	m_1	m_2	mm	m_1	m_2	mm	m_1	m_2	mm	m_1	m_2
$(15+15)M_\odot$	0.836	23.30	24.00	0.915	13.13	18.12	0.996	5.94	34.49	0.828	17.80	25.93
$(15+5)M_\odot$	0.714	3.85	30.31	0.955	3.25	21.85	0.988	2.97	23.38	0.972	3.82	18.42
$(5+5)M_\odot$	0.878	1.84	14.50	0.969	2.60	9.17	0.958	2.73	8.69	0.966	2.64	8.97

Table 4.6: Fitting factors [see Eq. (4.33)] for the projection of the L(2, 1) (target) waveforms onto the T(2, 5/2), P(2, 5/2), EP(2, 5/2), HT(2, 7/2) (search) models. The values quoted are obtained by maximizing the maxmax (mm) match over the search-model parameters m_1 and m_2 .

resummed up to 3PN order, here radiation-reaction effects are instantaneous and can be used to compute generic orbits, but are given accurate only to 1PN order beyond the leading quadrupole term.

We compute waveforms in the quadrupole approximation of Eq. (4.45), defining the orbital phase φ as the angle between \mathbf{x} and a fixed direction in the orbital plane, and the invariantly defined velocity v as $(M\dot{\varphi})^{1/3}$.

Definition of the models

For these models, just as for the HT and HP models, the choice of the endpoint of evolution is rather arbitrary. We decided to stop the integration of the dynamical equations when we begin to observe unphysical effects due to the failure of the PN expansion. Therefore, we stop the integration when the PN-expanded center-of-mass binding energy (given by Eqs. (2.7a)–(2.7e) of Ref. [19]) begins to increase, instead of continuing to decrease. The instantaneous GW frequency at that time will then be the *ending frequency* for these waveforms. We shall refer to these models as L(n PN, m PN), where n PN (n PN) denotes the maximum PN order of the terms included in the Hamiltonian (the radiation-reaction force). We shall consider $(n$ PN, m PN) = (1, 1), (2, 1). Table 4.6 shows the maxmax match between the L-approximants and some of the other two-body models.

4.4.3 Nonadiabatic PN resummed methods: the effective-one-body approach

The basic idea of the effective-one-body approach [14] is to map the *real* two-body conservative dynamics, generated by the Hamiltonian (4.72) and specified up to 3PN order, onto an *effective* one-body problem where a test particle of mass $\mu = m_1 m_2 / M$ (with m_1 and m_2 the BH masses, and $M = m_1 + m_2$) moves in an effective background metric $g_{\mu\eta}^{\text{eff}}$ given by

$$ds_{\text{eff}}^2 \equiv g_{\mu\eta}^{\text{eff}} dx^\mu dx^\eta = -A(r) c^2 dt^2 + \frac{D(r)}{A(r)} dr^2 + r^2 (d\theta^2 + \sin^2 \theta d\varphi^2), \quad (4.86)$$

where

$$A(r) = 1 + a_1 \frac{GM}{c^2 r} + a_2 \left(\frac{GM}{c^2 r} \right)^2 + a_3 \left(\frac{GM}{c^2 r} \right)^3 + a_4 \left(\frac{GM}{c^2 r} \right)^4 + \dots, \quad (4.87)$$

$$D(r) = 1 + d_1 \frac{GM}{c^2 r} + d_2 \left(\frac{GM}{c^2 r} \right)^2 + d_3 \left(\frac{GM}{c^2 r} \right)^3 + \dots. \quad (4.88)$$

The motion of the particle is described by the action

$$S_{\text{eff}} = -\mu c \int ds_{\text{eff}}. \quad (4.89)$$

For the sake of convenience, in this section we shall use same symbols of Sec. 4.4.1 to denote different physical quantities (such as coordinates in different gauges). The mapping between the real and the effective dynamics is worked out within the Hamilton-Jacobi formalism, by imposing that the action variables of the real and effective description coincide (i.e., $J_{\text{real}} = J_{\text{eff}}$, $\mathcal{I}_{\text{real}} = \mathcal{I}_{\text{eff}}$, where J denotes the total angular momentum, and \mathcal{I} the radial action variable [14]), but allowing the energy to change,

$$\frac{\mathcal{E}_{\text{eff}}^{\text{NR}}}{\mu c^2} = \frac{\mathcal{E}_{\text{real}}^{\text{NR}}}{\mu c^2} \left[1 + \alpha_1 \frac{\mathcal{E}_{\text{real}}^{\text{NR}}}{\mu c^2} + \alpha_2 \left(\frac{\mathcal{E}_{\text{real}}^{\text{NR}}}{\mu c^2} \right)^2 + \alpha_3 \left(\frac{\mathcal{E}_{\text{real}}^{\text{NR}}}{\mu c^2} \right)^3 + \dots \right], \quad (4.90)$$

here the nonrelativistic effective energy $\mathcal{E}_{\text{eff}}^{\text{NR}} = \mathcal{E}_{\text{eff}} - \mu c^2$, where the relativistic effective energy \mathcal{E}_{eff} is defined uniquely by the action (4.89). The nonrelativistic real energy $\mathcal{E}_{\text{real}}^{\text{NR}} \equiv H(\mathbf{q}, \mathbf{p})$ where $H(\mathbf{q}, \mathbf{p})$ is given by Eq. (4.72) with $H(\mathbf{q}, \mathbf{p}) = \mu \hat{H}(\mathbf{q}, \mathbf{p})$. From now on, we shall relax our notation and set $G = c = 1$.

Equations of motion

Damour, Jaranowski and Schäfer [16] found that, at 3PN order, this matching procedure contains more equations to satisfy than free parameters to solve for ($a_1, a_2, a_3, d_1, d_2, d_3$ and $\alpha_1, \alpha_2, \alpha_3$). These authors suggested the following two solutions to this conundrum. At the price of modifying the coefficients of the effective metric at 1PN and 2PN levels and the energy map, at 3PN order it is still possible to map uniquely the real two-body dynamics onto the dynamics of a test mass moving on a geodesic (for details, see App. A of Ref. [16]). However, this procedure appears very complicated; more importantly, it seems awkward to have to compute the 3PN Hamiltonian as a foundation for deriving the matching at the 1PN and 2PN levels. The second solution is to abandon the hypothesis that the effective test mass moves along a geodesic, and to augment the Hamilton-Jacobi equation with (arbitrary) higher-derivative terms that provide enough coefficients to complete the matching. With this procedure, the Hamilton-Jacobi equation reads

$$0 = \mu^2 + g_{\text{eff}}^{\mu\eta}(x) p_\mu p_\eta + A^{\mu\eta\rho\sigma}(x) p_\mu p_\eta p_\rho p_\sigma + \dots. \quad (4.91)$$

M	$f_{\text{GW}}^{\text{1PN}}(\text{Hz})$	$f_{\text{GW}}^{\text{2PN}}(\text{Hz})$	$f_{\text{GW}}^{\text{3PN}}(\text{Hz})$
$(5 + 5) M_{\odot}$	446	473	570
$(10 + 10) M_{\odot}$	223	236	285
$(15 + 15) M_{\odot}$	149	158	190
$(20 + 20) M_{\odot}$	112	118	143

Table 4.7: GW frequency at the ISCO, computed using the EOB-improved Hamiltonian.

Because of the quartic terms $A^{\alpha\beta\gamma\delta}$, the effective 3PN relativistic Hamiltonian is not uniquely fixed by the matching rules defined above; the general expression is:

$$\mathcal{E}_{\text{eff}}^{\text{NR}} \equiv \widehat{H}_{\text{eff}} = \sqrt{A(q) \left[1 + \mathbf{p}^2 + \left(\frac{A(q)}{D(q)} - 1 \right) (\mathbf{n} \cdot \mathbf{p})^2 + \frac{1}{q^2} (z_1 (\mathbf{p}^2)^2 + z_2 \mathbf{p}^2 (\mathbf{n} \cdot \mathbf{p})^2 + z_3 (\mathbf{n} \cdot \mathbf{p})^4) \right]}, \quad (4.92)$$

here we use the reduced relativistic effective Hamiltonian $\widehat{H}_{\text{eff}} = H_{\text{eff}}/\mu$, \mathbf{q} and \mathbf{p} are the reduced canonical variables, obtained by rescaling the canonical variables by M and μ , respectively. The coefficients z_1, z_2 and z_3 are arbitrary coefficients that satisfy the constraint

$$8z_1 + 4z_2 + 3z_3 = 6(4 - 3\eta)\eta. \quad (4.93)$$

In Eq. (4.92),

$$A(r) = 1 - \frac{2}{r} + \frac{2\eta}{r^3} + \left(\frac{94}{3} - \frac{41}{32}\pi^2 \right) \frac{\eta}{r^4}, \quad (4.94)$$

$$D(r) = 1 - \frac{6\eta}{r^2} + 2(3\eta - 26)\eta \frac{\eta}{r^3}, \quad (4.95)$$

where we set $r = |\mathbf{q}|$. The reduction to the one-body dynamics fixes the arbitrary coefficients in Eq. (4.90) uniquely to $\alpha_1 = \eta/2, \alpha_2 = 0, \alpha_3 = 0$, and provides the *resummed* (improved) Hamiltonian [obtained by solving for $\mathcal{E}_{\text{real}}^{\text{NR}}$ in Eq. (4.90) and imposing $H^{\text{improved}} \equiv \mathcal{E}_{\text{real}}^{\text{NR}}$]:

$$H^{\text{improved}} = M \sqrt{1 + 2\eta \left(\frac{H_{\text{eff}} - \mu}{\mu} \right)}. \quad (4.96)$$

Including radiation-reaction effects, we can then write the Hamilton equations in terms of the reduced quantities $\widehat{H}^{\text{improved}} = H^{\text{improved}}/\mu, \widehat{t} = t/M, \widehat{\omega} = \omega M$ [15],

$$\frac{dr}{d\widehat{t}} = \frac{\partial \widehat{H}^{\text{improved}}}{\partial p_r}(r, p_r, p_\varphi), \quad \frac{d\varphi}{d\widehat{t}} = \widehat{\omega} \equiv \frac{\partial \widehat{H}^{\text{improved}}}{\partial p_\varphi}(r, p_r, p_\varphi), \quad (4.97)$$

$$\frac{dp_r}{d\widehat{t}} + \frac{\partial \widehat{H}^{\text{improved}}}{\partial r}(r, p_r, p_\varphi) = 0, \quad \frac{dp_\varphi}{d\widehat{t}} = \widehat{F}^\varphi(\widehat{\omega}(r, p_r, p_\varphi)), \quad (4.98)$$

N	$(5 + 20) M_\odot$	$(10 + 10) M_\odot$	$(15 + 15) M_\odot$
	$\langle \text{EP}_N, \text{EP}_{N+1} \rangle$	$\langle \text{EP}_N, \text{EP}_{N+1} \rangle$	$\langle \text{EP}_N, \text{EP}_{N+1} \rangle$
0	0.310	0.389	0.481
1	0.768	0.775	0.873
2 ($\hat{\theta} = +2$)	0.868	0.864	0.899
2 ($\hat{\theta} = -2$)	0.915	0.929	0.950

Table 4.8: Cauchy convergence of the EP-approximants. The values quoted assume optimization on the extrinsic parameters but the same intrinsic parameters (i.e., they assume the same masses). At 3PN order, we used $z_1 = 0 = z_2$.

where for the φ component of the radiation-reaction force we use the T- and P-approximants of the flux function.

The innermost stable circular orbit (ISCO) is defined as the solution of $\partial H_0^{\text{improved}}/\partial r = 0 = \partial^2 H_0^{\text{improved}}/\partial r^2$, where $H_0^{\text{improved}}(r, p_r, p_\varphi) = H^{\text{improved}}(r, 0, p_\varphi)$. Here we find it convenient to consider the simple case where $z_1 = 0 = z_2$. In the following, we shall investigate the effect of different choices for these parameters. We also notice that

$$\hat{H}_{\text{eff}}^2(r, 0, p_\varphi) \equiv W_{p_\varphi} = A(r) \left(1 + \frac{p_\varphi^2}{r^2} \right), \quad (4.99)$$

so we can extract the ISCO by imposing $\partial W_{p_\varphi}(r)/\partial r = 0 = \partial^2 W_{p_\varphi}(r)/\partial^2 r$. Using the $A(r)$ given by Eq. (4.94) it is straightforward to prove that at 3PN order there is no ISCO. To improve the behavior of the PN expansion of $A(r)$ and introduce an ISCO, Damour, Jaranowski and Schäfer [16] proposed to replace $A(r)$ with the Padé approximants

$$A_{P_2}(r) = \frac{r(-4 + 2r + \eta)}{2r^2 + 2\eta + r\eta}, \quad (4.100)$$

$$A_{P_3}(r) = \frac{r^2[(a_4(\eta) + 8\eta - 16) + r(8 - 2\eta)]}{r^3(8 - 2\eta) + r^2(a_4(\eta) + 4\eta) + r(2a_4(\eta) + 8\eta) + 4\eta^2}, \quad a_4(\eta) = \left(\frac{94}{3} - \frac{41}{32}\pi^2 \right) \eta. \quad (4.101)$$

Using those expressions for $A(r)$, we show in Table 4.7 the GW frequency at the ISCO for some typical choices of the binary masses.

Definition of the models

For these models, we use the initial conditions laid down in Ref. [53], and also adopted in this chapter for the HT and HP models (see Sec. 4.4.1). At 2PN order we stop the integration of the Hamilton equations at the light ring given by the solution to the equation $r^3 - 3r^2 + 5\eta = 0$ [15]. At 3PN order we find that the orbital frequency and the binding energy start to decrease before the binary

can reach the 3PN light ring, so we stop the evolution when $\dot{\omega} = 0$. It may also happen that the radial velocity becomes comparable to the angular velocity; in this case, the approximation used to introduce the RR effects into the conservative dynamics is no longer valid, so we stop the integration when $\dot{r}/(r\dot{\phi})$ reaches -0.3 . In any of these cases, the instantaneous GW frequency at the time when the integration is stopped defines the *ending frequency* for these waveforms.

We shall refer to the EOB models (E-approximants) as ET(n PN, m PN) (when the T-approximant is used for the flux) or EP(n PN, m PN) (when the P-approximant is used for the flux), where n PN (m PN) denotes the maximum PN order of the terms included in the Hamiltonian (flux). We shall consider $(n\text{PN}, m\text{PN}) = (1, 1.5), (2, 2.5), (3, 3.5, \hat{\theta})$.

Waveforms and matches

In Table 4.13 we investigate the effect of the unknown parameters z_1 and z_2 that appear in the EOB-Hamiltonian at 3PN order. The coefficients z_1 and z_2 are in principle completely arbitrary. To keep the EOB description consistent, however, these coefficients cannot be set much larger than order unity. Thus, in Table 4.13 we perform a few tests with $z_1 = \pm 1$ and $z_2 = \pm 1$. With a few exceptions, it seems that the effect of changing z_1 and z_2 is nearly the same as a remapping of the BBH mass parameters. Therefore, in the following we shall consider only the case $z_1 = z_2 = 0$.

In Table 4.8, for three typical choices of BBH masses, we perform a convergence test using Cauchy's criterion. The values are quite high, especially if compared to the same test for the T- and HP-approximants, shown in Tables 4.2, 4.5. However, as for the P-approximants, we do not have a way of testing whether they are converging to the true limit. The frequency-domain amplitude of the EP-approximated (restricted) waveform is plotted in Fig. 4.10, at different PN orders, for a $(15 + 15)M_\odot$ BBH. The evolution of the EOB models contains a plunge characterized by quasi-circular motion [15]. This plunge causes the amplitude to deviate from the Newtonian prediction $f^{-7/6}$ around 200 Hz, which is a higher frequency than for the adiabatic models [see Figs. 4.4, 4.8].

In Table 4.12, for some typical choices of the masses, we evaluate the maxmax matches between the 2PN and 3PN ET-approximants and the 2PN and 3PN T-approximants. This comparison should emphasize the effect of moving from the adiabatic orbital evolution, ruled by the energy-balance equation, to the full Hamiltonian dynamics, ruled by the Hamilton equations. While the two models are quite distant at 2PN order, the matches are very high at 3PN order, but the estimation of the mass is not very good. The results of Table 4.12 suggest also that the effect of the unknown parameter $\hat{\theta}$ is rather small, at least if $\hat{\theta}$ is of order unity, so in the following we shall always set $\hat{\theta} = 0$.

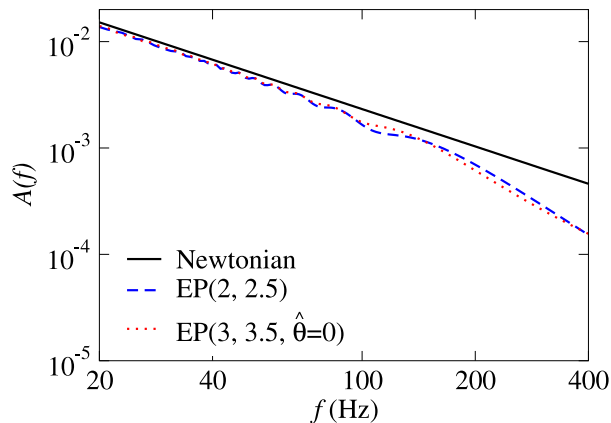


Figure 4.10: Frequency-domain amplitude versus frequency for the EP-approximated (restricted) waveform, at different PN orders, for a $(15 + 15)M_{\odot}$ BBH.

4.5 Comparison between the two-body models

In Fig. 4.11 we show the energy function $\mathcal{E}(v)$ for a few selected two-body models. Notice that the 2PN and 3PN T energies are much closer to each other than the 2PN and 3PN P energies and the 2PN and 3PN E energies are; notice also that the 3PN T and P energies are very close.

In Fig. 4.12 we plot the optimal signal-to-noise ratio ρ_{opt} for a few selected models. The value of ρ_{opt} is computed using Eqs. (4.10), (4.32), with the waveform given by Eq. (4.45), for a luminosity distance of 100 Mpc and the rms value of $\Theta = 8/5$ (see discussion below Eq. (4.45)). The very large result for the 2.5PN T-approximant waveform can be explained as follows. As shown in Fig. 4.4 and discussed in Sec. 4.3.1, the 2.5PN T flux function goes to zero before the orbit can reach the usual ending point at the MECO, so the 2.5PN GW amplitude differs considerably from the Newtonian result. For high-mass BBHs, this happens inside the LIGO frequency band. Of course we know that the true flux function should not go to zero, so we give little credit to the 2.5PN T-approximant.

Notice also that, because the EOB models have a plunge, their signal-to-noise ratios are much higher, at least for $M \geq 30M_{\odot}$, than those for the adiabatic models (which we artificially cut off before the plunge). This result confirms the similar conclusion drawn in Ref. [12].

4.6 Performance of the Fourier-domain detection templates

As we have seen in the previous sections, the PN models (expanded and resummed, adiabatic and nonadiabatic) that we have considered rely on a wide variety of very different dynamical equations, so the task of consolidating them under a single set of generic equations seems arduous. On the other hand, we have reason to suspect (from the values of the matches, and from direct investigations) that

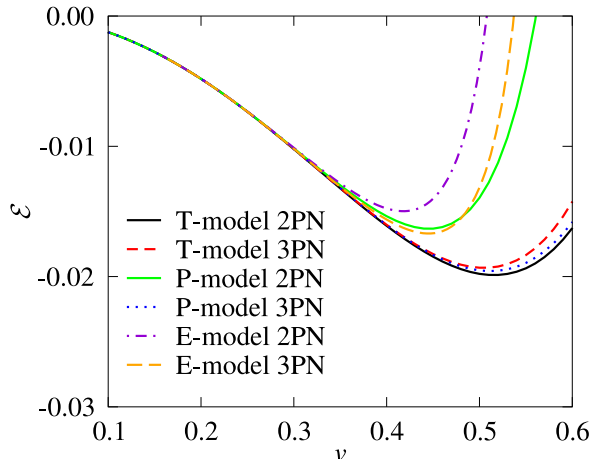


Figure 4.11: Binding energy $\mathcal{E}(v)$ as a function of the velocity parameter v , for equal-mass BBHs. We plot different PN orders for selected PN models.

the frequency-domain amplitude and phasing (the very ingredients that enter the determination of the matches) are quite similar for all the PN models. We therefore shall create a template bank that models *directly* the Fourier transform of the GW signals, by writing the amplitude and phasing as simple polynomials in the GW frequency f_{GW} . We shall take the specific powers of f_{GW} that appear in these polynomials from the Fourier transforms of PN expanded adiabatic signals, as computed in the stationary-phase approximation; however, we shall not constrain their coefficients to their functional dependence on the physical parameters. More specifically, we define our generic family of Fourier-domain detection templates as

$$h_{\text{eff}}(f) = \mathcal{A}_{\text{eff}}(f) e^{i\psi_{\text{eff}}(f)}, \quad (4.102)$$

where

$$\mathcal{A}_{\text{eff}}(f) = f^{-7/6} (1 - \alpha f^{1/3}) \theta(f_{\text{cut}} - f), \quad (4.103)$$

$$\psi_{\text{eff}}(f) = 2\pi f t_0 + \phi_0 + f^{-5/3} (\psi_0 + \psi_{1/2} f^{1/3} + \psi_1 f^{2/3} + \psi_{3/2} f + \psi_2 f^{4/3} + \dots) \quad (4.104)$$

where t_0 and ϕ_0 are the time of arrival and the frequency-domain phase offset, and where $\theta(\dots)$ is the Heaviside step function.

It turns out that we need only two of the phasing parameters, ψ_0 , and $\psi_{3/2}$, and two amplitude parameters, f_{cut} and α , to match all the PN models of Secs. 4.3, 4.4 with high fitting factor FF. This is possible largely because we restrict our focus to BBHs with relatively high masses, where the number of GW cycles in the LIGO range (and thus the total range of the phasing $\psi(f)$ that

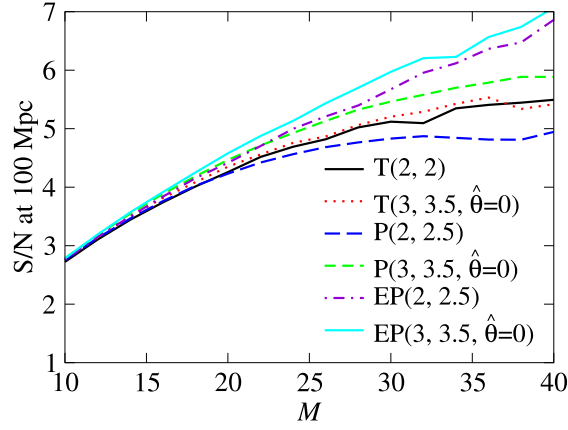


Figure 4.12: Signal-to-noise ratio at 100 Mpc versus total mass M , for selected PN models. We denote by SQP the model obtained with the standard quadrupole prediction for the inspiral energy spectrum and with the cutoff frequency $f_{\text{cutoff}} = 0.02/M$ used in Ref. [11].

we need to consider) is small. The amplitude parameters f_{cut} and α are useful because, unlike the case of BNSs, BBH waveforms might well end within the LIGO band. These parameters change the shape of the frequency-domain amplitude by respectively cutting it off and reducing it in a limited frequency range.

The significance of this cut with respect to true physical signals deserves some discussion. If the best match for the physical signal g is the template $h(f_{\text{cut}})$, which ends at the instantaneous GW frequency f_{cut} , then we can be certain to lose a fraction of the optimal ρ that is given approximately by

$$\frac{\rho_{\text{cut}}}{\rho_{\text{opt}}} \leq \frac{\sqrt{\int_0^{f_{\text{cut}}} \frac{|\tilde{g}(f)|^2}{S_n(f)} df}}{\sqrt{\int_0^\infty \frac{|\tilde{g}(f)|^2}{S_n(f)} df}} \simeq 1 - \frac{1}{2} \frac{\int_{f_{\text{cut}}}^\infty \frac{|\tilde{g}(f)|^2}{S_n(f)} df}{\int_0^\infty \frac{|\tilde{g}(f)|^2}{S_n(f)} df}. \quad (4.105)$$

On the other hand, if we try to match g with the same template family *without cuts* (and if indeed the h 's are completely inadequate at modeling the amplitude and phasing of g above f_{cut}), then even the best-match template $u(\text{no cut})$ will yield an additional loss in ρ caused by the fact that we are spreading the power of the template beyond the range where it can successfully match g . Mathematically, this loss comes from the normalization of the template, and it is given by

$$\frac{\rho_{\text{no cut}}}{\rho_{\text{cut}}} \leq \frac{\sqrt{\int_0^{f_{\text{cut}}} \frac{|\tilde{h}(f)|^2}{S_n(f)} df}}{\sqrt{\int_0^\infty \frac{|\tilde{h}(f)|^2}{S_n(f)} df}} \simeq 1 - \frac{1}{2} \frac{\int_{f_{\text{cut}}}^\infty \frac{|\tilde{h}(f)|^2}{S_n(f)} df}{\int_0^\infty \frac{|\tilde{h}(f)|^2}{S_n(f)} df}. \quad (4.106)$$

If we assume that g and $u(\text{no cut})$ have roughly the same amplitude distribution, the two losses are similar.

In the end, we might be better off cutting templates if we cannot be sure that their amplitude and phasing, beyond a certain frequency, are faithful representations of the true signal. Doing so, we approximately halve the *worst-case* loss of ρ , because instead of losing a factor

$$\frac{\rho_{\text{no cut}}}{\rho_{\text{cut}}} \frac{\rho_{\text{cut}}}{\rho_{\text{opt}}} \simeq 1 - \frac{1}{2} \frac{\int_{f_{\text{cut}}}^{\infty} \frac{|\tilde{h}(f)|^2}{S_n(f)} df}{\int_0^{\infty} \frac{|\tilde{h}(f)|^2}{S_n(f)} df} - \frac{1}{2} \frac{\int_{f_{\text{cut}}}^{\infty} \frac{|\tilde{g}(f)|^2}{S_n(f)} df}{\int_0^{\infty} \frac{|\tilde{g}(f)|^2}{S_n(f)} df} \simeq 1 - \frac{\int_{f_{\text{cut}}}^{\infty} \frac{|\tilde{g}(f)|^2}{S_n(f)} df}{\int_0^{\infty} \frac{|\tilde{g}(f)|^2}{S_n(f)} df}, \quad (4.107)$$

we lose only the factor $\rho_{\text{cut}}/\rho_{\text{opt}}$. On the other hand, we do not want to lose the signal-to-noise ratio that is accumulated at high frequencies if our templates have a fighting chance of matching the true signal there; so it makes sense to include in the detection bank the *same* template with several different values of f_{cut} .

In Table 4.15, we list the minmax (see Sec. 4.2) fitting factor for the projection of the PN models onto our frequency-domain detection templates, for a set of BBH masses ranging from $(5+5)M_{\odot}$ to $(20+20)M_{\odot}$. In computing the fitting factors we used the simplicial search algorithm `amoeba` [57] to search for the optimal set of parameters $(\psi_0, \psi_{3/2}, f_{\text{cut}}, \alpha)$ (as always, the template's time of arrival and initial phase were automatically optimized as described in Sec. 4.2). From Table 4.15 we draw the following conclusions:

1. All the adiabatic models (T and P) are matched with fitting factors $\text{FF} > 0.97$. Lower-mass BBHs are matched better than higher-mass BBHs, presumably because for the latter the inspiral ends at lower frequencies within the LIGO band, producing stronger edge effects that the detection templates cannot capture fully. 3PN models are matched better than 2PN models.
2. The effective-one-body models (ET and EP) are matched even better than the adiabatic models, presumably because they have longer inspirals and less severe edge effects at the end of inspiral. Unlike the adiabatic models, however, ET and EP are matched better for higher-mass BBHs. In fact, all the FFs are > 0.99 except for the $(5+5)M_{\odot}$, where $\text{FF} \gtrsim 0.979$. The reason for this is probably that this low-mass BBH has more GW cycles in the LIGO frequency band than any other one, and the two phasing parameters of our detection templates cannot quite model the evolution of the phasing. [In the adiabatic models, these effects may be overshadowed by the loss in signal-to-noise ratio due to the edge effects at high frequencies.]
3. The Hamiltonian models (HT and HP) are matched the worst: usually $\text{FF} > 0.96$, but there are several exceptions, with FF as low as 0.944. For these models, the overlaps are lower in the equal-mass cases, where the ending frequencies of the waveforms are much higher than for the other models; it seems that the detection templates are not able to reproduce this late portion of the waveforms (this might not be so bad, because it does not seem likely that this portion of the signal reflects the true behavior of BBH waveforms).

Finally, we note that our amplitude function $\mathcal{A}_{\text{eff}}(f)$ is a linear combination of two terms, so we can search automatically over the correction coefficient α , in essentially the same way as discussed in Sec. 4.2 for the orbital phase. In other words, α is an *extrinsic parameter*.

4.6.1 Internal match and metric

To understand the matches between the Fourier-domain templates and the PN models, and to prepare to compute the number of templates needed to achieve a given (internal) MM, we need first to derive an expression for the match between two Fourier-domain detection templates.

We shall first restrict our consideration to detection templates with the same amplitude function (i.e., the same α and f_{cutoff}). The overlap $\langle h(\psi_0, \psi_{3/2}), h(\psi_0 + \Delta\psi_0, \psi_{3/2} + \Delta\psi_{3/2}) \rangle$ between templates with close values of ψ_0 and $\psi_{3/2}$ can be described (to second order in $\Delta\psi_0$ and $\Delta\psi_{3/2}$) by the Owen metric g_{ij} [27]:

$$\langle h(\psi_0, \psi_{3/2}), h(\psi_0 + \Delta\psi_0, \psi_{3/2} + \Delta\psi_{3/2}) \rangle = 1 - \sum_{i,j=0,3/2} g_{ij} \Delta\psi_i \Delta\psi_j. \quad (4.108)$$

The metric coefficients g_{ij} can be evaluated analytically from the overlap

$$\langle h(\psi_0, \psi_{3/2}), h(\psi_0 + \Delta\psi_0, \psi_{3/2} + \Delta\psi_{3/2}) \rangle \simeq \left[\max_{\Delta\phi_0, \Delta t_0} \int df \frac{|\mathcal{A}(f)|^2}{S_h(f)} \cos \left(\sum_i \frac{\Delta\psi_i}{f^{n_i}} + \Delta\phi_0 + 2\pi f \Delta t_0 \right) \right] / \left[\int df \frac{|\mathcal{A}(f)|^2}{S_h(f)} \right] \quad (4.109)$$

or approximately

$$1 - \frac{1}{2} \left[\max_{\Delta\phi_0, \Delta t_0} \int df \frac{|\mathcal{A}(f)|^2}{S_h(f)} \left(\sum_i \frac{\Delta\psi_i}{f^{n_i}} + \Delta\phi_0 + 2\pi f \Delta t_0 \right)^2 \right] / \left[\int df \frac{|\mathcal{A}(f)|^2}{S_h(f)} \right]. \quad (4.110)$$

where $n_0 \equiv 5/3$ and $n_{3/2} \equiv 2/3$. Comparison with Eq. (4.108) then gives

$$\sum_{i,j} g_{ij} \Delta\psi_i \Delta\psi_j = \frac{1}{2} \min_{\Delta\phi_0, \Delta t_0} \left\{ \begin{pmatrix} \Delta\psi_0 & \Delta\psi_{3/2} \end{pmatrix} \mathbf{M}_{(1)} \begin{pmatrix} \Delta\psi_0 \\ \Delta\psi_{3/2} \end{pmatrix} + \right. \quad (4.111)$$

$$\left. \begin{pmatrix} \Delta\phi_0 & 2\pi\Delta t_0 \end{pmatrix} \mathbf{M}_{(2)} \begin{pmatrix} \Delta\psi_0 \\ \Delta\psi_{3/2} \end{pmatrix} + \right. \quad (4.112)$$

$$\left. 2 \begin{pmatrix} \Delta\phi_0 & 2\pi\Delta t_0 \end{pmatrix} \mathbf{M}_{(3)} \begin{pmatrix} \Delta\phi_0 \\ 2\pi\Delta t_0 \end{pmatrix} \right\} \quad (4.113)$$

where the $\mathbf{M}_{(1)\dots(3)}$ are the matrices

$$\mathbf{M}_{(1)} = \begin{bmatrix} J(2n_0) & J(n_0 + n_{3/2}) \\ J(n_0 + n_{3/2}) & J(2n_{3/2}) \end{bmatrix}, \quad (4.114)$$

$$\mathbf{M}_{(2)} = \begin{bmatrix} J(n_0) & J(n_{3/2}) \\ J(n_0 - 1) & J(n_{3/2} - 1) \end{bmatrix}, \quad (4.115)$$

$$\mathbf{M}_{(3)} = \begin{bmatrix} J(0) & J(-1) \\ J(-1) & J(-2) \end{bmatrix}, \quad (4.116)$$

and where

$$J(n) \equiv \left[\int df \frac{|\mathcal{A}(f)|^2}{S_h(f)} \frac{1}{f^n} \right] / \left[\int df \frac{|\mathcal{A}(f)|^2}{S_h(f)} \right]. \quad (4.117)$$

Since $\mathbf{M}_{(3)}$ describes the mismatch caused by $(\Delta\phi_0, \Delta t_0)$, it must be positive definite; because the right-hand side of (4.111) reaches its minimum with respect to variations of $\Delta\phi_0$ and Δt_0 when

$$2\mathbf{M}_{(2)} \begin{pmatrix} \Delta\psi_0 \\ \Delta\psi_{3/2} \end{pmatrix} + 2\mathbf{M}_{(3)} \begin{pmatrix} \Delta\phi_0 \\ 2\pi\Delta t_0 \end{pmatrix} = 0, \quad (4.118)$$

we obtain

$$g_{ij} = \frac{1}{2} \left[\mathbf{M}_{(1)} - \mathbf{M}_{(2)}^T \mathbf{M}_{(3)}^{-1} \mathbf{M}_{(2)} \right]_{ij}. \quad (4.119)$$

We note also that the mismatch $\langle h(\psi_0, \psi_{3/2}), h(\psi_0 + \Delta\psi_0, \psi_{3/2} + \Delta\psi_{3/2}) \rangle$ is translationally invariant in the $(\psi_0, \psi_{3/2})$ plane, so the metric g_{ij} is constant everywhere.

In the left panel of Fig. 4.13 we plot the iso-match contours (at matches of 0.99, 0.975 and 0.95) in the $(\Delta\psi_0, \Delta\psi_{3/2})$ plane, as given by the metric (4.119) [solid ellipses], compared with the actual values obtained from the numerical computation of the matches [dashed lines]. For our purposes, the second-order approximation given by the metric is quite acceptable. In this computation we use a Newtonian amplitude function $\mathcal{A}(f) = f^{-7/6}$ [i.e., we set $\alpha = 0$ and we do not cut the template in frequency domain].

We move now to the mismatch induced by different cutoff frequencies f_{cut} . Unlike the case of the $\psi_0, \psi_{3/2}$ parameters, this mismatch is first order in Δf_{cut} , so it cannot be described by a metric. Suppose that we have two detection templates $h(f_{\text{cut}})$ and $h(f_{\text{cut}} + \Delta f_{\text{cut}})$ with the same phasing

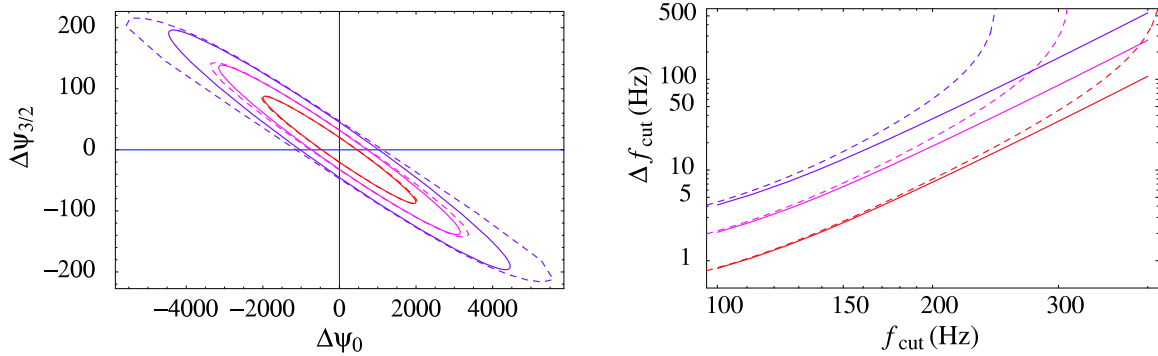


Figure 4.13: In the left panel, we plot the iso-match contours for the function $\langle h(\psi_0, \psi_{3/2}), h(\psi_0 + \Delta\psi_0, \psi_{3/2} + \Delta\psi_{3/2}) \rangle$; contours are given at matches of 0.99, 0.975 and 0.95. Solid lines give the indications of the Owen metric; dashed lines give actual values. Here we use a Newtonian amplitude function $\mathcal{A}(f) = f^{-7/6}$ [we set $\alpha = 0$ and we do not cut the template in the frequency domain]. In the right panel, we plot the values of Δf_{cut} (versus f_{cut}) required to obtain matches $\langle h(f_{\text{cut}}), h(f_{\text{cut}} + \Delta f_{\text{cut}}) \rangle$ of 0.95 (uppermost curve), 0.975 and 0.99 (lowermost). In the region below each contour the match is larger than the value quoted for the contour. Again, here we use a Newtonian amplitude function $\mathcal{A}(f) = f^{-7/6}$ [we set $\alpha = 0$].

and amplitude, but different cutoff frequencies. The match is then given by

$$\langle h(f_{\text{cut}}), h(f_{\text{cut}} + \Delta f_{\text{cut}}) \rangle = \frac{\left[\int_0^{f_{\text{cut}}} df \frac{|\mathcal{A}(f)|^2}{S_h(f)} \right]}{\left[\int_0^{f_{\text{cut}}} df \frac{|\mathcal{A}(f)|^2}{S_h(f)} \right]^{1/2} \left[\int_0^{f_{\text{cut}} + \Delta f_{\text{cut}}} df \frac{|\mathcal{A}(f)|^2}{S_h(f)} \right]^{1/2}} \quad (4.120)$$

$$= \left[\frac{\int_0^{f_{\text{cut}}} df \frac{|\mathcal{A}(f)|^2}{S_h(f)}}{\int_0^{f_{\text{cut}} + \Delta f_{\text{cut}}} df \frac{|\mathcal{A}(f)|^2}{S_h(f)}} \right]^{1/2} \quad (4.121)$$

$$\simeq 1 - \left[\frac{|\Delta f_{\text{cut}}|}{2} \frac{|\mathcal{A}(f)|^2}{S_h(f)} \right] / \left[\int_0^{f_{\text{cut}}} df \frac{|\mathcal{A}(f)|^2}{S_h(f)} \right]^{1/2}. \quad (4.122)$$

This result depends strongly on f_{cut} . In the right panel of Fig. 4.13 we plot the values of Δf_{cut} that correspond to matches of 0.95, 0.975 and 0.99, according to the first order approximation [solid lines], and to the exact numerical calculations [dashed lines], given respectively in Eqs. (4.122) and (4.121). In the region below each contour the match is larger than the value that characterizes the contour.

4.6.2 Construction of the detection template bank: parameter range

All the PN target models are parametrized by two independent numbers (e.g., the two masses or the total mass and the mass ratio); if we select a range of interest for these parameters, the resulting set of PN signals can be seen as a two-dimensional region in the (m_1, m_2) or (M, η) plane. Under the mapping that takes each PN signal into the Fourier-domain detection template that matches it best, this two-dimensional region is *projected* into a two-dimensional surface in the $(\psi_0, \psi_{3/2}, f_{\text{cut}})$

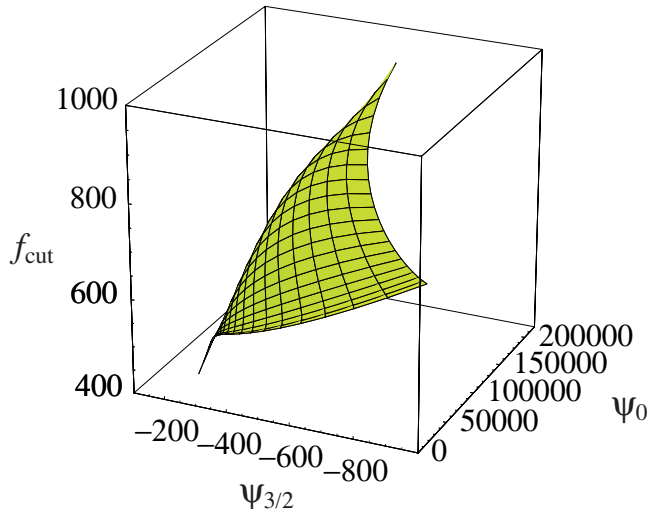


Figure 4.14: Projection of the ET(2, 5/2) waveforms onto the frequency-domain detection template space. The correction parameter α is set to 0. The $(\psi_0, \psi_{3/2}, f_{\text{cut}})$ surface is interpolated from the then mass pairs shown in Table 4.15.

parameter space (with the fourth parameter $\alpha = 0$). As an example, we show in Fig. 4.14 the projection of the ET(2,5/2) waveforms with (single-BH) masses 5–20 M_{\odot} . The 17 models tested in Secs. 4.3, 4.4 would be projected into 17 similar surfaces.

It is hard to visualize all three parameters at once, so we shall start with the phasing parameters ψ_0 and $\psi_{2/3}$. In Fig. 4.15, we plot the $(\psi_0, \psi_{3/2})$ section of the PN-model projections into the $(\psi_0, \psi_{3/2}, f_{\text{cutoff}})$ space, with solid diamonds showing the BBHs with the same set of ten mass pairs as in Table 4.15. Each PN model is projected to a curved-triangular region, with boundaries given by the sequences of BBHs with masses $(m + m)$ (equal mass), $(20 + m)$ and $(m + 5)$. In Fig. 4.15, these boundaries are plotted using thin dashed lines, for the models T(2,5/2) (the uppermost in the plot), HT(3,7/2, $\hat{\theta} = 2$) (in the middle), and P(2,5/2) (lowest).

As we can see, different PN models can occupy regions with very different areas, and thus require a very different number of detection templates to match them with a given MM_{T} . Among these three models, T(2,5/2) requires the least number of templates, P(2,5/2) requires a few times more, and HT(3,7/2, $\hat{\theta} = 2$) requires many more. This is consistent with the result by Porter [56] that for the same range of physical parameters, T waveforms are more closely spaced than P waveforms, so fewer are needed to achieve a certain MM. In this plot we have also linked the points that correspond to the same BBH parameters in different PN models. In Fig. 4.15, these lines (we shall call them *mass lines*) lie all roughly along one direction.

A simple way to characterize the difference between the PN target models is to evaluate the maxmax *end-to-end match* between detection templates at the two ends of the mass lines (i.e., the match between the detection templates with the largest and smallest $\psi_{3/2}$ among the projections

m_1	m_2	end-to-end match	$\mathcal{N}_{\text{end to end}}$
5	5	0.478	37
10	5	0.434	41
15	5	0.398	46
20	5	0.347	52
10	10	0.449	40
15	10	0.443	40
20	10	0.428	42
15	15	0.482	36
20	15	0.464	38
20	20	0.438	41

Table 4.9: End-to-end matches and number of templates (for $\text{MM} \simeq 0.98$) along the mass lines of Fig. 4.15.

of PN waveforms with the same mass parameters m_1, m_2); we wish to focus first on the effects of the phasing parameters, so we do not cut the templates in the frequency domain and we set $\alpha = 0$. We compute also a naive end-to-end number of templates, $\mathcal{N}_{\text{end to end}}$, by counting the templates required to step all along the mass line while maintaining at each step a match $\simeq 0.98$ between neighboring templates. A simple computation yields $\mathcal{N}_{\text{end to end}} = \log(\text{end-to-end match}) / \log(0.98)$. The results of this procedure are listed in Table 4.9. Notice that, as opposed to the fitting factors between template families computed elsewhere in this chapter (which are maximized over the BBH mass parameters of one of the families), these matches give a measure of the dissimilarity between different PN models *for the same values of the BBH parameters*; thus, they provide a crude estimate of how much the detection template bank must be enlarged to embed all the various PN models.

We expect that the projection of a true BBH waveform onto the $(\psi_0, \psi_{3/2})$ plane will lie near the mass line with the true BBH parameters, or perhaps near the extension of the mass line in either direction. For this reason we shall lay down our detection templates in the region traced out by the thick dashed lines in Fig. 4.15, which was determined by extending the mass lines in both directions by half of their length.

We move on to specifying the required range of f_{cut} for each $(\psi_0, \psi_{3/2})$. For a given PN model and BBH mass parameters, we have defined the *ending frequency* f_{end} as the instantaneous GW frequency at which we stop the integration of the PN orbital equations. We find that usually the f_{cut} of the optimally matched projection of a PN template is larger than the f_{end} of the PN template. This is because the abrupt termination of the PN waveforms in the time domain creates a tail in the spectrum for frequencies higher than f_{end} . With $f_{\text{cut}} > f_{\text{end}}$ and $\alpha > 0$, the detection templates can mimic this match and gain a higher match with the PN models. Now, since we do not know the details of the plunge for true BBH inspiral, it is hard to estimate where the optimal f_{cut} might lie, except perhaps imposing that it should be larger than f_{end} . A possible strategy is to set the range of f_{cut} as the range swept by f_{end} across the PN models.

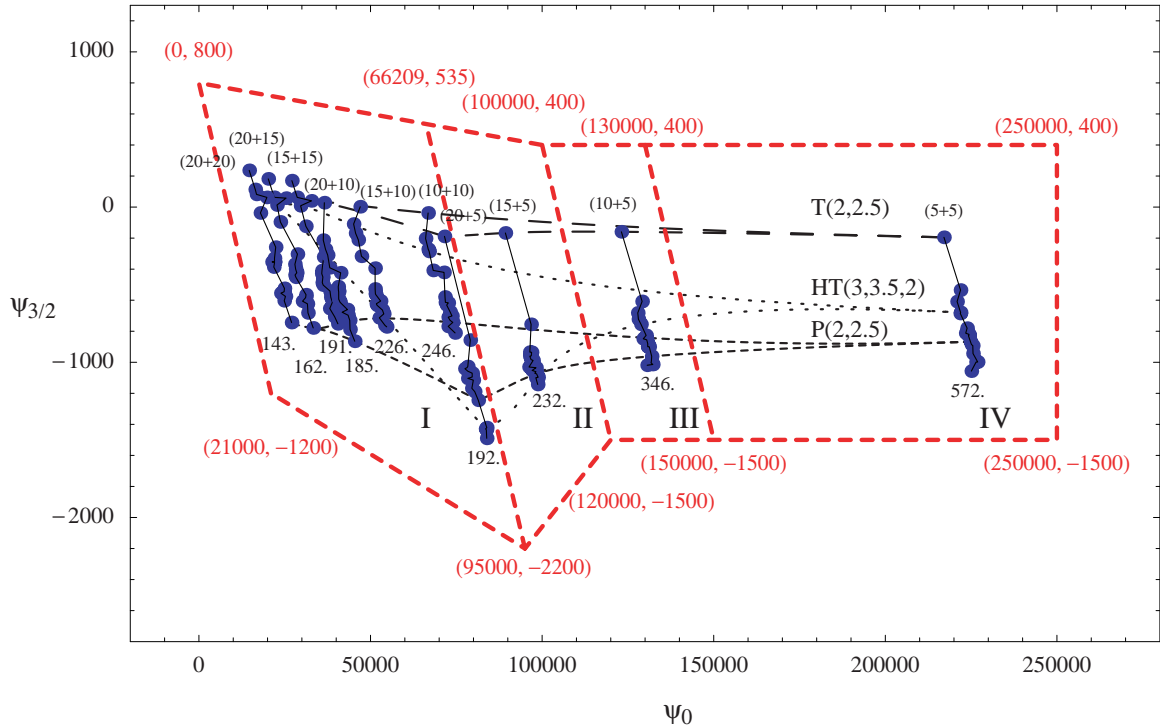


Figure 4.15: Projection of the PN waveforms onto the $(\psi_0, \psi_{3/2})$ plane, for BBHs with masses $(5+5)M_\odot$, $(10+5)M_\odot$, \dots , $(20+20)M_\odot$ (see Table 4.15). The projection was computed by maximizing the maxmax match over the parameters ψ_0 , $\psi_{3/2}$ and f_{cut} ; the correction coefficient α was set to zero. The thin dotted and dashed lines show the boundaries of the projected images for the models (from the top) T(2,5/2), HT(3,7/2, $\hat{\theta} = 2$) and P(2,5/2). Solid lines (the *mass lines*) link the images of the same BBH for different PN models. The ends of the mass lines are marked with the BBH masses and with the minimum value $f_{\text{end min}}$ (across all the PN models) of the instantaneous GW frequency at which we stop the integration of the PN orbital equations. Finally, the thick dashed lines delimit the region that will be covered by the detection template bank; a few $(\psi_0, \psi_{3/2})$ coordinates are marked around the contour. The region is further subdivided into four subregions I–IV that group the mass lines with very similar ending frequencies $f_{\text{end min}}$.

In Table 4.10 we show the minimum ($f_{\text{end min}}$) and maximum ($f_{\text{end max}}$) ending frequencies found across the PN models for given BBH mass parameters. We have also marked the minimum ending frequency in Fig. 4.15 under the corresponding mass lines. We show also the match of the two detection templates $h(f_{\text{cut}} = f_{\text{end min}})$ and $h(f_{\text{cut}} = f_{\text{end max}})$, and the number $\mathcal{N}_{\text{mass line}}^{\text{cut}}$ of intermediate templates with different f_{cut} needed to move from $h(f_{\text{end min}})$ to $h(f_{\text{end max}})$ while maintaining at each step a match $\simeq 0.98$ between neighboring templates. It is easy to see that this number is $\mathcal{N}_{\text{mass line}}^{\text{cut}} = \log\langle h(f_{\text{end min}}), h(f_{\text{end max}}) \rangle / \log(0.98)$. The match was computed using a Newtonian amplitude function $\mathcal{A}(f) = f^{-7/6}$ [we set $\alpha = 0$], and maximizing over the parameters ψ_0 and $\psi_{3/2}$.

Under our previous hypothesis that the projection of a true BBH waveform would lie near the corresponding mass line, we can use the numbers in Table 4.10 to provide a rough estimate of the

m_1	m_2	$f_{\text{end min}}$	$f_{\text{end max}}$	$\langle h(f_{\text{end min}}), h(f_{\text{end max}}) \rangle$	$\mathcal{N}_{\text{end to end}}$
5	5	571.9	>1000	0.997	0.2
10	5	370.1	>1000	0.986	0.7
15	5	267.5	452.7	0.968	1.6
20	5	196.0	358.0	0.919	4.2
10	10	286.0	>1000	0.968	1.6
15	10	226.3	>1000	0.936	3.3
20	10	185.1	>1000	0.889	5.8
15	15	190.6	>1000	0.897	5.4
20	15	162.5	>1000	0.844	8.4
20	20	143.0	933.1	0.787	11.9

Table 4.10: Ranges for the ending frequencies of PN waveforms along the mass lines of Fig. 4.15. The last two columns show the match between the two detection templates at the ends of the range and the number of templates needed to step along the range while always maintaining a match $\simeq 0.98$ between neighboring templates. When computing these matches, we use a Newtonian amplitude function $\mathcal{A}(f) = f^{-7/6}$ [we set $\alpha = 0$], and we maximize over the parameters ψ_0 and $\psi_{3/2}$ (which is equivalent to assuming perfect phasing synchronization).

range of f_{cut} that should be taken at each point $(\psi_0, \psi_{3/2})$ within the dashed contour of Fig. 4.15. We trace out four subregions I, II, III, IV, such that the mass lines of each subregion have approximately the same values of $f_{\text{end min}}$; we then use these minimum ending frequencies to set a lower limit for the values of f_{cut} required in each subregion: $f_{\text{cut min}}(\text{I}) = 143$, $f_{\text{cut min}}(\text{II}) = 196$, $f_{\text{cut min}}(\text{III}) = 268$, $f_{\text{cut min}}(\text{IV}) = 370$. The maximum f_{cut} is effectively set by the detector noise curve, which limits the highest frequency at which signal can be still accumulated.

Moving on to the last parameter, α , we note that it is only meaningful to have $0 \leq \alpha f_{\text{cut}}^{2/3} \leq 1$, so that $\mathcal{A}_{\text{eff}}(f)$ can become smaller than $f^{-7/6}$ at high frequencies, but cannot become negative for $f < f_{\text{cut}}$. Indeed, the optimized values found for α in Table 4.15 seem to follow this rule, except for a few slight violations that are probably due to numerical error.

4.6.3 Construction of the detection templates bank: parameter density

At this stage, we have completed the specification of the region in the $(\psi_0, \psi_{3/2}, f_{\text{cut}}, \alpha)$ parameter space where we shall lay down our bank of templates. We expect that the FF for the projection of the true physical signals (emitted by *nonspinning* BBHs with $M = 10\text{--}40M_{\odot}$) onto this template bank should be very good. We now wish to evaluate the total number of templates \mathcal{N} needed to achieve a certain MM.

We shall find it convenient to separate the mismatch due to the phasing from the mismatch due to the frequency cuts by introducing two minimum match parameters MM_{ψ} and MM_{cut} , with $\text{MM} = \text{MM}_{\psi} \cdot \text{MM}_{\text{cut}} \simeq \text{MM}_{\psi} + \text{MM}_{\text{cut}} - 1$. As mentioned at the beginning of this section, the correction coefficient α is essentially an *extrinsic* parameter [see Sec. 4.2.2]: we do not need to discretize the template bank with respect to α , and there is no corresponding MM parameter.

We evaluate \mathcal{N} in three refinement steps:

1. We start by considering only the phasing parameters, and we compute the parameter area S_i [in the $(\psi_0, \psi_{3/2})$ plane] for each of the subregions $i = \text{I, II, III, IV}$ of Fig. 4.15. We then multiply by the determinant \sqrt{g} of the constant metric, and divide by $2(1 - MM)$, according to Eq. (4.38), to get

$$\mathcal{N} = \sum_i \frac{S_i \sqrt{g}}{2(1 - MM_\psi)}. \quad (4.123)$$

This expression is for the moment only formal, because we cannot compute \sqrt{g} without considering the amplitude parameters α and f_{cut} .

2. Next, we include the effect of f_{cut} . In the previous section, we have set $f_{\text{min cut}}$ for each of the subregions by considering the range swept by f_{end} along the mass lines. Recalling our discussion of $\mathcal{N}_{\text{mass line}}^{\text{cut}}$, we approximate the number of distinct values of f_{cut} that we need to include for each parameter pair $(\psi_0, \psi_{3/2})$ as

$$n_i^{\text{cut}}(\psi_0, \psi_{3/2}, \alpha) = 1 + \frac{\log \langle h(\psi_0, \psi_{3/2}, \alpha, f_{\text{min cut}}), h(\psi_0, \psi_{3/2}, \alpha, \text{no cut}) \rangle}{\log MM_{\text{cut}}}. \quad (4.124)$$

For α in the physical range $0 \leq \alpha \leq f_{\text{cut}}^{-2/3}$ this match is minimized for $\alpha = 0$, so this is the value that we use to evaluate the n_i^{cut} 's.

3. The final step is to include the effect of α and f_{cut} on the computation of \sqrt{g} . For simplicity, we shoot for an upper limit by maximizing \sqrt{g} with respect to α . [Because α is essentially an extrinsic parameter, we do not multiply \mathcal{N} by the number of its discrete values: the matches are automatically maximized on the continuous range $0 \leq \alpha \leq f_{\text{cut}}^{-2/3}$.] Our final estimate for the total number of templates is

$$\mathcal{N} = \sum_i \frac{S_i n_i^{\text{cut}} \max_{\alpha, f_{\text{cut}}} [\sqrt{g}]}{2(1 - MM_\psi)}. \quad (4.125)$$

We have evaluated this \mathcal{N} numerically. *We find that the contributions to the total number of templates from the four subregions, for $MM = 0.96$ (taking $MM_\psi = MM_{\text{cut}} = 0.98$), are $\mathcal{N}(\text{I}) \simeq 6,140$, $\mathcal{N}(\text{II}) \simeq 1,680$, $\mathcal{N}(\text{III}) \simeq 630$, $\mathcal{N}(\text{IV}) \simeq 1,290$, for a total of $\mathcal{N} = 9,740$. This number scales approximately as $[0.04/(1 - MM)]^2$. Notice that subregion I, which contains all the BBHs with total mass above $25M_\odot$, requires by far the largest number of templates. This is mostly because these waveforms end in the LIGO band, and many values of f_{cut} are needed to match different ending frequencies.*

Remember that the optimal signal-to-noise ratio ρ for filtering the true GW signals by a template bank is approximately degraded (in the worst case) by the factor $MM_\Gamma = FF + MM - 1$. While

MM depends on the geometry of the template bank, we can only guess at the fitting factor FF for the projection of the true signal onto the template space. In this section we have seen that all PN models can be projected onto the detection frequency-domain templates with a good FF: for a vast majority of the waveforms $FF \gtrsim 0.96$ (and the few exceptions can be explained). *It is therefore reasonable to hope that the FF for the true GW signals is ~ 0.96 , so the total degradation from the optimal ρ will be $MM_T \gtrsim 0.92$, corresponding to a loss of $\lesssim 22\%$ in event rate.* This number can be improved by scaling up the number of templates, but of course the actual FF represents an upper limit for MM_T . For instance, about 39,000 templates should get us $MM_T \gtrsim 0.94$, corresponding to a loss of $\lesssim 17\%$ in event rate.

4.6.4 Parameter estimation with the detection templates

Although our family of detection templates was built for the main purpose of detecting BBHs, we can still use it (once a detection is made) to extract partial information about the BH masses. It is obvious from Fig. 4.15 that the masses cannot in general be determined unambiguously from the best-match parameters [i.e., the projection of the true waveform onto the $(\psi_0, \psi_{3/2})$ plane], because the images of different PN models in the plane have overlaps. Therefore different PN models will have different ideas, as it were, about the true masses. Another way of saying this is that the mass lines can cross.

However, it still seems possible to extract at least one mass parameter, the chirp mass $\mathcal{M} = M\eta^{3/5}$, with some accuracy. Since the phasing is dominated by the term $\psi_0 f^{-5/3}$ at low frequencies, we can use the leading Newtonian term $\psi_N(f) = \frac{3}{128}(\pi\mathcal{M}f)^{-5/3}$ obtained for a PN expanded adiabatic model in the stationary-phase approximation to infer

$$\psi_0 \sim \frac{3}{128} \left(\frac{1}{\pi\mathcal{M}} \right)^{5/3} \implies \mathcal{M}^{\text{approx}} = \frac{1}{\pi} \left(\frac{3}{128\psi_0} \right)^{3/5}. \quad (4.126)$$

If this correspondence was exact, the mass lines in Fig. 4.15 would all be vertical. They are not, so this estimation has an error that gets larger for smaller ψ_0 (i.e., for binaries with higher masses). In Table 4.11 we show the range of chirp-mass estimates obtained from Eq. 4.126 for the values of ψ_0 at the projections of the PN models in Fig. 4.15, together with their percentage error $\epsilon \equiv (\mathcal{M}_{\text{max}}^{\text{approx}} - \mathcal{M}_{\text{min}}^{\text{approx}})/\mathcal{M}$. In this table, \mathcal{M}_{max} and \mathcal{M}_{min} correspond to the endpoints of the mass lines. If we take into account the extension of the mass lines by a factor of two in the detection template bank, we should double the ϵ of the table.

It seems quite possible that a more detailed investigations of the geometry of the projections into the detection template space (and especially of the mass lines) could produce better algorithms to estimate binary parameters.

m_1	m_2	\mathcal{M}	$\mathcal{M}_{\min}^{\text{approx}}$	$\mathcal{M}_{\max}^{\text{approx}}$	$\epsilon\%$
5	5	4.35	4.15	4.27	2.7
10	5	6.08	5.74	5.99	4.1
15	5	7.33	6.84	7.30	6.2
20	5	8.33	7.55	8.34	9.4
10	10	8.71	8.14	8.72	6.7
15	10	10.62	9.77	11.26	14.0
20	10	12.17	11.04	12.57	12.5
15	15	13.06	11.68	15.49	29.2
20	15	15.05	13.18	17.79	30.6
20	20	17.41	14.92	21.40	37.2

Table 4.11: Estimation of the chirp masses \mathcal{M} from the projections of the PN target models onto the Fourier-domain detection template space. The numbers in the third column (labeled “ \mathcal{M} ”) give the values of the chirp mass corresponding to the BH masses (m_1, m_2) to their right; the numbers in the fourth and fifth columns give the range of estimates obtained from Eq. (4.126) for the values of ψ_0 at the projections of the target models shown in Fig. 4.15. The last column shows the percentage error $\epsilon \equiv (\mathcal{M}_{\max}^{\text{approx}} - \mathcal{M}_{\min}^{\text{approx}})/\mathcal{M}$.

4.7 Performance of the time-domain detection templates

Another possibility is to adopt one or more of the physical models discussed in Secs. 4.4 as the detection template bank used for detection. Under the general hypothesis that underlies this work (that is, that the *target* models span the region in signal space where the true physical signals reside), if we find that one of the target models matches all the others very well, we can use it as the detection model; and we can estimate its effectualness in matching the true physical signal from its effectualness in matching all the other models.

As shown in Table 4.14 and discussed in Sec. 4.5, the fitting factors FF for the projection of the PN models onto each other are quite low (at least for PN order $n \leq 5/2$); in other words, the models appear to be quite distant in signal space. This conclusion is overturned, however, if we let the dimensionless mass ratio η move beyond its physical range $0 \leq \eta \leq 1/4$. For instance, the P(2, 5/2) and EP(3, 7/2, 0) models can be extended formally to the range $0 \leq \eta \leq 1$. Beyond those ranges, either the equations (of energy-balance, or motion) become singular, or the determination of the MECO or light ring (the evolutionary endpoint of the inspiral for the P(2, 5/2) model and the EP(3, 7/2, 0) model, respectively) fails.

When the models are extended to $0 < \eta \leq 1$, they appear to lie much closer to each other in signal space. In particular, the P(2, 5/2) and EP(3, 7/2, 0) models are able to match all the other models, with minmax FF > 0.95 , for almost all the masses in our range, and in any case with much improved FF for most masses; see Tables 4.16 and 4.17. Apparently, part of the effect of the different resummation and approximation schemes is just to modulate the strength of the PN effects in a way that can be simulated by changing η to nonphysical values in any one model. This fact can be appreciated by looking at Figs. 4.16 and 4.17, which show the projection of several models onto the

P(2, 5/2) and EP(3, 7/2, 0) detection template spaces, respectively. For instance, in comparison with T(2, 5/2), the model P(2, 5/2) seems to underestimate systematically the effect of η , so a satisfactory FF for $\eta_T = 0.25$ can be obtained only if we let $\eta_P > 0.25$ (quite consistently, in the comparison of Table 4.14, where η was confined to its physical range, T(2, 5/2) could match P(2, 5/2) effectively, but the reverse was not true).

The other (and perhaps crucial) effect of raising η is to change the location of the MECO for the P-approximant model (or the light ring, for the EP model), where orbital evolution ends. (Remember that one of the differences between the Padé and the EOB models is that the latter includes a plunge part between the ISCO and the light ring.) More specifically, for P(2, 5/2) [EP(3, 7/2, 0)] the position of the MECO [light ring] is pushed to smaller radii as η is increased. This effect can increase the FF for target models that have very different ending frequencies from those of P(2, 5/2) and EP(3, 7/2) at comparable η 's.

Because for the EP model the frequency at the light ring is already quite high, we cannot simply operate on η to improve the match between the EP model and other models that end at much lower frequencies [see the values of minmax matches in Table 4.17]. Thus, we shall enhance the effectualness of EP by adding an arbitrary *cut* parameter that modifies the radius r (usually the light-ring radius) at which we stop the integration of the Hamilton equations (4.97)–(4.98); the effect is to modify the final instantaneous GW frequency of the waveform. This is therefore a *time-domain cut*, as opposed to the frequency-domain cuts of the frequency-domain detection templates examined in the previous section.

We can then compute the FF by searching over f_{cut} in addition to M and η , and we shall correspondingly account for the required number of distinct f_{cut} when we estimate the number of templates required to give a certain MM_{tot} . Even so, if we are unsure whether we can model successfully a given source over a certain range of frequencies that falls within LIGO range (as it is the case for the heavy BBHs with MECOs at frequencies < 200 Hz), the correct way to estimate the optimal ρ (and therefore the expected detection rate) is to include only the signal power in the frequency range that we know well.

The best matches shown in Tables 4.16 and 4.17, and in Figs. 4.16 and 4.17 were obtained by searching over the target model parameter space with the simplicial `amoeba` algorithm [57]. We found (empirically) that it was expedient to conduct the searches on the parameters $\beta \equiv M\eta^{2/5}$ and η rather than on M and η . This is because iso-match surfaces tend to look like thin ellipses clustered around the best match parameter pair, with principal axes along the β and η directions. As shown in Table 4.16, the values of the maxmax and minmax FFs are very close to each other for the P(2, 5/2) model; the same is true for the EP(3, 7/2) model (so in Table 4.17 we do not show both). For EP(3, 7/2), the search over the three parameters ($\beta, \eta, f_{\text{cut}}$) was performed as a refinement step after a first search on (β, η).

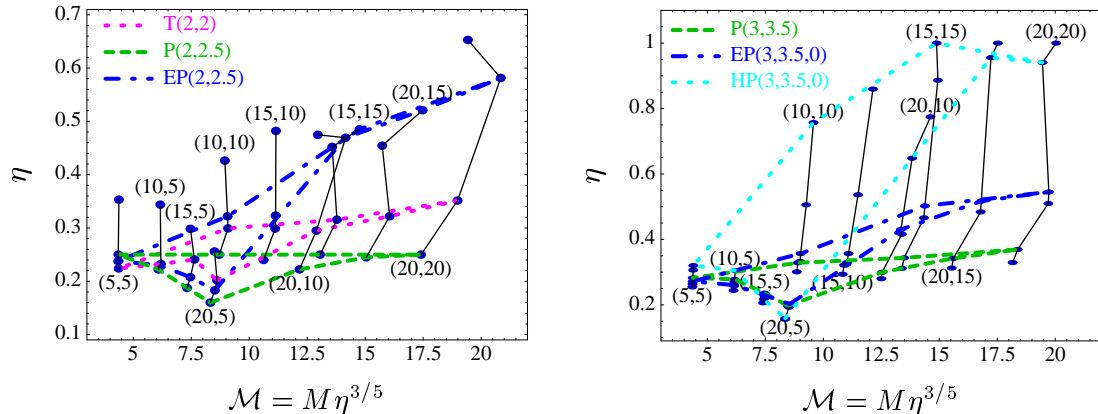


Figure 4.16: Projection of PN waveforms onto the P(2, 5/2) detection template space. Dots are shown for the same BBH masses of Table 4.15, for PN models T(2, 5/2), P(2, 5/2), ET(2, 5/2), and EP(2, 5/2) in the left panel, and for PN models T(3, 7/2, +2), P(3, 7/2, +2), ET(3, 7/2, +2), EP(3, 7/2, +2), HT(3, 7/2, +2), and HP(3, 7/2, +2) in the right. The dots for $\hat{\theta} = -2$ are only slightly displaced, and they are not shown. The thin solid lines show the *mass lines* (introduced in Sec. 4.6.2), while the dashed and dotted lines show the contours of the projections of selected PN models.

We have evaluated the Owen metric [27] g_{ij} (see Sec. 4.2) with respect to the parameters (β, η) for the models P(2, 5/2) and EP(3, 7/2, 0) (while evaluating g_{ij} , the EP waveforms were not cut). The metric components at the point (β_0, η_0) were obtained by first determining the ranges $(\beta_{\min}, \beta_{\max})$, $(\eta_{\min}, \eta_{\max})$ for which

$$\langle u(\beta_0, \eta_0), u(\beta_{\min}, \eta_0) \rangle = \langle u(\beta_0, \eta_0), u(\beta_{\max}, \eta_0) \rangle = 1 - 0.05 \quad (4.127)$$

$$\langle u(\beta_0, \eta_0), u(\beta_0, \eta_{\min}) \rangle = \langle u(\beta_0, \eta_0), u(\beta_0, \eta_{\max}) \rangle = 1 - 0.05; \quad (4.128)$$

then a quadratic form was least-squares-fit to 16 values of the match along the ellipse Γ_1 with axes given by $(\beta_{\min}, \beta_{\max})$ and $(\eta_{\min}, \eta_{\max})$. The first quadratic form was used only to determine the principal axes of two further ellipses Γ_2 and Γ_3 , at projected matches of $1 - 0.025$ and $1 - 0.0125$. Another quadratic form (giving the final result for the metric) was then fit at the same time to 16 points along Γ_2 and to 16 points along Γ_3 , but the two ellipses were given different fitting weights to cancel the quartic correction terms in the Taylor expansion of the match around (β_0, η_0) [the cubic terms were canceled automatically by taking symmetric points along the ellipses]. The rms error of the fit was in all cases very good, establishing that the quadratic approximation held in the close vicinity (matches ~ 0.95) of each point.

The resulting $\sqrt{|g|}$ for P(2, 5/2) and EP(3, 7/2, 0) is shown in Fig. 4.18. It is evident that most of the mismatch volume is concentrated near the smallest β 's and η 's in parameter space. This is encouraging, because it means that the extension of the detection template family to high masses and high η 's (necessary, as we have seen, to match several target models with very high FF) will be

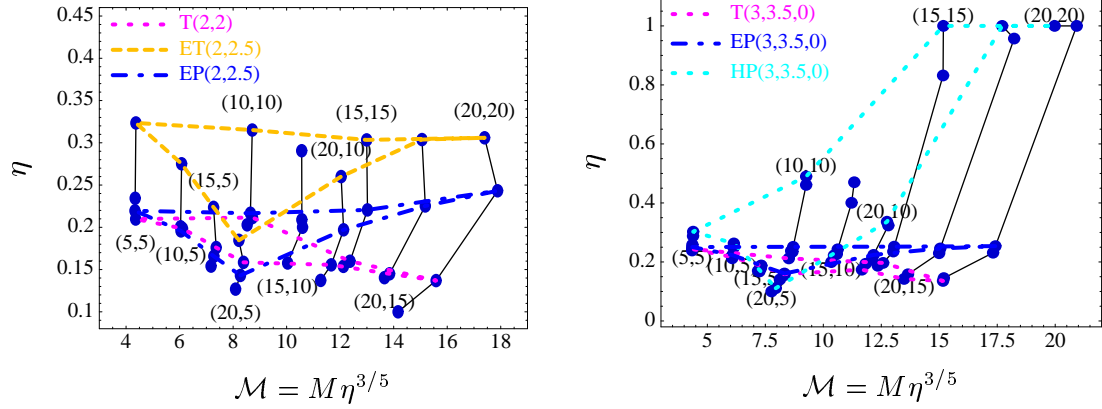


Figure 4.17: Projection of PN waveforms onto the EP(3, 7/2) detection template space. This projection includes the effect of the frequency cut. Dots are shown for the same BBH masses of Table 4.15, and for PN models T(2, 5/2), P(2, 5/2), ET(2, 5/2), and EP(2, 5/2) in the left panel, and for PN models T(3, 7/2, +2), P(3, 7/2, +2), ET(3, 7/2, +2), EP(3, 7/2, +2), HT(3, 7/2, +2), and HP(3, 7/2, +2) in the right panel. The dots for $\hat{\theta} = -2$ are only slightly displaced, and they are not shown. The thin solid lines show the *mass lines* (introduced in Sec. 4.6.2), while the dashed and dotted lines show the contours of the projections of selected PN models.

relatively cheap with respect to the size of the template bank. With the $\sqrt{|g|}$'s we then computed the number of P and EP templates necessary to cover the parameter range $\beta : (4, 24)$, $\eta : (0.15, 1.00)$, which spans comfortably all the projected images of the target spaces onto the P and EP template spaces. We obtained

$$\mathcal{N}_P \simeq 6520 \left(\frac{0.01}{1 - \text{MM}} \right), \quad \mathcal{N}_E \simeq 9750 \left(\frac{0.01}{1 - \text{MM}} \right), \quad (4.129)$$

where MM is the required minimum match. By comparison, these numbers are reduced to respectively 2460 and 3180 if we restrict η to the physical range.

The number \mathcal{N}_E does not include the effect of multiple ending frequencies (cuts). We estimate the number of distinct f_{cut} needed for each β by an argument similar to the one used for the Fourier-domain detection templates (see Sec. 4.6). The resulting number is $\mathcal{N}_{E_c} \simeq 32,000$ for $\text{MM} = 0.98$, which is comparable to the result for the detection Fourier-domain templates.

If we assume that the distance between the time-domain templates and the target models is representative of the distance to the true physical signal, we can guess that $\text{FF} \gtrsim 0.95$ for P and $\text{FF} \gtrsim 0.97$ for EP with cuts. Under these hypotheses, 6,500 P templates can buy us a (worst-case) $\text{MM}_T \simeq 0.94$, corresponding to a loss in event rate of $\sim 17\%$. For 32,000 EP templates, we get $\text{MM}_T \simeq 0.95$, corresponding to a loss in event rate of $\sim 14\%$.

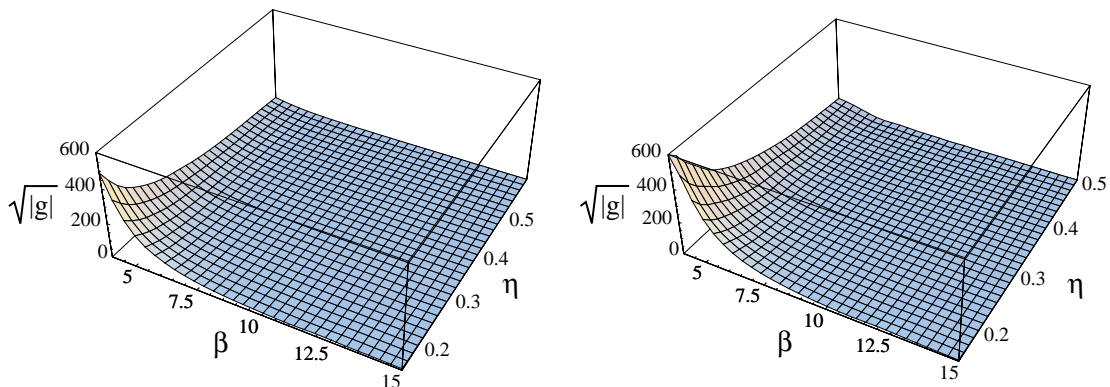


Figure 4.18: Determinant of the Owen metric [27] for the $P(2, 5/2)$ models [left panel], and for the $EP(3, 7/2, 0)$ models [right panel]. The determinant $\sqrt{|g|}$ is shown as a function of η and $\beta = M\eta^{2/5}$.

4.8 Summary

This chapter deals with the problem of detecting GWs from the most promising sources for ground-based GW interferometers: comparable-mass BBHs with total mass $M = 10\text{--}40M_\odot$ moving on quasi-circular orbits. The detection of these sources poses a delicate problem, because their transition from the adiabatic phase to the plunge, at least in the nonspinning case, is expected to occur in the LIGO and VIRGO frequency bands. Of course, the true GW signals from these inspirals should be obtained from exact solutions of the Einstein equations for two bodies of comparable mass. However, the theoretical templates used to search for these signals will be, at best, finite-order approximations to the exact solutions, usually derived in the PN formalism. Because the perturbative PN approach begins to fail during the final stages of the inspiral, when strong curvature and nonlinear effects can no longer be neglected, various PN resummation methods have been introduced [14, 15, 16] to improve the convergence of the PN series.

In the first part of this chapter [see Sec. 4.3, 4.4 and 4.5], we studied and compared in detail all the PN models of the relativistic two-body dynamics currently available, including PN Taylor-expanded and resummed models both in the adiabatic approximation and in the nonadiabatic case. We noticed the following features. At least for PN orders $n \leq 5/2$, the *target* models T, P, and E have low cross matches. For example, for almost all the masses in our range, we found $\max\max FF \leq 0.9$; the matches were much better only for P against E (and viceversa). However, at 3PN order we found much higher matches between T, P, and E, and also with the nonadiabatic model H. These results make sense because at 3PN order the various approximations to the binding energy and the flux seem to be much closer to each other than at lower orders. This “convergence” of the different analytical approaches, which at 3PN order are also much closer to some examples of numerical

quasi-equilibrium BBH models [25], was recently pointed out in Refs. [51, 60]. On the other hand, the extraction of BBH parameters from a true measured signal, if done using the 3PN models, would still give a range of rather different estimates.

In addition, by studying the frequency-domain amplitude of the GW signals that end inside the LIGO frequency band [see Figs. 4.4, 4.8, 4.10, 4.9], we understood that if high matches are required, it is crucial to reproduce their deviations from the Newtonian amplitude evolution, $f^{-7/6}$ (on the contrary, the Newtonian formula seems relatively adequate to model the PN amplitude for GW frequencies below the instantaneous GW frequency at the endpoint of orbital evolution).

Finally, the introduction of the H model provided another example of two-body nonadiabatic dynamics, quite different from the E models. In the H models, the conservative dynamics does not have an ISCO. As a consequence, the transition to the plunge is due to the secular radiation-reaction effects, and it is pushed to much higher frequencies. This means that, for the H models, the GW signals for BBHs of total mass $M = 10\text{--}40M_\odot$ end outside the LIGO frequency band, and the frequency-domain amplitude does not deviate much from the Newtonian result, at least until very high frequencies [see Fig. 4.9].

In the second part of the chapter [Secs. 4.6, 4.7] we pursued the following strategy. We assumed that the target models spanned a region in signal space that (almost) included the true GW signal. We were then able to provide a few detection template banks (either chosen among the time-domain target models, or built directly from polynomial amplitude and phasings in the frequency domain) that approximate quite well all the targets [FF ≥ 0.95 for almost all the masses in our range, with much better FFs for most masses]. We speculate that the effectualness of the detection model in approximating the targets is indicative of its effectualness in approximating the true signals.

The Fourier-domain detection template bank, discussed in Sec. 4.6, is simple and versatile. It uses a PN polynomial structure for the frequency-domain amplitude and phasing, but it does not constrain the coefficients to the PN functional dependencies on the physical parameters. In this sense this bank follows the basic idea that underlies the fast chirp transform [58]. However, because for the masses that we consider the GW signal can end within the LIGO frequency band, we were forced to modify the Newtonian-order formula for the amplitude, introducing a cutoff frequency and a parameter to modify the shape of the amplitude curve (the parameter α). A theoretical explanation for the good performance of this bank (especially the fact that it can cover all the target models with only two arbitrary parameters in the phasing, and one arbitrary parameter to cut the signal) might be found in the results of Ref. [59].

We showed that our Fourier-domain detection template space has a FF higher than 0.97 for the T, P and E models, and $\gtrsim 0.96$ for most of the HT, HP models; we then speculate that it will match true BBH waveforms with FF ~ 0.96 . We have computed the number of templates required to give $MM \simeq 0.96$ (about 10^4). The total MM_T should be larger than $FF \cdot MM \sim 0.92$, which corresponds

to a loss of event rate of $1 - \text{MM}_T^3 \approx 22\%$. This performance could be improved at the price of introducing a larger number of templates, with the rough scaling law of $\mathcal{N} = 10^4 [0.04 / (0.96 - \text{MM})]^2$.

The time-domain detection template banks, discussed in Sec. 4.7, followed a slightly different philosophy. The idea in this case was to provide a template bank that, for some choices of the parameters, could coincide with one of the approximate two-body models. Quite interestingly, this can be achieved by relaxing the physical hypothesis that $0 \leq \eta \leq 0.25$. However, the good performances of these banks are less systematic, and harder to generalize than the performance of the Fourier-domain detection bank. The detection template banks based on the extension of the P(2, 5/2) and EP(3, 7/2) to nonphysical values of η were shown to have FF $\gtrsim 0.95$ and $\gtrsim 0.97$ for all the PN target models, and considerably higher for most models and masses. We have computed the number of P templates needed to obtain a $\text{MM} = 0.99$ (about 6,500) and of EP templates to obtain a $\text{MM} = 0.98$ (about 32,000). The expected total MM_T is then $\gtrsim 0.94$ for the P model, and $\gtrsim 0.95$ for the EP model, corresponding to losses in event rate of $\lesssim 17\%$ and $\lesssim 14\%$. The MMs scale roughly as $[0.01 / (1 - \text{MM})]$ for P and $[0.02 / (1 - \text{MM})]^2$ for EP (because of the additional frequency-cut parameter).

When numerical relativity provides the first good examples of waveforms for the last stages of BBH inspiral and plunge, we will be able to sharpen our indications further. Last, we note that the comparison between the PN expanded and resummed methods and the quasi-equilibrium approach of Ref. [25] (recently discussed in Refs. [51, 60]), could also be used to improve our suggestions.

	T(2, 5/2)		ET(2, 5/2)		T(3, 7/2, +2)		T(3, 7/2, -2)		ET(3, 7/2, +2)		ET(3, 7/2, -2)	
	mm	M	mm	M	mm	M	mm	M	mm	M	mm	M
T(2, 5/2)	(15+15) M_{\odot}		0.893	27.80	0.245							
	(15+5) M_{\odot}		0.909	16.74	0.250							
	(5+5) M_{\odot}		0.902	9.93	0.250							
ET(2, 5/2)	(15+15) M_{\odot}	0.912	34.23	0.238								
	(15+5) M_{\odot}	0.922	28.87	0.100								
	(5+5) M_{\odot}	0.978	13.29	0.153								
T(3, 7/2, +2)	(15+15) M_{\odot}				0.999	31.12	0.238					
	(15+5) M_{\odot}				1.000	20.99	0.172					
	(5+5) M_{\odot}				1.000	10.55	0.228					
T(3, 7/2, -2)	(15+15) M_{\odot}				0.955	30.19	0.244					
	(15+5) M_{\odot}				0.984	19.84	0.192					
	(5+5) M_{\odot}				0.996	10.21	0.241					
ET(3, 7/2, +2)	(15+15) M_{\odot}				0.933	29.75	0.241					
	(15+5) M_{\odot}				0.986	18.85	0.210					
	(5+5) M_{\odot}				0.984	9.97	0.250					
ET(3, 7/2, -2)	(15+15) M_{\odot}				0.961	30.76	0.241					
	(15+5) M_{\odot}				0.982	20.60	0.180					
	(5+5) M_{\odot}				0.985	10.29	0.239					

Table 4.12: Fitting factors between T and ET models, at 2PN and 3PN orders, and for different choices of the arbitrary flux parameter $\hat{\theta}$. For three choices of BBH masses, this table shows the maxmax matches [see Eq. (4.22)] between the *search* models at the top of the columns and the *target* models at the left end of the rows, *maximized over the mass parameters of the models in the columns*. For each intersection, the three numbers mm, m_1 and m_2 denote the maximized match and the search-model mass parameters at which the maximum is attained. The matches can be interpreted as the fitting factors for the projection of the target models onto the search models. See the caption to Table 4.14 for further details.

	EP(3, 7/2, 0, -1, 0)		EP(3, 7/2, 0, 0, -1)		EP(3, 7/2, 0, 0, 0)		EP(3, 7/2, 0, 0, 1)		EP(3, 7/2, 0, 1, 0)					
	mm	M	mm	M	mm	M	mm	M	mm	M	η			
(15+15) M_\odot			0.991	31.11	0.240	0.992	31.18	0.239	0.992	31.02	0.239	0.948	31.67	0.239
(15+5) M_\odot			0.998	21.25	0.167	0.999	21.31	0.166	0.999	21.30	0.167	0.987	22.92	0.145
(5+5) M_\odot			0.995	10.23	0.240	0.995	10.22	0.241	0.995	10.22	0.241	0.996	10.85	0.216
(15+15) M_\odot	0.980	29.82	0.241			0.999	30.47	0.241	0.999	30.42	0.241	0.989	31.18	0.239
(15+5) M_\odot	0.998	18.85	0.209			1.000	19.95	0.188	1.000	19.95	0.188	0.996	21.50	0.164
(5+5) M_\odot	0.979	10.10	0.245			0.996	10.19	0.241	1.000	10.00	0.250	0.995	10.24	0.240
(15+15) M_\odot	0.980	29.82	0.241	0.999	30.48	0.240			0.999	30.42	0.241	0.990	31.18	0.239
(15+5) M_\odot	0.998	18.86	0.209	1.000	20.07	0.186			1.000	20.02	0.187	0.998	21.58	0.162
(5+5) M_\odot	0.988	9.98	0.250	1.000	10.03	0.249			0.996	10.18	0.242	0.995	10.24	0.240
(15+15) M_\odot	0.985	29.85	0.242	0.999	30.46	0.240	0.999	30.46	0.240			0.983	31.24	0.239
(15+5) M_\odot	0.999	18.93	0.207	1.000	19.98	0.188	1.000	20.11	0.185			0.996	21.67	0.161
(5+5) M_\odot	0.988	9.98	0.250	0.996	10.19	0.241	0.996	10.18	0.242			0.995	10.24	0.240
(15+15) M_\odot	0.932	29.31	0.240	0.975	29.89	0.240	0.971	29.82	0.242	0.970	29.66	0.242		
(15+5) M_\odot	0.989	17.49	0.241	0.998	18.58	0.215	0.998	18.50	0.217	0.997	18.50	0.217		
(5+5) M_\odot	0.950	10.11	0.243	0.986	9.97	0.250	0.986	9.98	0.250	0.985	9.98	0.249		

Table 4.13: Fitting factors for the projection of EP(3, 7/2, 0) templates onto themselves, for various choices of the parameters z_1 and z_2 . The values quoted are obtained by maximizing the maxmax (mm) match over the mass parameters of the (search) models in the columns, while keeping the mass parameters of the (target) models in the rows fixed to their quoted values, $(15+15)M_\odot$, $(15+5)M_\odot$, $(5+5)M_\odot$. The three numbers shown at each intersection are the maximized match and the search parameters at which the maximum was attained. In labeling rows and columns we use the notation EP(3, 7/2, $\hat{\theta}_1, z_1, z_2$). See the caption to Table 4.14 for further details.

	T(2,5/2)		T(3,7/2,0)		P(2,5/2)		P(3,7/2,0)		EP(2,5/2)		EP(3,7/2,0)		HT(3,7/2,0)		HP(3,7/2,0)	
	mm	M	mm	M	mm	M	mm	M	mm	M	mm	M	mm	M	mm	M
T(2,5/2)	(15+15) M_{\odot}		0.804	25.99 0.24	0.765	25.97 0.24	0.813	26.68 0.24	0.841	25.33 0.24	0.876	26.01 0.25	0.901	27.33 0.24	0.934	28.30 0.25
	(5+15) M_{\odot}		0.848	16.01 0.25	0.861	16.24 0.25	0.889	16.33 0.25	0.816	15.84 0.25	0.857	16.27 0.25	0.893	16.26 0.25	0.950	16.46 0.25
	(5+5) M_{\odot}		0.819	9.72 0.25	0.822	9.71 0.25	0.838	9.75 0.25	0.810	9.70 0.25	0.825	9.93 0.24	0.834	9.73 0.25	0.859	9.82 0.25
T(3,7/2,0)	(15+15) M_{\odot}		0.838	42.60 0.24	0.983	29.61 0.25	0.998	31.00 0.24	0.958	30.41 0.24	0.944	31.15 0.24	0.995	33.17 0.20	0.760	32.02 0.24
	(5+15) M_{\odot}		0.881	30.05 0.10	0.997	18.95 0.21	1.000	20.80 0.18	0.983	19.82 0.19	0.985	21.18 0.17	0.998	19.84 0.19	0.999	20.22 0.18
	(5+5) M_{\odot}		0.821	10.48 0.24	0.998	10.01 0.25	1.000	10.58 0.23	0.992	9.98 0.25	0.996	10.47 0.23	0.992	10.57 0.23	0.993	10.93 0.21
P(2,5/2)	(15+15) M_{\odot}		0.803	45.51 0.24	0.990	30.76 0.24	0.983	31.37 0.24	0.899	30.53 0.24	0.885	31.33 0.24	0.991	33.74 0.19	0.994	34.18 0.19
	(5+15) M_{\odot}		0.860	29.20 0.11	0.997	21.18 0.17	0.999	21.96 0.16	0.966	20.27 0.18	0.965	21.87 0.16	0.993	20.40 0.18	0.996	20.63 0.18
	(5+5) M_{\odot}		0.969	16.99 0.10	0.998	10.19 0.24	0.999	10.66 0.22	0.992	9.98 0.25	0.994	10.45 0.23	0.988	10.58 0.23	0.990	10.95 0.21
P(3,7/2,0)	(15+15) M_{\odot}		0.836	38.38 0.24	0.995	29.49 0.25	0.962	29.44 0.24	0.976	29.93 0.24	0.957	30.72 0.24	0.988	32.59 0.20	0.993	33.09 0.20
	(5+15) M_{\odot}		0.907	29.63 0.10	1.000	19.11 0.20	0.999	18.41 0.22	0.976	19.28 0.20	0.979	20.69 0.17	0.991	19.63 0.19	0.996	19.90 0.19
	(5+5) M_{\odot}		0.846	10.53 0.24	0.985	9.97 0.25	0.983	9.97 0.25	0.960	9.94 0.25	0.990	10.16 0.24	0.991	10.17 0.24	0.991	10.57 0.23
EP(2,5/2)	(15+15) M_{\odot}		0.886	38.51 0.24	0.948	30.30 0.24	0.889	30.39 0.24	0.950	30.97 0.24	0.993	31.35 0.24	0.888	33.61 0.24	0.998	33.58 0.21
	(5+15) M_{\odot}		0.840	31.18 0.10	0.982	20.18 0.19	0.968	19.57 0.20	0.974	20.76 0.18	0.999	21.45 0.17	0.994	19.86 0.19	0.986	20.38 0.18
	(5+5) M_{\odot}		0.813	10.57 0.24	0.997	10.25 0.24	0.995	10.23 0.24	0.996	10.80 0.22	0.999	10.74 0.22	0.995	10.83 0.22	0.997	11.13 0.21
EP(3,7/2,0)	(15+15) M_{\odot}		0.903	36.98 0.24	0.926	29.73 0.24	0.874	29.29 0.25	0.941	30.17 0.24	0.985	29.32 0.25	0.917	31.14 0.24	0.999	32.62 0.21
	(5+15) M_{\odot}		0.873	30.19 0.10	0.985	18.65 0.22	0.976	17.62 0.24	0.973	20.34 0.18	0.999	18.49 0.22	1.000	19.31 0.20	0.997	19.65 0.20
	(5+5) M_{\odot}		0.838	10.46 0.24	0.988	9.97 0.25	0.986	9.98 0.25	0.996	10.20 0.24	0.969	9.95 0.25	0.992	10.22 0.24	0.995	10.70 0.22
HT(3,7/2,0)	(15+15) M_{\odot}		0.923	34.13 0.24	0.794	28.74 0.24	0.751	28.67 0.24	0.814	29.70 0.24	0.853	28.17 0.24	0.878	29.54 0.24	0.985	20.79 0.18
	(5+15) M_{\odot}		0.855	30.96 0.10	0.998	20.42 0.18	0.985	19.71 0.19	0.993	20.70 0.18	0.991	20.54 0.18	0.985	20.79 0.18	0.981	10.02 0.25
	(5+5) M_{\odot}		0.988	16.96 0.10	0.963	10.13 0.24	0.971	9.98 0.25	0.984	10.21 0.24	0.945	9.96 0.25	0.981	10.02 0.25	0.999	20.39 0.18
HP(3,7/2,0)	(15+15) M_{\odot}		0.927	32.46 0.24	0.749	28.05 0.24	0.716	27.65 0.25	0.761	28.42 0.24	0.801	26.92 0.25	0.825	28.32 0.24	0.938	28.98 0.25
	(5+15) M_{\odot}		0.876	29.97 0.10	0.999	19.67 0.19	0.992	18.18 0.23	0.996	20.03 0.19	0.988	19.91 0.19	0.990	20.88 0.17	0.999	19.62 0.19
	(5+5) M_{\odot}		0.991	15.72 0.11	0.938	9.94 0.25	0.943	9.95 0.25	0.968	9.97 0.25	0.913	9.93 0.25	0.949	9.97 0.25	0.966	9.96 0.25

Table 4.14: Fitting factors between several PN models, at 2PN and 3PN orders. For three choices of BBH masses, this table shows the maximum matches [see Eq. (4.22)] between the *search* models at the top of the columns and the *target* models at the left end of the rows, *maximized over the intrinsic parameters of the search models in the columns*. For each intersection, the three numbers mm, $M = m_1 + m_2$ and $\eta = m_1 m_2 / M^2$ denote the maximized match and the search-model mass parameters at which the maximum is attained. In computing these matches, the parameter η of the search models was restricted to its physical range $0 < \eta \leq 1/4$. The arbitrary flux parameter $\hat{\theta}$ was always set equal to zero.

These matches represent the fitting factors [see Eq. (4.33)] for the projection of the target models onto the search models. The reader will notice that the values shown are not symmetric across the diagonal: for instance, the match for the target model T(2, 5/2) against the target model P(2, 5/2) is higher than the converse. This is because the matches represent the inner product (4.10) between two different pairs of model parameters: in the first case, the target parameters ($m_1 = 15M_{\odot}, m_2 = 15M_{\odot}$) $P \equiv (M = 30M_{\odot}, \eta = 0.25)$ P are mapped to the maximum-match search parameters ($M = 45.51M_{\odot}, \eta = 0.24$) T ; in the second case, the target parameters ($m_1 = 15M_{\odot}, m_2 = 15M_{\odot}$) $T \equiv (M = 30M_{\odot}, \eta = 0.25)$ T are mapped to the maximum-match search parameters ($M = 25.97M_{\odot}, \eta = 0.24$) P [so the symmetry of the inner product (4.10) is reflected by the fact that the search parameters ($M = 25.97M_{\odot}, \eta = 0.24$) P are mapped into the target parameters ($M = 30M_{\odot}, \eta = 0.25$) T].

PN model	FF for projection onto the Fourier-domain detection models													
	f_{end}	mn	ψ_0	$\psi_{3/2}$	$\alpha f_{\text{cut}}^{2/3}$	f_{cut}	f_{end}	mn	ψ_0	$\psi_{3/2}$	$\alpha f_{\text{cut}}^{2/3}$	f_{cut}		
T(2, 5/2)	(20 + 20) M_{\odot}	167.2	0.970	18291.	-158.09	0.342	204.0	(20 + 5) M_{\odot}	289.8	0.986	71171.	-170.01	0.155	322.8
	(20 + 15) M_{\odot}	193.2	0.974	23965.	142.93	0.038	230.6	(10 + 10) M_{\odot}	336.0	0.982	66410.	-16.43	0.009	359.7
	(15 + 15) M_{\odot}	222.9	0.977	31046.	134.05	0.008	261.1	(15 + 5) M_{\odot}	355.3	0.982	88800.	-142.12	0.507	774.2
	(20 + 10) M_{\odot}	228.6	0.979	36081.	55.66	0.068	266.7	(10 + 5) M_{\odot}	458.2	0.983	123370.	-173.74	0.831	779.0
	(15 + 10) M_{\odot}	270.3	0.975	46422.	34.15	0.566	580.5	(5 + 5) M_{\odot}	674.0	0.993	216750.	-180.89	0.000	675.7
T(3, 7/2, +2)	(20 + 20) M_{\odot}	202.2	0.982	24740.	-550.57	0.987	249.4	(20 + 5) M_{\odot}	268.0	0.985	80175.	-1128.00	0.937	302.3
	(20 + 15) M_{\odot}	228.0	0.984	31815.	-635.05	0.940	239.7	(10 + 10) M_{\odot}	404.8	0.988	73612.	-697.27	1.022	514.6
	(15 + 15) M_{\odot}	269.6	0.987	38935.	-617.73	0.995	314.0	(15 + 5) M_{\odot}	352.0	0.988	97603.	-1001.20	0.878	375.9
	(20 + 10) M_{\odot}	251.8	0.985	43612.	-713.36	1.093	342.6	(10 + 5) M_{\odot}	504.3	0.989	131080.	-893.94	0.880	584.8
	(15 + 10) M_{\odot}	315.4	0.986	53770.	-682.52	0.887	318.3	(5 + 5) M_{\odot}	809.7	0.986	224390.	-826.75	0.817	927.6
T(3, 7/2, -2)	(20 + 20) M_{\odot}	202.4	0.979	25238.	-628.12	1.001	249.9	(20 + 5) M_{\odot}	268.2	0.987	80459.	-1194.50	0.945	300.8
	(20 + 15) M_{\odot}	227.6	0.985	31698.	-677.89	0.982	258.7	(10 + 10) M_{\odot}	404.3	0.989	74084.	-782.54	1.014	496.1
	(15 + 15) M_{\odot}	269.9	0.987	39544.	-706.50	0.964	287.4	(15 + 5) M_{\odot}	352.4	0.989	98187.	-1091.00	0.836	352.4
	(20 + 10) M_{\odot}	252.4	0.985	43869.	-778.12	0.941	253.5	(10 + 5) M_{\odot}	504.2	0.988	131480.	-972.32	0.908	515.5
	(15 + 10) M_{\odot}	315.1	0.988	54129.	-759.15	1.038	386.7	(5 + 5) M_{\odot}	808.5	0.982	226160.	-972.81	0.721	808.5
P(2, 5/2)	(20 + 20) M_{\odot}	143.0	0.972	26976.	-745.63	0.987	205.0	(20 + 5) M_{\odot}	207.9	0.978	81733.	-1266.10	0.843	209.2
	(20 + 15) M_{\odot}	162.5	0.976	33158.	-769.35	0.919	191.4	(10 + 10) M_{\odot}	286.0	0.983	73895.	-746.01	0.814	293.4
	(15 + 15) M_{\odot}	190.6	0.980	40579.	-759.45	0.976	232.9	(15 + 5) M_{\odot}	267.5	0.982	98602.	-1090.80	0.794	270.2
	(20 + 10) M_{\odot}	185.1	0.975	44531.	-803.19	0.900	195.1	(10 + 5) M_{\odot}	370.1	0.983	132430.	-988.92	0.700	370.1
	(15 + 10) M_{\odot}	226.3	0.981	54598.	-764.93	0.847	226.3	(5 + 5) M_{\odot}	571.9	0.983	225180.	-884.21	0.607	571.9
P(3, 7/2, +2)	(20 + 20) M_{\odot}	143.0	0.979	25363.	-563.91	1.016	240.1	(20 + 5) M_{\odot}	207.9	0.983	79257.	-1051.20	0.764	219.0
	(20 + 15) M_{\odot}	162.5	0.982	31357.	-578.36	0.962	233.4	(10 + 10) M_{\odot}	286.0	0.987	72966.	-635.31	0.633	300.8
	(15 + 15) M_{\odot}	190.6	0.982	38639.	-567.75	0.886	243.3	(15 + 5) M_{\odot}	267.5	0.989	96539.	-915.69	0.638	269.8
	(20 + 10) M_{\odot}	185.1	0.981	43270.	-662.60	0.915	245.4	(10 + 5) M_{\odot}	370.1	0.992	130120.	-816.32	0.545	371.0
	(15 + 10) M_{\odot}	226.3	0.984	52889.	-601.36	0.801	263.2	(5 + 5) M_{\odot}	571.9	0.989	223660.	-770.64	0.593	733.9
P(3, 7/2, -2)	(20 + 20) M_{\odot}	143.0	0.979	25682.	-602.71	1.000	235.1	(20 + 5) M_{\odot}	207.9	0.983	79776.	-1104.70	0.776	223.8
	(20 + 15) M_{\odot}	162.5	0.983	31516.	-614.40	1.019	266.1	(10 + 10) M_{\odot}	286.0	0.989	72873.	-655.62	0.642	288.5
	(15 + 15) M_{\odot}	190.6	0.983	38789.	-606.93	0.983	275.0	(15 + 5) M_{\odot}	267.5	0.988	96652.	-947.76	0.683	267.5
	(20 + 10) M_{\odot}	185.1	0.982	43576.	-704.21	0.987	269.3	(10 + 5) M_{\odot}	370.1	0.990	130470.	-867.71	0.612	388.8
	(15 + 10) M_{\odot}	226.3	0.984	53278.	-652.03	0.732	238.8	(5 + 5) M_{\odot}	571.9	0.989	224240.	-828.78	0.490	577.4
ET(2, 5/2)	(20 + 20) M_{\odot}	231.0	0.992	22501.	-265.89	0.909	436.6	(20 + 5) M_{\odot}	359.4	0.995	79626.	-884.06	0.946	642.0
	(20 + 15) M_{\odot}	263.5	0.992	28787.	-308.42	0.938	516.6	(10 + 10) M_{\odot}	462.0	0.995	71558.	-428.56	0.674	757.1
	(15 + 15) M_{\odot}	308.0	0.993	36279.	-318.01	0.740	540.8	(15 + 5) M_{\odot}	452.7	0.994	96651.	-748.31	0.674	681.7
	(20 + 10) M_{\odot}	305.1	0.993	41355.	-424.18	0.788	525.5	(10 + 5) M_{\odot}	610.1	0.993	129150.	-607.32	0.641	793.7
	(15 + 10) M_{\odot}	368.3	0.994	51719.	-412.34	0.849	609.2	(5 + 5) M_{\odot}	924.0	0.991	221900.	-533.53	0.369	924.2
ET(3, 7/2, +2)	(20 + 20) M_{\odot}	214.5	0.991	22070.	-355.33	0.918	341.3	(20 + 5) M_{\odot}	352.6	0.993	78755.	-1076.90	0.738	389.2
	(20 + 15) M_{\odot}	244.3	0.992	28411.	-416.70	0.974	426.4	(10 + 10) M_{\odot}	428.7	0.995	72334.	-639.59	0.758	659.6
	(15 + 15) M_{\odot}	285.9	0.992	36224.	-454.79	0.939	540.1	(15 + 5) M_{\odot}	434.4	0.994	97025.	-993.73	0.869	742.2
	(20 + 10) M_{\odot}	285.8	0.993	40883.	-553.27	1.117	649.0	(10 + 5) M_{\odot}	577.8	0.994	130850.	-899.89	0.606	830.2
	(15 + 10) M_{\odot}	342.3	0.993	51551.	-565.33	0.924	625.0	(5 + 5) M_{\odot}	847.7	0.986	225160.	-875.85	0.557	848.9
ET(3, 7/2, -2)	(20 + 20) M_{\odot}	204.2	0.991	21968.	-393.93	0.953	351.6	(20 + 5) M_{\odot}	348.4	0.992	78490.	-1112.40	0.739	379.4
	(20 + 15) M_{\odot}	236.8	0.992	28226.	-448.43	0.995	412.3	(10 + 10) M_{\odot}	409.6	0.994	72835.	-720.60	0.617	468.4
	(15 + 15) M_{\odot}	272.2	0.993	36311.	-506.61	1.061	535.3	(15 + 5) M_{\odot}	431.2	0.993	97319.	-1064.30	1.024	807.2
	(20 + 10) M_{\odot}	277.4	0.992	40889.	-599.37	0.996	519.8	(10 + 5) M_{\odot}	559.6	0.995	131780.	-1004.80	0.784	783.4
	(15 + 10) M_{\odot}	329.1	0.992	51582.	-618.21	0.956	622.1	(5 + 5) M_{\odot}	818.9	0.983	226630.	-1005.30	0.571	818.9
EP(2, 5/2)	(20 + 20) M_{\odot}	218.1	0.991	21159.	-345.94	0.823	410.5	(20 + 5) M_{\odot}	345.8	0.991	79743.	-1178.70	0.713	358.6
	(20 + 15) M_{\odot}	249.1	0.992	27741.	-423.65	0.995	567.1	(10 + 10) M_{\odot}	436.2	0.993	72886.	-715.34	0.604	514.6
	(15 + 15) M_{\odot}	290.8	0.990	35543.	-466.47	1.006	712.0	(15 + 5) M_{\odot}	433.1	0.993	98112.	-1097.80	0.918	708.3
	(20 + 10) M_{\odot}	289.8	0.990	40526.	-582.83	0.682	404.5	(10 + 5) M_{\odot}	579.6	0.993	132360.	-1019.30	0.780	906.5
	(15 + 10) M_{\odot}	348.5	0.990	51692.	-620.53	0.977	770.9	(5 + 5) M_{\odot}	872.5	0.979	227160.	-1008.80	0.589	875.8
EP(3, 7/2, +2)	(20 + 20) M_{\odot}	219.5	0.991	22114.	-334.89	1.005	403.0	(20 + 5) M_{\odot}	358.0	0.994	78307.	-1024.50	0.764	403.8
	(20 + 15) M_{\odot}	250.0	0.991	28406.	-391.73	0.995	453.7	(10 + 10) M_{\odot}	439.1	0.995	71669.	-578.87	0.721	663.4
	(15 + 15) M_{\odot}	292.6	0.991	35794.	-406.91	0.904	506.6	(15 + 5) M_{\odot}	446.4	0.995	96288.	-930.06	0.908	720.3
	(20 + 10) M_{\odot}	291.6	0.992	40343.	-498.71	0.981	602.9	(10 + 5) M_{\odot}	585.1	0.995	130140.	-839.47	0.674	867.3
	(15 + 10) M_{\odot}	353.7	0.993	51234.	-521.92	0.946	678.8	(5 + 5) M_{\odot}	870.7	0.989	224200.	-812.19	0.538	870.7
EP(3, 7/2, -2)	(20 + 20) M_{\odot}	214.8	0.991	21821.	-336.53	0.955	368.0	(20 + 5) M_{\odot}	353.9	0.993	78195.	-1040.20	0.731	405.0
	(20 + 15) M_{\odot}	244.8	0.992	28059.	-393.32	0.957	430.2	(10 + 10) M_{\odot}	433.5	0.994	71738.	-611.36	0.763	653.2
	(15 + 15) M_{\odot}	286.4	0.992	35969.	-438.72	0.963	542.8	(15 + 5) M_{\odot}	443.8	0.994	96309.	-954.89	0.879	751.4
	(20 + 10) M_{\odot}	288.6	0.993	40432.	-525.35	1.101	652.0	(10 + 5) M_{\odot}	576.7	0.995	130750.	-899.09	0.702	837.9
	(15 + 10) M_{\odot}	346.9	0.993	51238.	-548.55	1.028	708.2	(5 + 5) M_{\odot}	866.6	0.988	225240.	-891.94	0.491	866.6
HT(3, 7/2, +2)	(20 + 20) M_{\odot}	933.1	0.976	16506.	93.72	0.687	941.3	(20 + 5) M_{\odot}	196.2	0.983	83749.	-1440.80	0.952	266.5
	(20 + 15) M_{\odot}	1096.7	0.971	21255.	72.04	0.468	1000.0	(10 + 10) M_{\odot}	1866.3	0.962	67097.	-284.34	0.660	1000.0
	(15 + 15) M_{\odot}	1244.2	0.966	28096.	66.27	0.077	1000.0	(15 + 5) M_{\odot}	303.6	0.992	98509.	-1077.90	0.795	386.8
	(20 + 10) M_{\odot}	1525.8	0.979	36560.	-263.16	0.709	1000.0	(10 + 5) M_{\odot}	3051.7	0.990	128490.	-739.94	0.261	1000.0
	(15 + 10) M_{\odot}	1581.0	0.963	45686.	-176.01	0.345	1000.0	(5 + 5) M_{\odot}	3732.3	0.991	222			

		FF for projection onto $P(2,5/2)$, for $0 < \eta < 1$																																								
		mm			M			mn			M			mm			M			η			mn			M			η													
T(2,5/2)	$(20+20)M_{\odot}$	0.970	19.35	0.91	0.952	20.79	0.77	$(20+5)M_{\odot}$	0.989	12.61	0.54	0.985	12.27	0.57	$(20+20)M_{\odot}$	0.970	19.35	0.91	0.952	20.79	0.77	$(20+5)M_{\odot}$	0.989	12.61	0.54	0.985	12.27	0.57	$(20+20)M_{\odot}$	0.970	19.35	0.91	0.952	20.79	0.77	$(20+5)M_{\odot}$	0.989	12.61	0.54	0.985	12.27	0.57
	$(20+15)M_{\odot}$	0.973	16.60	0.94	0.957	17.53	0.84	$(10+10)M_{\odot}$	0.987	10.26	0.84	0.982	9.88	0.90	$(20+15)M_{\odot}$	0.973	16.60	0.94	0.957	17.53	0.84	$(10+10)M_{\odot}$	0.987	10.26	0.84	0.982	9.88	0.90	$(20+15)M_{\odot}$	0.973	16.60	0.94	0.957	17.53	0.84	$(10+10)M_{\odot}$	0.987	10.26	0.84	0.982	9.88	0.90
	$(15+15)M_{\odot}$	0.978	14.25	0.97	0.963	15.00	0.88	$(15+5)M_{\odot}$	0.990	10.23	0.62	0.987	9.90	0.66	$(15+15)M_{\odot}$	0.978	14.25	0.97	0.963	15.00	0.88	$(15+5)M_{\odot}$	0.990	10.23	0.62	0.987	9.90	0.66	$(15+15)M_{\odot}$	0.978	14.25	0.97	0.963	15.00	0.88	$(15+5)M_{\odot}$	0.990	10.23	0.62	0.987	9.90	0.66
	$(20+10)M_{\odot}$	0.976	15.41	0.73	0.971	14.84	0.79	$(10+5)M_{\odot}$	0.987	8.49	0.61	0.984	8.29	0.64	$(20+10)M_{\odot}$	0.976	15.41	0.73	0.971	14.84	0.79	$(10+5)M_{\odot}$	0.987	8.49	0.61	0.984	8.29	0.64	$(20+10)M_{\odot}$	0.976	15.41	0.73	0.971	14.84	0.79	$(10+5)M_{\odot}$	0.987	8.49	0.61	0.984	8.29	0.64
	$(15+10)M_{\odot}$	0.981	12.81	0.80	0.940	14.92	0.59	$(5+5)M_{\odot}$	0.986	6.55	0.52	0.985	6.51	0.53	$(15+10)M_{\odot}$	0.981	12.81	0.80	0.940	14.92	0.59	$(5+5)M_{\odot}$	0.986	6.55	0.52	0.985	6.51	0.53	$(15+10)M_{\odot}$	0.981	12.81	0.80	0.940	14.92	0.59	$(5+5)M_{\odot}$	0.986	6.55	0.52	0.985	6.51	0.53
T(3,7/2,-2)	$(20+20)M_{\odot}$	0.997	37.03	0.31	0.994	37.01	0.31	$(20+5)M_{\odot}$	0.996	23.67	0.18	0.990	23.28	0.19	$(20+20)M_{\odot}$	0.997	37.03	0.31	0.994	37.01	0.31	$(20+5)M_{\odot}$	0.996	23.67	0.18	0.990	23.28	0.19	$(20+20)M_{\odot}$	0.997	37.03	0.31	0.994	37.01	0.31	$(20+5)M_{\odot}$	0.996	23.67	0.18	0.990	23.28	0.19
	$(20+15)M_{\odot}$	0.997	32.60	0.29	0.995	32.47	0.30	$(10+10)M_{\odot}$	0.998	19.70	0.26	0.993	19.03	0.28	$(20+15)M_{\odot}$	0.997	32.60	0.29	0.995	32.47	0.30	$(10+10)M_{\odot}$	0.998	19.70	0.26	0.993	19.03	0.28	$(20+15)M_{\odot}$	0.997	32.60	0.29	0.995	32.47	0.30	$(10+10)M_{\odot}$	0.998	19.70	0.26	0.993	19.03	0.28
	$(15+15)M_{\odot}$	0.998	28.89	0.28	0.994	28.07	0.30	$(15+5)M_{\odot}$	0.997	19.20	0.21	0.993	18.76	0.22	$(15+15)M_{\odot}$	0.998	28.89	0.28	0.994	28.07	0.30	$(15+5)M_{\odot}$	0.997	19.20	0.21	0.993	18.76	0.22	$(15+15)M_{\odot}$	0.998	28.89	0.28	0.994	28.07	0.30	$(15+5)M_{\odot}$	0.997	19.20	0.21	0.993	18.76	0.22
	$(20+10)M_{\odot}$	0.997	28.69	0.25	0.995	27.99	0.26	$(10+5)M_{\odot}$	0.997	14.92	0.23	0.993	14.63	0.24	$(20+10)M_{\odot}$	0.997	28.69	0.25	0.995	27.99	0.26	$(10+5)M_{\odot}$	0.997	14.92	0.23	0.993	14.63	0.24	$(20+10)M_{\odot}$	0.997	28.69	0.25	0.995	27.99	0.26	$(10+5)M_{\odot}$	0.997	14.92	0.23	0.993	14.63	0.24
	$(15+10)M_{\odot}$	0.998	24.35	0.26	0.994	23.78	0.27	$(5+5)M_{\odot}$	0.998	10.20	0.24	0.997	10.27	0.24	$(15+10)M_{\odot}$	0.998	24.35	0.26	0.994	23.78	0.27	$(5+5)M_{\odot}$	0.998	10.20	0.24	0.997	10.27	0.24	$(15+10)M_{\odot}$	0.998	24.35	0.26	0.994	23.78	0.27	$(5+5)M_{\odot}$	0.998	10.20	0.24	0.997	10.27	0.24
T(3,7/2,+2)	$(20+20)M_{\odot}$	0.999	36.20	0.31	0.995	35.63	0.32	$(20+5)M_{\odot}$	0.997	22.95	0.19	0.993	22.52	0.20	$(20+20)M_{\odot}$	0.999	36.20	0.31	0.995	35.63	0.32	$(20+5)M_{\odot}$	0.997	22.95	0.19	0.993	22.52	0.20	$(20+20)M_{\odot}$	0.999	36.20	0.31	0.995	35.63	0.32	$(20+5)M_{\odot}$	0.997	22.95	0.19	0.993	22.52	0.20
	$(20+15)M_{\odot}$	0.999	31.39	0.31	0.996	31.09	0.32	$(10+10)M_{\odot}$	0.999	18.74	0.28	0.995	18.18	0.30	$(20+15)M_{\odot}$	0.999	31.39	0.31	0.996	31.09	0.32	$(10+10)M_{\odot}$	0.999	18.74	0.28	0.995	18.18	0.30	$(20+15)M_{\odot}$	0.999	31.39	0.31	0.996	31.09	0.32	$(10+10)M_{\odot}$	0.999	18.74	0.28	0.995	18.18	0.30
	$(15+15)M_{\odot}$	0.999	27.63	0.29	0.997	27.02	0.31	$(15+5)M_{\odot}$	0.997	18.61	0.22	0.995	18.15	0.23	$(15+15)M_{\odot}$	0.999	27.63	0.29	0.997	27.02	0.31	$(15+5)M_{\odot}$	0.997	18.61	0.22	0.995	18.15	0.23	$(15+15)M_{\odot}$	0.999	27.63	0.29	0.997	27.02	0.31	$(15+5)M_{\odot}$	0.997	18.61	0.22	0.995	18.15	0.23
	$(20+10)M_{\odot}$	0.999	27.42	0.27	0.996	26.85	0.28	$(10+5)M_{\odot}$	0.998	14.09	0.25	0.994	13.87	0.26	$(20+10)M_{\odot}$	0.999	27.42	0.27	0.996	26.85	0.28	$(10+5)M_{\odot}$	0.998	14.09	0.25	0.994	13.87	0.26	$(20+10)M_{\odot}$	0.999	27.42	0.27	0.996	26.85	0.28	$(10+5)M_{\odot}$	0.998	14.09	0.25	0.994	13.87	0.26
	$(15+10)M_{\odot}$	0.998	23.20	0.28	0.996	22.60	0.29	$(5+5)M_{\odot}$	0.998	9.57	0.27	0.997	9.70	0.26	$(15+10)M_{\odot}$	0.998	23.20	0.28	0.996	22.60	0.29	$(5+5)M_{\odot}$	0.998	9.57	0.27	0.997	9.70	0.26	$(15+10)M_{\odot}$	0.998	23.20	0.28	0.996	22.60	0.29	$(5+5)M_{\odot}$	0.998	9.57	0.27	0.997	9.70	0.26
P(3,7/2,-2)	$(20+20)M_{\odot}$	0.999	35.24	0.33	0.996	35.93	0.32	$(20+5)M_{\odot}$	0.999	23.33	0.18	0.999	23.04	0.19	$(20+20)M_{\odot}$	0.999	35.24	0.33	0.996	35.93	0.32	$(20+5)M_{\odot}$	0.999	23.33	0.18	0.999	23.04	0.19	$(20+20)M_{\odot}$	0.999	35.24	0.33	0.996	35.93	0.32	$(20+5)M_{\odot}$	0.999	23.33	0.18	0.999	23.04	0.19
	$(20+15)M_{\odot}$	1.000	31.72	0.30	0.998	31.59	0.30	$(10+10)M_{\odot}$	0.999	18.74	0.28	0.997	18.27	0.30	$(20+15)M_{\odot}$	1.000	31.72	0.30	0.998	31.59	0.30	$(10+10)M_{\odot}$	0.999	18.74	0.28	0.997	18.27	0.30	$(20+15)M_{\odot}$	1.000	31.72	0.30	0.998	31.59	0.30	$(10+10)M_{\odot}$	0.999	18.74	0.28	0.997	18.27	0.30
	$(15+15)M_{\odot}$	0.999	27.19	0.31	0.998	27.28	0.30	$(15+5)M_{\odot}$	0.999	18.76	0.21	0.998	18.43	0.22	$(15+15)M_{\odot}$	0.999	27.19	0.31	0.998	27.28	0.30	$(15+5)M_{\odot}$	0.999	18.76	0.21	0.998	18.43	0.22	$(15+15)M_{\odot}$	0.999	27.19	0.31	0.998	27.28	0.30	$(15+5)M_{\odot}$	0.999	18.76	0.21	0.998	18.43	0.22
	$(20+10)M_{\odot}$	1.000	27.25	0.27	0.998	27.16	0.27	$(10+5)M_{\odot}$	0.999	14.20	0.25	0.997	13.94	0.26	$(20+10)M_{\odot}$	1.000	27.25	0.27	0.998	27.16	0.27	$(10+5)M_{\odot}$	0.999	14.20	0.25	0.997	13.94	0.26	$(20+10)M_{\odot}$	1.000	27.25	0.27	0.998	27.16	0.27	$(10+5)M_{\odot}$	0.999	14.20	0.25	0.997	13.94	0.26
	$(15+10)M_{\odot}$	0.999	23.01	0.28	0.998	22.80	0.29	$(5+5)M_{\odot}$	0.999	9.61	0.27	0.996	9.60	0.27	$(15+10)M_{\odot}$	0.999	23.01	0.28	0.998	22.80	0.29	$(5+5)M_{\odot}$	0.999	9.61	0.27	0.996	9.60	0.27	$(15+10)M_{\odot}$	0.999	23.01	0.28	0.998	22.80	0.29	$(5+5)M_{\odot}$	0.999	9.61	0.27	0.996	9.60	0.27
P(3,7/2,+2)	$(20+20)M_{\odot}$	1.000	34.70	0.33	0.997	35.41	0.32	$(20+5)M_{\odot}$	1.000	23.15	0.18	0.999	22.85	0.19	$(20+20)M_{\odot}$	1.000	34.70	0.33	0.997	35.41	0.32	$(20+5)M_{\odot}$	1.000	23.15	0.18	0.999	22.85	0.19	$(20+20)M_{\odot}$	1.000	34.70	0.33	0.997	35.41	0.32	$(20+5)M_{\odot}$	1.000	23.15	0.18	0.999	22.85	0.19
	$(20+15)M_{\odot}$	1.000	30.92	0.31	0.998	31.01	0.31	$(10+10)M_{\odot}$	0.999	18.08	0.30	0.998	17.79	0.31	$(20+15)M_{\odot}$	1.000	30.92	0.31	0.998	31.01	0.31	$(10+10)M_{\odot}$	0.999	18.08	0.30	0.998	17.79	0.31	$(20+15)M_{\odot}$	1.000	30.92	0.31	0.998	31.01	0.31	$(10+10)M_{\odot}$	0.999	18.08	0.30	0.998	17.79	0.31
	$(15+15)M_{\odot}$	1.000	26.55	0.32	0.998	26.67	0.31	$(15+5)M_{\odot}$	1.000	18.38	0.22	0.998	18.12	0.23	$(15+15)M_{\odot}$	1.000	26.55	0.32	0.998	26.67	0.31	$(15+5)M_{\odot}$	1.000	18.38	0.22	0.998	18.12	0.23	$(15+15)M_{\odot}$	1.000	26.55	0.32	0.998	26.67	0.31	$(15+5)M_{\odot}$	1.000	18.38	0.22	0.998	18.12	0.23
	$(20+10)M_{\odot}$	1.000	26.62	0.28	0.998	26.78	0.28	$(10+5)M_{\odot}$	0.999	13.84	0.26	0.998	13.64	0.26	$(20+10)M_{\odot}$	1.000	26.62	0.28	0.998	26.78	0.28	$(10+5)M_{\odot}$	0.999	13.84	0.26	0.998	13.64	0.26	$(20+10)M_{\odot}$	1.000	26.62	0.28	0.998	26.78	0.28	$(10+5)M_{\odot}$	0.999	13.84	0.26	0.998	13.64	0.26
	$(15+10)M_{\odot}$	0.999	22.49	0.29	0.999	22.26	0.30	$(5+5)M_{\odot}$	0.999	9.31	0.28	0.996	9.39	0.28	$(15+10)M_{\odot}$	0.999	22.49	0.29	0.999	22.26	0.30	$(5+5)M_{\odot}$	0.999	9.31	0.28	0.996	9.39	0.28	$(15+10)M_{\odot}$	0.999	22.49	0.29	0.999	22.26	0.30	$(5+5)M_{\odot}$	0.999	9.31				

		FF for projection onto EP(3,7/2,0), for $0 < \eta < 1$														
		mn				M				mnc						
		mm	M	η	f_{cut}	mm	M	η	f_{cut}	mm	M	η	f_{cut}			
T(2,5/2)	(20+20) M_{\odot}	0.946	26.51	0.48	0.946	26.32	0.49	303.0	(20+5) M_{\odot}	0.978	13.92	0.45	0.992	13.84	0.46	387.6
	(20+15) M_{\odot}	0.953	21.91	0.55	0.953	21.90	0.55	354.7	(10+10) M_{\odot}	0.983	12.13	0.61	0.983	12.13	0.61	624.9
	(15+15) M_{\odot}	0.961	18.61	0.58	0.961	18.55	0.58	413.4	(15+5) M_{\odot}	0.983	10.91	0.56	0.984	11.81	0.48	620.8
	(20+10) M_{\odot}	0.970	15.51	0.75	0.970	15.60	0.74	464.4	(10+5) M_{\odot}	0.989	9.22	0.53	0.989	9.22	0.53	853.3
	(15+10) M_{\odot}	0.972	15.03	0.59	0.989	13.83	0.70	384.9	(5+5) M_{\odot}	0.988	6.83	0.49	0.989	6.92	0.47	639.2
T(3,7/2,-2)	(20+20) M_{\odot}	0.979	53.03	0.12	0.990	41.41	0.25	125.0	(20+5) M_{\odot}	0.955	25.92	0.15	0.999	25.85	0.15	202.7
	(20+15) M_{\odot}	0.970	45.77	0.13	0.986	34.24	0.27	133.9	(10+10) M_{\odot}	0.979	22.82	0.19	0.981	19.40	0.27	217.5
	(15+15) M_{\odot}	0.965	38.14	0.14	0.997	33.58	0.20	174.2	(15+5) M_{\odot}	0.978	22.03	0.15	0.998	20.78	0.18	248.7
	(20+10) M_{\odot}	0.962	34.66	0.16	0.981	28.60	0.26	151.3	(10+5) M_{\odot}	0.985	16.44	0.19	0.999	15.88	0.20	329.1
	(15+10) M_{\odot}	0.971	28.59	0.18	0.998	27.43	0.20	201.8	(5+5) M_{\odot}	0.993	10.70	0.22	0.999	10.66	0.22	474.0
T(3,7/2,+2)	(20+20) M_{\odot}	0.975	50.20	0.14	0.991	39.34	0.27	130.3	(20+5) M_{\odot}	0.956	25.15	0.16	0.998	24.73	0.16	203.5
	(20+15) M_{\odot}	0.964	43.47	0.14	0.996	36.64	0.22	152.4	(10+10) M_{\odot}	0.980	21.67	0.21	0.997	20.80	0.23	262.2
	(15+15) M_{\odot}	0.961	33.63	0.19	0.998	31.35	0.23	175.8	(15+5) M_{\odot}	0.973	20.04	0.19	0.999	20.16	0.18	258.0
	(20+10) M_{\odot}	0.963	32.90	0.18	0.998	31.04	0.21	175.7	(10+5) M_{\odot}	0.985	15.27	0.21	0.999	15.12	0.22	339.6
	(15+10) M_{\odot}	0.971	27.32	0.20	0.998	26.01	0.22	211.3	(5+5) M_{\odot}	0.995	10.06	0.25	0.999	10.02	0.25	493.4
P(2,5/2)	(20+20) M_{\odot}	0.931	51.44	0.13	0.997	42.91	0.22	109.1	(20+5) M_{\odot}	0.938	27.91	0.13	0.998	26.56	0.14	171.5
	(20+15) M_{\odot}	0.932	47.52	0.11	0.991	34.56	0.26	119.4	(10+10) M_{\odot}	0.961	24.07	0.17	0.997	21.50	0.22	213.0
	(15+15) M_{\odot}	0.948	37.45	0.15	0.997	32.77	0.21	145.2	(15+5) M_{\odot}	0.961	22.22	0.15	0.994	20.01	0.19	201.9
	(20+10) M_{\odot}	0.941	37.07	0.14	0.997	32.21	0.19	143.8	(10+5) M_{\odot}	0.977	16.12	0.19	0.998	15.80	0.20	282.2
	(15+10) M_{\odot}	0.949	30.16	0.16	0.998	27.08	0.21	175.2	(5+5) M_{\odot}	0.992	10.36	0.23	0.999	10.34	0.24	410.4
P(3,7/2,-2)	(20+20) M_{\odot}	0.964	51.21	0.13	0.995	40.49	0.25	126.9	(20+5) M_{\odot}	0.951	25.45	0.15	0.999	25.10	0.16	195.2
	(20+15) M_{\odot}	0.949	39.73	0.18	0.999	35.96	0.23	146.3	(10+10) M_{\odot}	0.977	21.76	0.21	0.999	20.23	0.24	247.0
	(15+15) M_{\odot}	0.959	33.53	0.19	0.999	30.68	0.24	170.5	(15+5) M_{\odot}	0.970	20.36	0.18	0.998	20.09	0.18	239.4
	(20+10) M_{\odot}	0.956	33.61	0.17	0.998	31.24	0.20	172.2	(10+5) M_{\odot}	0.985	14.97	0.22	0.999	15.07	0.22	331.1
	(15+10) M_{\odot}	0.964	27.56	0.19	0.998	25.57	0.23	201.1	(5+5) M_{\odot}	0.994	10.07	0.25	1.000	10.09	0.25	493.0
P(3,7/2,+2)	(20+20) M_{\odot}	0.962	50.35	0.13	0.996	42.28	0.21	135.7	(20+5) M_{\odot}	0.951	25.37	0.15	0.998	24.69	0.16	191.9
	(20+15) M_{\odot}	0.953	43.10	0.14	0.997	35.06	0.24	147.8	(10+10) M_{\odot}	0.976	21.04	0.22	0.999	19.62	0.26	253.0
	(15+15) M_{\odot}	0.959	32.97	0.20	0.996	31.31	0.22	185.3	(15+5) M_{\odot}	0.970	20.00	0.19	1.000	19.42	0.20	242.2
	(20+10) M_{\odot}	0.955	32.79	0.18	0.996	31.11	0.20	177.0	(10+5) M_{\odot}	0.986	14.63	0.23	0.999	14.68	0.23	322.5
	(15+10) M_{\odot}	0.964	26.97	0.20	0.998	24.86	0.24	204.0	(5+5) M_{\odot}	0.994	9.76	0.26	0.999	9.83	0.26	498.3
ET(2,5/2)	(20+20) M_{\odot}	0.997	35.38	0.30	0.998	35.47	0.30	244.7	(20+5) M_{\odot}	0.994	22.55	0.19	0.996	22.18	0.19	337.2
	(20+15) M_{\odot}	0.997	30.97	0.30	0.998	30.66	0.31	281.2	(10+10) M_{\odot}	0.998	17.75	0.30	0.999	17.47	0.31	490.2
	(15+15) M_{\odot}	0.998	26.44	0.31	0.998	26.57	0.30	325.5	(15+5) M_{\odot}	0.996	17.98	0.22	0.997	17.77	0.23	439.9
	(20+10) M_{\odot}	0.998	26.97	0.26	0.998	26.99	0.26	324.0	(10+5) M_{\odot}	0.997	13.16	0.28	0.997	13.15	0.28	663.7
	(15+10) M_{\odot}	0.999	22.21	0.29	0.998	22.19	0.29	387.3	(5+5) M_{\odot}	0.999	8.61	0.32	0.999	8.63	0.32	987.2
ET(3,7/2,-2)	(20+20) M_{\odot}	0.997	43.91	0.21	0.998	43.90	0.21	202.1	(20+5) M_{\odot}	0.999	26.17	0.15	0.999	26.22	0.15	338.1
	(20+15) M_{\odot}	0.998	37.31	0.22	0.999	37.68	0.22	232.0	(10+10) M_{\odot}	1.000	21.67	0.22	1.000	21.70	0.22	403.1
	(15+15) M_{\odot}	0.997	32.97	0.21	0.998	32.66	0.21	269.5	(15+5) M_{\odot}	1.000	21.20	0.17	1.000	21.20	0.17	421.1
	(20+10) M_{\odot}	0.998	32.56	0.19	1.000	32.22	0.20	275.1	(10+5) M_{\odot}	1.000	16.09	0.20	1.000	16.10	0.20	545.8
	(15+10) M_{\odot}	1.000	26.98	0.21	1.000	26.98	0.21	328.1	(5+5) M_{\odot}	0.999	10.79	0.22	0.999	10.82	0.22	810.2
ET(3,7/2,+2)	(20+20) M_{\odot}	0.996	40.97	0.24	1.000	41.43	0.23	212.6	(20+5) M_{\odot}	1.000	25.46	0.15	1.000	25.47	0.15	346.5
	(20+15) M_{\odot}	1.000	36.14	0.23	1.000	36.18	0.23	243.9	(10+10) M_{\odot}	1.000	20.68	0.24	1.000	20.58	0.24	401.5
	(15+15) M_{\odot}	1.000	30.87	0.24	1.000	30.87	0.24	285.4	(15+5) M_{\odot}	0.999	20.47	0.18	1.000	20.49	0.18	432.2
	(20+10) M_{\odot}	0.998	30.88	0.21	1.000	30.77	0.21	287.4	(10+5) M_{\odot}	0.999	15.40	0.21	1.000	15.37	0.21	570.3
	(15+10) M_{\odot}	0.999	25.98	0.22	0.999	25.81	0.23	340.2	(5+5) M_{\odot}	0.999	10.25	0.24	0.999	10.24	0.24	861.9
EP(2,5/2)	(20+20) M_{\odot}	0.993	42.28	0.23	0.994	41.85	0.24	210.8	(20+5) M_{\odot}	0.998	26.65	0.14	0.998	26.68	0.14	335.4
	(20+15) M_{\odot}	0.994	37.02	0.23	0.994	36.85	0.23	238.2	(10+10) M_{\odot}	0.998	21.68	0.22	0.998	21.68	0.22	408.9
	(15+15) M_{\odot}	0.993	31.81	0.23	0.994	31.85	0.23	278.3	(15+5) M_{\odot}	0.998	21.37	0.17	0.999	21.42	0.17	420.1
	(20+10) M_{\odot}	0.995	32.05	0.20	0.995	32.07	0.20	277.4	(10+5) M_{\odot}	0.998	16.15	0.19	0.998	16.06	0.20	553.4
	(15+10) M_{\odot}	0.995	26.91	0.21	0.995	26.73	0.21	331.7	(5+5) M_{\odot}	0.998	10.74	0.22	0.998	10.74	0.22	817.3
EP(3,7/2,-2)	(20+20) M_{\odot}	0.999	40.75	0.24	1.000	40.80	0.24	213.6	(20+5) M_{\odot}	1.000	25.26	0.16	1.000	25.26	0.16	353.0
	(20+15) M_{\odot}	1.000	35.81	0.24	1.000	35.92	0.23	244.5	(10+10) M_{\odot}	0.999	20.52	0.24	1.000	20.49	0.24	426.7
	(15+15) M_{\odot}	0.999	30.78	0.24	1.000	30.53	0.24	284.6	(15+5) M_{\odot}	1.000	20.30	0.18	1.000	20.28	0.18	434.7
	(20+10) M_{\odot}	1.000	30.66	0.21	1.000	30.60	0.21	286.9	(10+5) M_{\odot}	1.000	15.29	0.21	1.000	15.31	0.21	572.7
	(15+10) M_{\odot}	0.999	25.50	0.23	1.000	25.55	0.23	342.8	(5+5) M_{\odot}	0.999	10.18	0.24	1.000	10.21	0.24	855.0
EP(3,7/2,+2)	(20+20) M_{\odot}	0.999	39.67	0.25	1.000	39.68	0.25	218.4	(20+5) M_{\odot}	0.999	24.99	0.16	1.000	24.93	0.16	354.4
	(20+15) M_{\odot}	0.999	34.65	0.25	1.000	34.82	0.25	252.8	(10+10) M_{\odot}	0.998	20.00	0.25	1.000	19.99	0.25	441.9
	(15+15) M_{\odot}	0.998	30.00	0.25	1.000	29.94	0.25	289.9	(15+5) M_{\odot}	0.999	19.92	0.19	1.000	19.93	0.19	443.1
	(20+10) M_{\odot}	1.000	29.93	0.22	1.000	29.86	0.22	292.2	(10+5) M_{\odot}	1.000	14.94	0.22	1.000	14.96	0.22	584.7
	(15+10) M_{\odot}	1.000	24.88	0.24	1.000	24.87	0.24	350.4	(5+5) M_{\odot}	1.000	9.98	0.25	1.000	9.98	0.25	881.1
HT(3,7/2,-2)	(20+20) M_{\odot}	0.981	22.27	0.98	0.981	22.23	0.98	302.5</								

4.9 Bibliography

- [1] A. Abramovici et al., *Science* **256**, 325 (1992); B. Caron et al., *Class. Quantum Grav.* **14**, 1461 (1997); H. Lück et al., *Class. Quantum Grav.* **14**, 1471 (1997); M. Ando et al., [astro-ph/0105473](#).
- [2] C. L. Fryer and V. Kalogera, *Astrophys. J.* **554**, 548 (2001).
- [3] C. W. Lincoln and C. M. Will, *Phys. Rev. D* **42**, 1123 (1990).
- [4] K. S. Thorne, in *300 Years of Gravitation*, S. W. Hawking and W. Israel, eds. (Cambridge University Press, Cambridge, England, 1987); pp. 330–458.
- [5] V. M. Lipunov, K. A. Postnov and M. E. Prokhorov, *New Astron.* **2**, 43 (1997).
- [6] K. Belczynski, V. Kalogera, and T. Bulik, *Astrophys. J.* **572**, in print (2002); V. Kalogera, R. Narayan, D. N. Spergel, and J. H. Taylor, *ibid.* **556**, 340 (2001); V. Kalogera, in *Gravitational Waves, Proceedings of the Third Edoardo Amaldi Conference*, S. Meshkov, ed. (AIP, Woodbury NY, 2000), [astro-ph/9911532](#); V. Kalogera, *Astrophysical Sources of Gravitational Radiation for Ground-Based Gravitational-Wave Detectors*, J. M. Centrella, ed. (AIP, Woodbury NY, 2001), [astro-ph/0101047](#).
- [7] K. S. Thorne, “The scientific case for mature LIGO interferometers,” LIGO Document Number P000024-00-R, www.ligo.caltech.edu/docs/P/P000024-00.pdf.
- [8] S. F. Portegies Zwart and S. L. McMillan, *Astrophys. J.* **528**, L17 (2000).
- [9] M. C. Miller and D. P. Hamilton, [astro-ph/0202298](#).
- [10] T. Damour, *300 Years of Gravitation*, S. W. Hawking and W. Israel, eds. (Cambridge University Press, Cambridge, England, 1987); L. Blanchet, *Gravitational radiation from postnewtonian sources and inspiraling compact binaries*, *Living Reviews in Relativity*, www.livingreviews.org (2000).
- [11] É. É. Flanagan and S. A. Hughes, *Phys. Rev. D* **57**, 4535 (1998); **57**, 4566 (1998).
- [12] T. Damour, B. R. Iyer, and B. S. Sathyaprakash, *Phys. Rev. D* **63**, 044023 (2001).
- [13] G. B. Cook, *Phys. Rev. D* **50**, 5025 (1994).
- [14] A. Buonanno and T. Damour, *Phys. Rev. D* **59**, 084006 (1999).
- [15] A. Buonanno and T. Damour, *Phys. Rev. D* **62**, 064015 (2000).
- [16] T. Damour, P. Jaranowski, and G. Schäfer, *Phys. Rev. D* **62**, 084011 (2000).

- [17] A. Buonanno and T. Damour, proceedings of the IX Marcel Grossmann Meeting, Rome, July 2000, [gr-qc/0011052](#).
- [18] J. Baker, B. Brüggmann, M. Campanelli, C. O. Lousto, and R. Takahashi, *Phys. Rev. Lett.* **87**, 121103 (2001); J. Baker, M. Campanelli, C. O. Lousto, and R. Takahashi, “Modeling gravitational radiation from coalescing binary black holes,” [astro-ph/0202469](#).
- [19] L. E. Kidder, C. M. Will and A. G. Wiseman, *Phys. Rev. D* **47**, 4183(R) (1993); L. E. Kidder, *ibid.* **52**, 821 (1995).
- [20] T. A. Apostolatos, C. Cutler, G. J. Sussman and K. S. Thorne, *Phys. Rev. D* **15**, 6274 (1994); T. A. Apostolatos, *ibid.* **54**, 2438 (1996).
- [21] A. Buonanno, Y. Chen, and M. Vallisneri, in preparation.
- [22] P. R. Brady, J. D. E. Creighton, and K. S. Thorne, *Phys. Rev. D* **58**, 061501 (1998).
- [23] T. W. Baumgarte, *Phys. Rev. D* **62**, 024018 (2000).
- [24] H. P. Pfeiffer, S. A. Teukolsky, and G. B. Cook *Phys. Rev. D* **62**, 104018 (2000).
- [25] E. Gourgoulhon, P. Grandclément, and S. Bonazzola, *Phys. Rev. D* **65**, 044020 (2002); P. Grandclément, E. Gourgoulhon, and S. Bonazzola, *ibid.* **65**, 044021 (2002).
- [26] T. Damour, B. R. Iyer, and B. S. Sathyaprakash, *Phys. Rev. D* **57**, 885 (1998).
- [27] B. J. Owen, *Phys. Rev. D* **53**, 6749–6761 (1996).
- [28] L. S. Finn, *Phys. Rev. D* **46**, 5236–5249 (1992).
- [29] M. H. A. Davis, in *Gravitational Wave Data Analysis*, B. F. Schutz, ed. (Kluwer, Dordrecht, 1989).
- [30] L. S. Finn and D. F. Chernoff, *Phys. Rev. D* **47**, 2198–2219 (1993).
- [31] L. A. Wainstein and L. D. Zubakov, *Extraction of signals from noise* (Prentice-Hall, Englewood Cliffs NJ, 1962).
- [32] A. V. Oppenheim, A. S. Willskly. and I. T. Young, *Signals and systems* (Prentice-Hall, Englewood Cliffs, NJ, 1983).
- [33] J. C. Hancock and P. A. Wintz, *Signal detection theory* (McGraw-Hill, New York, 1966).
- [34] C. Cutler and É. É. Flanagan, *Phys. Rev. D* **49**, 2658 (1994).
- [35] M. Abramowitz and I. A. Stegun, *Handbook of mathematical functions* (Dover, New York, 1972), pp. 299–300.

- [36] B. F. Schutz, in *The Detection of Gravitational Radiation*, D. Blair, ed. (Cambridge University Press, Cambridge, England, 1989).
- [37] C. Cutler et al., *Phys. Rev. Lett.* **70**, 2984 (1993).
- [38] T. A. Apostolatos, *Phys. Rev. D* **52**, 605 (1995).
- [39] B. S. Sathyaprakash and S. V. Dhurandhar, *Phys. Rev. D* **44**, 3819 (1991); S. V. Dhurandhar and B. S. Sathyaprakash, *ibid.* **49**, 1707 (1994); B. S. Sathyaprakash, *ibid.* **50**, R7111 (1994).
- [40] B. J. Owen and B. Sathyaprakash, *Phys. Rev. D* **60**, 022002 (1999).
- [41] A. E. Chronopoulos and T. A. Apostolatos, *Phys. Rev. D* **64**, 042003 (2001).
- [42] T. Damour and N. Deruelle, *Phys. Lett.* **87A**, 81 (1981); T. Damour, *C. R. Séances Acad. Sci. Ser. 2* **294**, 1355 (1982).
- [43] P. Jaranowski and G. Schäfer, *Phys. Rev. D* **57**, 7274 (1998); *ibid.* **60**, 124003 (1999); T. Damour, P. Jaranowski, and G. Schäfer, *Phys. Rev. D* **62**, 044024 (2000); *ibid.*, 021501(R) (2000); **63**, 044021 (2001).
- [44] L. Blanchet and G. Faye, *Phys. Lett.* **A271**, 58 (2000); *J. Math. Phys* **42**, 4391 (2001); *Phys. Rev. D* **63**, 062005 (2000); V. C. de Andrade, L. Blanchet, and G. Faye, *Class. Quant. Grav.* **18**, 753 (2001).
- [45] T. Damour, P. Jaranowski, and G. Schäfer, *Phys. Lett. B* **513**, 147 (2001).
- [46] R. V. Wagoner and C. M. Will, *Astrophys. J.* **210**, 764 (1976).
- [47] L. Blanchet, T. Damour, B. R. Iyer, C. M. Will, and A. G. Wiseman, *Phys. Rev. Lett.* **74**, 3515 (1995); L. Blanchet, T. Damour, and B. R. Iyer, *Phys. Rev. D* **51**, 536 (1995); C. M. Will and A. G. Wiseman, *ibid.* **54**, 4813 (1996).
- [48] L. Blanchet, *Phys. Rev. D* **54**, 1417 (1996); L. Blanchet, *Class. Quantum Grav.* **15**, 113 (1998).
- [49] L. Blanchet, G. Faye, B. R. Iyer, and B. Joguet, *Phys. Rev. D* **65**, 061501 (2002); L. Blanchet, B. R. Iyer, and B. Joguet, *ibid.* **65**, 064005 (2002).
- [50] L. Blanchet, G. Faye, B. R. Iyer, and B. Joguet, [gr-qc/0105098](#).
- [51] L. Blanchet, “Innermost circular orbit of binary black holes at the third postnewtonian approximation,” [gr-qc/0112056](#).
- [52] C. M. Bender and S. A. Orszag, *Advanced Mathematical Methods for Scientists and Engineers* (McGraw Hill, Singapore, 1984).

- [53] T. Damour, B. R. Iyer, and B. S. Sathyaprakash, *Phys. Rev. D* **62**, 084036 (2000).
- [54] L. E. Kidder, C. M. Will, and A. G. Wiseman, *Class. Quantum Grav.* **9**, L127 (1992); *Phys. Rev. D* **47**, 3281 (1993).
- [55] B. R. Iyer and C. Will, *Phys. Rev. Lett.* **70**, 113 (1993); *Phys. Rev. D* **52**, 6882 (1995); A. Gopakumar, B. R. Iyer, and C. Will, *ibid.* **55**, 6030 (1997).
- [56] E. Porter, “Computational resources to filter gravitational wave data with P approximant templates,” [gr-qc/0203020](#).
- [57] W. H. Press, S. A. Teukolsky, W. T. Vetterling, and B. P. Flannery, *Numerical recipes in C: the art of scientific computing* (Cambridge University Press, Cambridge, England, 1992).
- [58] F. A. Jenet and T. Prince, *Phys. Rev. D* **62**, 122001 (2000).
- [59] J. Edlund, T. Prince, and M. Tinto, in preparation.
- [60] T. Damour, P. Grandclément, and E. Gourgoulhon, “Circular orbits of corotating binary black holes: comparison between analytical and numerical results,” [gr-qc/0204011](#).